Organic Scintillators in Nonproliferation Applications With a Hybridized Double-Pulse Rejection Technique

by
Mark Mitchell Bourne

A dissertation submitted in partial fulfillment
of the requirements for the degree of
Doctor of Philosophy
(Nuclear Engineering and Radiological Sciences)
in the University of Michigan
2016

Doctoral Committee:

Professor Sara A. Pozzi, Chair
Associate Research Scientist Shaun D. Clarke
Staff Scientist Andrey Gueorguiev, Radiation Monitoring Devices, Inc.
Assistant Professor Thomas A. Schwarz
Professor David K. Wehe

Acknowledgements

There is a long list of people without whom I would not have made it this far. I can say with confidence that my career would have turned out very different had it not been for my advisor, Dr. Sara Pozzi. She provided me with numerous opportunities to build my career in nonproliferation research, starting with research at Michigan, then travelling to conferences and connecting me to her colleagues at Los Alamos National Laboratory. I developed and fine-tuned my technical writing, presentation, and MCNP skills with the generous assistance of Dr. Shaun Clarke, my supervisor from my first modeling project in 2008 through the end of this thesis. Through classwork and lectures, my professors in the NERS department provided a strong foundation to build my academic career, from the radiation detection class taught by Professor Zhong He to the reactor kinetics class taught by Professor Thomas Downar.

I also thank Angela DiFulvio, Marc Paff, and Marc Ruch for taking time during their measurement campaigns at Idaho National Laboratory and the Joint Research Centre in Ispra, Italy to conduct additional experiments and make this thesis possible. Really, every student in the Detection for Nuclear Nonproliferation Group was willing to lend me their assistance and expertise at a moment's notice.

My dad, mom, brothers, and extended family provide me with a constant stream of praise, love, and encouragement throughout my academic career. Constant nicknames of genius give me a goalpost to work towards. This degree is hopefully just the beginning.

This work was funded in-part by the National Science Foundation and the Domestic Nuclear Detection Office of the Department of Homeland Security through the Academic Research Initiative Award # CMMI 0938909. This research was also funded in-part by the Consortium for Verification Technology under Department of Energy National Nuclear Security Administration award number DE-NA0002534.

Table of Contents

List of Figures

List of Tables

List of Appendices

List of Abbreviations

α	alpha particle, or ^{4}He nucleus
γ	gamma ray photon
DNNG	Detection for Nuclear Nonproliferation Group
FOM	figure of merit, used for optimizing PSD
HEU	highly-enriched uranium
INL	Idaho National Laboratory
IO	Inrad Optics, Inc.
JRC	Joint Research Centre
keVee	kilo-electron volt electron equivalent, amount of light from 1 keV of electron energy deposited into an organic scintillator
LLNL	Lawrence Livermore National Laboratories
MeVee	mega-electron volt electron equivalent
MOX	mixed uranium-plutonium oxide
n	neutron particle
NN	neutron-neutron correlation
NNN	neutron-neutron-neutron correlation
NP	neutron-gamma ray correlation
PHD	pulse height distribution

PMT	photomultiplier tube
PN	gamma ray-neutron correlation
PP	gamma ray-gamma ray correlation
PSD	pulse-shape discrimination
RMD	Radiation Monitoring Devices, Inc.
SF	spontaneous fission
SHV	safe high voltage
SNM	Special Nuclear Material, defined as plutonium and enriched uranium

Chapter 1. Introduction

In 2012, United States President Barack Obama declared that nuclear terrorism is "one of the most urgent and serious threats to global security" in today's society [1]. The greatest barrier against building a nuclear weapon is the difficulty of acquiring special nuclear material (SNM), which is defined as plutonium or uranium enriched in ^{233}U or ^{235}U beyond 20%. The synthesis of this material requires costly and heavily regulated infrastructure, so a rogue entity is more likely to acquire existing SNM rather than produce their own.

The ability to accurately account for and safeguard SNM in all current (and former) weapon states is necessary to combat nuclear terrorism. Tens of thousands of nuclear weapons were produced between the United States and the Soviet Union in an arms race during the Cold War. The arms race ended with the fall of the Soviet Union in 1991, and the Strategic Arms Reduction Treaty was signed to both limit and reduce stockpiles between the two countries. However, some nuclear material located in former Soviet Union states became either unaccounted for or inadequately guarded during a prolonged period of political instability in that region of the world. As a result, it is insufficient to only account for SNM in known stockpiles because material is already presumed missing.

Demand for detection of nuclear materials has increased following the September 11, 2001 terrorist attacks in the United States [2]. The most common detector used for detecting SNM in homeland security applications is ^{3}He-gas filled proportional counters. The primary means of producing ^{3}He is as a decay product from tritium (^{3}H), with a half-life of 12.3 years. While tritium was produced in large quantities during the nuclear weapons program, it is only produced today in minimal quantities to maintain the weapons stockpile. As a result, the nuclear weapons program no longer produces enough ^{3}He to satisfy the increased demand by itself, and the price of ^{3}He has increased from $200 per liter to $2,000 per liter [2]. This price increase has driven investments in alternative detection technologies, reducing demand for ^{3}He to levels that can be met by current production levels [3].

One alternative detection technology is organic scintillation detectors, which have significant advantages over ^{3}He when used in certain safeguards applications. The timing of scintillators is on the order of nanoseconds [4], allowing for greater fidelity in measurements of correlated particles than ^{3}He, whose timing is on the order of microseconds. ^{3}He tubes function best after thermalizing incident neutrons, so they cannot obtain original fast energy information from the incident thermalized neutron flux. Organic scintillators, on the other hand, detect fast neutrons, so measured light pulses can be related to the incident neutron energy spectrum. Organic scintillators are also sensitive to gamma-ray radiation, and through the use of pulse-shape discrimination (PSD), organic scintillators can identify neutron and gamma ray pulses separately. Sensitivity to gamma rays can sometimes yield useful information about measured source emissions compared to ^{3}He proportional counters.

1.1. Problem Description

Detector sensitivity to gamma rays can be a disadvantage when counting neutrons with organic scintillators, including SNM measurements of plutonium. When the number of gamma rays is much greater than the number of neutrons in an environment, gamma-ray events can overlap in the scintillator. These events, called double pulses or pileup pulses, can make gamma rays look more like neutrons when using the PSD technique. Many homeland security applications set alarm thresholds on the detection of neutrons, so alarming on gamma rays misclassified as neutrons increases the rate of false alarm events. To be considered for homeland security applications, ANSI standards state the false alarm rate cannot exceed 1 per 1000 measurements [5]. ^{3}He is the default technology to mitigate this problem because it is nearly insensitive to gamma rays, so false alarms from incident gamma rays are rare. To prevent organic scintillators from alarming on gamma rays that look like neutrons, one can use lead shielding, which is very heavy and difficult to implement in a portable system, or change the PSD settings to reduce the number of gamma-ray misclassifications, which sacrifices neutron detection efficiency. Pileup rejection electronics have been utilized in gamma-ray spectroscopic applications to improve energy resolution in gamma-ray spectra [6, 7]. This work seeks to develop double-pulse rejection algorithms that removes gamma-ray pileup pulses, reducing gamma-ray misclassifications while preserving as many true neutron counts as possible in organic scintillators.

Contrary to gamma-ray sources, neutron sources are inherently interesting to measure because only a few types of materials can even emit neutrons, and SNM is included in this short list. Some neutron sources such as AmLi or ^{252}Cf emit neutrons but aren't classified as SNM. Neutron correlation measurements can be used to distinguish SNM from other neutron sources. ^{3}He can measure correlated neutrons by measuring multiplicity, but is limited by the timescale of acquisition. Organic scintillators operate on the order of nanoseconds, short enough to differentiate between particles emitted from separate fission events [4]. When combined with the scintillator's sensitivity to gamma rays and detection of fast neutrons, this larger set of parameters allows for better distinction between SNM and non-threat neutron sources. This work shows how cross-correlation can be used to distinguish plutonium sources from ^{252}Cf using organic scintillators.

Innovations in stilbene and plastic scintillators motivate further investigation on the range of applications for these scintillators in nonproliferation. Traditional plastic scintillators have never possessed significant PSD capabilities, which require organic molecules to diffuse through the scintillator following excitation events. The diffusion length of organic molecules was increased in EJ-299-33 with the increased concentration of the fluorophore inside the scintillator, enabling PSD in the scintillator at the cost of light production [8]. The capability of PSD in plastic scintillators, when combined with plastic scintillator scalability to larger sizes, may allow for plastic scintillators to replace liquid scintillators in certain applications.

Stilbene scintillators, on the other hand, have exhibited excellent PSD for very accurate identification of neutron and gamma ray induced detector responses. Traditional melt-based stilbene scintillators synthesis techniques cannot reliably grow crystals to sizes greater than 2.5 centimeters in diameter [9]. In 2013, improvements in stilbene synthesis techniques were demonstrated that yielded crystals that can be more reliably grown to sizes of 5 centimeters in diameter or larger [10]. Larger stilbene crystals can now be inserted into any application using same-size liquid or plastic scintillators and thus improve PSD accuracy. Better PSD allows for increased flexibility during neutron and gamma-ray measurements, including lowering the detection threshold for improved efficiency. Although stilbene crystals cannot be scaled into large sizes as easily as liquids or plastics, one could imagine applications that utilize several smaller stilbene crystals together to obtain a similar effect. This work seeks to determine the

performance gains and losses by using stilbene and PSD-capable plastic scintillators over an equal-volume liquid scintillator in nonproliferation applications.

1.2. Contributions from this Work

This work increased the range of application for organic scintillators when measuring neutrons in a high-gamma ray field. A hybridized double-pulse rejection algorithm was developed that focuses on removing overlapping gamma-ray events without significantly sacrificing neutron efficiency. Stilbene, EJ-309 liquid, and PSD-capable plastic scintillators were tested with ^{252}Cf experiments in fields of 1000 gamma rays per ^{252}Cf neutron. It was found that each organic scintillator could detect neutrons in this environment without using lead. In particular, stilbene was capable of detecting neutrons with intrinsic efficiency of 13-20%, greater than EJ-309 liquid and PSD-capable plastic, while misclassifying gamma rays as neutrons only 10^{-6}-10^{-5} of the time, lower than EJ-309 liquid and PSD-capable plastic.

The double-pulse rejection algorithm was applied directly to measurements of various plutonium samples. In the process, accurate Monte Carlo models were developed in a separate experiment using time-of-flight to measure the neutron energy-to-light output relationship. Experimental data were processed with each method of double-pulse rejection to show how double pulses affected the measured neutron light output spectrum. These spectra were benchmarked to Monte Carlo models of each source, using the known neutron response from stilbene to determine which rejection method yielded the most accurate answer. A simple, measureable metric was identified that would allow a user to immediately determine which rejection method is most appropriate for measuring the neutron emissions from an unknown source. It was found that, after filtering data with the fractional rejection algorithm, data with a measured gamma ray-to-neutron ratio of greater than 100 should be processed with fractional or hybrid rejection, while data with a gamma ray-to-neutron ratio of 10 or less should be processed with template rejection, or no double-pulse rejection at all.

Stilbene, EJ-309 liquid, and PSD-capable plastic scintillators were used in cross-correlation experiments with ^{252}Cf, mixed uranium-plutonium oxide (MOX) powder, and plutonium metal. Each detector utilized the varying multiplicity between ^{252}Cf and plutonium to discriminate between each sample from their respective correlated and uncorrelated neutron emissions. The hybridized double-pulse rejection algorithm allowed for neutron detection to

most accurately predict true neutron-neutron correlations, improving the efficiency in each detector. It was found that each scintillator could differentiate plutonium samples from a ^{252}Cf source using the single and correlated neutron counts from each source. This capability is especially important for the EJ-299-33 plastic scintillator, which sacrifices both neutron efficiency and PSD accuracy relative to stilbene and the EJ-309 liquid.

Chapter 2. Neutron and Gamma Ray Detection

Radiation sources, including SNM, are characterized by their neutron and gamma ray emissions. The optimal detector system for any given application will vary based on the sources measured, the geometry of the measurement, and desired information from the measurement.

Gamma ray spectroscopy systems predominantly detect gamma rays by photoelectric absorption, yielding the full energy from a radiation source that can be directly tied to a particular radioisotope. Uranium samples are easily identified by their 186-keV and 1001-keV gamma emissions, and the ratio of the intensity of these gamma-ray emissions are directly related to enrichment in 235U [11]. Some international safeguards applications desire verification of SNM quantities without revealing details about source isotopics; in these applications, state-of-the-art gamma ray spectroscopy systems such as high-purity germanium (HPGe) cannot be used because they reveal too much information about the source composition [12]. Self-shielding in large-volume or high-density samples reduce the intensity of gamma-ray emissions relative to the mass of the sample, further limiting verification of SNM content in some safeguards applications. [13].

Neutron emissions, on the other hand, are not subject to these limitations. Materials release neutrons either as a result of fission or from nuclear reactions such as (α, n), (γ, n), (p, n), etc. Both fission neutrons and alpha particles are predominant in higher actinides, including SNM, so it is easier to identify SNM without revealing additional source information. Neutrons from fission are highly energetic and can easily penetrate the SNM emitting them. As a result, the intensity of neutron emissions is more closely tied to the mass of source material regardless of size [14]. This work focuses on scintillation detectors, which detect both neutrons and gamma rays. For neutron detection, organic scintillation detectors should match or exceed the performance of ^{3}He gas tubes, which function primarily as thermal neutron counters.

2.1. Helium-3 Detectors

As stated in Chapter 1, ^{3}He proportional counters are the safeguards standard for detecting neutron emissions from SNM. ^{3}He functions by detecting neutron capture reactions in a gas tube filled with ^{3}He typically to pressures between 2 and 10 atmospheres, although tubes are sold with gas pressures as high as 20 atmospheres [15]. A neutron capture event produces ions in the gas, creating free electrons in the gas. Measuring the electron charge over time yields an electronic pulse in data acquisition [16]. The electronic pulse occurs on the order of microseconds after the initial neutron capture [17].

Neutron sources like ^{240}Pu have energies in the MeV range, but the neutron capture cross section for ^{3}He peaks at thermal energies of approximately 0.025 eV. The thermal neutron capture cross section for 3He is 5,330 barns, greater than similar detection systems using ^{10}B (3,840 barns) or ^{6}Li (940 barns), and decreases inversely as neutron energy increases [16]. To reduce incident neutron energies to thermal levels, ^{3}He is used in conjunction with a moderating material such as polyethylene. Thus, incident neutron energy information is lost. ^{3}He can still characterize SNM samples by measuring the multiplicity of neutrons emitting from the sample [16]. ^{3}He will naturally detect approximately 1 out of 10,000 incident gamma rays with energy of 1 MeV [11]. By slightly raising its detection threshold, ^{3}He can obtain gamma-ray rejection rates, defined as the fraction of incident gamma rays that are detected and misclassified as neutrons, as low as 10^{-8} [18, 19].

2.2. Organic Scintillation Detectors

Organic scintillation detectors are sensitive to both neutrons and gamma rays. Incident gamma rays interact with electrons primarily through Compton scattering, while neutrons interact with scintillator nuclei primarily through elastic scattering. The recoiling nuclei excite neighboring scintillator molecules, which de-excite by emitting visible light a few nanoseconds after particles are excited [16]. Ideally, scintillation materials are transparent, so all visible light will be preserved when transporting through the medium [16]. All sides of the scintillator are usually covered by a reflective coating, usually created by paint or thread seal tape that diffuses light back into the crystal, except for the side(s) facing a light collecting device such as a photomultiplier tube (PMT) or silicon photomultiplier (SiPM). Light photons that strike the PMT window will hit the photocathode, creating free electrons that are guided into the PMT by an

electric field. Electrons are guided to several dynode stages, multiplying the number of electrons to amplify the measured signal.

For organic scintillators, neutron scatters on hydrogen allow for the maximum neutron energy transfer from incident neutrons. For an incident neutron with energy E_n, the energy of the recoiling nucleus E_R varies with the scattering angle θ according to the elastic scattering equation:

$$E_R = \frac{4A}{(1+A)^2} E_n \cos^2\theta\,, 0 \le \theta \le \frac{\pi}{2}, \tag{2-1}$$

where A is the mass number of the recoiling nucleus [16]. For hydrogen (A=1), neutrons can deposit as much as all of their initial energy, while carbon (A=12) can only receive as much as 28% of the neutrons' initial energy [16]. For neutron energies less than 10 MeV, elastic scattering with hydrogen is isotropic, and the recoil proton energy distribution is uniform from 0 to the incident neutron energy [16].

For hydrogen, Compton scattering is the dominant interaction for gamma rays. Rather than measuring the full gamma-ray energy via photoelectric absorption, the energy transferred into the scintillator will range over a distribution. This distribution, called the Compton continuum, will vary with the angle θ of the scattering gamma ray with initial energy E_γ. The energy deposition E_{dep} is defined by the Compton Scattering Equation:

$$E_{dep} = E_\gamma \left(1 - \frac{1}{1+\frac{E_\gamma}{m_e c^2}(1-\cos\theta)}\right), \tag{2-2}$$

where $m_e c^2$ is the electron rest mass energy, equal to 511 keV [16]. Organic scintillators can be calibrated using mono-energetic gamma-ray sources such as ^{137}Cs and locating the maximum possible scattering energy, or Compton edge, and computing the energy deposition using Equation 2-2. This energy deposition is directly related to light output by defining keVee, or keV electron equivalent light pulse, where a 1-keV electron produces 1 keVee of light in the scintillator. The scale is linear for light produced from Compton electrons; for protons or heavier nuclei, the amount of light produced is significantly less per unit of particle energy, and is nonlinear on the keVee scale [16].

Figure 2-1a shows the measured pulse height spectrum from an EJ-309 organic liquid scintillator measuring ^{137}Cs. Figure 2-1b shows a similar spectrum after converting pulse height to light output using the Compton edge. The measured spectrum appears more broadened than Equation 2-2 predicts due to inherent resolution within the scintillator. The peak of the unbroadened simulation corresponds to the true Compton edge. The Compton edge was taken at approximately 80% of the measured edge maximum, yielding the simulation that best matched the measurement after accounting for resolution. 80% of the measured Compton edge was used as the calibration point for all scintillator experiments in this thesis, although resolution effects and multiple scatters of gamma rays in larger scintillators may cause the true Compton edge to vary in different scintillators.

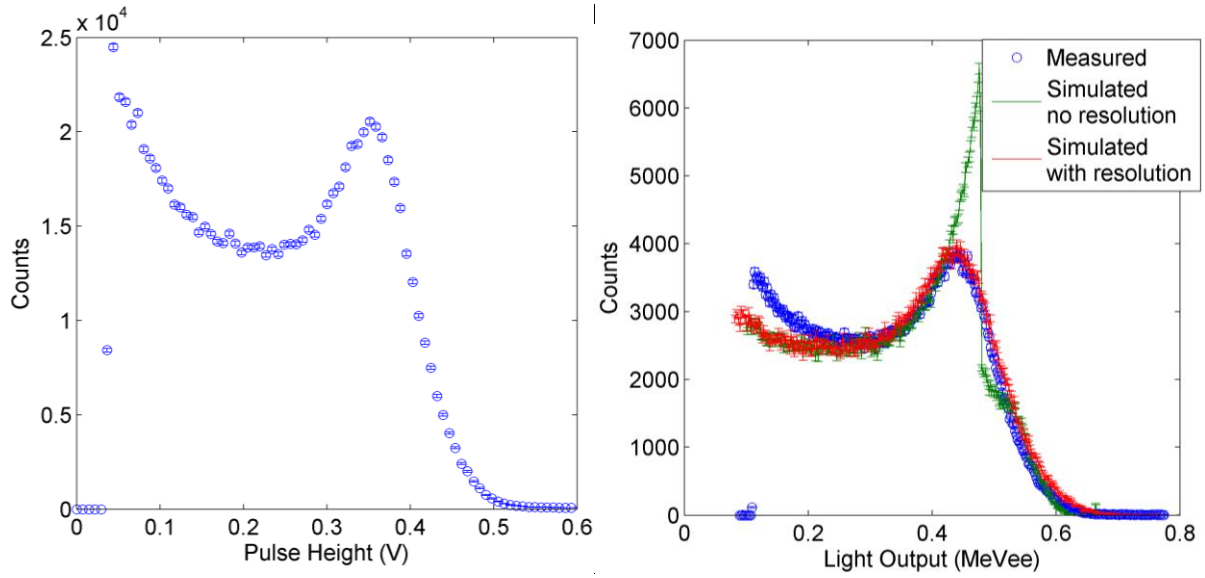

Fig. 2-1. Measured ^{137}Cs pulse height (a) and light output (b) spectra from an EJ-309 organic liquid scintillator. The simulation best matches the measured light output spectrum when sampling the Compton edge at 80% of the edge maximum.

2.2.1. Pulse-Shape Discrimination by Charge Integration

The de-excitation process of scintillation molecules with π-electron structure makes PSD possible in organic scintillators. Figure 2-1a illustrates the energy levels for an organic molecule used for illustration following the absorption, or excitation of the molecule into one of its singlet states. De-excitation can occur by fluorescence, or prompt light emission from the excited singlet state, and phosphorescence, or transition into a triplet state before de-excitation. Two molecules excited to triplet states can annihilate, producing one molecule at the ground energy level and the other at an excited singlet state, which can then de-excite to ground via fluorescence [16]. The

delayed signal is expected to increase in intensity as the density of triplet states increases. Since triplet-state de-excitation gives another method for the exciting particle to lose energy, the delayed signal fraction should be greatest for particles with the greatest linear stopping particle *S*. From the Bethe Formula, it is known that, for a nonrelativistic particle,

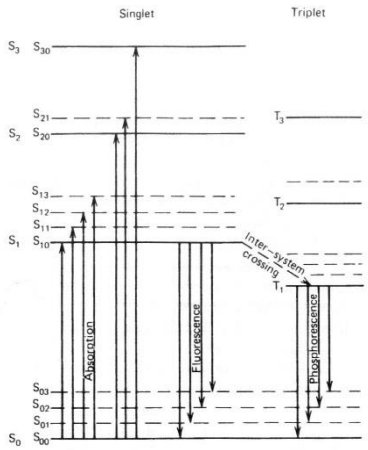

Fig. 2-2. Energy levels for an organic scintillation molecule with π-electron structure, from [16].

$$S = -\frac{dE}{dx} \sim \frac{(ze)^2}{v^2}, \tag{2-3}$$

where *v* and *ze* are the velocity and charge of the exciting particle [16]. Since recoil protons will travel slower than Compton electrons in the scintillator, it follows that recoil proton pulses will contain a greater fraction of light in the tail region than electron pulses. Figure 2-3 shows the measured signal pulses from stilbene, EJ-309 liquid, and BB3-5 plastic organic scintillators for neutron and gamma rays. Equation 2-3 also suggests that heavier charged particles such as alpha particles would yield an even greater fraction of light in the tail region than proton pulses.

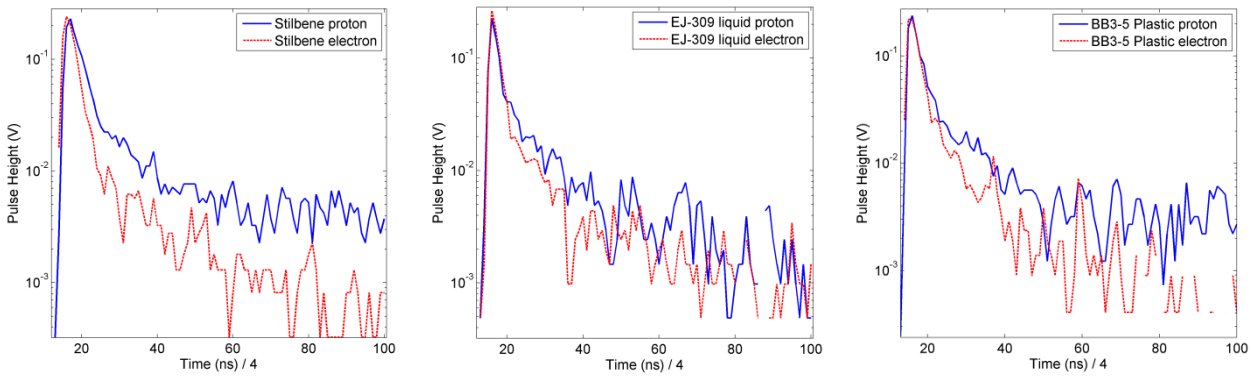

(a) (b) (c)

Fig. 2-3. Sample 250-mV pulses from stilbene (a), EJ-309 liquid (b), and BB3-5 plastic (c). Proton and electron pulses are identified using the charge integration technique.

This work focused on using charge integration for performing PSD with organic scintillators. To quantify the difference in pulse shape shown in Figure 2-2, two separate integrals are computed: one over the decay (tail) region of the pulse, and one over the entire (total) pulse. Then the ratio of the tail integral to the total integral should be greater for pulses produced by neutrons than for gamma rays. Figure 2-4 shows a histogram of the tail-to-total integral ratios for stilbene measuring ^{252}Cf, showing two peaks corresponding to gamma ray and neutron pulses. PSD was optimized by varying the integration ranges to maximize the PSD figure-of-merit FOM, defined as

$$FOM = \frac{d}{FWHM_\gamma + FWHM_n}, \tag{2-4}$$

where *d* and *FWHM* are defined in Figure 2-4 as the distance between the two peaks and the full-width at half maximum of the gamma ray and neutron peaks, respectively. The most sensitive parameter to optimize is the start time of the tail integral; PSD was optimized when as much of the pulse was integrated as possible.

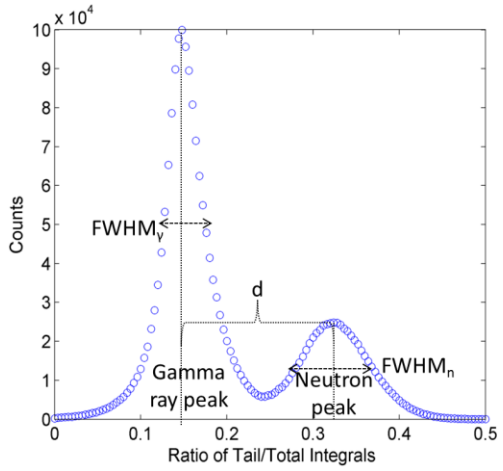

Fig. 2-4. Tail-to-total integral ratio of stilbene measuring ^{252}Cf.

Figure 2-5 shows the PSD capability of stilbene measuring ^{252}Cf. PSD capability is expressed as a surface plot of tail and total integrals. The separation between neutron and gamma ray pulses is clearly defined, with neutron pulses having a larger tail integral than gamma ray pulses for a given total integral. A curve is drawn that visually separates between the neutron and gamma ray regions. The separation between the neutron and gamma-ray regions is less for smaller pulses, creating the potential for gamma ray pulses to be misclassified as neutron pulses and vice versa. Increasing the measured light threshold will decrease the total amount of misclassifications at the cost of detection efficiency. Additionally, the discrimination curve can be shifted up or down to bias the misclassification towards one particle or the other [20].

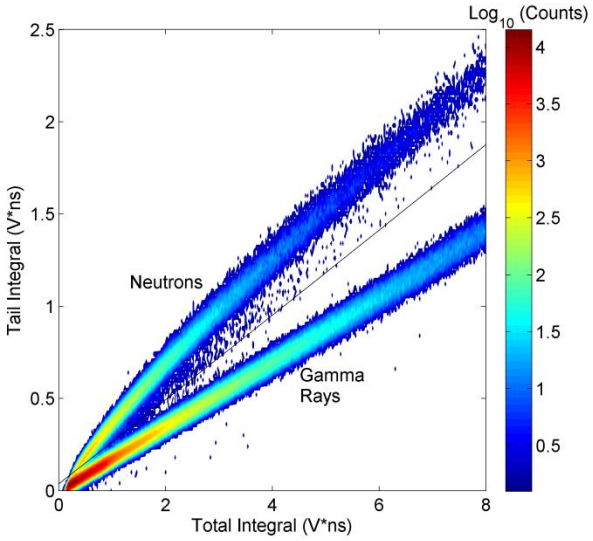

Fig. 2-5. PSD tail-vs-total integral plot for stilbene measuring ^{252}Cf at a 42-keVee threshold. A PSD discrimination curve is drawn visually that separates between neutron and gamma ray pulses.

2.2.2. Types of Organic Scintillators

Organic scintillators can exist as liquids, plastics, and crystals. Table 2-1 shows a few properties of scintillators grouped by scintillator type provided from a few manufacturers of these crystals. Most of these are materials properties that remain constant regardless of the readout electronics. Light production, however, can vary based on numerous experimental parameters ranging from the size, shape, surface treatment, packing of scintillator samples, and fraction of light reaching the photomultiplier tube [21]. Any of these parameters may vary from experiment to experiment, making it difficult to yield perfectly accurate results. Actual light output is unknown for solution-grown stilbene, but experiments performed in [22] conclude it exceeds light output for both melt-based stilbene (50% anthracene) and EJ-309 liquid. The Detection for Nuclear Nonproliferation Group (DNNG) performed experiments that also show solution-grown stilbene produces larger pulses than EJ-309 liquid when coupled to the same PMT model and powered with the same voltage gain.

Table 2-1. Properties of various organic scintillators by the listed manufacturer [16, 22-25].

Scintillator Type	Model or Manufacturer	Density (g/cm^3)	Light Production (% Anthracene)	Decay Constant (ns)	Attenuation Length (cm)	Softening or Flash Point (°C)	PSD ?
Plastic	EJ-200	1.032	64	2.1	380	70	No
	EJ-299-33	1.08	56	13	*	**	Yes
Liquid	EJ-301	0.874	78	3.2	> 1000	26	Yes
	EJ-309	0.959	75	3.5	> 1000	144	Yes
Stilbene	Inrad Optics	1.16	***	4.5	> 1000	125	Yes
Anthracene	--	1.25	100	30	> 1000	217	Yes

*EJ-299-33 has been grown with lengths up to 15 cm. True attenuation length is unknown.

**EJ-299-33 is difficult to manufacture due to its softness.

***See text above table.

The lack of mobility of organic scintillator molecules in plastic scintillators prevents older compositions such as EJ-200 from exhibiting PSD capabilities, as triplet-triplet annihilation is rare. The diffusion of excited molecules in liquid and stilbene scintillators is long enough that, compared to the lifetime of triplet states, the probability of triplet-triplet annihilation is much higher, allowing for PSD [8]. One way to enable PSD capability in a plastic scintillator is to increase the concentration of the fluorophore that is most likely to exhibit a triplet event. This technique was successfully demonstrated with the EJ-299-33 plastic scintillator from Eljen

Technologies, one of the first plastics grown with PSD capability [8]. Additional plastics were later developed by Radiation Monitoring Devices, Inc. (RMD) that improved on the PSD capabilities of the EJ-299-33 [26]. The EJ-299-33 plastic scintillator and the BB3-5 plastic scintillator from RMD are shown in Figure 2-6. Both scintillators are right circular cylinders with diameter and height of 5.08 centimeters.

Eljen is currently working to consistently supply EJ-299-33 scintillators longer than 15 centimeters, but the plastic's softness makes it difficult to machine [23]. An important advantage for traditional plastic scintillators is their ability to easily scale to larger sizes; without this advantage, the application range will be very limited for EJ-299-33 plastics, which underperform in light production and PSD accuracy relative to liquids and stilbene. EJ-299-34 was developed by Eljen as a harder alternative that sacrifices some PSD capabilities compared to EJ-299-33 but can be consistently cast to lengths of 30 centimeters [25].

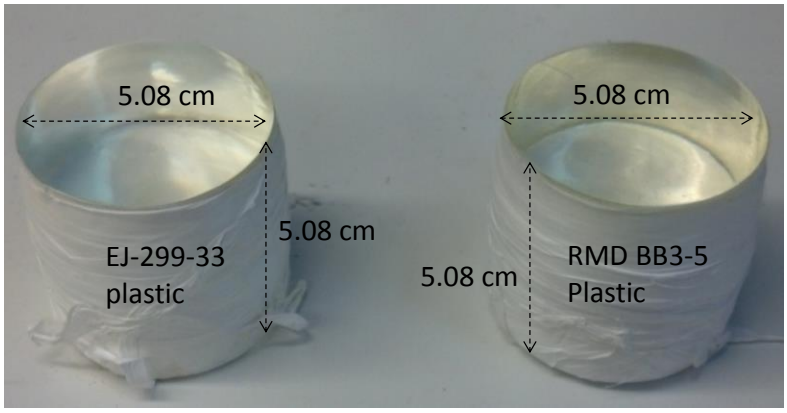

Fig. 2-6. Photo of wrapped, PSD-capable organic plastic scintillation crystals.

Liquids have numerous advantages for large-scale applications such as portal monitoring, including consistent PSD capability of liquid scintillators, higher light yield and longer attenuation length compared to plastic scintillators. Previous compositions such as EJ-301 were shown to have limited field use because of their low flash point and chemical toxicity, both of which are hazardous to the environment if the scintillator leaks. EJ-309 was developed as an alternative to EJ-301 that sacrifices a little in PSD characteristics but has a much higher flash point and is not classified as 'hazardous' [24]. Many studies have been performed to demonstrate the capabilities of EJ-309 in the DNNG research group at the University of Michigan [27-29].

One downside of a liquid scintillation detector is that any leak both reduces detection volume and damages performance of the scintillator, even if the liquid poses little environmental hazard.

Stilbene is an organic crystal scintillator known best for its excellent PSD capabilities, which are even better than liquids as illustrated by the different waveforms in Figure 2-3. Stilbene has higher light production from incident radiation than liquids such as EJ-309 while preserving similar timing properties [25, 30]. Anthracene crystals exhibit the highest measured light output of any organic scintillator, but exhibit slower timing response, so gamma-ray and neutron pulses appear more similar in their tail regions [16]. More research is needed to better understand what material properties, such as physical state, molecular and crystal structure, and presence of impurities, yield the best PSD capabilities in organic crystals. For example, diphenylacetylene has similar crystal structure as stilbene but has no PSD capabilities [31].

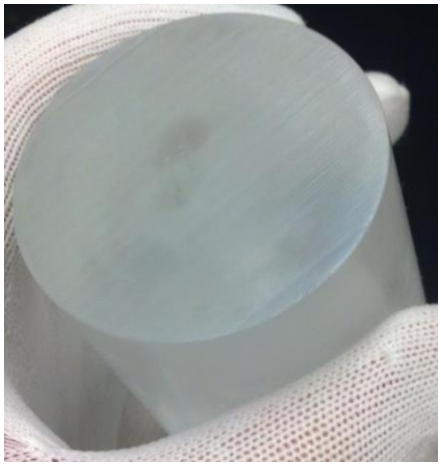

Fig. 2-7. Photo of bare, solution-grown organic stilbene scintillation crystal.

Traditionally, stilbene crystals are grown from a melt using the Bridgman technique, often leading to crystals stressing and cracking during the growth and cooling processes. This process limits the maximum crystal size that can be grown reliably [9]. A solution-based growth technique was developed by Lawrence Livermore National Laboratory that can more consistently grow crystals to 5 centimeters or larger in diameter without sacrificing PSD capabilities [9, 29]. Figure 2-7 shows a photo of a solution-grown stilbene crystal provided by Inrad Optics. Any application that previously utilized liquid or plastic scintillators can theoretically be replaced with stilbene and see an improvement in both detection efficiency and accuracy of particle classification. As of the writing of this thesis, companies such as Inrad

Optics are working to improve their solution-grown stilbene synthesis process to consistently grow larger crystals, lowering the price of crystals grown to diameters larger than 5 centimeters.

2.2.3. Detector Assembly

As stated in Section 2.2, scintillation crystals de-excite by releasing visible light. It is desired to preserve as many light photons as possible to minimize light output resolution and improve the PSD quality of the scintillator. Each crystal was wrapped with white Teflon tape on its sides and top to scatter visible light within the crystal. Enough layers were applied until the scintillators appeared opaque. Next, optical grease was applied to the bottom, uncovered face of the crystal. The crystal was coupled to the PMT window, pressing liberally to ensure no air bubbles are created in the coupling process and to push out excess optical grease. The coupling was determined to be complete when the scintillator proved difficult to remove from the PMT when pulling directly away from the PMT. This assembly technique was not designed to be permanent—crystals could still be removed by sliding off the side of the PMT window—but the coupling allowed for measurements of clean, consistent waveforms from the full assembly.

The PMT collects and amplifies visible light created by the crystal to produce the outputted signal. The environment contains many more photons of visible light than that created by the crystal, so direct exposure to the environment risks damaging the PMT by overloading the amplification. To ensure no ambient light leaked through the crystal, the wrapped crystal was covered with black electrical tape. Additional black electrical tape was applied to reinforce the position of the crystal covering the PMT window. A mu metal shield was positioned to surround the PMT, reducing magnetic interference with PMT performance. The voltage divider base fit the bottom of the PMT, providing connections for both the safe high voltage (SHV) power cable and coaxial cable that carries the measured signal to data acquisition electronics. The PMT components were held in place with black electrical tape. Figure 2-8 shows a wrapped stilbene crystal and the full detector assembly.

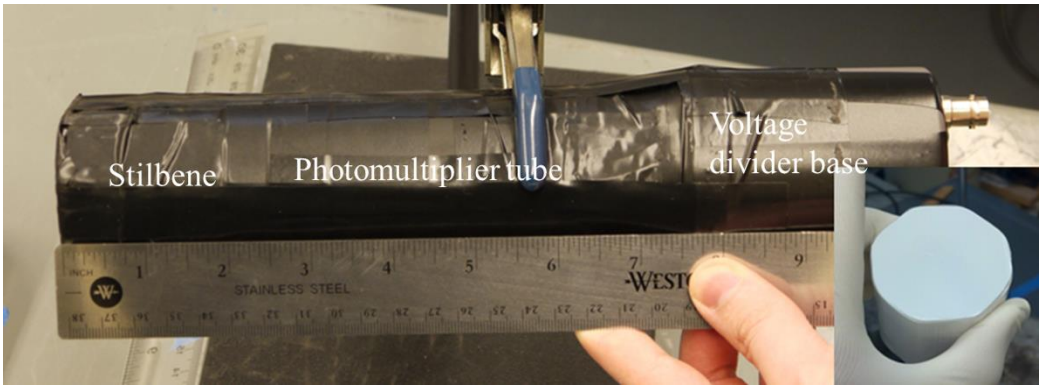

Fig. 2-8. Wrapped stilbene scintillation crystal and full detector assembly.

2.3. Digital Data Acquisition

Figure 2-9 shows the experimental electronic setup utilized for each experiment detailed in this thesis. A power supply was connected directly to the detector, providing power to the PMT. Varying the voltage varies the amplification to the measured signal, although the PMT will break if the voltage exceeds manufacturer limits or is set with the wrong polarity.

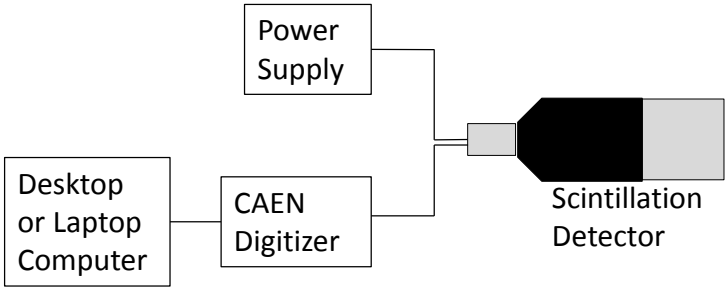

Fig. 2-9. Experimental schematic for digital data acquisition system.

Pulse signals from each detector were stored using commercial waveform digitizers from CAEN [32]. CAEN digitizers function by sampling signals at a fixed sampling rate from all sources into a constant buffer. The range of collected charge is determined by the acceptable dynamic range of the digitizer and is subdivided into voltage bins determined by its vertical resolution. For example, both the V1720 and the DT5720 digitizers have a 250-MHz sampling rate, 2-Volt dynamic range, and 12-bit vertical resolution, meaning waveforms are sampled every 4 nanoseconds, with each sample stored into one of 2^{12} voltage bins with a 2-Volt range and bin width of 0.049 mV. The V1730 digitizer, with a 500-MHz sampling rate, 2-Volt dynamic range, and 14-bit vertical resolution, was also used in experiments reported in this thesis.

Measurement data are recorded using acquisition software either provided by CAEN or custom-written by DNNG that configures the digitizer to start a measurement. A configuration file sets parameters for the digitizer that defines, among other things, the pulse window length, trigger location within the pulse, trigger threshold, and trigger channels. When a trigger event occurs, signals in the buffer are converted into waveforms that are written to a file. Each digitizer can handle up to 80 MB/s of data at a time, although most measurement systems will be further reduced by the hard drive write speed for the computer running the data acquisition software [32]. Figure 2-10 shows photographs of the DT5720 and V1730 digitizers.

Fig. 2-10. Photographs of the CAEN V1730 (top) and DT5720 (bottom) digitizers.

Output can be suppressed further through the use of zero suppression, which eliminates channels with empty waveforms, and multi-trigger logic, which forces multiple channels to experience a trigger event before writing. These techniques are most commonly used with correlated experiments with numerous detectors, where correlated events will be much rarer than single-particle events.

Chapter 3. Modeling Stilbene and Plastic Scintillation Light Output with MCNPX-PoliMi and MPPost

For their use in safeguards or nonproliferation applications it is necessary to know how organic scintillation detectors will respond to SNM such as plutonium samples. Validation measurements of each source and geometry are not practical in the design phase; it is more efficient to design detector systems in simulation. Accurate models of detector response to incident radiation can be applied to more complex environments and geometries such as the experiments discussed in Chapters 5 and 6.

An important property for scintillation detectors is the amount of light produced from energy transfer from Compton or elastic scattering. As discussed in Chapter 2, light output is represented in kiloelectronvolt electron equivalent (keVee), defined as the light produced from 1 keV of energy transferred from a gamma ray to a scintillator electron. On the electron-equivalent scale, proton recoil produces light photons that are both fewer in number than from Compton electrons and relate nonlinearly to the incident neutron energy [16]. A time-of-flight experiment was designed that measures the energy-to-light relationship for proton recoil in EJ-299-33 plastic, BB3-5 plastic from Radiation Monitoring Devices, Inc. (RMD), and stilbene scintillators. This relationship was used in MPPost, a specialized FORTRAN post-processing script, to convert the collision output from MCNPX-PoliMi simulations into the neutron light output distribution for each detector.

3.1. Experimental Setup

The stilbene scintillator was obtained from Lawrence Livermore National Laboratory. The crystal was an irregular circular cylinder with length and diameter both 5.08 centimeters. The BB3-5 plastic scintillator, a regular circular cylinder with the same dimensions as the stilbene crystal, was obtained from RMD. Each detector was assembled at the University of Michigan using a photomultiplier tube (PMT) manufactured by Electron Tubes with model number ETL 9214B [33]. The assembly procedure is described in Section 2.2.3.

The EJ-299-33 plastic scintillation detector was manufactured by Eljen Technologies. The scintillator was a right circular cylinder with both diameter and length 7.62 centimeters. The PMT, with diameter of 7.62 centimeters, has model number ETL 9821B. Experiments were compared to a similar experiment performed for the EJ-309 liquid scintillation detector, manufactured by SCIONIX with the same PMT model and scintillator dimensions as the EJ-299-33 plastic detector [34]. Anode signals from each detector were read out using a CAEN V1720 digitizer. Pulses were sampled for a window length of 1 μs and analyzed offline.

3.1.1. Detector Calibration

A 1 μCi ^{137}Cs source was used to calibrate each detector. Emitting a single gamma ray with energy 662 keV, ^{137}Cs is commonly used to characterize organic scintillator systems because its Compton edge occurs at a fixed energy of 477 keV. Each detector was biased such that the ^{137}Cs Compton edge, measured at 80% of the edge maximum based on Figure 2-1, occurred at approximately 0.4 Volts for the BB3-5 plastic scintillator and 0.37 Volts for the EJ-299-33 plastic and LLNL stilbene scintillators. Figure 3-1 shows the calibration for each detector. The measured light threshold was set to 39 keVee for each detector.

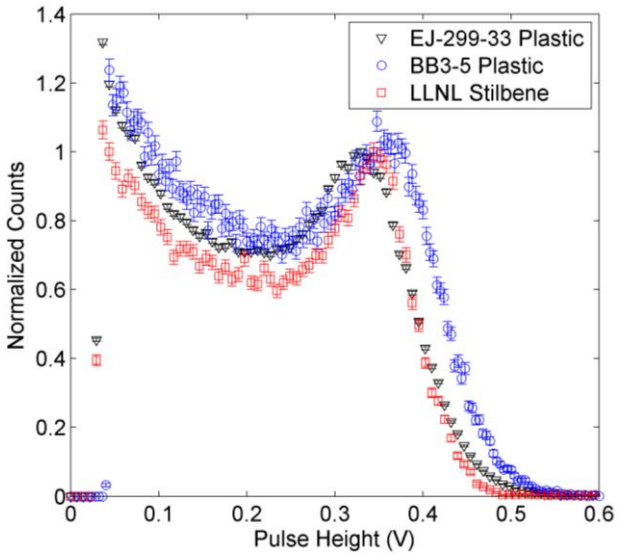

Fig. 3-1. ^{137}Cs gamma ray calibration of the plastic and stilbene detectors.

3.1.2. Time-of-Flight Experiment

A time-of-flight experiment was designed that measured ^{252}Cf emissions using a start detector. Figure 3-2a shows the setup for the experiment. The stilbene and plastic detectors were positioned 1 meter from a ^{252}Cf source, with a spontaneous fission activity of approximately

60,000 fissions per second and neutron energy distribution given in Figure 3-2b. Each spontaneous fission of ^{252}Cf yields 3.757 neutrons and over 8 gamma rays on average [11]. An EJ-309 liquid scintillation detector, with length and diameter each 12.7 centimeters, was placed next to the source to measure the times at which most fissions occurred by detecting one or more fission gamma rays and neutrons. The stilbene and plastic detectors triggered the data acquisition system to record waveforms that occurred in coincidence with a pulse in the start detector within the 1-μs pulse window.

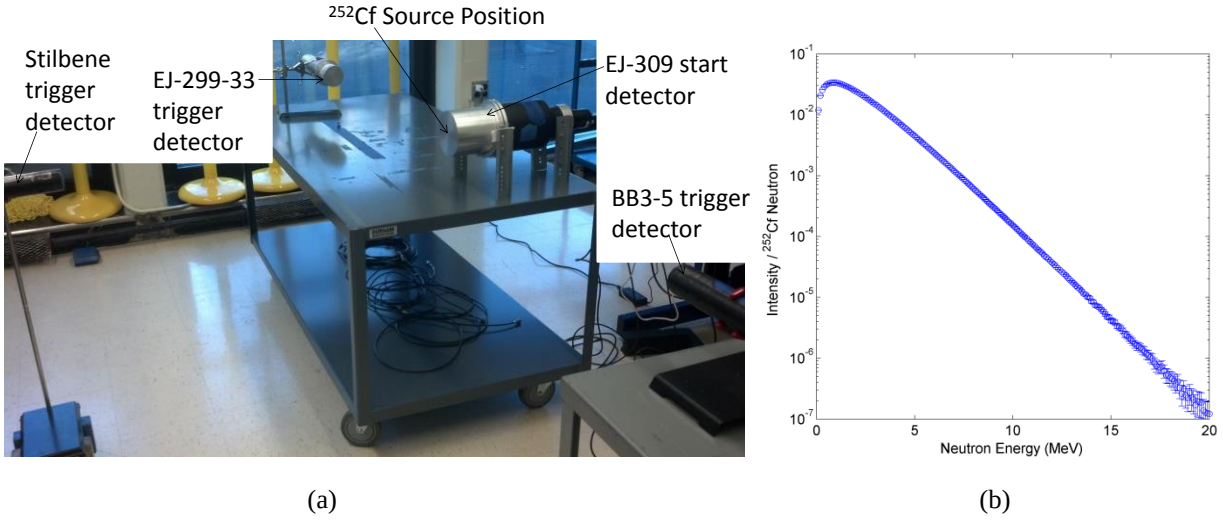

(a) (b)

Fig. 3-2. (a) Time-of-flight experimental setup showing the ^{252}Cf source and start detector (center) and the stilbene and EJ-299-33 plastic trigger detectors at 1 meter from the source. (b) ^{252}Cf neutron energy distribution.

3.1.3. Time-of-Flight Results

The time difference between pulses in the start and trigger detectors were histogrammed into the time-of-flight distribution shown in Figure 3-3. At a distance of 1 meter, gamma rays have a fixed flight time of 3.3 nanoseconds. The flight time for neutrons is dependent on particle energy, where the range from 20 to 100 nanoseconds covers neutron energies between 500 keV and 13 MeV. From Figure 3-2b, this energy range is sufficient to cover over 88% of the ^{252}Cf Watt spectrum. The neutron continuum extends to later times-of-flight for stilbene than for the EJ-299-33 and BB3-5 plastics. Since each detector was operated at the same light output threshold, it is expected that stilbene produces more light from neutron collisions than the plastic and liquid detectors, consistent with light outputs reported in Table 2-1.

The presence of delayed gamma rays ranging from 10 to 20 nanoseconds gives less clarity to the starting point for the neutron continuum. Increasing the flight path to 2 meters or

longer gives greater separation between the gamma ray and neutron regions at the expense of count rate. Time-of-flight experiments are often performed at an accelerator facility possessing long flight paths and high intensity of energy-gated neutron emissions [34].

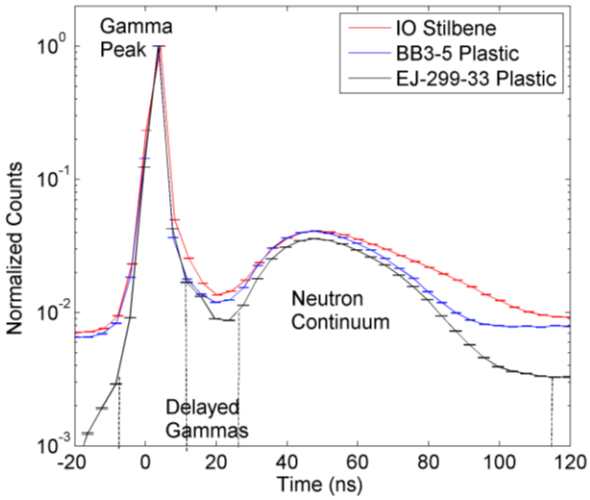

Fig. 3-3. Time-of-flight distribution of gamma rays and neutrons detected in stilbene, EJ-299-33 plastic, and BB3-5 plastic scintillators using a 39-keVee threshold. Distributions were normalized to the gamma-ray peak maximum.

Pulses lying in the neutron continuum were sorted into 100-keV energy bins, ranging from 0.5-4.7 MeV (33-102 ns) for stilbene, 0.9-5.3 MeV (31-76 ns) for BB3-5 plastic, and 0.8-5.2 MeV (32-81 ns) for EJ-299-33 plastic. Within each energy bin, charge integration was used to filter accidental gamma-ray pulses from neutron pulses. Remaining neutron pulses are histogrammed into a light output distribution. Light output distributions measured in time-of-flight for ^{252}Cf are given in Figure 3-4 for stilbene. As predicted by Equation 2-1, each distribution appears relatively flat, ranging from the detection threshold to the maximum possible energy that can be transferred during proton recoil. Detector resolution broadening makes it difficult to directly observe the light output corresponding to the maximum energy transfer. Instead, the energy-light output relationship was determined by taking a fraction of the overall maximum of each distribution. This fraction was kept constant for all energy bins and varied separately for the stilbene and plastic detectors. Each fraction computed a different neutron energy-to-light output relationship, which was applied to MCNPX-PoliMi simulations of pulse height distributions for these detectors. The simulated pulse height distribution that most accurately matched measured data determined which neutron energy-to-light output relationship corresponded to each scintillator, and which fraction was most valid for the scintillator.

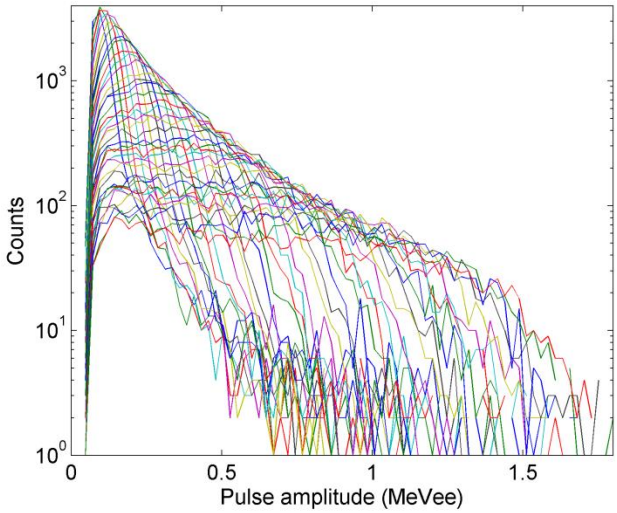

Fig. 3-4. Neutron pulse height distributions as a function of incident energy for stilbene measuring ^{252}Cf.

3.2. MCNPX-PoliMi

The Monte Carlo simulation code MCNPX is a powerful simulation tool for simulating neutron and gamma ray emissions. Sampling from the included cross-section data libraries such as ENDF-VII allows for accurate calculation of the overall behavior of particles transported through complex environments and geometries as a function of particle energy and momentum. MCNPX was initially designed to sample particle behavior from averaged distributions of the physics of interaction between particles, decreasing program runtime. However, interactions at the per-collision basis don't have energy and momentum correlated to the incident particle. This approximation was insufficient for modeling the response of scintillation detectors, so MCNP-PoliMi was developed as a modification to MCNP4C that could model detailed interaction physics for every particle simulated [35]. Later patches of MCNPX included the option to model detailed interaction physics for every particle, so MCNPX-PoliMi was developed that combined features in MCNP-PoliMi with MCNPX-2.6.0 [35].

One of the features of MCNPX-PoliMi is the implementation of built-in sources with correlated neutron and gamma ray emissions. These sources, including ^{252}Cf and ^{240}Pu spontaneous fission and plutonium oxide (α, n), make it possible to simulate scintillator response of these samples in correlated applications. Collisions of source particles in one or more specified detector cells are stored in a collision output file, containing detailed information about each collision, including the particle energy, collision nucleus, and time of collision after the source event [35]. Each ^{252}Cf MCNPX-PoliMi model is given in Appendix A.

3.3. MCNPX-PoliMi Post Processor (MPPost)

MPPost was developed and maintained by the DNNG research group for converting the MCNPX-PoliMi collision output file into detector response [36]. For organic scintillators, pulses are reconstructed by finding the total light output in each history that occurs within each scintillator's pulse generation time. Light output is calculated from the energy transfer of incident particles according to the particle type and collision nucleus. As stated earlier in this chapter, this relationship is defined as one-to-one for gamma rays. From Equation 2-1, neutron collisions on carbon nuclei can only transfer up to 28% of their incident energy, and the carbon nucleus can only recoil at 15% of the velocity of a recoil proton; when combined with the increased stopping power of carbon nuclei, carbon pulses are unlikely to get detected above threshold. Light produced from carbon collisions was taken to be 2% of the energy deposited from neutron scatters based on previous experiments with liquid scintillators [37]. Light produced from neutron recoils with hydrogen was measured using the time-of-flight technique discussed in Section 3.1.

This light output is taken as the peak of a broadened Gaussian distribution based on the detector resolution. Light output is sampled randomly from this distribution for use in the pulse height distribution. For measuring continuous, featureless neutron energy sources like ^{252}Cf in organic scintillators, resolution effects are most prominent near the measured light threshold, both because the effect of resolution is greater and because resolution in higher-light output bins cancel out [34]. Since resolution is insignificant throughout the measured light output spectra, detector resolution is not accounted for while modeling the detector response to ^{252}Cf spontaneous fission.

3.4. Measured Results

For validating the measured neutron energy-to-light output functions, separate measurements of ^{252}Cf were recorded with the stilbene, BB3-5 plastic, and EJ-299-33 plastic detectors. Neutron pulses were identified using the charge integration PSD technique described in Section 2.2.1, setting the light output threshold to 70 keVee for stilbene and BB3-5 plastic and 300 keVee for EJ-299-33 plastic. The PSD figure-of-merit defined in Equation 2-4 was maximized when integrating as much of each waveform as possible and starting the tail integral at 20 ns after the pulse maximum for stilbene, 28 ns after the maximum for BB3-5 plastic, and 32

ns after the maximum for EJ-299-33 plastic. Figure 3-5 shows the tail-vs-total integral surfaces for stilbene, BB3-5 plastic, and EJ-299-33 plastic. The discrimination curve was drawn visually halfway between the neutron and gamma ray regions, with the goal to equally minimize each particle type on the incorrect side of the curve. At lower light output, overlap of neutron and gamma ray particles increases, so the shape and intensity of the neutron light output distribution becomes less clear. When matching the simulation to the measured neutron light output distribution, the shape of the distribution at higher light output was prioritized over the distribution at lower light output.

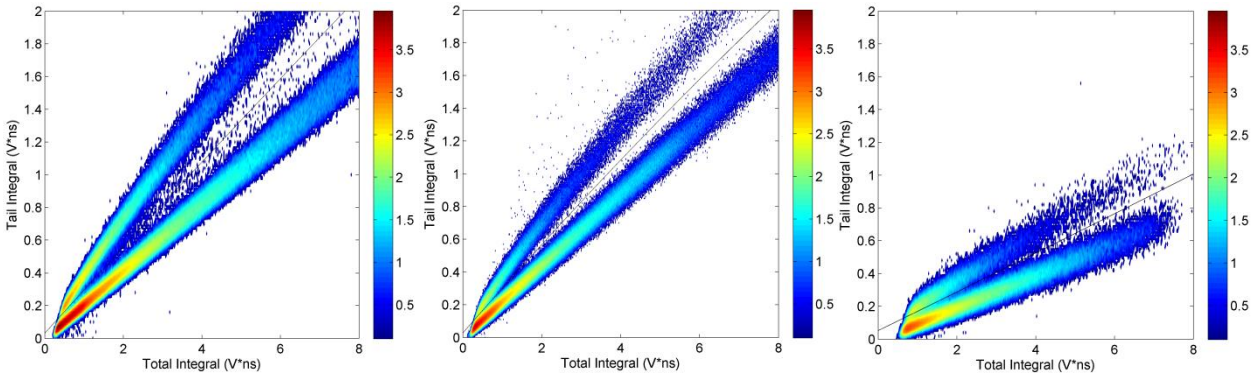

(a) (b) (c)

Fig. 3-5. PSD surface plots for stilbene and BB3-5 plastic measuring ^{252}Cf at a 70-keVee threshold (a, b) and EJ-299-33 plastic measuring ^{252}Cf at a 300-keVee threshold (c).

Each neutron energy slice was sampled at a fraction of its maximum along the edge to compute the energy-to-light conversion. The full dataset was fit to the following functional form for light output L as a function of neutron energy deposition on hydrogen E:

$$L = aE - b(1 - e^{-cE}), \tag{3-1}$$

where a, b, and c are constants determined by the fit [36]. The light output functions measured from this experiment are given in Figure 3-6a for the stilbene, BB3-5 plastic, and EJ-299-33 plastic detectors, directly compared to the 7.62-cm EJ-309 liquid from [34].

Corresponding neutron light output spectra are given in Figures 3.6b-d. By reading the neutron energy-to-light output conversion at 3% of the maximum of each neutron energy bin, the stilbene and the BB3-5 plastic detector (both of which are the same size) light output functions allowed MCNPX-PoliMi with MPPost to directly predict the ^{252}Cf light output distribution. At

5% of the neutron energy bin maxima, the EJ-299-33 plastic light output function predicted the correct shape of the light output distribution but over-predicted the intensity by approximately 40%. Adjustments to the maximum neutron energy fraction changed both the shape and the intensity of the distribution, so the neutron energy fraction was kept at 5%. Instead, the *b* parameter in Equation 3-1 was increased, decreasing the intensity of the light output function in Figure 3-6d, until the simulation better matched the measured light output distribution. Some deviation between the simulation and measurement still exists near the threshold, where particle misclassification is expected to distort the shape of the measured distribution. The light output functions for stilbene L_s, BB3-5 plastic $L_{BB3\text{-}5}$, and EJ-299-33 plastic L_{EJ299} are given as the following:

$$L_s = 0.651E - 2.21(1 - e^{-0.266E}), \tag{3-2}$$

$$L_{BB3-5} = 1.01E - 6.19(1 - e^{-0.152E}), \tag{3-3}$$

and

$$L_{EJ299} = 0.578E - 1.98(1 - e^{-0.296E}). \tag{3-4}$$

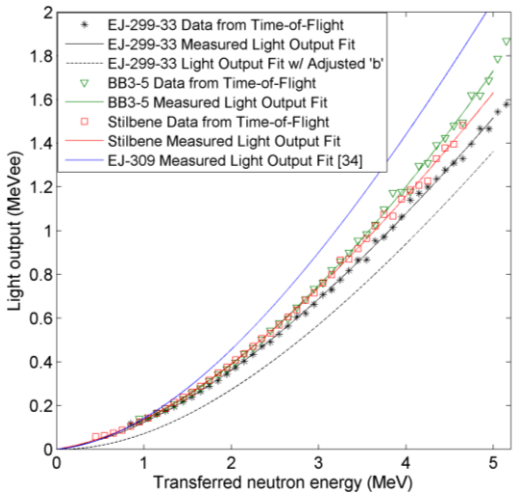

(a)

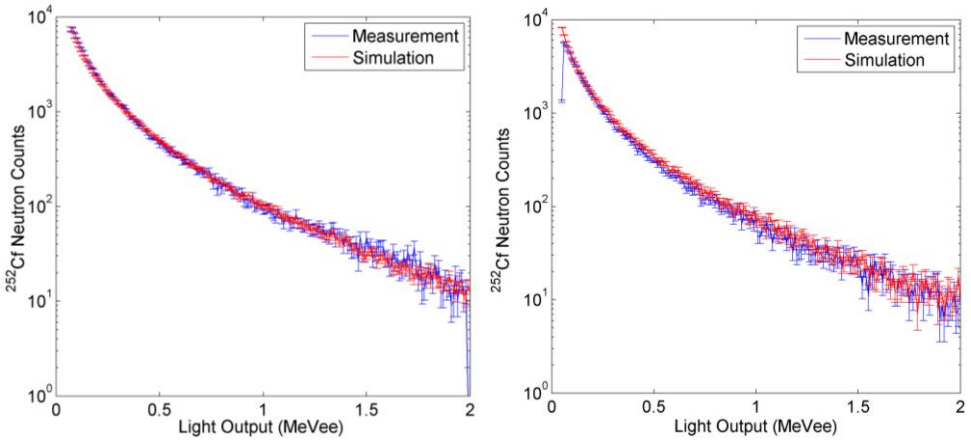

(b) (c)

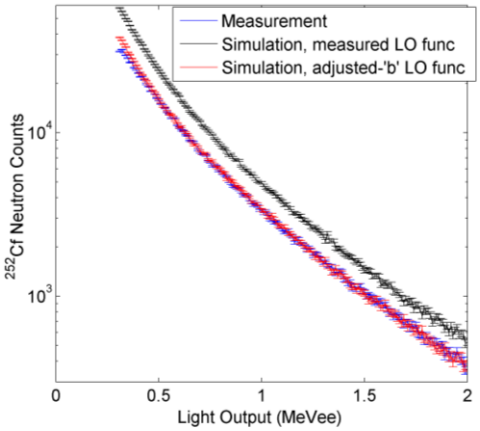

(d)

Fig. 3-6. Stilbene, BB3-5 plastic, and EJ-299-33 plastic scintillation light output from neutron recoils with hydrogen, along with EJ-309 light output as measured in [34] (a). Implementing these functions into MPPost gives the simulated ^{252}Cf light output functions for stilbene at a 70-keVee threshold (b), BB3-5 plastic at a 70-keVee threshold (c), and EJ-299-33 plastic at a 300-keVee threshold (d).

3.5. Remarks

A time-of-flight experiment measuring ^{252}Cf at 1 meter was used to measure the neutron light output function for two separate scintillator samples. Comparisons to measured ^{252}Cf light output distributions confirmed this technique can characterize organic scintillator light production from proton recoils from incident neutrons. The accuracy of this technique is encouraging due to the experiment's limitations in flight path length, source intensity, and measurement time when compared to experiments such as [34]. More importantly, the neutron energy-to-light relationship for proton recoil in each scintillator can be used to model experiments of more interesting sources such as the plutonium experiments discussed in Chapters 5 and 6.

Both the stilbene and BB3-5 plastic detectors' light output functions were measured directly using this technique, both using the same fraction of the neutron light output maximum of 3%. Future work will seek to directly measure the light output function for larger scintillators like the EJ-299-33 plastic without manipulating the functional fit.

Chapter 4. Neutron Detection in a High-Gamma Ray Field Using Scintillation Detectors

Sensitivity of scintillation detectors to gamma rays becomes a disadvantage for neutron counting when the gamma ray count rate is much higher than the neutron count rate. The near-simultaneous detection of two or more gamma rays creates a double pulse that affects particle classification when using charge integration PSD. A 400-mV double pulse is compared directly to gamma-ray and neutron pulses in Figure 4-1. The tail integral between the gamma-ray and neutron pulses give clear separation between the two pulses, but the double pulse is likely to be classified as a neutron by charge integration PSD even though its shape more closely resembles the gamma-ray pulse. Classifying too many gamma-ray double pulses runs the risk of false alarming an organic scintillation detector system that believes it is detecting a neutron source. For accurate neutron counting, double pulses must be removed from data analysis. However, double pulses containing a neutron will also be removed, lowering the detector's neutron efficiency.

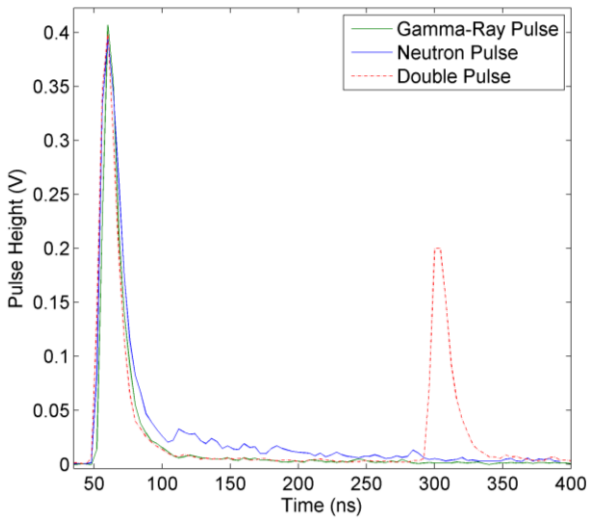

Fig. 4-1. Sample gamma ray and neutron pulses compared directly to a double pulse.

This work seeks to determine how well stilbene, EJ-309 liquid, and RMD's BB3-5 plastic scintillators can measure unshielded ^{252}Cf in fields of at least 1,000 gamma rays per ^{252}Cf

neutron [38]. A 1,000-to-1 gamma ray-to-neutron ratio was chosen to make ^{252}Cf, which emits approximately 2-10 gamma rays per neutron, appear more like plutonium samples, which can easily emit 100 or more gamma rays per neutron. Both ^{60}Co and ^{137}Cs were used in separate experiments to increase the gamma-ray count rate to determine how the rejection methods are affected by incident gamma-ray energy. The measured count rate for these experiments was approximately 100 kHz.

4.1. ^{252}Cf and Gamma Ray Experiments

Experiments were conducted to obtain data sets with each organic scintillation detector known to contain both numerous and very few double pulses. Two stilbene detectors and one BB3-5 plastic detector were assembled at the University of Michigan using the procedure described in Section 2.2.3. All three scintillators were right-circular cylinders with diameter and length each 5.08 centimeters. These were coupled to separate photomultiplier tubes from Electron Tubes with model number either 9214A or 9214B [33]. The EJ-309 liquid scintillator was manufactured by SCIONIX with the same scintillator dimensions, the 9214B photomultiplier tube from Electron Tubes, and equivalent base electronics as used for the other scintillators [24]. Anode signals from each detector were digitized using the CAEN DT5720 digitizer, a desktop digitizer with specifications described in Section 2.3. Pulses were sampled over a 400-ns data acquisition window, long enough to obtain good PSD in each scintillator.

All scintillation detectors were gain-matched to equal electron-equivalent light output. A 1-μCi ^{137}Cs source was used for calibrating each detector; the gain for each detector was set to align the ^{137}Cs Compton edge—chosen at 80% of the edge maximum—at 0.4 Volts. Figure 4-2 shows the ^{137}Cs pulse height spectra recorded in separate calibration measurements for each assembly.

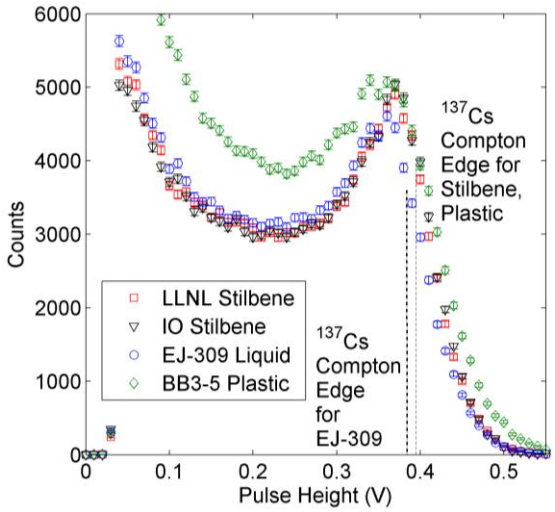

Fig. 4-2. ^{137}Cs calibration of the stilbene, EJ-309 liquid, and RMD BB3-5 plastic scintillation detectors.

Figure 4-3 shows the experimental setup used for each scintillator. Separate experiments were performed using either ^{60}Co or ^{137}Cs to create the high-gamma ray field. In each experiment, the gamma ray source was positioned such that the count rate for each scintillator was approximately 100 kHz. Attempting to increase the count rate above this value would max out the data transfer rate of the system, artificially lowering detection efficiency. The ^{252}Cf source, with neutron emission rate of approximately 141,000 neutrons per second, was then positioned such that at least 1,000 gamma rays were incident on the scintillator face per incident ^{252}Cf neutron. Measurements were recorded using the ^{252}Cf and gamma ray sources together and separately. Finally, background data were recorded overnight. Table 4-1 shows the source position for each measurement recorded by each detector. The measured light threshold was set to 42 keVee for each detector. From results acquired for the stilbene and liquid scintillation detectors, only ^{137}Cs was measured using the BB3-5 plastic scintillation detector.

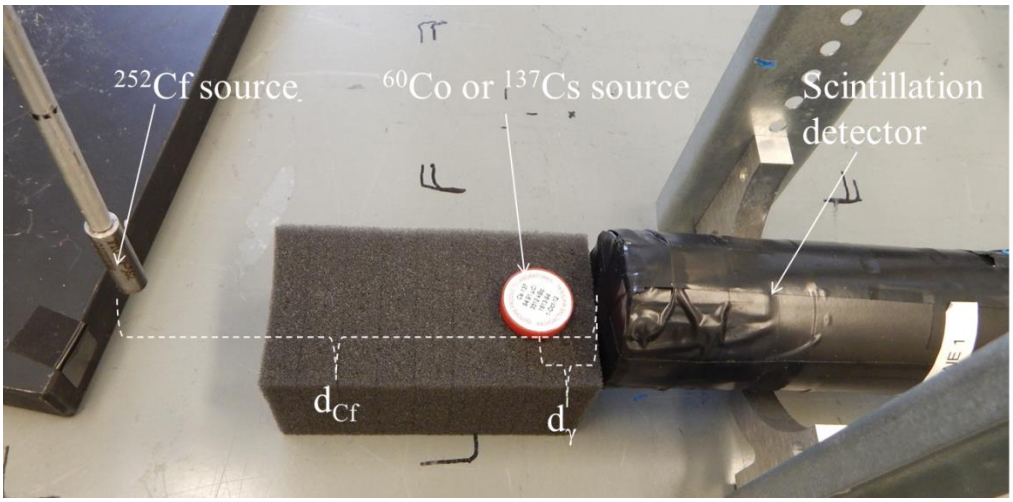

Fig. 4-3. Experimental setup showing ^{252}Cf source, gamma ray source, and scintillation detector assembly.

Table 4-1. Experimental setups used for each detector. Distances are illustrated in Figure 4-2.

		LLNL Stilbene		IO Stilbene		EJ-309 Liquid		BB3-5 Plastic	
Gamma Ray Source	Activity (γ/s)	d_γ (cm)	d_{Cf} (cm)	d_γ (cm)	d_{Cf} (cm)	d_γ (cm)	d_{Cf} (cm)	d_γ (cm)	d_{Cf} (cm)
^{137}Cs	2.8×10^6	1.64	17.6	1.51	12.3	1.04	9.79	1.59	17.8
^{60}Co	5.0×10^6	2.14	15.4	2.53	13.8	1.94	11.4	--	--

Charge integration was used for PSD with each detector. Figure 2-2 shows sample 250-mV pulses for each detector. The integration ranges were optimized separately for each detector to maximize the PSD figure-of-merit as defined by Equation 2-4. The full pulse length ranged from 12 ns before the pulse amplitude until 300 ns after the pulse amplitude. The optimal tail start times (following the pulse maximum) were found to be 20 ns for the EJ-309 liquid, 24 ns for the LLNL stilbene, 28 ns for the Inrad Optics stilbene, and 36 ns for the BB3-5 plastic scintillator.

4.2. Neutron Detection Evaluation Criteria

The neutron detection capabilities of each detector are evaluated by their intrinsic neutron efficiency *Eff* and gamma-ray misclassification rate *MR*. These parameters are defined by Equations 4-1 and 4-2:

$$Eff = \frac{N_{Cf}}{A_{Cf} t \frac{\Omega}{4\pi}} \tag{4-1}$$

$$MR = \frac{N_\gamma}{C_\gamma}. \tag{4-2}$$

Here, N and C represent the respective neutron and total counts after background subtraction from the ^{252}Cf or gamma ray experiments (denoted by subscripts), A is the total neutron emission rate from the ^{252}Cf source, t is the measurement time, and Ω is the source-to-detector solid angle. Intrinsic neutron efficiency was compared for each detector measuring ^{252}Cf with and without the high-gamma ray field, and the misclassification rates were computed before and after each double-pulse rejection method. It was decided that the gamma-ray misclassification rate was a better metric for characterizing the scintillation detectors than the gamma-ray rejection rate defined in Section 2.1 because the gamma-ray misclassification rate is independent of shielding. In the design of the double-pulse rejection algorithms, it is preferred to avoid using lead to preserve both portability and dual sensitivity to gamma rays in organic scintillators.

The energy threshold, PSD discrimination curve, and double-pulse rejection parameters can be changed to favor one parameter at the expense of another. A higher energy threshold leads to fewer gamma rays misclassified as neutron, but also lowers neutron efficiency. Biasing the PSD discrimination curve towards neutrons will classify fewer pulses as neutrons but more pulses as gamma rays, improving misclassification rate at the cost of neutron efficiency. Classifying more pulses as double pulses reduces misclassification rate but runs the risk of removing more neutron pulses.

4.3. Measured Results Before Double-Pulse Rejection

Pulses from ^{252}Cf experiments with and without each gamma-ray source are sorted by their tail and total integrals. The tail-vs-total integral surface plots are shown in Figure 4-4 for each detector. The measured light threshold remained at 42 keVee for the stilbene detectors, but was increased to 60 keVee for the EJ-309 liquid detector and 96 keVee for the BB3-5 plastic detector. When measuring ^{252}Cf without the high-gamma ray field, the stilbene detectors exhibited clear separation between the neutron and gamma-ray regions. Despite raising the EJ-309 liquid and BB3-5 plastic detector thresholds, both stilbene scintillators had greater separation between the neutron and gamma-ray regions than the liquid and plastic detectors. EJ-309 liquid had greater separation than the BB3-5 plastic scintillator despite operating at a lower threshold. Detection thresholds for the liquid and plastic scintillators could be further raised to better match the separation exhibited by the stilbene detectors, but neutron efficiency would be sacrificed in the process. It is worth noting that the liquid scintillator distribution has fewer

pulses than the stilbene and BB3-5 plastic scintillators that fall either between or above the neutron and gamma-ray regions, possibly due to the differences in how these detectors were assembled. These pulses are few enough to assume their contribution will be negligible to the calculated neutron intrinsic efficiency and gamma-ray misclassification rate for each detector.

Adding either the ^{60}Co or ^{137}Cs gamma-ray source increases the relative intensity of the gamma-ray band through the total integrals that correspond to monoenergetic gamma rays scattering through the scintillator. This continuum extends further for ^{60}Co than for ^{137}Cs because ^{60}Co gamma ray emissions are higher in energy than those from ^{137}Cs. Double pulses produced from each high-gamma ray field extend through a wide range of tail integrals, overlapping with the neutron region in the tail-vs-total integral surface plot. The overlapping double pulses interferes with the charge integration technique, making it difficult to visually separate neutron pulses from gamma-ray pulses, even in the stilbene detectors. From Poisson statistics, the probability of two or more particles interacting in the same time window is given by

$$DoublePulseProbability = 1 - e^{-\mu t}, \tag{4-3}$$

where μ is the average count rate and t is the time window length [16]. For a time window of 400 ns and average count rate of 100 kHz, the probability of multiple particles interacting in a single window is about 0.035, yielding a double-pulse count rate of approximately 3500 Hz. This double-pulse count rate is high when compared to a neutron count rate of approximately 100 Hz. Since these double pulses look like neutrons when using charge-integration PSD, the intrinsic neutron efficiency in Equation 4-1 is measured as greater than the true intrinsic neutron efficiency when double pulses aren't removed from these measurements.

The charge integration technique is most difficult for lower-energy pulses. ^{137}Cs has lower-energy gamma-ray emissions than ^{60}Co while measuring at the same count rate, so the intensity of double pulses appears greater in Figure 4-4 for experiments with ^{137}Cs than those with ^{60}Co.

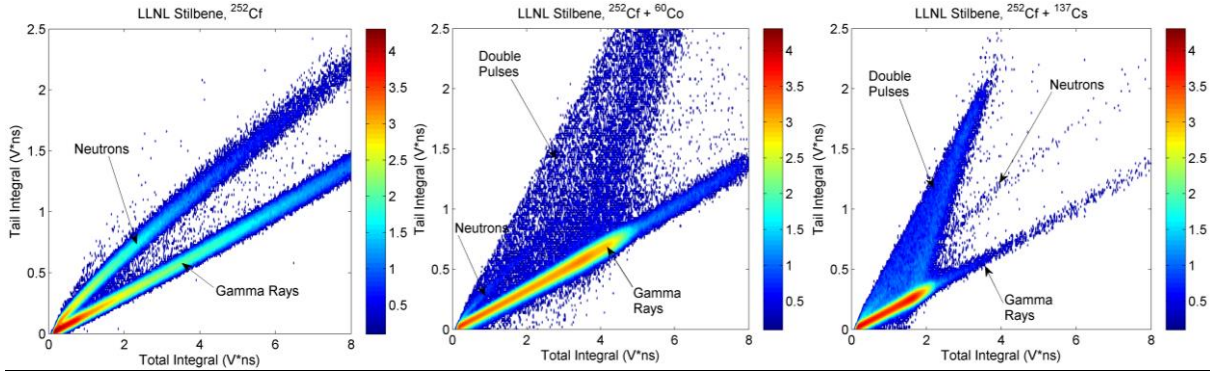
LLNL Stilbene, ^{252}Cf
Neutrons
Gamma Rays
Tail Integral (V*ns)
Total Integral (V*ns)
LLNL Stilbene, ^{252}Cf + ^{60}Co
Double Pulses
Neutrons
Gamma Rays
LLNL Stilbene, ^{252}Cf + ^{137}Cs
Double Pulses
Neutrons
Gamma Rays

(a) (b) (c)

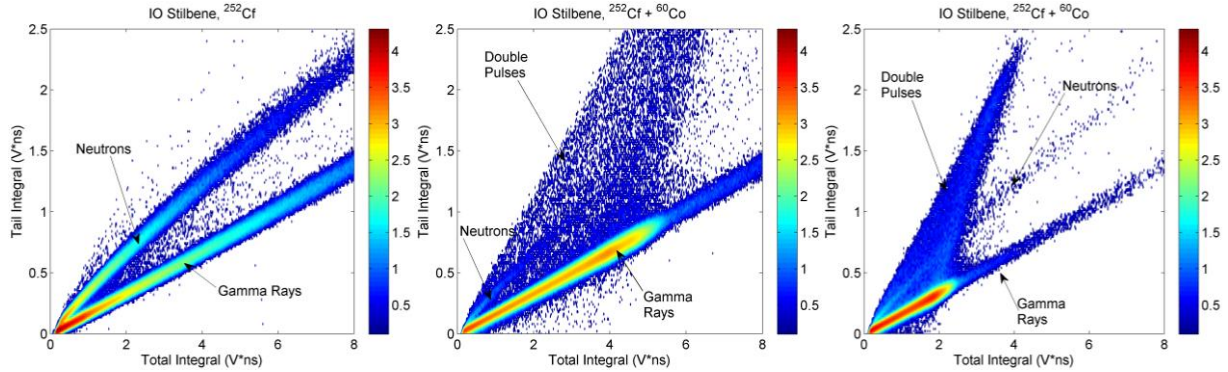
IO Stilbene, ^{252}Cf
Neutrons
Gamma Rays
Tail Integral (V*ns)
Total Integral (V*ns)
IO Stilbene, ^{252}Cf + ^{60}Co
Double Pulses
Neutrons
Gamma Rays
IO Stilbene, ^{252}Cf + ^{60}Co
Double Pulses
Neutrons
Gamma Rays

(d) (e) (f)

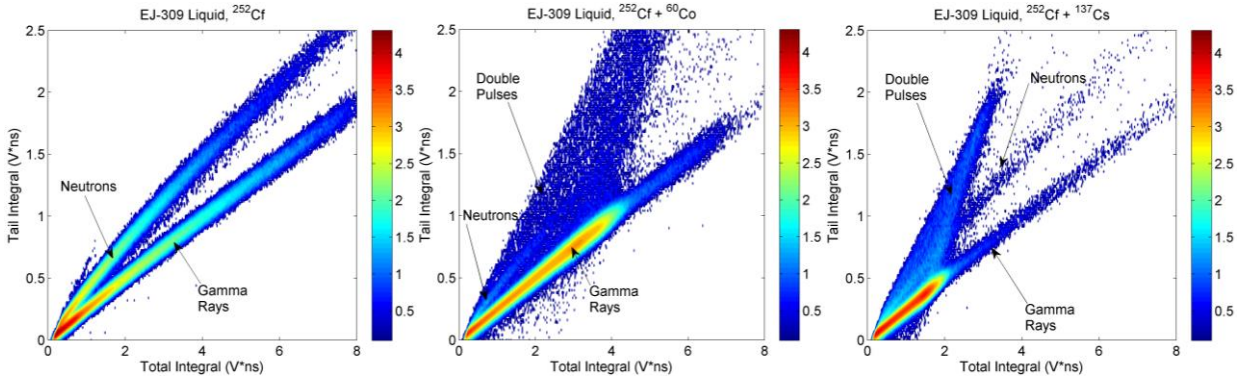
EJ-309 Liquid, ^{252}Cf
Neutrons
Gamma Rays
Tail Integral (V*ns)
Total Integral (V*ns)
EJ-309 Liquid, ^{252}Cf + ^{60}Co
Double Pulses
Neutrons
Gamma Rays
EJ-309 Liquid, ^{252}Cf + ^{137}Cs
Double Pulses
Neutrons
Gamma Rays

(g) (h) (i)

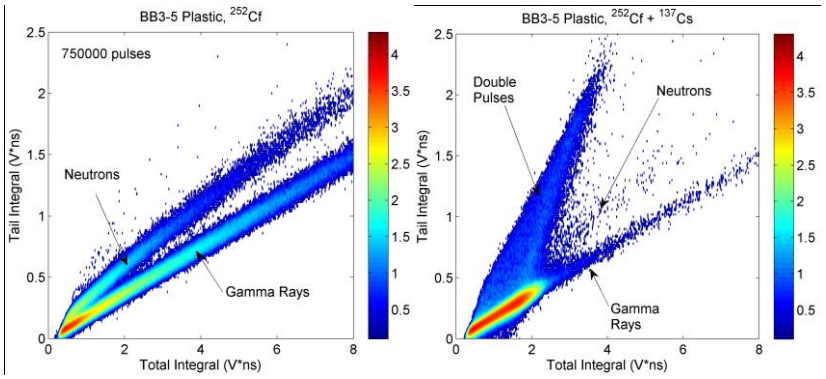

(j) (k)

Fig. 4-4. PSD surfaces for 1,200,000 pulses from the ^{252}Cf, ^{252}Cf-^{60}Co, and ^{252}Cf-^{137}Cs experiments, respectively, for the LLNL stilbene (a-c), Inrad Optic stilbene (d-f), EJ-309 liquid (g-i), and BB3-5 plastic (j, k).

Table 4-2 shows the measured neutron intrinsic efficiency and gamma-ray misclassification rate for each detector before any double-pulse rejection algorithm is implemented. Bare ^{252}Cf efficiencies are 19-20% for stilbene, slightly higher than EJ-309 and a factor-of-2 higher than BB3-5 plastic due to the differences in detection threshold. Inclusion of the high-gamma field, whether using ^{60}Co or ^{137}Cs, increases the measured neutron efficiency close to or above the theoretical limit of 100% due to the high rate of misclassified gamma rays and the high gamma-ray count rate. Differences between the two stilbene crystals exist primarily due to the differences in the PSD tail integration range and the discrimination curve. The discrimination curve was defined using the method described in Section 4.4.3 for all detectors. The gamma-ray misclassification rate was consistently worse when using ^{137}Cs to create the field than when using ^{60}Co, motivating experiments with the BB3-5 plastic to ignore using ^{60}Co.

Table 4-2. Neutron intrinsic efficiency and gamma-ray misclassification rate for each detector before any double-pulse rejection. Stilbene data was processed at a 42-keVee threshold, while EJ-309 liquid and BB3-5 plastic data was processed at a 60-keVee and 96-keVee threshold, respectively. Statistical error is given in parentheses when not negligibly low.

Detector	***Eff***			***MR*** ($\times 10^{-6}$)	
	^{252}Cf	^{252}Cf + ^{60}Co	^{252}Cf + ^{137}Cs	^{60}Co	^{137}Cs
LLNL Stilbene	18.9%	176%	230%	12921 (15)	13641 (15)
IO Stilbene	19.9%	130%	121%	12840 (15)	14363 (16)
EJ-309 Liquid	17.1%	93.3%	80.5%	13375 (15)	14938 (16)
BB3-5 Plastic	8.3%	--	216%	--	15726 (10)

4.4. Effects of Double-Pulse Rejection

A naïve approach to eliminate double pulses involves dividing the ^{252}Cf tail-vs-total integral plots into the regions defined by Figure 2-5, where neutron and gamma-ray pulses are expected to appear for organic scintillators. Each ^{252}Cf tail-vs-total integral plot from Figure 4-4 was traced around their neutron and gamma-ray regions, defining the pulses that are kept and removed in the rejection process. The tail integral varies essentially linearly with the total integral for the gamma-ray regions and slightly less than linear for the neutron region. As a result, the lower and upper bounds were defined as lines for each gamma-ray region and as 2nd-order polynomials for each neutron region. Figure 4-5 shows the effect of implementing these regions of interest into the tail-vs-total integral plots in Figure 4-4. The lower and upper bounds are shown in the ^{252}Cf experiment for each detector, where bounds defining the negative space between the neutron and gamma-ray regions converged to a single point. The point of convergence was selected visually for each detector using the ^{252}Cf data in Figure 4-4.

This method of rejection is very effective at removing pulses that don't lie in the neutron or gamma-ray regions, where there exists the greatest uncertainty in the classification of each pulse at higher total integrals. Therefore, rejection the ^{252}Cf experiments with this method could yield neutron intrinsic efficiency closest to the true neutron efficiency for ^{252}Cf. Uncertainty still exists in particle classification at lower total integrals, where this method does not remove any pulses. The naïve double-pulse rejection algorithm creates separation between the neutron and gamma-ray regions for stilbene while exposed to the gamma-ray source, making it possible to separately identify the neutron and gamma-ray regions in stilbene. The amount of separation is still nearly negligible for EJ-309 liquid and BB3-5 plastic after implementing the double-pulse rejection technique. More importantly, the intensity of the neutron region is significantly greater through the total integrals that the double-pulse region overlapped with the neutron region in Figure 4-4, since this double-pulse rejection algorithm does not target double pulses lying inside the gamma-ray or neutron regions.

So long as double pulses are rare within the neutron region, this rejection technique would still have value over using no double-pulse rejection at all due to the greater certainty of particle classification of pulses lying between or above the neutron and gamma-ray regions. The PSD discrimination curve is shown in results for the ^{252}Cf – ^{60}Co and ^{252}Cf – ^{137}Cs experiments.

These PSD curves were determined for 1,200,000 pulses using the method described in Section 4.4.3, and applied to each experiment performed by each detector.

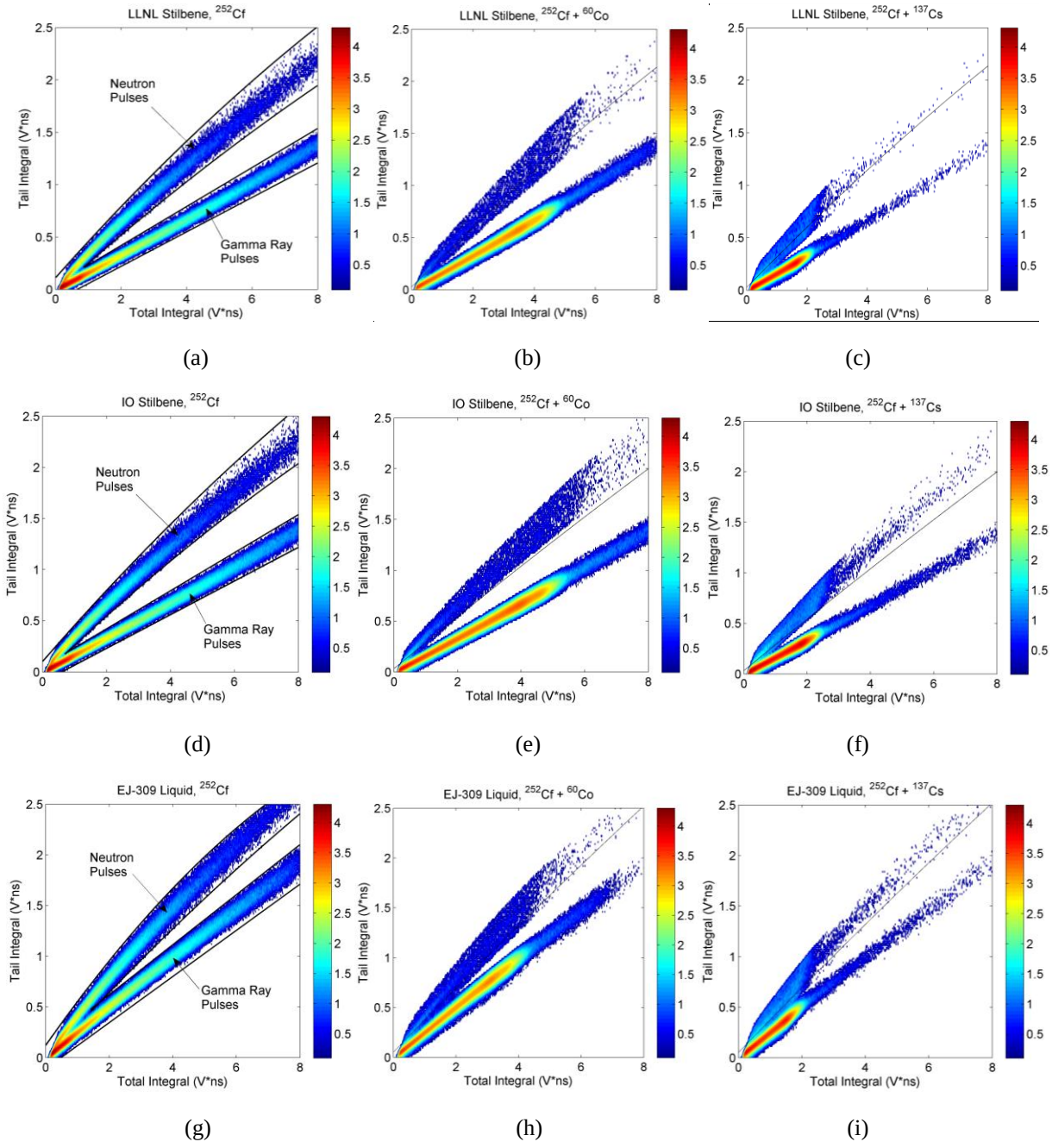

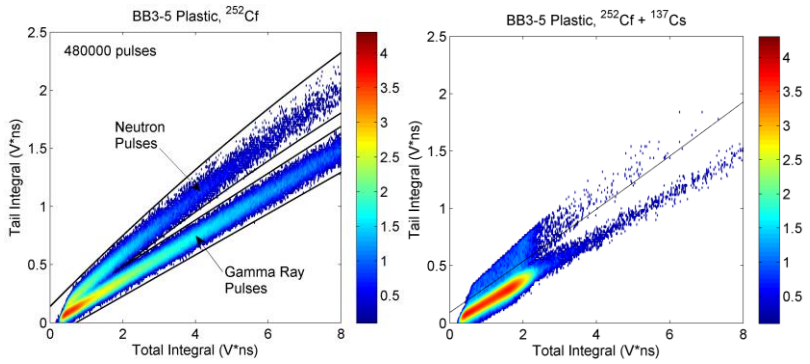

(j) (k)

Fig. 4-5. PSD surfaces after the naïve rejection technique for 1,200,000 pulses from the ^{252}Cf, ^{252}Cf-^{60}Co, and ^{252}Cf-^{137}Cs experiments, respectively, for the LLNL stilbene (a-c), Inrad Optic stilbene (d-f), EJ-309 liquid (g-i), and BB3-5 plastic (j, k).

Table 4-3 shows the neutron intrinsic efficiency and gamma-ray misclassification rate for each detector after implementing this naïve double-pulse rejection technique. Neutron intrinsic efficiency remained nearly constant for every detector when measuring ^{252}Cf, and the gamma-ray misclassification rate decreased by factors of 2-3 in each detector for each gamma-ray source. However, the intensity of double-pulse gamma rays in the neutron region increased the neutron intrinsic efficiency by factors of 2-3 for stilbene and EJ-309 liquid and nearly a factor-of-10 for BB3-5 plastic. To prevent gamma rays from artificially increasing the measured neutron efficiency at a 100-kHz count rate and 1000-to-1 gamma ray-to-neutron ratio, it is insufficient to only remove pulses that lie outside of the predetermined neutron and gamma-ray regions for each scintillation detector. Rather, more robust algorithms are needed to separately identify double pulses, even when their tail and total integrals overlap with neutron pulses.

Consistent with the experimental data with no double-pulse rejection, gamma-ray misclassification rate is worse when measuring ^{137}Cs gamma rays than when measuring ^{60}Co gamma rays at the same count rate. When designing separate double-pulse rejection algorithms, the ^{252}Cf – ^{137}Cs experiments were used to optimize rejection parameters for each detector. Settings for this experiment were then applied to the ^{252}Cf – ^{60}Co and bare ^{252}Cf experiments.

Table 4-3. Neutron intrinsic efficiency and gamma-ray misclassification rate for each detector after naïve double-pulse rejection. Stilbene data was processed at a 42-keVee threshold, while EJ-309 liquid and BB3-5 plastic data was processed at a 60-keVee and 96-keVee threshold, respectively. Statistical error is given in parentheses when not negligibly low.

Detector	***Eff***			***MR*** ($\times 10^{-6}$)	
	^{252}Cf	^{252}Cf + ^{60}Co	^{252}Cf + ^{137}Cs	^{60}Co	^{137}Cs
LLNL Stilbene	18.8%	47.7%	87.6%	2730 (7)	4680 (9)
IO Stilbene	19.8%	47.6%	60.2%	3396 (8)	5926 (10)
EJ-309 Liquid	16.9%	41.1%	47.9%	4483 (9)	7703 (12)
BB3-5 Plastic	8.2%	--	78.0%	--	1824 (3)

4.4.1. Fractional Double-Pulse Rejection Technique

The fractional double-pulse rejection technique utilizes an algorithm inspired in part by traditional pileup rejection electronics [6]. The algorithm examines the tail region of each pulse, comparing consecutive samples in time. Pulses are classified as double pulses if these samples increase by more than a threshold, set as a fixed fraction of the pulse amplitude [39]. Figure 4-6 illustrates this technique on a clear double pulse; however, the technique can also reject low-amplitude, good pulses if the fractional rejection threshold is set too low. The fractional rejection threshold was set to 6% of the pulse amplitude for each detector after determining its effect on the neutron intrinsic efficiency and gamma-ray misclassification rate. The threshold attempts to balance thorough double-pulse rejection with retention of low-energy pulses as shown in Figure 4-7 for Inrad Optic stilbene and EJ-309 liquid. Increasing the fractional rejection threshold to 7% or larger will increase the neutron efficiency, but will also reject fewer double pulses, misclassifying more gamma rays as neutrons.

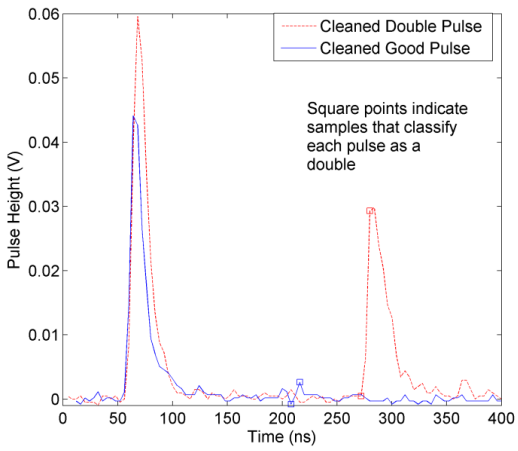

Fig. 4-6. Fractional double pulse rejection technique, illustrated for the Inrad Optics stilbene. This technique removes double pulses while preserving as many low-amplitude good neutron pulses as possible.

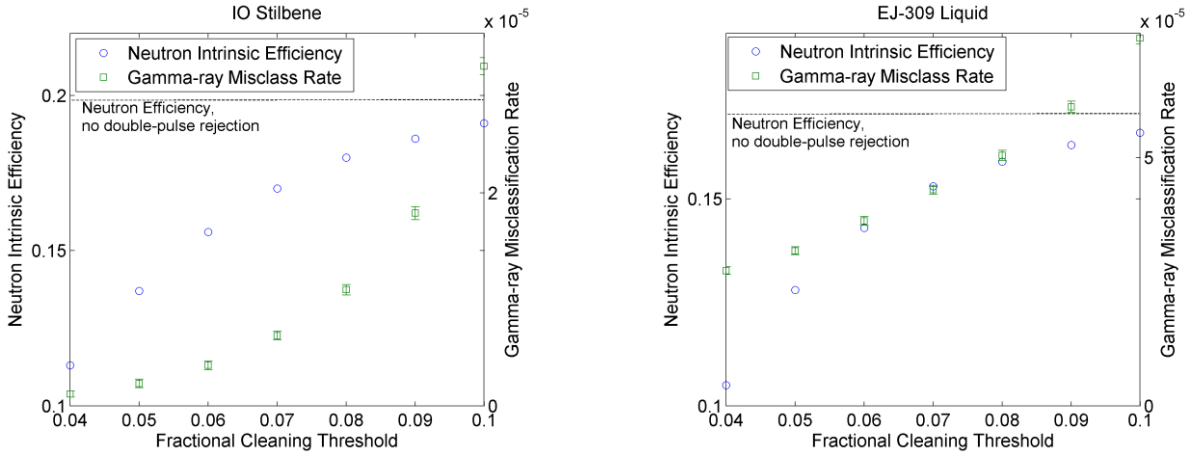

(a) (b)

Fig. 4-7. Dependence of neutron intrinsic efficiency and gamma-ray misclassification rate on the fractional rejection threshold for Inrad Optic stilbene (a) and EJ-309 liquid (b).

Figure 4-8 shows the effect of implementing this fractional rejection technique to the measured data of Figure 4-4. Comparing the ^{252}Cf results without the high-gamma ray field in Figure 4-4 to Figure 4-8 shows nearly all pulses lying above the neutron region have been removed, although pulses remain between the two regions for stilbene and BB3-5 plastic. At lower total integrals, separation between the neutron and gamma-ray regions is essentially the same, but the intensity of the neutron region decreases significantly for the stilbene and EJ-309 liquid detectors. Very little change is otherwise noted in the bare ^{252}Cf experiments, particularly for the BB3-5 plastic detector.

Meanwhile the fractional rejection technique makes a dramatic difference in experiments containing the ^{60}Co or ^{137}Cs sources. The double-pulse region is suppressed into the gamma-ray

region enough to accurately identify the neutron region, making PSD possible in each organic scintillation detector. The stilbene detectors each exhibit clear separation for each gamma-ray source. The separation is hard to notice in the EJ-309 liquid, although slightly better in ^{60}Co than in ^{137}Cs. For total integrals less than 2.5 V-ns, separation is essentially nonexistent between the neutron and gamma-ray regions in the BB3-5 plastic detector. All four detectors exhibit a reduction in the intensity of the neutron region in the high-gamma ray field when using fractional rejection compared to bare ^{252}Cf when using the naïve double-pulse rejection approach.

The discrimination curve was chosen that separates between neutron and gamma rays for 1,200,000 pulses using the method described in Section 4.4.3. The same discrimination curve was applied to experimental data before and after fractional rejection.

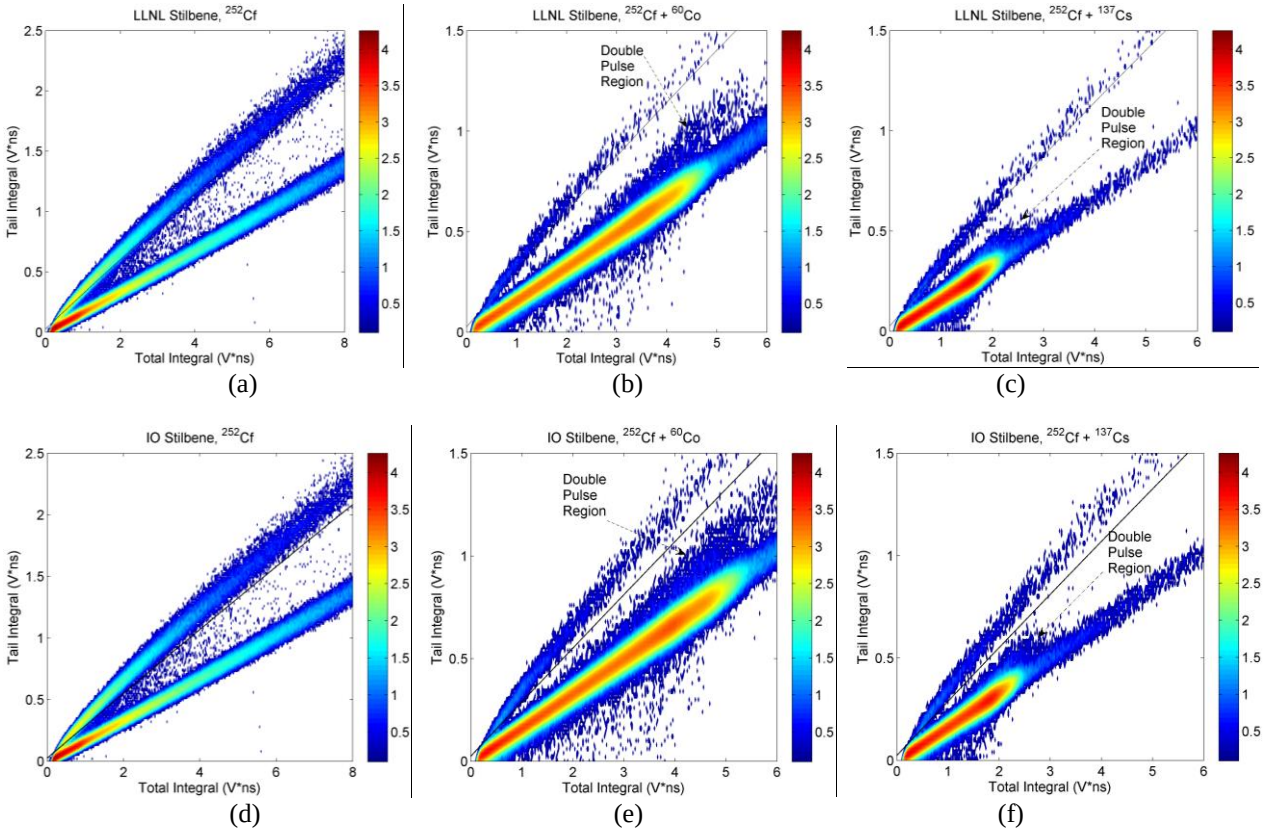

(a) (b) (c)

(d) (e) (f)

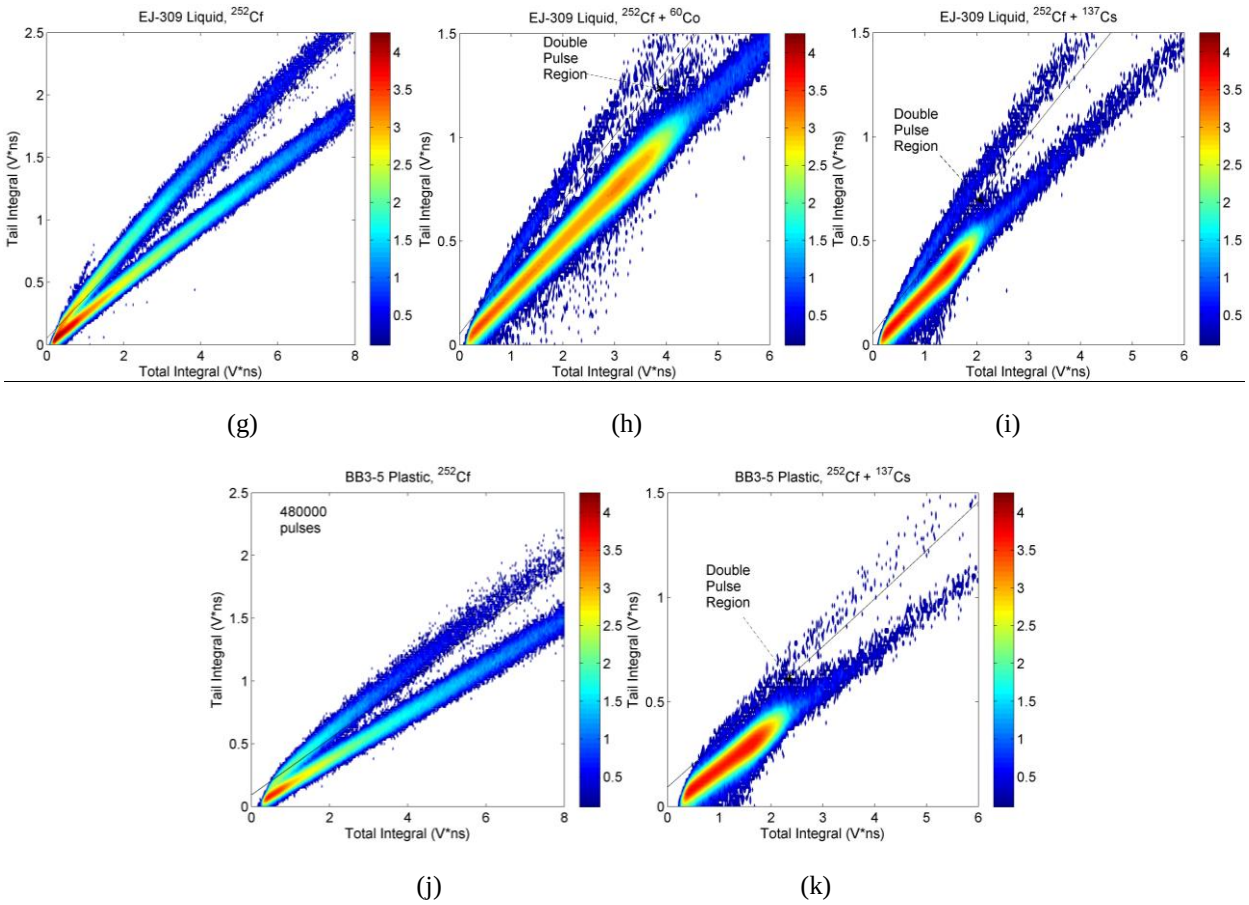

Fig. 4-8. PSD surfaces after fractional double-pulse rejection for 1,200,000 pulses from ^{252}Cf bare, ^{252}Cf + ^{60}Co, and ^{252}Cf + ^{137}Cs respectively for LLNL stilbene (a-c), Inrad Optic stilbene (d-f), EJ-309 liquid (g-i), and BB3-5 plastic (j-k).

Table 4-4 shows the intrinsic neutron efficiency and gamma-ray misclassification rate for each detector after applying the fractional rejection technique to each experiment. The removal of numerous double pulses in each high-gamma ray dataset improves gamma-ray misclassification rate by over 3 orders of magnitude in stilbene and over 2 orders of magnitude in EJ-309 liquid and BB3-5 plastic. However, the fractional rejection technique's focus on removing low-energy pulses sacrifices approximately 20% efficiency in stilbene and EJ-309 liquid and 13% in BB3-5 plastic when measuring ^{252}Cf by itself.

When using fractional rejection, inclusion of the high-gamma ray field actually reduces neutron efficiency by approximately 13% of ^{252}Cf neutrons in stilbene and EJ-309 liquid. Since the rejection algorithm has such low gamma-ray misclassification rate, it is more likely to reject neutron pulses contained within a double pulse than to misclassify gamma-ray double pulses as neutrons, an improvement over the naïve double-pulse rejection technique. The higher threshold

in BB3-5 plastic, when combined with the conservative discrimination curve chosen in Section 4.4.3, softens the reduction in neutron intrinsic efficiency when using fractional double-pulse rejection, as many neutron pulses that would have been removed by this technique are already below threshold or included in the gamma-ray region.

Table 4-4. Neutron intrinsic efficiency and gamma-ray misclassification rate for each detector after fractional double-pulse rejection. Stilbene data was processed at a 42-keVee threshold, while EJ-309 liquid and BB3-5 plastic data was processed at a 60-keVee and 96-keVee threshold, respectively. Statistical error is given in parentheses when not negligibly low.

	Eff			***MR*** ($\times 10^{-6}$)	
	^{252}Cf	^{252}Cf + ^{60}Co	^{252}Cf + ^{137}Cs	^{60}Co	^{137}Cs
LLNL Stilbene	14.9%	12.7%	13.7%	10.2(5)	6.0(4)
IO Stilbene	15.6%	13.6%	13.8%	6.6(5)	3.8(4)
EJ-309 Liquid	14.2%	12.1%	11.3%	46.2 (1.0)	37.2(9)
BB3-5 Plastic	7.4%	--	7.0%	--	23.4(4)

4.4.2. Template Double-Pulse Rejection Technique

The template double-pulse rejection technique makes use of digitized pulse templates from data acquired from the low count rate experiments of ^{252}Cf. The charge integration technique identifies each ^{252}Cf pulse as a neutron or gamma-ray pulse. These pulses are grouped by type and sorted into 20-mV pulse amplitude bins ranging from 0.02-2 Volts. Pulses are averaged point-for-point to build gamma ray and neutron pulse templates for each detector as a function of pulse amplitude. These templates are unique for each detector and gain setting, but can be applied to pulses from any neutron or gamma-ray source.

The ^{252}Cf gamma ray and neutron pulse templates are shown in Figure 4-9 for all four scintillation detectors. As expected from the physics of pulse-shape discrimination in organic scintillators, pulses in the neutron template have more light in their tail region than pulses in the gamma-ray template for each detector. Stilbene templates contain smooth waveforms for all pulse amplitudes, while the EJ-309 liquid templates contain a dip in each template at around 100 ns. As it is a consistent feature in each template, it is expected to be an artifact created by the light collection of the detector assembly, which differs from the stilbene and BB3-5 plastic detector assemblies. The BB3-5 plastic detector has the least difference in its tail region between the two templates, consistent with figures 4-4, 4-5, and 4-8, but is otherwise featureless, although

neutron templates for higher pulse amplitudes are not as converged as the stilbene and EJ-309 liquid detectors.

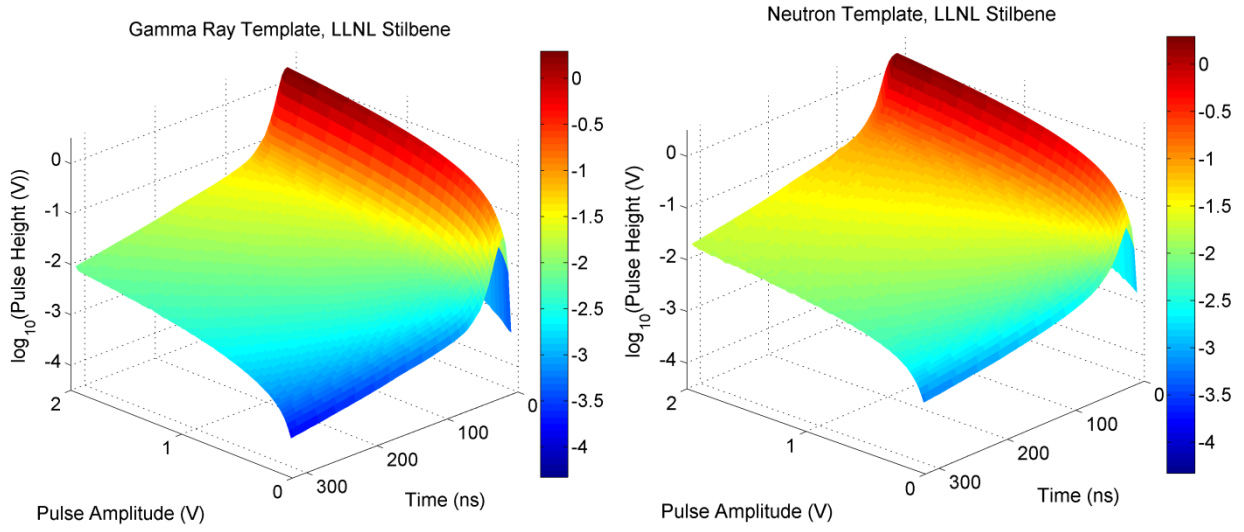

(a)

(b)

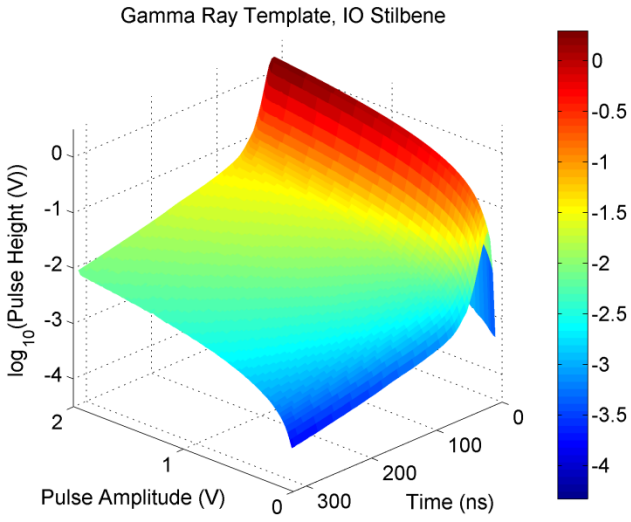

(c)

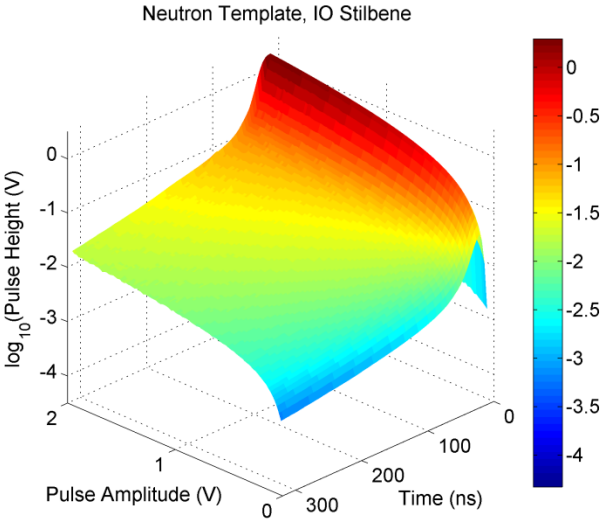

(d)

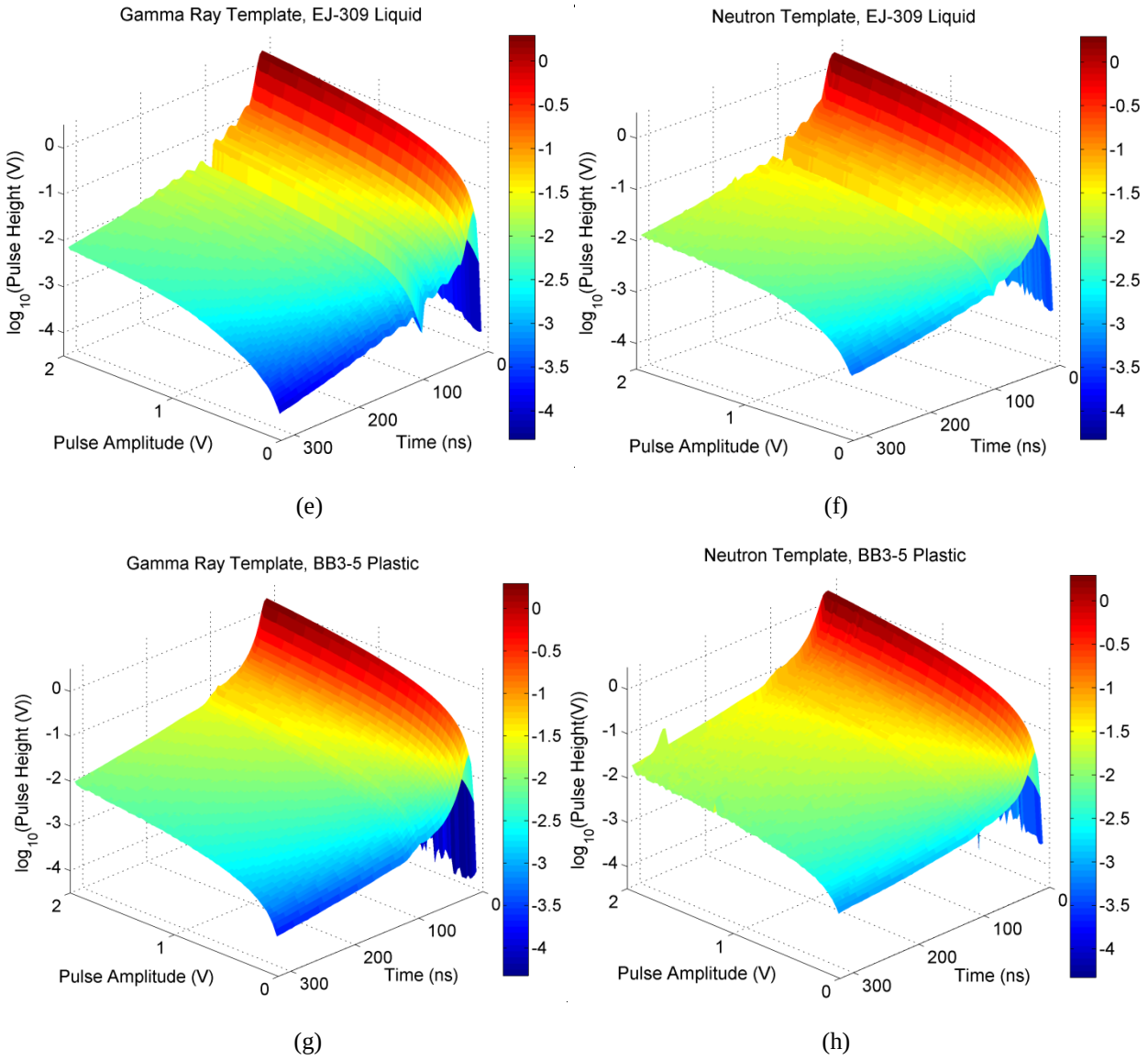

Fig. 4-9. Gamma ray and neutron templates, respectively, used for the LLNL stilbene (a, b), Inrad Optic stilbene (c, d), EJ-309 liquid (e, f), and BB3-5 plastic (g, h) scintillators.

The template technique compares pulses to their respective pulse template and rejects pulses that exceed the pulse template by more than a fixed threshold in their tail regions. Figure 4-10 shows examples of pulses removed by template rejection. The fast rise time of scintillation pulses, when sampled in 4-ns intervals, increases the likelihood that the true pulse amplitude is not sampled accurately. Because templates are created as a function of pulse amplitude, selecting the wrong template can remove good pulses. To minimize removal of good pulses and maximize removal of double pulses, the template threshold was chosen based on the standard deviation for every sample of the combined neutron and gamma-ray pulse templates in each detector.

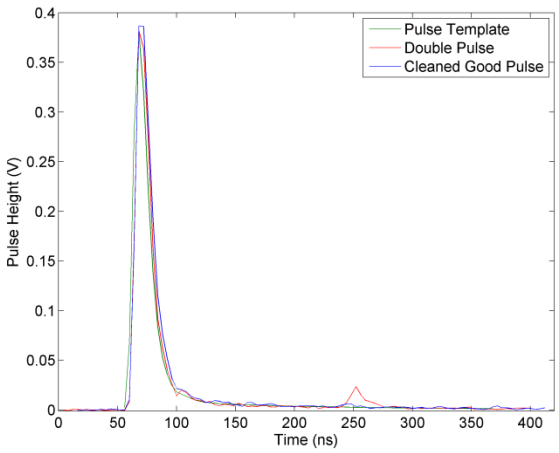

Fig. 4-10. Template double pulse rejection technique, illustrated for the Inrad Optic stilbene. This technique removes double pulses while limiting pulses removed from selecting the wrong template.

Figure 4-11 shows the standard deviation for every sample of the pulse templates for each detector. Local peaks are prevalent in all four detectors at later times in each template, but their intensity remains relatively low. The standard deviation is greatest near the falling edge of each pulse template, and is most intense for detectors whose pulse tail regions are defined to begin earliest in time. As discussed in Section 4.1, the EJ-309 liquid detector has the longest tail region, while the BB3-5 plastic detector has the shortest tail region. The template threshold was chosen to be 15 mV for all four detectors because the standard deviation for ^{252}Cf pulses stayed below 15 mV (yellow on the scale shown in Figure 4-11) through each template. Some pulses may get removed with pulse amplitudes near the maximum accepted threshold, especially in the stilbene and EJ-309 liquid detectors, but the template rejection method should still preserve the overwhelming majority of good pulses in each experiment.

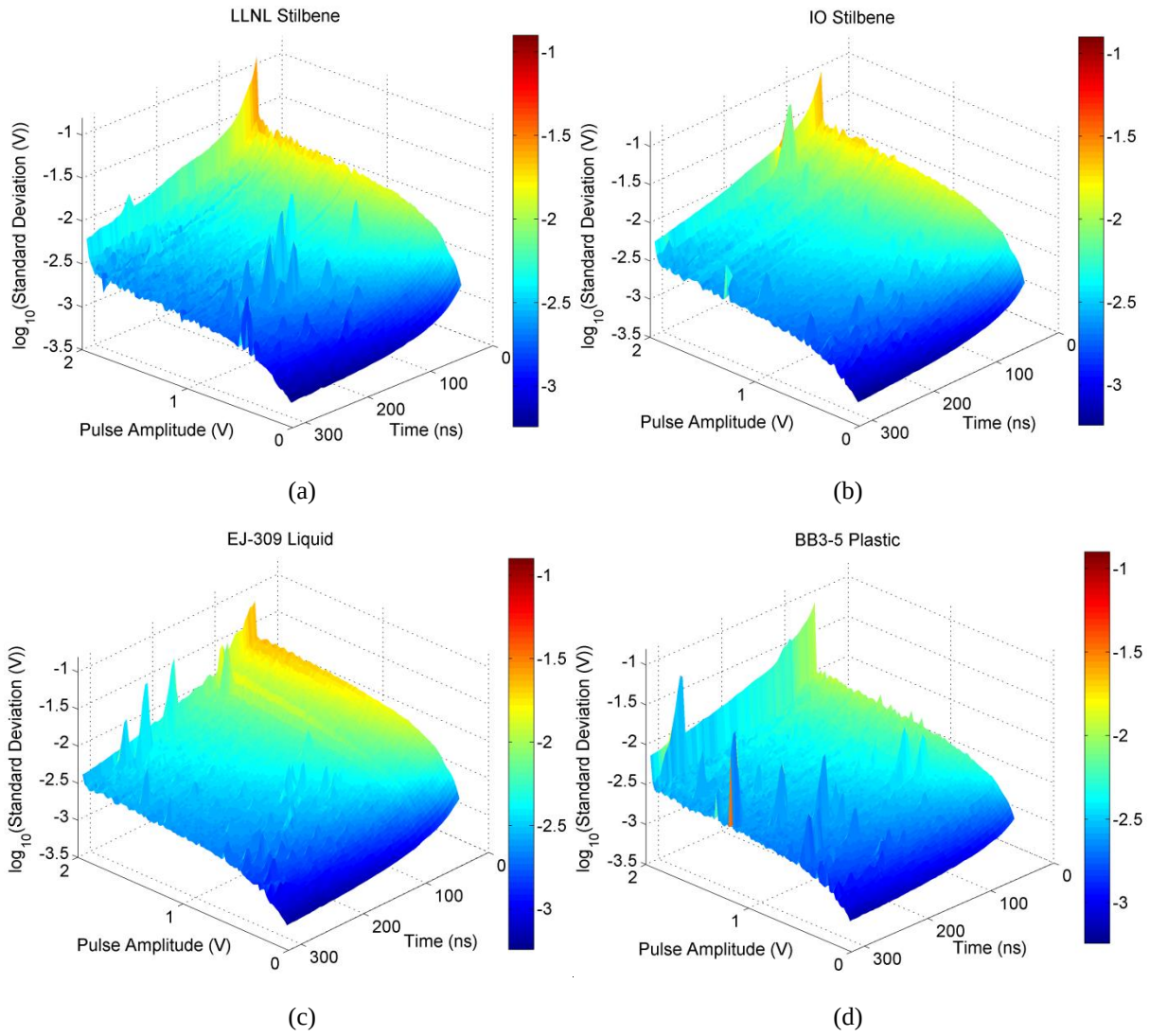

Fig. 4-11. Standard deviation of templates for all pulses in the LLNL stilbene (a), Inrad Optic stilbene (b), EJ-309 liquid (c), and BB3-5 plastic (d) scintillators.

Figure 4-12 shows the effect of implementing this template rejection technique to the experimental data in Figure 4-4. Template rejection removes more pulses above and between the neutron and gamma-ray regions in the ^{252}Cf experiments, making stilbene and BB3-5 plastic appear cleaner than fractional rejection. At lower total integrals, template rejection preserves more neutrons than fractional rejection in each detector and similar in magnitude to naïve double-pulse rejection.

In the presence of the gamma-ray source, template rejection is capable of removing enough double pulses to discriminate between the neutron and gamma-ray regions, similar to fractional rejection. Template rejection improves on fractional rejection in stilbene by yielding

greater separation between the neutron and double-pulse regions at the total integral near the Compton edge of each gamma-ray source, occurring at approximately 5 V-ns for ^{60}Co and 2.5 V-ns for ^{137}Cs. More pulses in the neutron region are preserved in template rejection near the detection threshold, which is expected to improve neutron efficiency but increase the gamma-ray misclassification rate, as there is now less separation between the neutron and gamma-ray regions at lower energies. Separation appears very similar in both the EJ-309 liquid and BB3-5 plastic, whether using fractional or template rejection.

The PSD discrimination curve was chosen that separates between neutron and gamma rays for 1,200,000 pulses using the method described in Section 4.4.3.

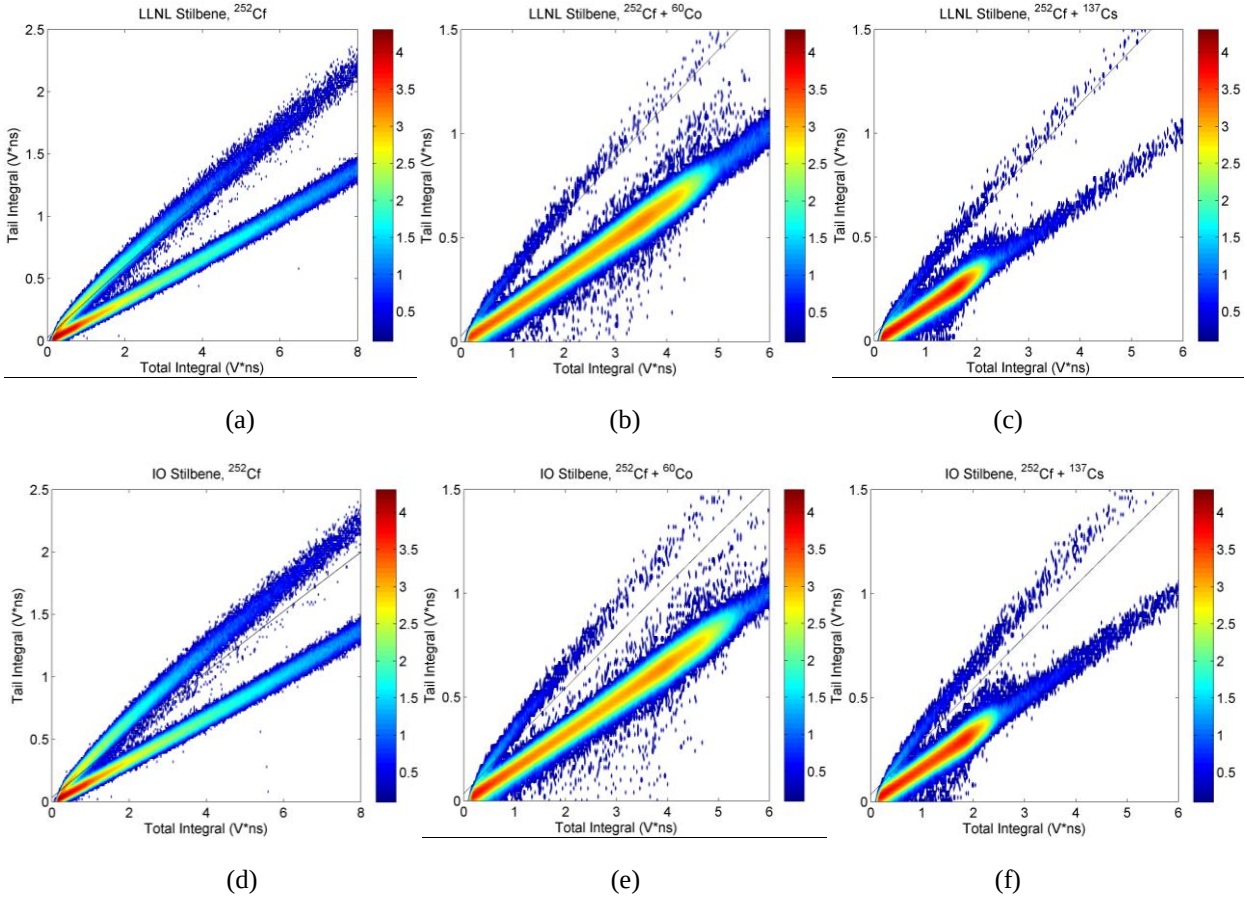

(a) (b) (c)

(d) (e) (f)

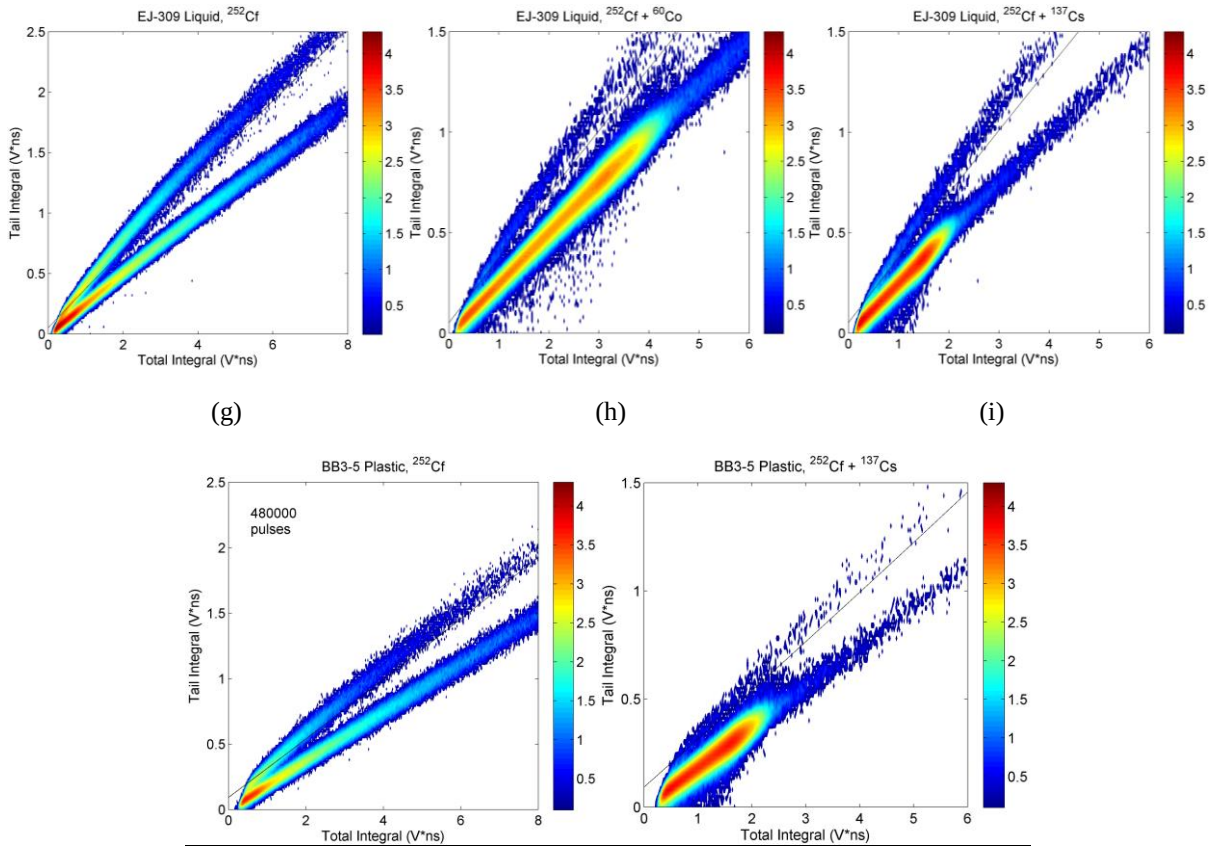

Fig. 4-12. PSD surfaces after template double-pulse rejection for 1,200,000 pulses from ^{252}Cf bare, ^{252}Cf + ^{60}Co, and ^{252}Cf + ^{137}Cs respectively for LLNL stilbene (a-c), Inrad Optic stilbene (d-f), EJ-309 liquid (g-i), and BB3-5 plastic (j-k).

Table 4-5 shows the intrinsic neutron efficiency and gamma-ray misclassification rate after applying the template rejection technique to each experiment for each detector. For stilbene, the template rejection technique reduces the gamma-ray misclassification rate by over 3 orders of magnitude in ^{60}Co, similar to the fractional rejection technique. Due to its focus on reducing higher-energy double pulses, only 3% of intrinsic efficiency is lost in stilbene when measuring bare ^{252}Cf. However, the template rejection technique is significantly worse with ^{137}Cs creating the high-gamma ray field than with ^{60}Co. The higher light output threshold in the EJ-309 liquid and BB3-5 plastic, when combined with the low separation between the neutron and double-pulse regions, allows for improvements in both efficiency and misclassification rate when using template rejection over fractional rejection. To consistently improve misclassification rate by over 3 orders of magnitude independent of gamma-ray energy or detector type, a rejection

method is needed that gives greater separation between the neutron and double-pulse regions at lower total integrals.

Table 4-5. Neutron intrinsic efficiency and gamma-ray misclassification rate for each detector after template double-pulse rejection. Stilbene data was processed at a 42-keVee threshold, while EJ-309 liquid and BB3-5 plastic data was processed at a 60-keVee and 96-keVee threshold, respectively. Statistical error is given in parentheses when not negligibly low.

Detector	***Eff***			***MR*** ($\times 10^{-6}$)	
	^{252}Cf	^{252}Cf + ^{60}Co	^{252}Cf + ^{137}Cs	^{60}Co	^{137}Cs
LLNL Stilbene	18.4%	15.8%	17.6%	11.0(5)	50.3(9)
IO Stilbene	19.2%	16.8%	17.5%	10.4(1.0)	60.1(4)
EJ-309 Liquid	15.3%	12.9%	12.2%	13.1(5)	28.0(7)
BB3-5 Plastic	7.7%	--	7.2%	--	19.8(4)

4.4.3. Hybrid Double-Pulse Rejection Technique

Figures 4-8 and 4-12 show separation between the neutron and gamma-ray regions is more pronounced when using fractional rejection, while the double-pulse region is more suppressed at higher integrals when using template rejection. The proposed hybrid double-pulse rejection technique combines these two features to split the method of double-pulse rejection at 180 keVee. For pulses with light output less than 180 keVee, the fractional rejection technique was used to obtain clear separation between the neutron and gamma-ray regions. For pulses with light output greater than 180 keVee, the template rejection technique was used to suppress the double pulse region. The hybrid rejection technique is expected to lower the gamma-ray misclassification rate relative to using either technique alone, but the measured intrinsic neutron efficiency will be lower. Pulses not removed by the hybrid rejection technique were compiled into PSD tail integral vs total integral distributions.

The PSD discrimination curve was obtained using a specialized MATLAB routine on bare ^{252}Cf data from each detector, inspired in part by the PSD algorithm described in [20]. This routine slices each tail-to-total integral distribution vertically, dividing pulses by total integral with a slice width of 0.1 V-ns. For the first 40 slices, pulses are histogrammed within each slice by their ratio of tail-to-total integrals to create separate gamma ray and neutron peaks similar to Figure 2-4. Histograms are fit to a sum of two Gaussians, where each Gaussian represents

particles classified as either gamma rays or neutrons. A discrimination point is selected along the left edge of the neutron peak where the edge is equivalent to a fraction of the neutron peak maximum. This method is illustrated in Figure 4-13. This fraction was set more conservatively for lower-energy slices than higher-energy slices. Discrimination points from each slice were fit to a 2nd-order polynomial. Both the neutron peak fraction used for each slice and the slices used for generating the fit of each detector are provided in Table 4-6.

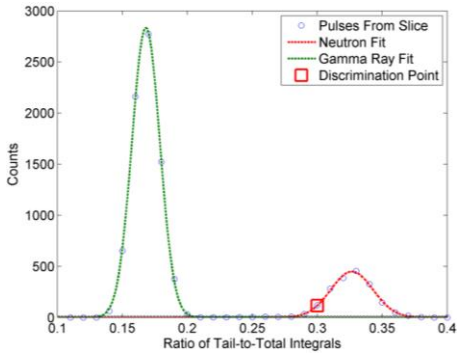

Fig. 4-13. Sample histogram of the ratio of tail-to-total integrals from a single slice obtained from ^{252}Cf pulses recorded by the Inrad Optic stilbene. The discrimination point is chosen along the left side of the neutron peak using a fraction of the peak maximum.

Table 4-6. Neutron peak fraction for each detector as a function of slice.

Slice Interval	Neutron Peak Fraction			
	LLNL Stilbene	IO Stilbene	EJ-309 Liquid	BB3-5 Plastic
4	0.9	0.9	--	--
5-6	0.6	0.6	--	--
7-8	0.2	0.15	0.8	--
9-10	0.1	0.04	0.55	1
11	0.05	0.01	0.2	1
12-13	0.05	0.01	0.2	0.9
14	0.03	0.005	0.07	0.9
15-16	0.03	0.005	0.07	0.8
17-18	0.03	0.003	0.05	0.5
19	0.02	0.002	0.04	0.3
20-21	0.02	0.002	0.02	0.3
22-26	0.02	0.002	0.02	0.2
27	0.02	0.002	0.02	0.1
28-30	0.03	0.002	0.02	0.1
31-33	0.03	0.002	0.02	0.03
34-35	0.03	0.002	0.02	0.01
36-37	0.03	0.002	0.01	0.005
38	--	--	--	0.08
39-40	--	--	--	0.2

This discrimination curve and the fractional and template rejection thresholds were applied to the bare ^{252}Cf, ^{252}Cf-^{60}Co, and ^{252}Cf-^{137}Cs experiments. Figure 4-14 shows the tail integral vs. total integral surfaces obtained from 1,200,000 pulses from each detector in each experiment after hybrid rejection unless otherwise specified. Hybrid rejection appears very similar to fractional rejection for each case when measuring ^{252}Cf. Inclusion of the gamma-ray source yields separation between the neutron and double-pulse regions that is significant enough to classify most remaining double pulses as gamma rays in stilbene. These pulses will no longer contribute to the calculated intrinsic neutron efficiency for stilbene. Separation for the EJ-309 liquid and BB3-5 plastic, on the other hand, is much worse in the high-gamma ray experiments, so the discrimination curve was drawn more conservatively to compensate. Raising the PSD discrimination curve lowered the observed intrinsic neutron efficiency but improved the gamma-ray misclassification rate in each detector.

Equation 4-3 predicts that, for an experiment with a 100-kHz count rate and 400-ns window length, approximately 1.18 million double pulses will be recorded in five minutes. Using the hybrid rejection algorithm, the Inrad Optic stilbene classified 1.17 million pulses as double pulses over the same time period, or 99.5% of the expected amount of double pulses. The rejection method conforms well to what theory would expect, although some of these classified double pulses are actually neutron pulses.

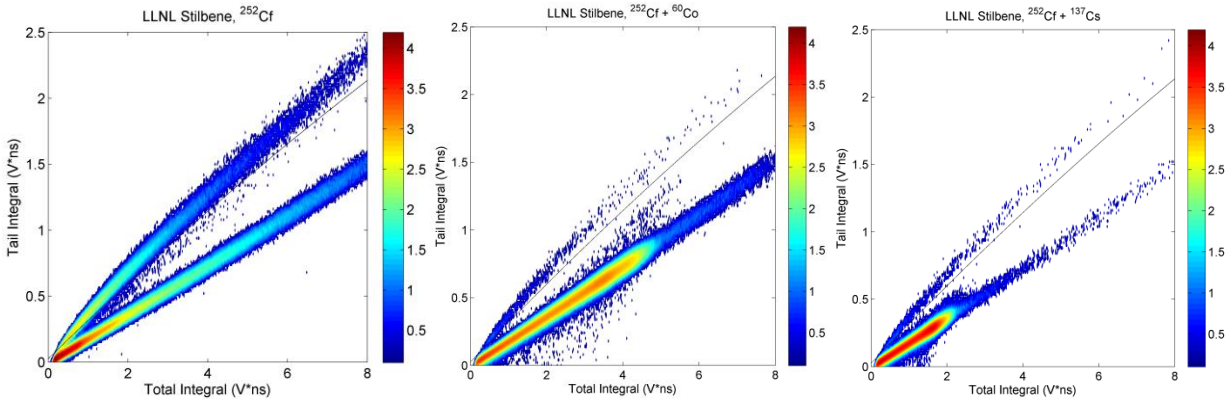

(a) (b) (c)

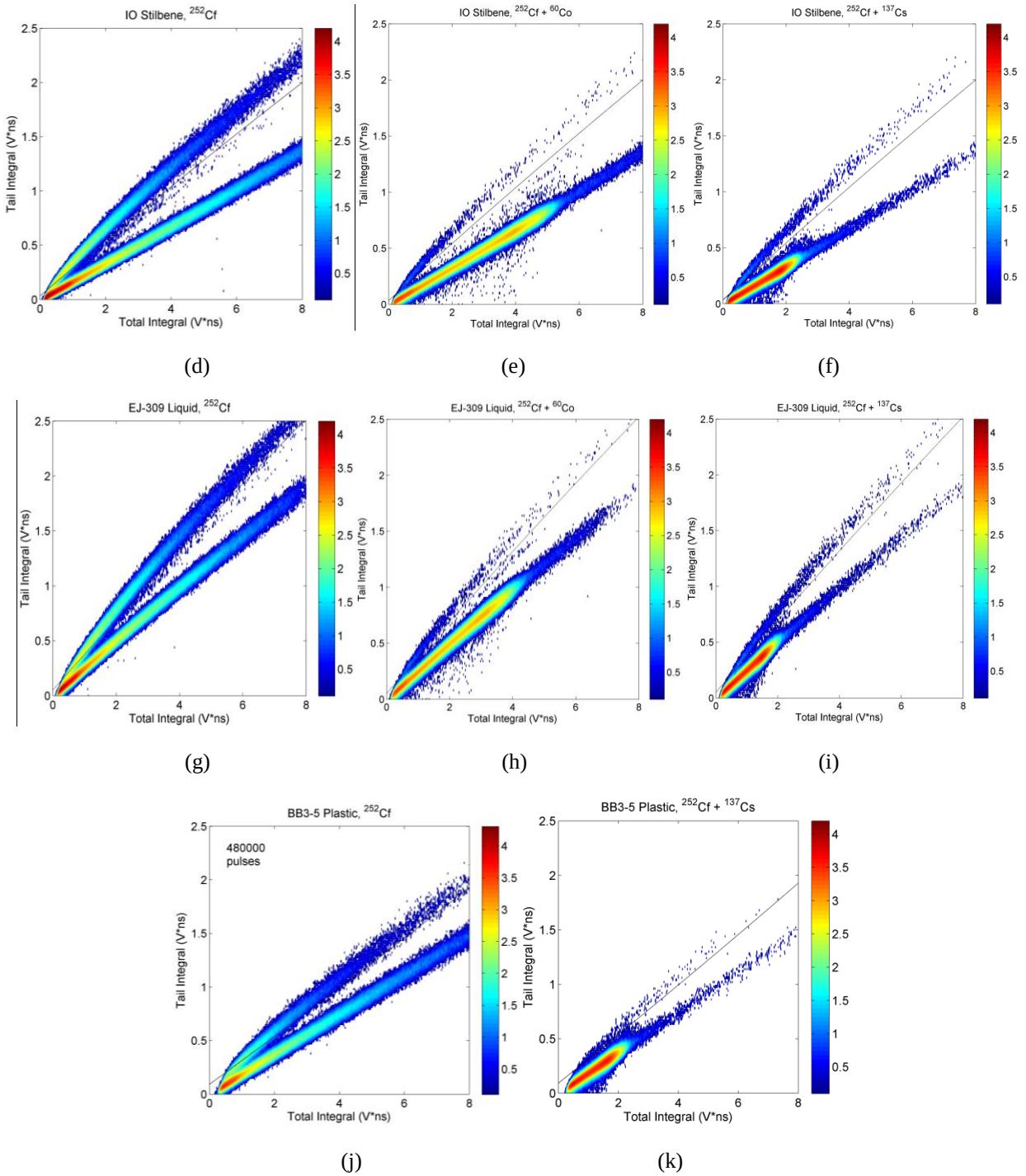

Fig. 4-14. PSD surfaces after hybrid double-pulse rejection for 1,200,000 pulses from ^{252}Cf bare, ^{252}Cf + ^{60}Co, and ^{252}Cf + ^{137}Cs respectively for LLNL stilbene (a-c), Inrad Optic stilbene (d-f), EJ-309 liquid (g-i), and BB3-5 plastic (j-k). Neutron and gamma-ray regions can be visually distinguished and separated, although some double pulses still remain.

Table 4-7 shows the intrinsic neutron efficiency and gamma-ray misclassification rate after applying the hybrid rejection technique to our experimental data. The hybrid rejection

technique consistently improves misclassification to the order of 10^{-6} in stilbene while losing approximately 20% neutron efficiency compared to template rejection. This method is less effective in EJ-309 liquid, but still yields a 35% reduction in misclassification rate compared to fractional rejection while sacrificing 16% efficiency compared to template rejection. The high threshold in BB3-5 plastic makes this method largely insensitive to its neutron efficiency and gamma-ray misclassification rate when compared to template rejection. Misclassification was generally better when the detectors were exposed to ^{60}Co than ^{137}Cs because higher-energy gamma-ray interactions are classified more accurately than lower-energy gamma-ray interactions. Chapter 5 contains experiments using stilbene measuring plutonium samples containing significant ^{241}Am content. The 59-keV gamma rays from ^{241}Am make PSD performance even worse than 662-keV gamma rays from ^{137}Cs, requiring more aggressive double-pulse rejection parameters or lead shielding.

An additional column references the gamma-ray rejection rate, *GRR*, defined in Section 2.1 as the fraction of incident gamma rays that are misclassified as neutrons. Stilbene can obtain gamma-ray rejection rates consistently on the order of 10^{-7} while measuring ^{137}Cs or ^{60}Co gamma rays, nearly an order-of-magnitude better than EJ-309 liquid and BB3-5 plastic. Stilbene would need more aggressive double-pulse rejection settings, biased PSD classification, or lead shielding to obtain gamma-ray rejection rates that match the lowest gamma-ray rejection rate obtained in ^{3}He detectors [18].

Table 4-7. Neutron intrinsic efficiency, gamma-ray misclassification rate, and gamma-ray rejection rate for each detector after hybrid double-pulse rejection. Stilbene data was processed at a 42-keVee threshold, while EJ-309 liquid and RMD plastic data was processed at a 60-keVee and 96-keVee threshold, respectively. Statistical error is given in parentheses when not negligibly low.

Detector	***Eff***			***MR*** ($\times 10^{-6}$)		***GRR*** ($\times 10^{-7}$)	
	^{252}Cf	^{252}Cf + ^{60}Co	^{252}Cf + ^{137}Cs	^{60}Co	^{137}Cs	^{60}Co	^{137}Cs
LLNL Stilbene	14.4%	12.2%	13.2%	3.2(3)	4.1(3)	3.7(3)	6.1(5)
IO Stilbene	15.1%	13.1%	13.4%	1.3(2)	2.9(3)	3.6(6)	9.3(8)
EJ-309 Liquid	12.9%	10.8%	10.1%	9.9(4)	16.0(6)	22.8 (1.0)	27.4 (9)
BB3-5 Plastic	7.1%	--	6.6%	--	19.3(4)	--	23.5 (4)

4.5. Remarks

The stilbene, EJ-309 liquid, and BB3-5 plastic scintillation detectors used in conjunction with the digital signal processing algorithms developed in this thesis showed the capability to measure neutrons from an unshielded ^{252}Cf source in a field of at least 1000 incident gamma rays per incident ^{252}Cf neutron when using ^{60}Co or ^{137}Cs sources. Despite using a lower light output threshold, the stilbene detectors in conjunction with the hybrid rejection technique gave gamma-ray misclassification rates on the order of 10^{-6}, a factor-of-5 better than EJ-309 liquid and BB3-5 plastic scintillation detectors using the same technique. When measuring bare ^{252}Cf, after hybrid double-pulse rejection, the stilbene detectors exhibited intrinsic neutron efficiency of approximately 14.5%, 10% greater than the EJ-309 liquid and 100% better than the BB3-5 plastic. The efficiency decreases to 13% when the gamma-ray source is added since the presence of the source forces rejection of neutron pulses overlapping with gamma-ray pulses. Differences between the LLNL and Inrad Optic stilbenes were on the order of 5%, further verified when PSD settings were set identically in each stilbene detector. The significant drop-off in performance for the BB3-5 plastic (and thus the EJ-299-33 plastic based on PSD results in Figure 3-5) suggests applications of these plastics in high-gamma ray fields are limited unless lead shielding reduces the gamma-ray count rate.

Using the hybrid double-pulse rejection method, it was found that stilbene could obtain gamma-ray rejection rates on the order of 10^{-7}, while the EJ-309 liquid and BB3-5 plastic were on the order of 10^{-6}. While stilbene falls short of the lowest gamma-ray rejection rates obtained in ^{3}He, it is important to note that ^{3}He must operate while embedded in a block of moderator at least 5 centimeters thick. Gamma rays incident on a ^{3}He panel will often scatter away from or outright miss all ^{3}He tubes in the array, while the geometry of the experiments in Chapter 4 dictate that every gamma ray incident on stilbene will pass through the crystal first. It is expected that, if accounting for gamma rays that can't possibly interact with ^{3}He, the difference between ^{3}He and stilbene will be smaller, and require only minimal changes for stilbene to match the most accurate ^{3}He performance.

The reported intrinsic neutron efficiency and gamma-ray misclassification rate are dependent on double-pulse rejection and PSD settings. We found that lowering the fractional or template rejection thresholds, increasing the energy threshold, or drawing a more conservative

discrimination line will improve the misclassification rate at the cost of intrinsic efficiency. On the other hand, using a template-based double-pulse rejection approach is more desirable for applications where a misclassification of 10^{-5} is sufficient due to the improved intrinsic efficiency. The best rejection method for a given application requires knowledge of how the detector system and rejection method will respond to a variety of SNM samples, including plutonium oxide and plutonium metal.

Chapter 5. Double-Pulse Rejection of Plutonium Experiments with Stilbene Scintillators

Chapter 4 discusses the development of a hybrid double-pulse rejection technique that improves organic scintillator PSD accuracy when measuring ^{252}Cf neutrons in a high count rate environment dominated by gamma rays. The elevated gamma-ray count rate was designed to make the ^{252}Cf, which naturally emits 2-10 gamma rays per neutron, look more like some plutonium samples, which can easily emit over 100 gamma rays per neutron. Gamma-ray emissions from plutonium are most intense for energies of up to 800 keV [11]. The presence of ^{241}Am further increases gamma-ray emissions in the sample, mostly with energy 59 keV [11].

The development of the hybridized double-pulse rejection technique makes measurements of plutonium more promising, but the question still remains regarding which rejection method is best for each sample. False alarming on numerous gamma-ray double pulses should be avoided, but neutron efficiency must be preserved such that neutron sources will still alarm correctly. A variety of plutonium and ^{252}Cf samples were measured with stilbene scintillators, each with varying source composition, source strength, and ratio of gamma ray emissions to neutron emissions. Measured pulses before and after each rejection method described in Chapter 4 are compared to models developed in MCNPX-PoliMi. The rejection method that most closely matches the simulation determines which rejection method is most appropriate in each case. A metric was developed that easily determines which rejection method is most appropriate for experiments of plutonium samples containing unknown content.

5.1. Plutonium Experiments

Experiments with stilbene were performed during two measurement campaigns: one at the Joint Research Centre (JRC) at Ispra, Italy in November 2014 and one at Idaho National Laboratory (INL) in August 2015. Two stilbene detectors were assembled at the University of Michigan using crystals provided by Inrad Optics with dimensions matching the crystals described in Section 4.1. Scintillators were positioned in front of five different sources at the

JRC: two plutonium oxide samples with varying ^{240}Pu content labeled “CBNM”, two sets of five plutonium-gallium metal disks with varying ^{240}Pu content, and a canister of mixed oxide (MOX) powder labeled ENEA-02. Lead was used for experiments with the MOX canister, while the plutonium-gallium metal disks were measured both with and without a piece of lead with thickness of 0.635 centimeters. No lead was used for the plutonium oxide experiments. Waveforms were digitized at a 36-keVee threshold using the CAEN DT5720 digitizer for each measurement, sampling for a window length of 400 ns. Only one stilbene was utilized for analysis.

The measurement campaign at INL used a stilbene detector from Inrad Optics with the same dimensions to measure a single PAHN plutonium plate. The detector was positioned such that the count rate was approximately 90 kHz (mostly from 59-keV ^{241}Am gamma rays) when measuring at a 36-keVee threshold. Waveforms were digitized with the CAEN V1730 digitizer, sampling for 416 ns per waveform. The data acquisition system and settings from this measurement campaign were duplicated at the University of Michigan using a ^{252}Cf source labeled FTC-CF-5276, where experiments were performed at varying count rates. The source-detector distance, measurement times, and lead thicknesses are given in Table 5-1. For each measurement campaign site, ^{252}Cf data were acquired in addition to various plutonium samples at low count rates for building the neutron and gamma ray pulse templates needed for template and hybrid double-pulse rejection.

Table 5-1. Details for stilbene experiments of each source.

Source Name	Measurement Campaign Site	Distance (cm)	Measurement Time (s)	Lead Thickness (cm)	CAEN Digitizer
FTC-CF-5276	Univ. Michigan	22, 60	600	0	V1730
CBNM061	JRC in Ispra	13	300	0	DT5720
CBNM084	JRC in Ispra	13	300	0	DT5720
PuGa Disks 207-211	JRC in Ispra	10	1800	0, 0.635	DT5720
PuGa Disks 73240 (5)	JRC in Ispra	10	1800	0.635	DT5720
ENEA-02	JRC in Ispra	52	1800	0.635	DT5720
PAHN Plate	INL, Idaho	48.5	720	0	V1730

Each detector was calibrated to a ^{137}Cs source such that the Compton edge was nearly 400 mV. Figure 5-1 shows the ^{137}Cs pulse height distribution for each stilbene at each measurement campaign site, normalized to the maximum channel near the Compton edge.

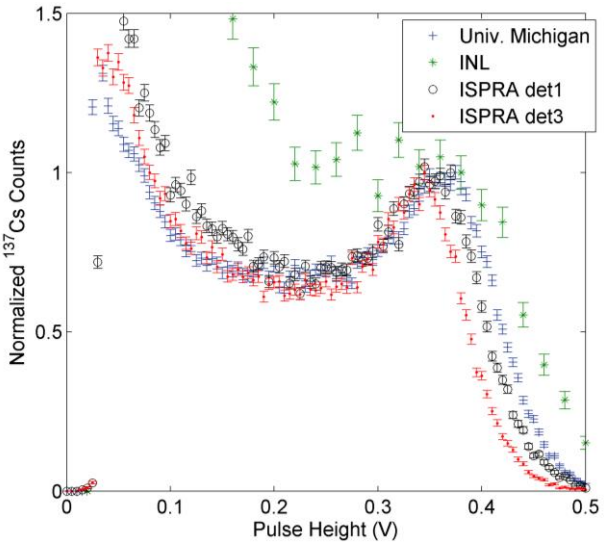

Fig. 5-1. ^{137}Cs calibration curve for stilbene when used at each measurement campaign site.

5.1.1. Plutonium Samples

The mass composition of each sample is provided in Table 5-2. Each plutonium sample was aged from its known isotopics to the same month of each experiment. It was assumed that no new material was bred in the process (such as ^{241}Am from neutron absorption of ^{240}Pu and subsequent beta decay of ^{241}Pu) since neutron emissions are minimal from these isotopes. The intensity of gamma-ray emissions is unknown for each plutonium source, although intensity of isotope emissions such as the 59-keV gamma ray from ^{241}Am can be determined from the aged isotope mass. Specification sheets for each sample are provided in Appendix B. The known mass of each plutonium isotope, along with the presence of oxygen, was used to calculate the neutron emission rate at the time of the experiment separately from spontaneous fission and from (α, n). The neutron emission rates for each source are provided in Figure 5-2 for each source.

Table 5-2. Aged composition of heavier actinides in each sample and the aged neutron emission rate.

Source Name	Source Type	Aged Wt % by Isotope (%)						Mass (g)	Neutron Emission Rate (n/s)
		^{238}Pu	^{239}Pu	^{240}Pu	^{241}Pu	^{242}Pu	^{241}Am		
FTC-CF-5276	^{252}Cf SF	N/A							2.14×10^{7}
CBNM061	Pu Oxide	0.1	61.6	25.0	1.5	4.1	5.5	6.626	4440
CBNM084	Pu Oxide	0.06	83.1	14.0	0.3	0.4	0.9	6.69	1580
PuGa 207-211	Pu Alloy	0.1	73.8	20.9	0.8	0.7	0.02	18.57	4200
PuGa 73240	Pu Alloy	0.01	92.0	5.8	0.07	0.03	0.001	18.50	1100
ENEA-02	MOX	0.02	11.0	4.6	0.1	0.3	0.5	1151.7	93800
PAHN Plate	Pu Alloy	0.0002	74.6	22.4	0.6	0.6	1.7	106.8	25600

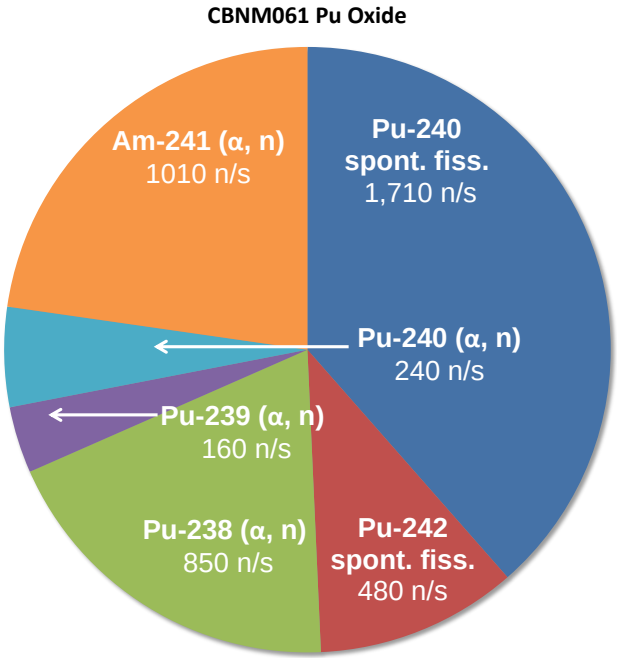
CBNM061 Pu Oxide
Am-241 (α, n)
1010 n/s
Pu-240
spont. fiss.
1,710 n/s
Pu-240 (α, n)
240 n/s
Pu-239 (α, n)
160 n/s
Pu-238 (α, n)
850 n/s
Pu-242
spont. fiss.
480 n/s

(a)

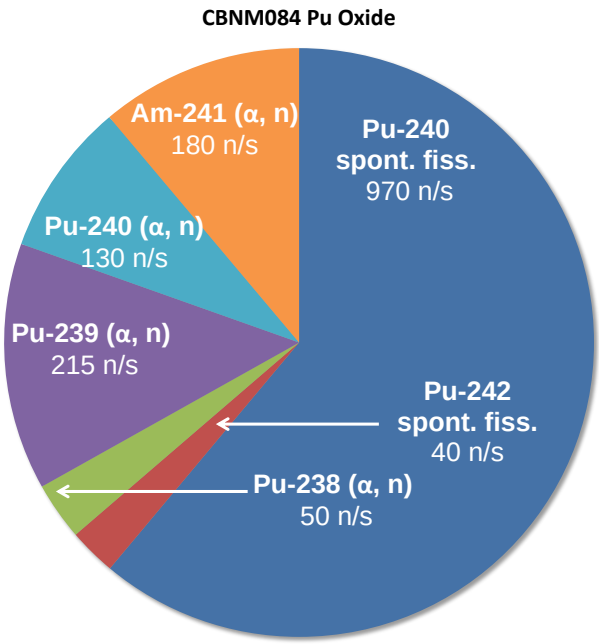
CBNM084 Pu Oxide
Am-241 (α, n)
180 n/s
Pu-240
spont. fiss.
970 n/s
Pu-240 (α, n)
130 n/s
Pu-239 (α, n)
215 n/s
Pu-242
spont. fiss.
40 n/s
Pu-238 (α, n)
50 n/s

(b)

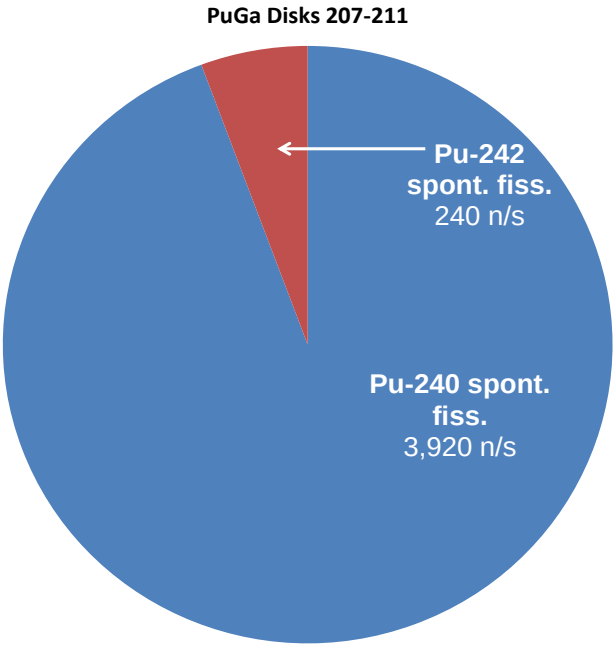
PuGa Disks 207-211
Pu-242
spont. fiss.
240 n/s
Pu-240 spont.
fiss.
3,920 n/s

(c)

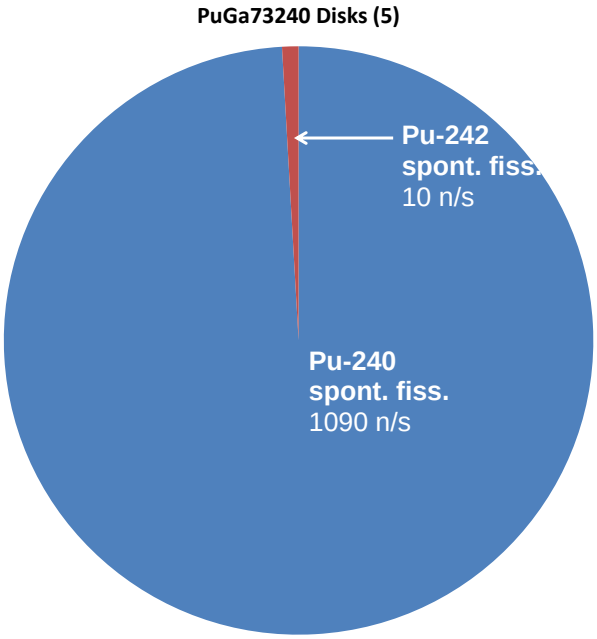
PuGa73240 Disks (5)
Pu-242
spont. fiss.
10 n/s
Pu-240
spont. fiss.
1090 n/s

(d)

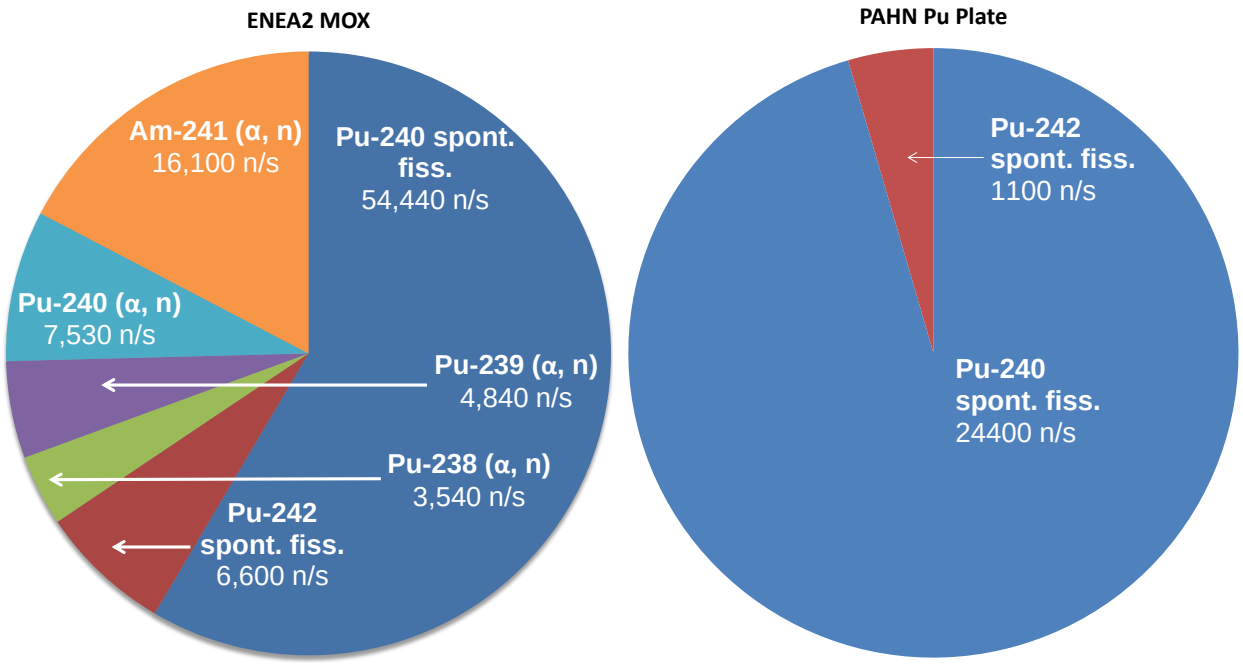

(e) (f)

Fig. 5-2. Neutron emission rate from plutonium oxide samples CBNM61 (a) and CBNM84 (b), PuGa disks 207-211 (c), five PuGa73240 disks (d), mixed oxide sample ENEA2 (e), and the PAHN plutonium metal plate (f).

5.2. MCNPX-PoliMi Benchmark

PSD was optimized in each experiment using each set of bare ^{252}Cf data. Double-pulse rejection was performed using the three separate techniques described in Chapter 5. The gamma-ray misclassification rate defined in Equation 4-2 is only useful when both the emitted gamma rays and neutrons are known from the source. For the plutonium samples, the neutron emissions are well characterized but the gamma-ray emissions are not as well-known due to the numerous decay channels of plutonium isotopes. As a result, Equation 4-2 cannot be used to determine the accuracy of each plutonium experiment. Instead, MCNPX-PoliMi was used to replicate each experiment. This model is used as a benchmark that is compared directly to measured neutron pulse height spectra from the double-pulse rejection techniques. Because the model contains no double pulses or pulses removed from the rejection techniques, the model represents the ideal case that each rejection technique seeks to replicate. This benchmark is only useful if stilbene's response to incident neutrons is modeled correctly, which was verified in Chapter 3 against ^{252}Cf. Each plutonium sample's neutron emissions, in terms of both energy and intensity, must also be modeled correctly. Specifications for each sample are provided in Appendix B by the University of Michigan, the Joint Research Centre in Ispra, Italy, and Idaho National laboratory.

MCNPX-PoliMi models were simplified to include the source, support structures, and detector cells. MPPost was used to convert neutron energy deposition into detector pulses using the measured light output in Chapter 3. Figure 5-3 shows the simulated geometry for each plutonium sample. The MCNPX-PoliMi models for each measurement are provided in Appendix A.

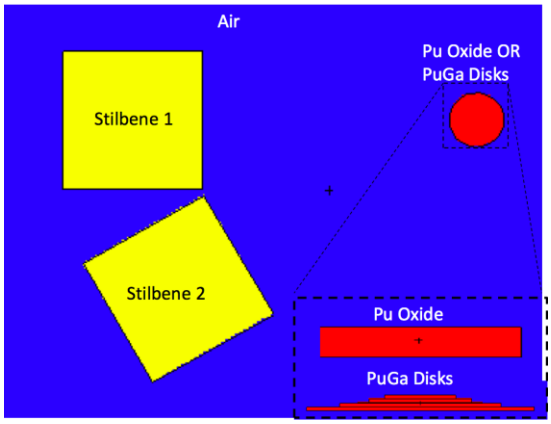

(a)

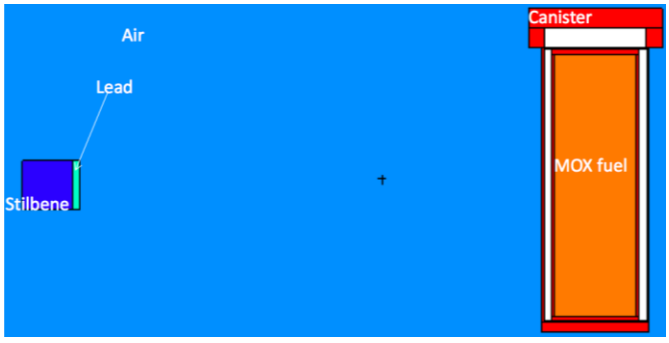

(b)

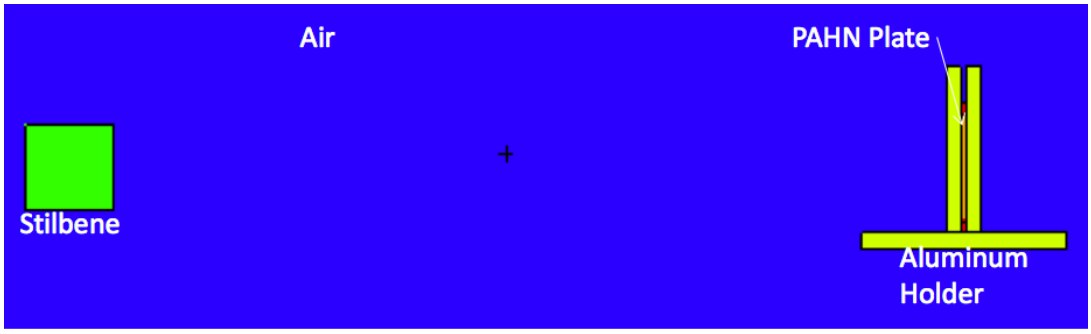

(c)

Fig. 5-3. Simulated geometry for plutonium oxide and plutonium-gallium disks (a), mixed oxide powder (b), and a PAHN plutonium plate (c).

5.3. Measured Results

The measured ^{252}Cf data was used to optimize the PSD integration ranges for each measurement campaign to maximize the PSD figure-of-merit as defined by Equation 2-3. It was found that PSD was best when integrating as much of the pulse as possible for the total integral and starting the tail integral at 28 ns after the maximum when using the V1730 digitizer and 24 ns after the maximum when using the DT5720. The discrimination curve was visually set for each detector. Pulses were processed with each method of double-pulse rejection, with a template double-pulse rejection threshold of 15 mV. The fractional double-pulse threshold threshold was set to 6% of the pulse maximum for experiments performed with the DT5720 digitizer and 12% of the pulse maximum for experiments with the V1730 digitizer.

5.3.1. ^{252}Cf at Varying Count Rates

The FTC-CF-5276 ^{252}Cf spontaneous fission source was measured at count rates of 18 and 106 kHz, reading in data at rates of 7.7 and 46.4 megabytes per second. Although the digitizer can theoretically handle data throughput rates of over 80 megabytes per second, the software executable and computer write speed limited the system to approximately 48 megabytes per second. Figure 5-4 shows the PSD tail-to-total integral surfaces for each ^{252}Cf experiment after processing 1,000,000 pulses with each double-pulse rejection method.

The primary difference between each ^{252}Cf experiment is the amount of measured double pulses, which scales with count rate according to Equation 4-3. Double pulses are dispersed evenly throughout each distribution before implementing any double-pulse rejection. Template rejection removes excess double pulses between and above the neutron and gamma-ray regions while preserving low-energy neutrons. Fractional rejection creates clear separation between the gamma-ray and neutron regions but does not remove as many pulses that lie outside the gamma-ray and neutron regions. Hybrid rejection combines the effects of each rejection method, creating clear separation between the neutron and gamma-ray regions, removing pulses lying outside of the gamma-ray and neutron regions, and overall classifying the greatest amount of pulses as double pulses.

It is expected that neutrons removed at lower total integrals are much more numerous than neutrons removed above and between the two double-pulse regions. When counting neutrons from ^{252}Cf, the correct rejection method will correspond directly to how many neutron

pulses are removed in the rejection process versus gamma-ray double pulses misclassified as neutrons.

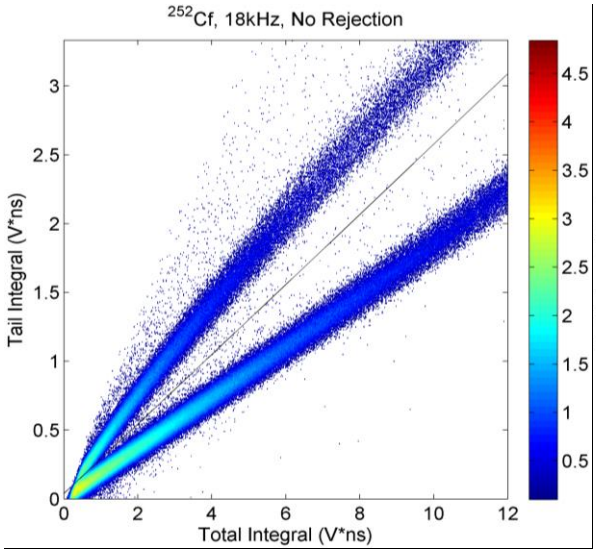

(a)

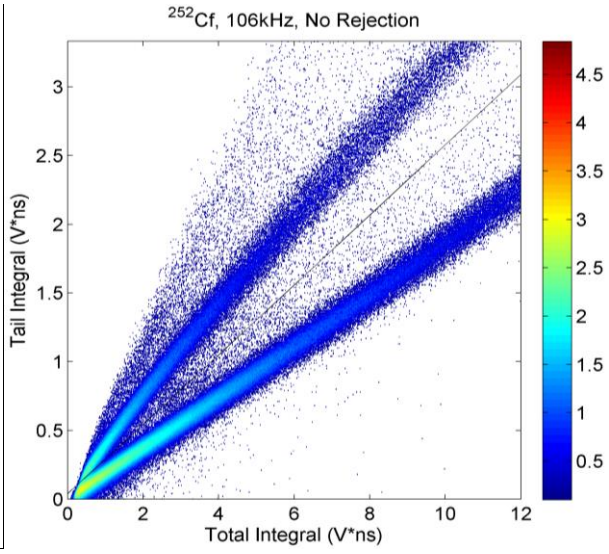

(b)

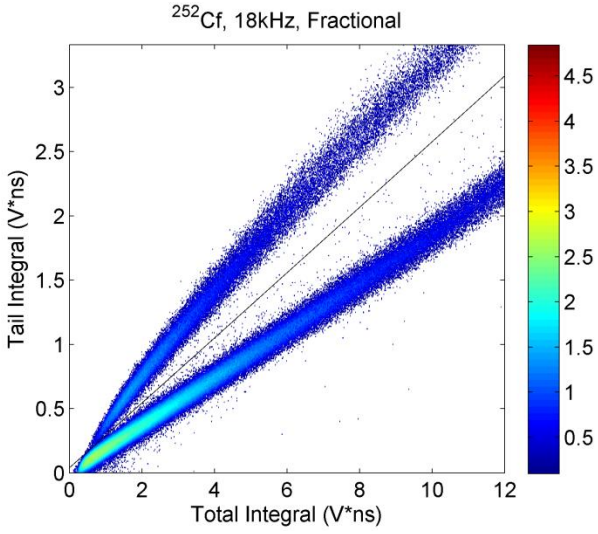

(c)

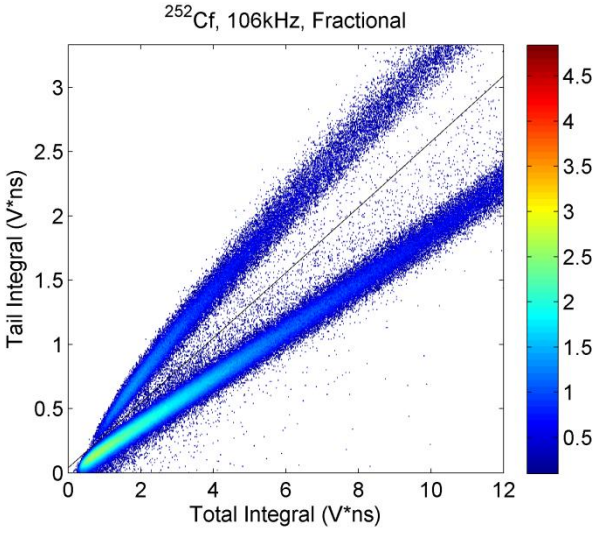

(d)

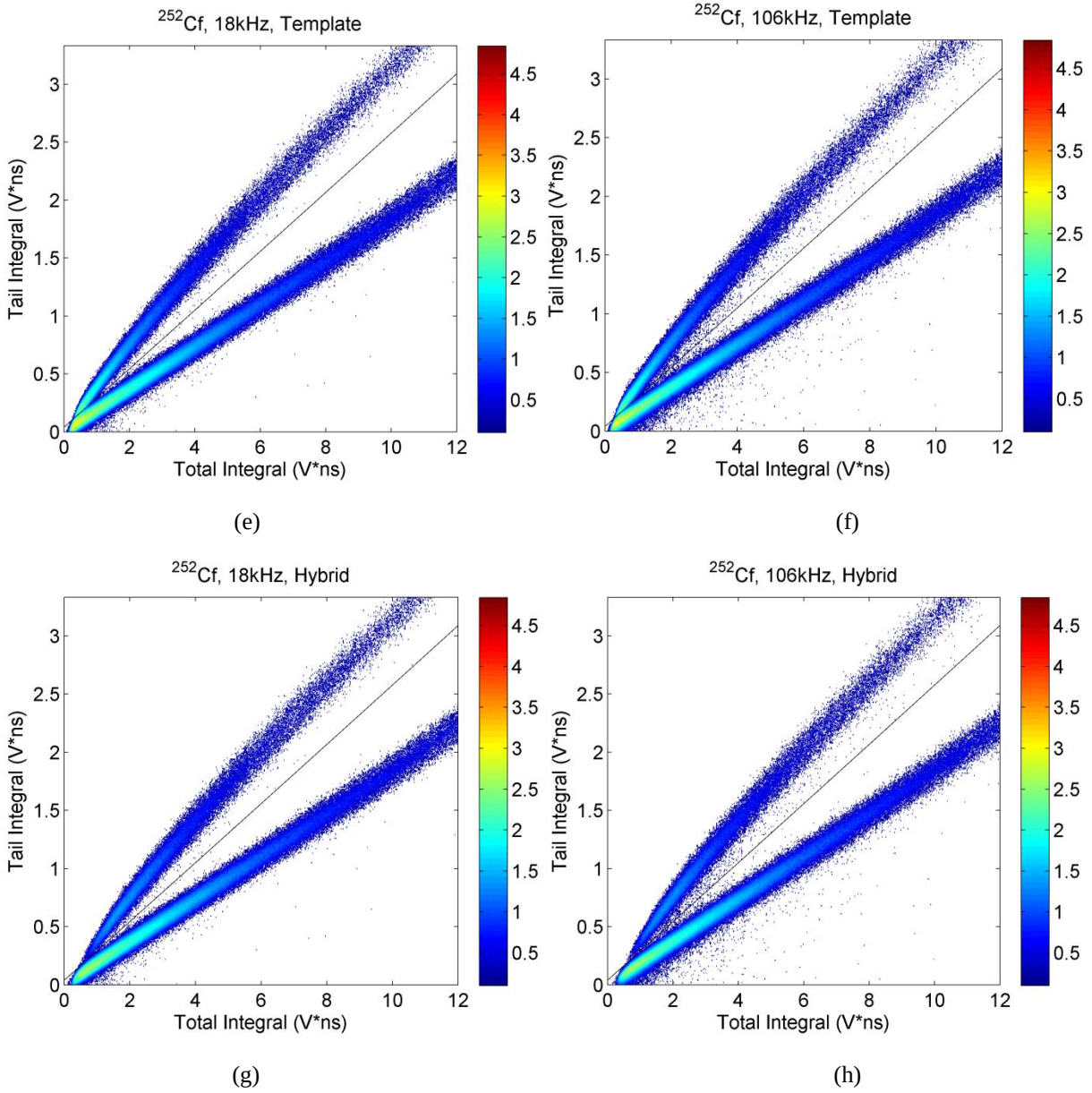

Fig. 5-4. PSD surfaces after processing 1,000,000 pulses from ^{252}Cf when measured at 18-kHz and 106-kHz count rates, respectively, after implementing no (a, b), fractional (c, d), template (e, f), and hybrid double-pulse rejection (g, h).

Figure 5-5 shows measured and simulated neutron light output distributions for each ^{252}Cf experiment after each method of double-pulse rejection. Although the double-pulse count rate is expected to be 0.042 in the 106-kHz experiment (six times higher than in the 18-kHz experiment), the effect of each double-pulse rejection method is the same for each experiment. Differences in measured light output spectra for the same type of rejection are solely due to intensity from the varied count rate. The best double-pulse rejection algorithm appears to remove very few double pulses, as many double pulses contain neutrons from a ^{252}Cf source.

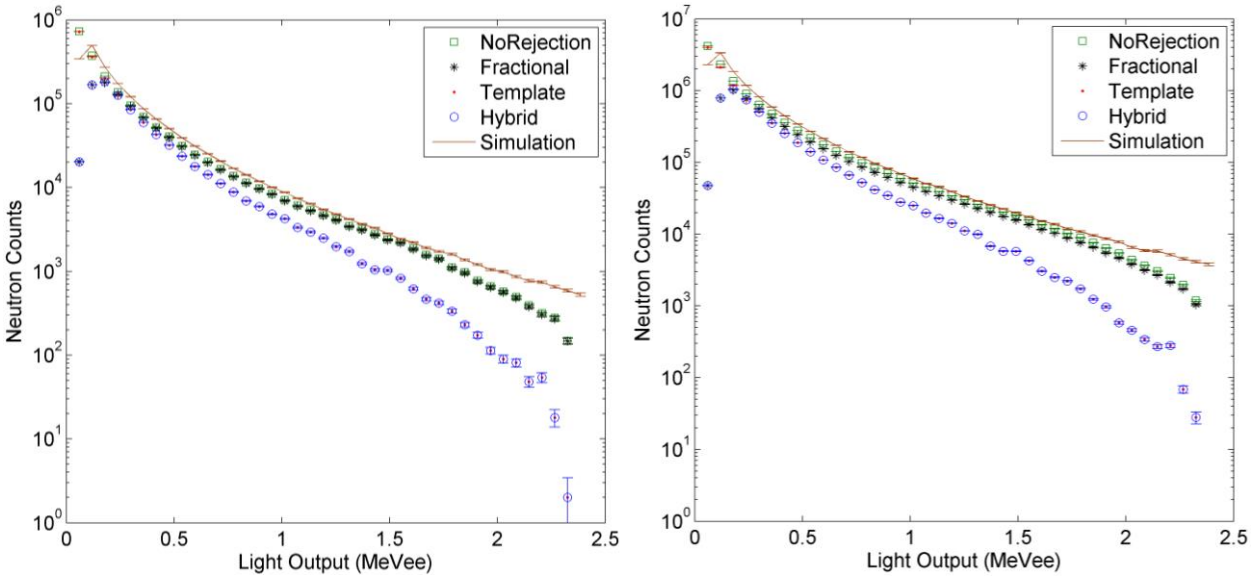

Fig. 5-5. Simulated and measured light output distributions for ^{252}Cf measured at 18-kHz (a) and 106-kHz (b) count rates.

5.3.2. Plutonium Oxide Samples

Figure 5-6 shows the PSD tail-to-total integral surfaces for each plutonium oxide experiment after processing 1,000,000 pulses with each method of double-pulse rejection. The CBNM61 source was measured with a count rate of approximately 16 kHz, while the CBNM84 source was measured with a count rate of approximately 4 kHz, yielding double-pulse count rates of approximately 0.0064 and 0.0016, respectively. Differences in count rate can be attributed entirely to the differences in ^{240}Pu content in each sample. The elevated double-pulse count rate is evident in the PSD surface plots before double-pulse rejection, as more pulses lay both between the neutron and gamma-ray regions.

The ^{241}Am content in each source releases 59-keV gamma rays with high enough intensity to produce a band of double pulses near the detection threshold. Experiments with these plutonium oxide samples did not use lead, so it was best to remove these gamma rays with double-pulse rejection. Fractional and template rejection are both effective at removing these double pulses, though template rejection leaves more pulses in the neutron region than fractional rejection. Whether these are gamma-ray double pulses or neutron pulses cannot be determined from the surface plot by itself. The PSD surfaces from hybrid rejection, which are the cleanest and contain the fewest neutron pulses, are shown in Appendix C.

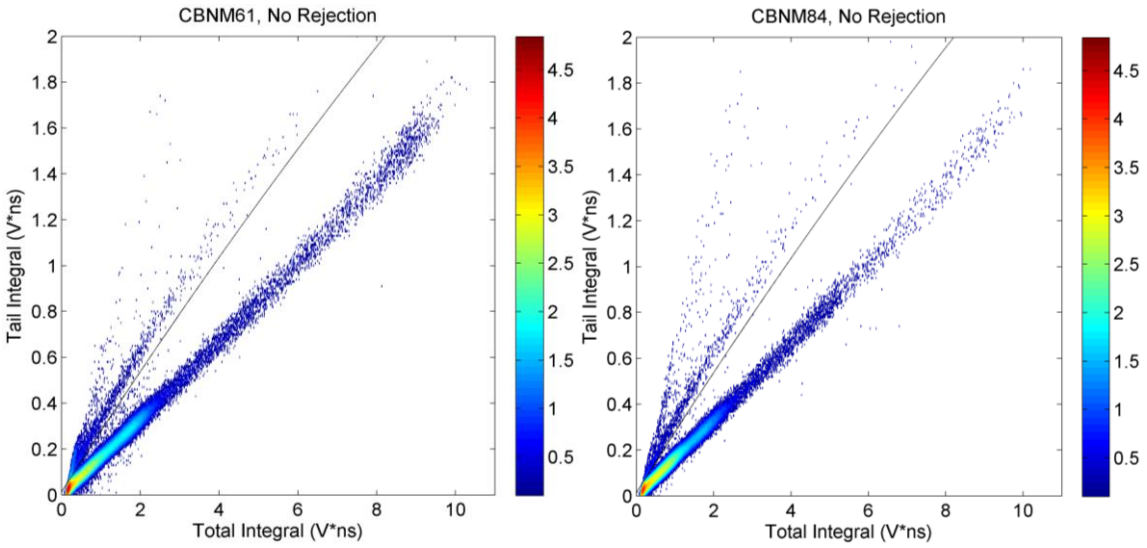
CBNM61, No Rejection
Tail Integral (V*ns)
Total Integral (V*ns)
CBNM84, No Rejection
Tail Integral (V*ns)
Total Integral (V*ns)

(a) (b)

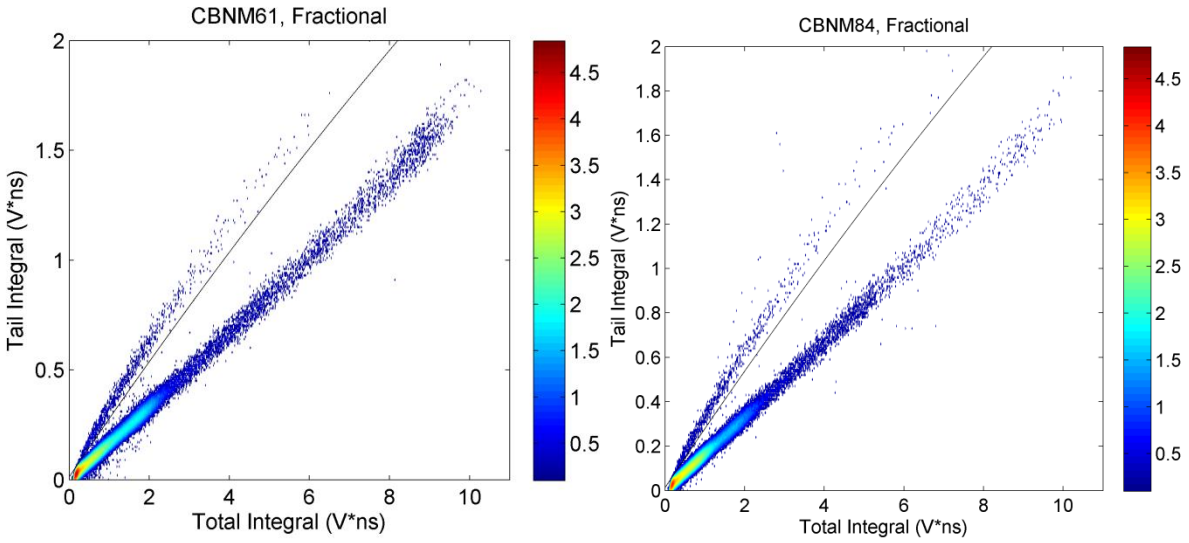
CBNM61, Fractional
Tail Integral (V*ns)
Total Integral (V*ns)
CBNM84, Fractional
Tail Integral (V*ns)
Total Integral (V*ns)

(c) (d)

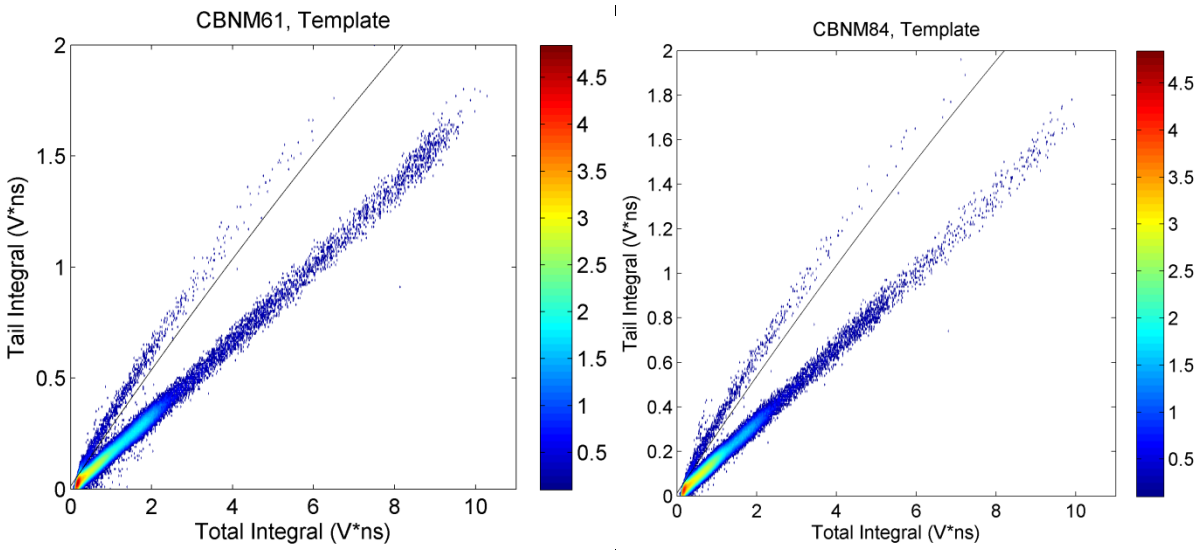

(e) (f)

Fig. 5-6. PSD surfaces after processing 1,000,000 pulses from the CBNM61 and CBNM84 plutonium oxide sources, respectively, when implementing no (a, b), fractional (c, d), and template double-pulse rejection (e, f). Hybrid double-pulse rejection results are provided in Appendix C.

Figure 5-7 shows the measured and simulated neutron light output distributions for each CBNM plutonium oxide sample. The light output spectra show the low-light pulses in the PSD surface plots are gamma rays misclassified as neutrons, as they do not appear in the MCNPX-PoliMi model for the plutonium oxide sources. The fractional and hybrid rejection methods are preferred because these rejection methods adequately remove misclassified gamma rays at low light outputs. Template rejection over-predicts the simulated plutonium oxide spectrum the most for the sample with more ^{241}Am content; should the ^{241}Am content become negligible in a different plutonium oxide sample, the amount of misclassifications would also decrease to the point where template rejection may be preferred over fractional and hybrid rejection.

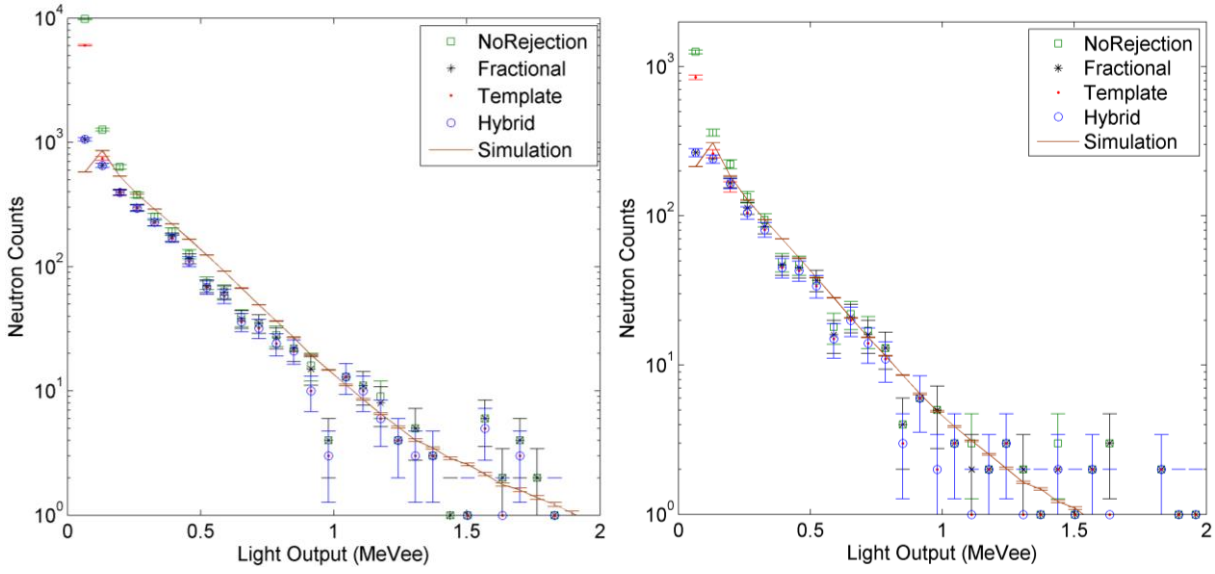

Fig. 5-7. Simulated and measured light output distributions for CBNM61 (a) and CBNM84 (b).

5.3.3. Mixed Oxide (MOX) Sample

Figure 5-8 shows the PSD tail-to-total integral surface plots for the ENEA-2 MOX experiment after processing 1,000,000 pulses with each method of double-pulse rejection. Each PSD surface looks very similar to the plutonium oxide, but the inclusion of lead makes each distribution appear cleaner. Each rejection technique removes pulses above the neutron region and near the threshold, forming clean distributions in each case. Template rejection preserves slightly more neutrons at lower total integrals than fractional or hybrid rejection.

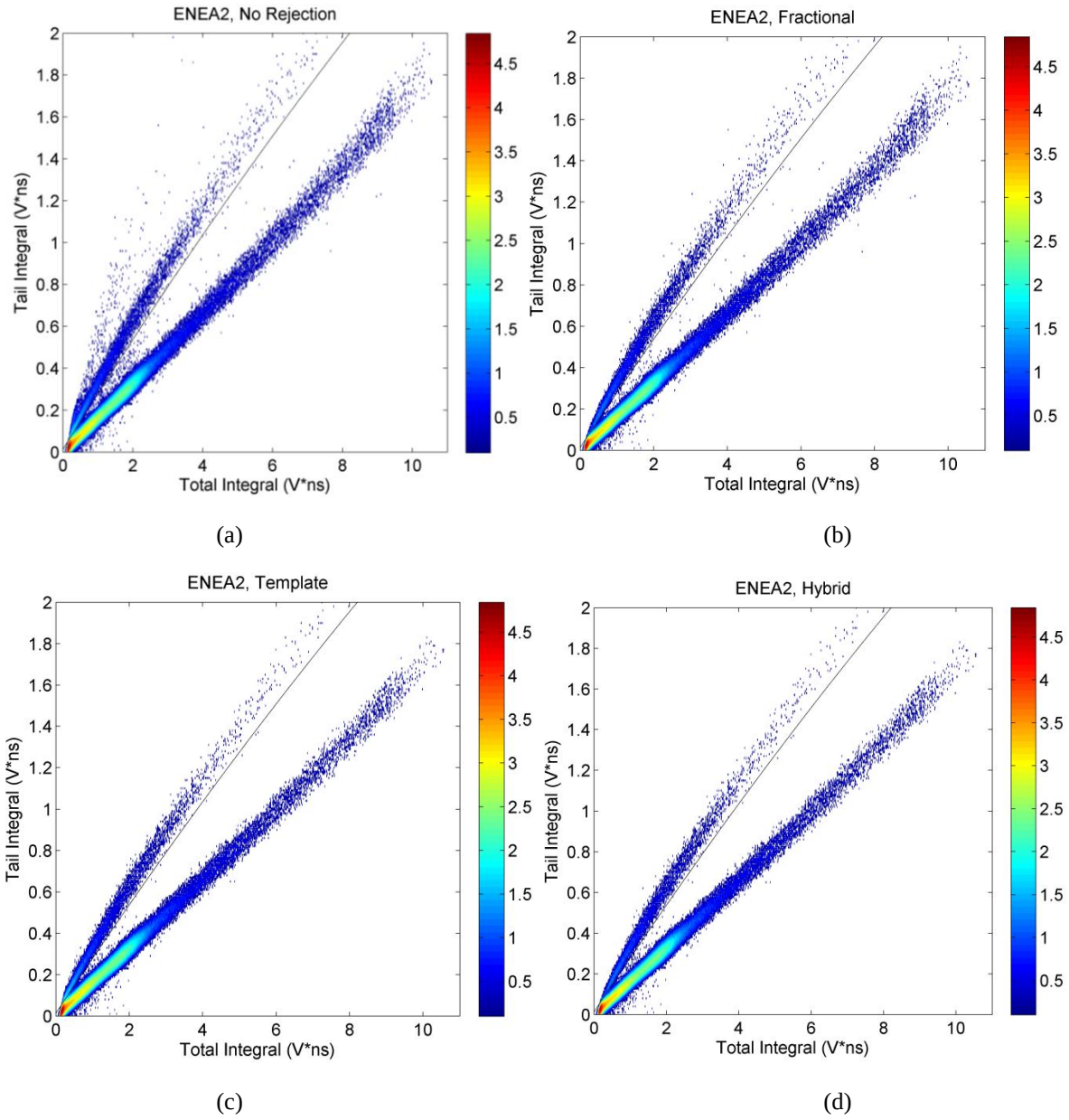

Fig. 5-8. PSD tail-to-total surface plots after processing 1,000,000 pulses from the ENEA-2 MOX canister experiment when implementing no (a), fractional (b), template (c), and hybrid double-pulse rejection (d).

Figure 5-9 shows the measured and simulated neutron light output distributions for the ENEA2 MOX sample. The lead shielding, combined with the long measurement distance, assists with measuring the correct light output spectrum, as very few gamma-ray pulses are misclassified as neutrons. The primary difference occurs near the detection threshold, where misclassified gamma rays are most likely to remain when using lead shielding.

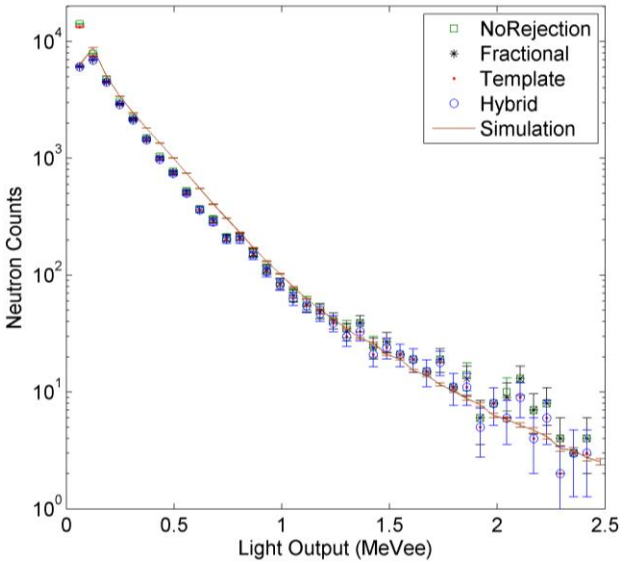

Fig. 5-9. Simulated and measured light output distributions from the ENEA-2 MOX sample.

5.3.4. Plutonium-Gallium Metal Disks

Figure 5-10 shows the PSD tail-to-total integral surface plots for each plutonium-gallium experiment after processing 1,000,000 pulses with each method of double-pulse rejection. The effect of adding 0.6 centimeters of lead is clearly illustrated in Figures 5-8a and 5-8b, where separation between the neutron and gamma-ray regions is more clearly defined and the intensity of pulses in the neutron region decreases near the threshold. The measured count rate for the PuGa207-211 disks was 32 kHz without lead and 6 kHz with lead, so most pulses at lower total integrals are gamma-ray double pulses. Reducing the ^{240}Pu content has the effect of lowering the overall count rate. PSD surfaces for the PuGa73240 experiment are shown in Appendix C.

Introducing fractional rejection removes enough double pulses to yield clear separation between the neutron and gamma-ray regions, simplifying the PSD algorithm. More interesting is the effect of template rejection on each experiment; the bare PuGa data contains numerous pulses between the neutron and gamma-ray regions, while the lead PuGa data appears much cleaner. Reducing the volume of ^{241}Am gamma rays may allow for the use of the double-pulse rejection technique that preserves greater neutron efficiency than when measuring without lead, although detector assembly weight is sacrificed in the process. More experiments are needed to examine the trade-off between gains in neutron efficiency by using template rejection over fractional rejection, loss in neutron efficiency due to scatters in the lead, and assembly weight. PSD surfaces when using hybrid rejection are also shown in Appendix C.

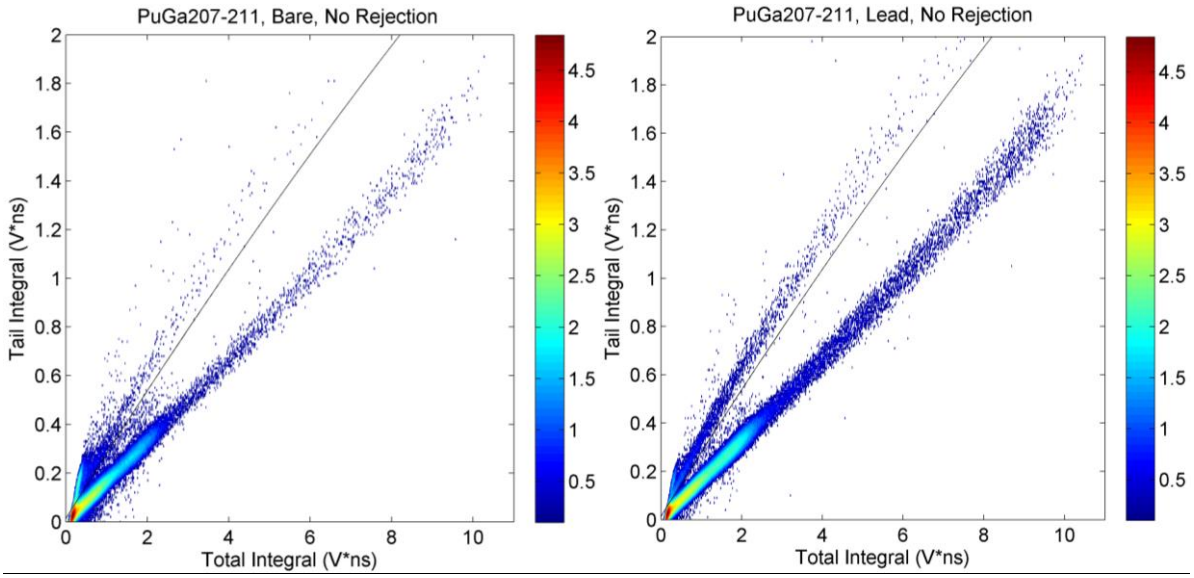
PuGa207-211, Bare, No Rejection
Tail Integral (V*ns)
Total Integral (V*ns)
PuGa207-211, Lead, No Rejection
Tail Integral (V*ns)
Total Integral (V*ns)

(a) (b)

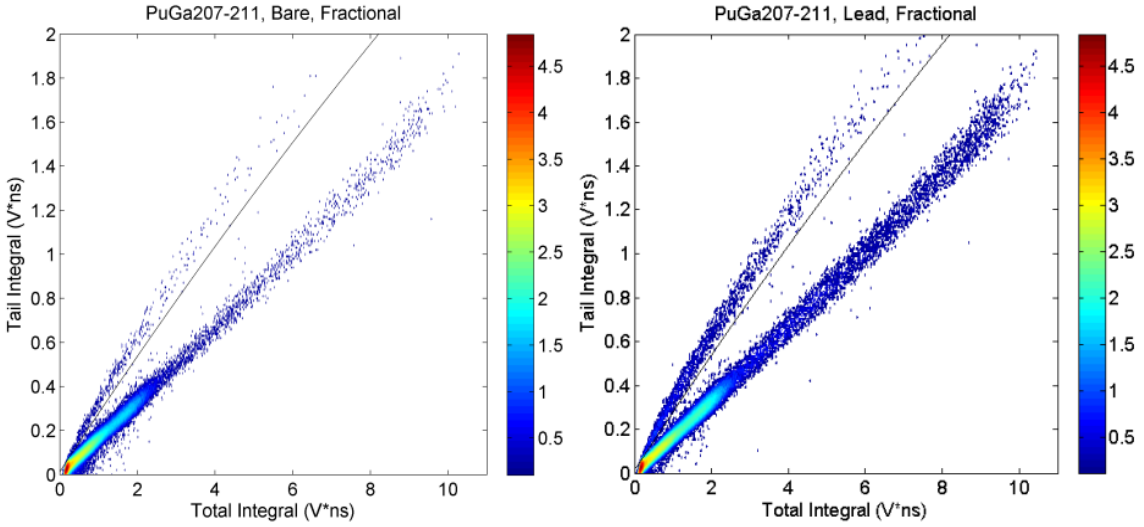
PuGa207-211, Bare, Fractional
Tail Integral (V*ns)
Total Integral (V*ns)
PuGa207-211, Lead, Fractional
Tail Integral (V*ns)
Total Integral (V*ns)

(c) (d)

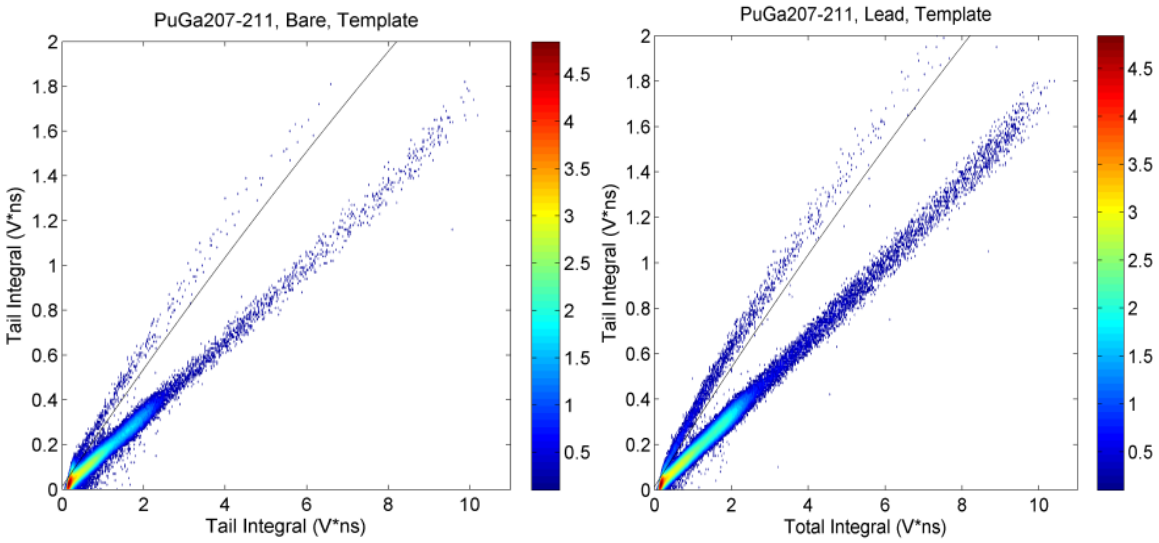

(e) (f)

Fig. 5-10. PSD surfaces after processing 1,000,000 pulses from the plutonium-gallium disks 207-211 when measured without and with lead, respectively, when implementing no (a-b), fractional (c-d), and template double-pulse rejection (e-f). PSD surfaces for disks 207-211 after hybrid double-pulse rejection for disks 207-211, along with PuGa73240 after each method of rejection, are given in Appendix C.

Figure 5-11 show the measured and simulated neutron light output distributions for each PuGa experiment. The lead makes a large difference in the gamma-ray intensity (and thus the gamma-ray double pulse intensity), so experimental data conform better to the MCNPX-PoliMi model. For the PuGa sources, it appears that fractional and hybrid rejection are the preferred methods of rejection, even when including lead. If the rejection algorithms were optimized for an environment containing 59-keV gamma rays, then template rejection may be preferable for the shielded PuGa disks.

From Figure 5-9c, it appears higher-energy neutrons are not being modeled with the correct intensity in the PuGa73240 experiment. The effect of this correction is small since the majority of the spectrum still lies below 500 keVee, which is modeled accurately.

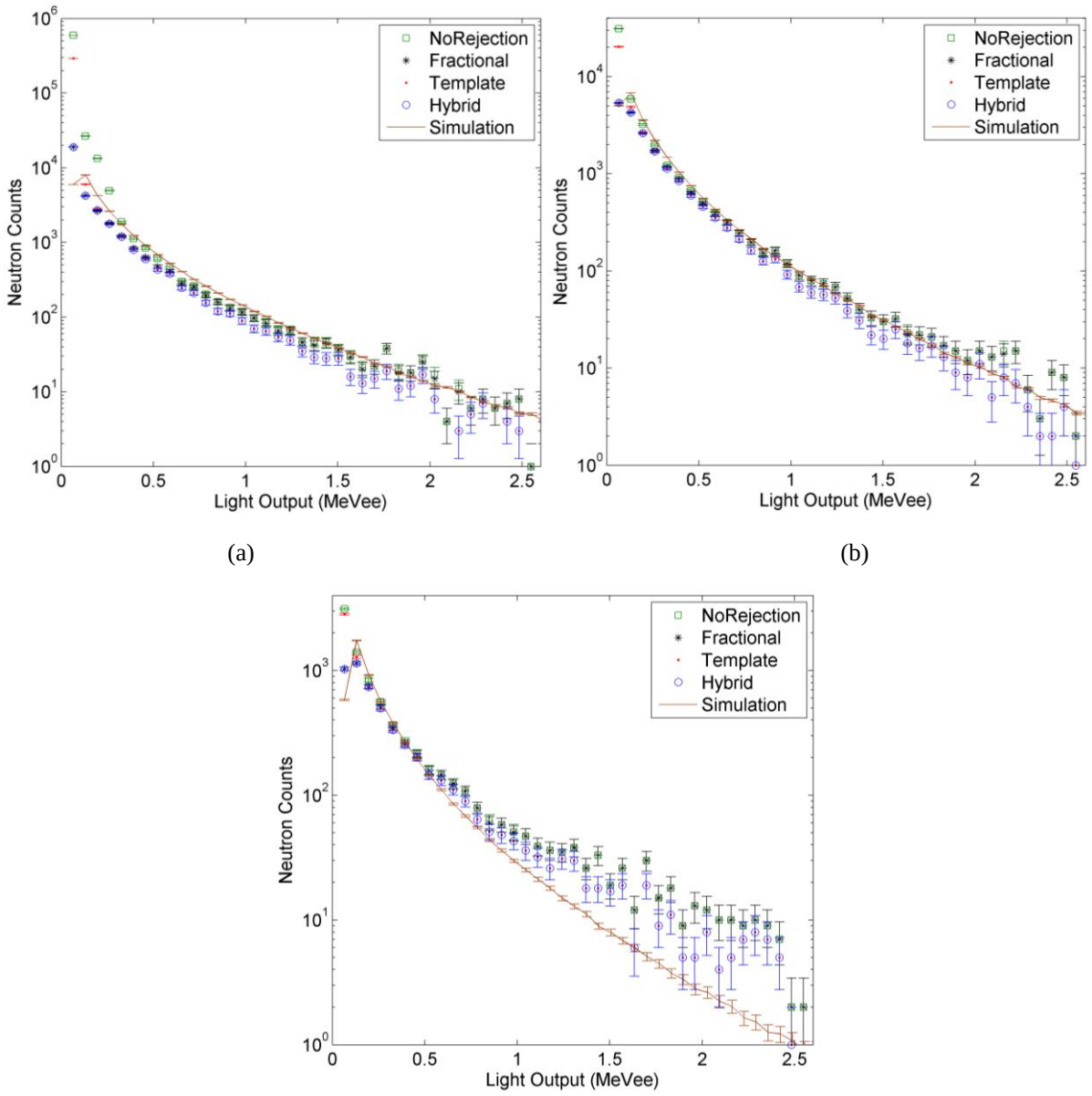

Fig. 5-11. Simulated and measured light output distributions from the plutonium-gallium disks when measured without lead (a), with lead (b), and with lead at a lower enrichment (c).

5.3.5. PAHN Plutonium Metal Plate

Figure 5-12 shows the PSD tail-to-total integral surface plots the for PAHN plutonium plate experiment after processing 1,000,000 pulses with each method of double-pulse rejection. The PAHN plate experiment yields a more extreme version of the bare PuGa experiment, where the incredibly high emission rate of 59-keV gamma rays produces an intense field of double pulses near the detection threshold. Without lead to shield these gamma rays, heavy double-pulse rejection is necessary for accurate determination of neutron emissions. Template rejection

will reduce the intensity of the double-pulse region, but not enough for charge-integration PSD to classify these pulses as gamma rays. Fractional and hybrid double-pulse rejection are sufficient to consistently classify these double pulses as rays, but reduce the neutron efficiency at low energies.

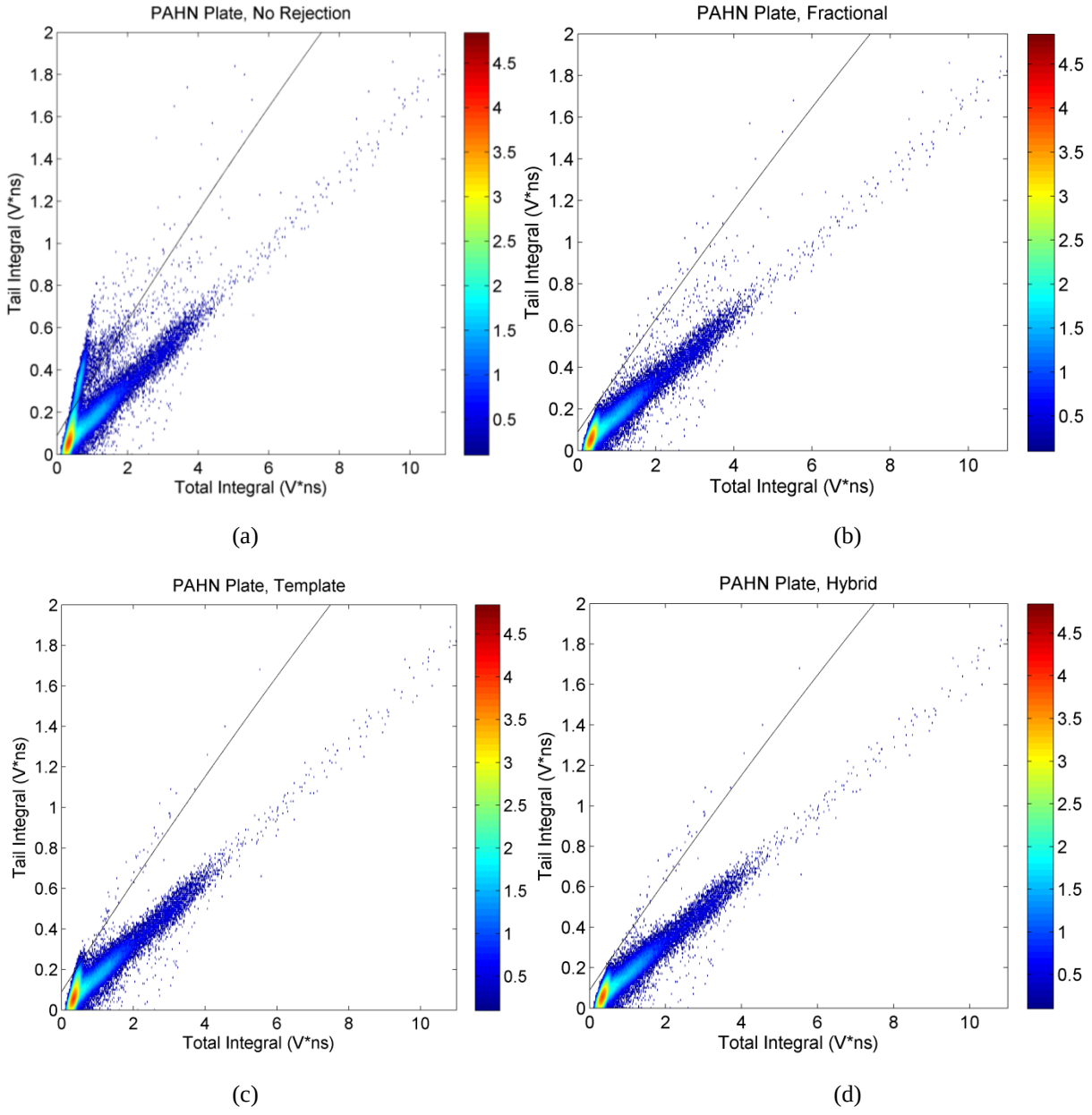

Fig. 5-12. PSD tail-to-total surface plots after processing 1,000,000 pulses from the PAHN plutonium plate experiment when implementing no (a), fractional (b), template (c), and hybrid double-pulse rejection (d).

Figure 5-13 shows measured and simulated neutron light output distributions from the PAHN plate source. The neutron signal is swamped by the 59-keV gamma rays emitting from

the source, which need accurate rejection for effective identification of the source. Fractional and hybrid rejection can sufficiently remove the 59-keV gamma rays, but also reject approximately 30-40% of the true neutron signal. Lead would reduce the need to remove as many low-energy neutrons while adding detector weight, while raising the detection threshold to 150 keVee would measure closer to the true neutron spectrum while sacrificing neutron efficiency.

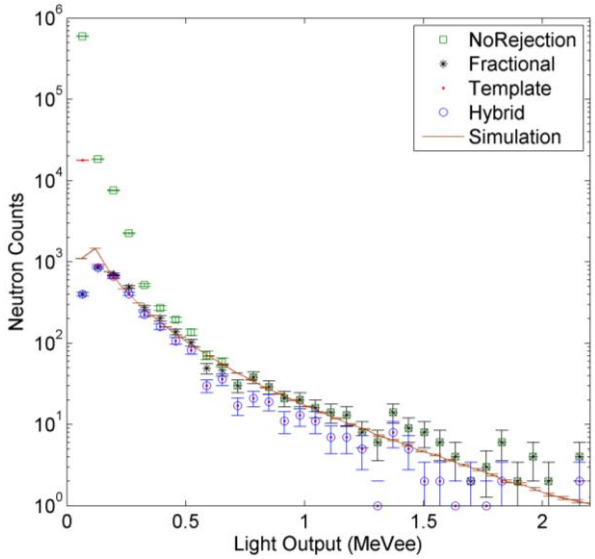

Fig. 5-13. Simulated and measured light output distributions from the PAHN plutonium plate sample.

5.4. Hybrid Double-Pulse Rejection Algorithm Optimization

Experiments were sorted by both measured count rate and measured gamma ray-to-neutron ratio after each rejection method. Figure 5-14 shows the ratio of measured-to-simulated neutron counts as a function of both measured count rate before double-pulse rejection and gamma ray-to-neutron ratio after each method of double-pulse rejection. The goal was to determine which rejection method should be used to measure the neutron spectrum that best matched the simulated benchmark. From the measured count rate, there does not appear to be a consistent metric separating the rejection methods from one another, even though double-pulse count rate scales with measured count rate. Plutonium samples with count rates ranging from 700 Hz to 75 kHz yield measured neutron count rates that most closely match the simulated benchmark after implementing fractional or hybrid rejection, while the ^{252}Cf source, with count rates ranging from 5-100 kHz, should be processed with template or no double-pulse rejection.

On the other hand, the measured gamma ray-to-neutron ratio also changes with different rejection algorithms. In cases such as the PAHN plate, rejected pulses are composed mostly of

double-pulsed gamma rays, so fractional or hybrid rejection is desired to remove these double pulses and measure closer to the ideal ratio of 1. In the case of ^{252}Cf, too many neutrons are being removed when removing double pulses, so using template or no rejection is preferred. Figure 5-14b shows the MOX sample and plutonium sources have gamma ray-to-neutron ratio of 100 or greater, and are best processed with either fractional or hybrid rejection. The ^{252}Cf have gamma ray-to-neutron ratio less than 10 and are best processed with template or no rejection. Additional experiments are needed to determine which rejection method is best for gamma ray-to-neutron ratios between 10 and 100.

Figure 5-14 also shows the fractional and hybrid rejection methods give the greatest variation in measured gamma ray-to-neutron ratio. When recording neutron measurements of an unknown sample, it is best to apply one of these rejection methods first to determine if the sample's gamma ray-to-neutron ratio lies in one of these regions.

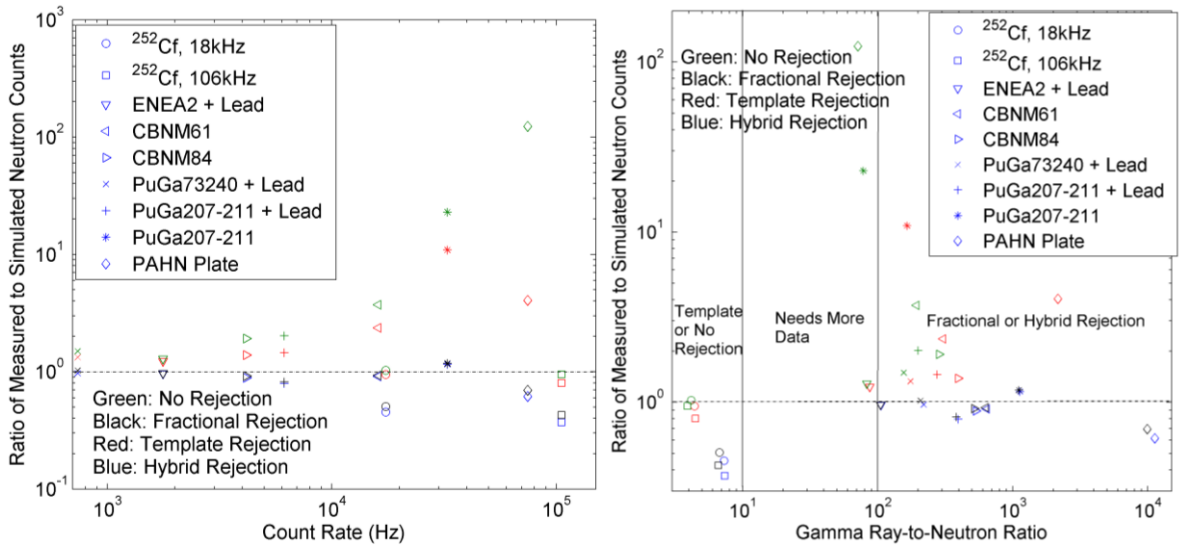

(a) (b)

Fig. 5-14. Ratio of measured-to-simulated neutron counts for each experiment processed with each method of double-pulse rejection, represented as functions of measured count rate (a) and gamma ray-to-neutron ratio (b). Fractional or hybrid rejection are the preferred rejection methods for gamma ray-neutron ratios greater than 100, and template or no rejection for ratios below 10. The best rejection method cannot be directly determined with measured count rate.

5.5. Remarks

The measured gamma ray-to-neutron ratio can be used as a metric that determines which rejection method is best for measuring the correct neutron emissions from plutonium and ^{252}Cf samples. Each dataset was first filtered by fractional and/or hybrid rejection to compute the

gamma ray-to-neutron ratio. Experiments whose gamma ray-to-neutron ratio exceeded 100 should be processed with fractional and hybrid rejection to measure the neutron count rate that most closely matches the true neutron count rate, while experiments with ratio below 10 should be processed with template rejection, or with no double-pulse rejection. Additional experiments are needed for greater fidelity of samples with measured gamma ray-to-neutron ratios from 10 to 100.

The hybridized double-pulse rejection algorithm was most noticeable in the PAHN plutonium plate case, where the algorithm was forced to remove numerous neutron pulses in order to perform accurate PSD. The inclusion of lead helps solve this problem by lowering the gamma ray-to-neutron ratio, which may reduce the need for such intensive rejection when performing PSD in the elevated gamma-ray environment. Additional experiments are needed to determine the sensitivity of the gamma ray-to-neutron ratio on lead thickness beyond the 0.635-cm piece used to shield the 59-keV ^{241}Am emission.

Most experiments with gamma ray-to-neutron ratio greater than 100 yielded ratios closer to 1 when processed with fractional double-pulse rejection instead of hybrid rejection. Chapter 4 concluded that hybrid rejection maintains value over fractional rejection in applications where accurate particle classification is more important than preserving neutron emissions. Likewise, template rejection yields slightly worse answers when measuring ^{252}Cf than implementing no rejection, but its level of gamma-ray misclassification is over 2-3 orders of magnitude lower in these applications than using no double-pulse rejection. However, the measured count rate does not affect which rejection method is best for the application; only if the elevated count rate is caused by gamma-ray emissions.

Chapter 6. Cross-Correlation Experiments of ^{252}Cf and Plutonium Samples Using Scintillation Detectors

For nonproliferation applications, it is desired to discriminate SNM samples of plutonium from non-SNM neutron sources such as ^{252}Cf and AmBe. Since ^{252}Cf emits neutrons with a similar energy spectrum as ^{240}Pu spontaneous fission, it is insufficient to simply measure individual neutrons emitted from these sources. To prevent a neutron detection system from alarming on ^{252}Cf or (α, n) sources such as AmBe, correlated neutron measurements are needed to identify plutonium samples separate from ^{252}Cf and AmBe. The organic scintillator equivalent to a ^{3}He-based coincidence counter uses cross-correlation for passive measurements of neutron sources.

Cross-correlation experiments exploit the PSD capabilities and fast timing properties of organic scintillators to characterize sources with correlated neutron and gamma-ray emissions. Typical experiments use two or more scintillator detectors at known distances from a source, measuring separate particles in two detectors within a fixed time window. PSD is used to identify each particle as either a neutron or gamma ray, and the time difference between the two detectors is recorded. These time differences are separated by neutron-neutron (NN), neutron-gamma ray (NP), gamma ray-neutron (PN), or gamma ray-gamma-ray (PP) correlations, which are then histogrammed into separate cross-correlation distributions. Cross-correlation distributions for ^{252}Cf are shown in Figure 6-1.

Both NN and PP correlations shown in Figure 6-1 have peaks symmetric around 0 ns, where NN time differences vary much more than PP correlations. Because gamma rays have a constant speed while neutron speed varies with energy, it can be concluded that these neutrons and gamma rays are emitted from the source simultaneously from fission. Sources without spontaneous fission would not contain NN correlations distributed in this manner, allowing for easy discrimination of fission sources from single neutron emitters such as (α, n) sources [40]. Varying multiplicity of spontaneous fission sources means the intensity of neutron-neutron

correlations may allow for separate identification of ^{252}Cf from plutonium-based samples. Energy information can be extracted from the NP and PN distributions, as the gamma ray provides a start signal for the time at which a fission occurs, as demonstrated in Chapter 3. Varying the angle between detector pairs yields information on the anisotropy of the source [41]. Even uncorrelated coincidences, or "accidentals", can yield relevant information on decay product buildup; these have been previously used to identify varying levels of burnup in plutonium-based fuel samples [28].

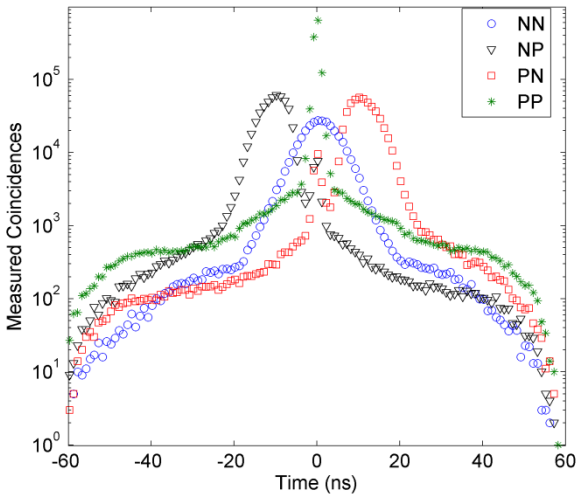

Fig. 6-1. Cross-correlation distribution for ^{252}Cf.

The fast timing of organic scintillators allow for them to potentially outperform ^{3}He-based coincidence counting systems. Since ^{3}He operates on the order of microseconds, counting systems must open detection gates, counting for several microseconds at a time. Through the counting process, numerous accidentals are also counted and later removed before determining the real number correlated neutron events through knowledge of the Rossi-alpha distribution of the source [11]. Cross-correlation experiments, on the other hand, correlate particles directly within window lengths much shorter than a microsecond, reducing the contribution from accidentals. The longer timescale of ^{3}He systems, when combined with the moderating process, prevent ^{3}He from assessing the anisotropy of a correlated sample.

Cross-correlation experiments work best when pulses in each detector are created by separate particles. While adding more detectors improves counting statistics and gives added information about the anisotropy of the source, it also increases the likelihood of a single particle scattering from one detector into another detector. This is called "crosstalk", which overestimates

the correlated source strength if crosstalk is too frequent. Crosstalk appears as secondary peaks in the NN and PP distributions offset from the centroid, so it is possible but difficult to correct for crosstalk. Crosstalk can be mitigated by increasing the detector-detector distance or adding shielding between detectors.

The EJ-299-33 plastic detector described in Chapter 3 was utilized in cross-correlation experiments of separate ^{252}Cf and mixed uranium-plutonium oxide (MOX) samples. The stilbene scintillator was utilized in cross-correlation experiments of ^{252}Cf and plutonium plate samples. These detectors are directly benchmarked to EJ-309 liquid scintillators [27].

6.1. Experimental Setup

The ^{252}Cf experiment was performed at the Department of Nuclear Engineering and Radiological Sciences at the University of Michigan in Ann Arbor, Michigan. The ^{252}Cf experimental setup is shown in Figure 6-2. Two EJ-309 detectors and two EJ-299-33 detectors were placed in 180-degree pairs at a distance of 20 centimeters from a ^{252}Cf spontaneous fission source emitting 175,000 neutrons per second. Two stilbene scintillators were utilized in a separate experiment with the same source at the same distance and 180-degree geometry. All six detectors were gain-matched such that the ^{137}Cs Compton edge aligned with approximately 400-mV pulse height. Correlated gamma ray and neutron emissions from the ^{252}Cf source were measured for 18 hours, recording digitizer waveforms using the CAEN V1720 digitizer.

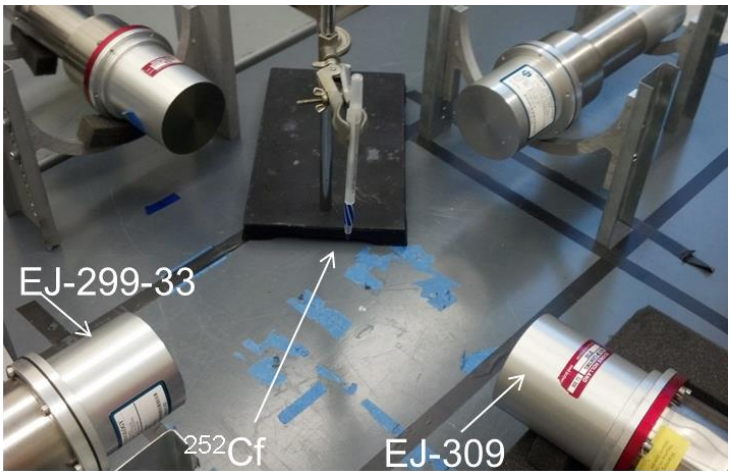

Fig. 6-2. The setup of the ^{252}Cf cross-correlation experiment.

The MOX experiment was performed at the Joint Research Centre in Ispra, Italy with the setup shown in Figure 6-3a. Twelve EJ-309 detectors and two EJ-299-33 detectors were placed

in similar 180-degree pairs at a 16.8-cm source-detector distance. Detectors were arranged octagonally around a MOX sample, stacking the EJ-309 liquids for improved efficiency. All fourteen detectors were gain-matched to a ^{137}Cs Compton edge of 300 mV. Due to the high gamma-ray emission rate from the source, a 1-centimeter thick lead sleeve was placed around the MOX sample. The MOX has a mass of 1.01 kg and consists of 66.8 wt% ^{238}U, 0.4 wt% ^{235}U, 11.1 wt% ^{239}Pu, 4.6 wt% ^{240}Pu, 0.2 wt% ^{241}Pu, 0.3 wt% ^{242}Pu, 0.02 wt% ^{238}Pu, 0.5 wt% ^{241}Am, and 16.4 wt% O_2. The neutron source emissions from the MOX sample are given in Figure 6-3b; the source emitted approximately 80,000 neutrons per second, of which 53,000 neutrons per second came from spontaneous fission and the remainder from (α, n) events in the oxide. Correlated photon and neutron emissions were measured for 68 minutes.

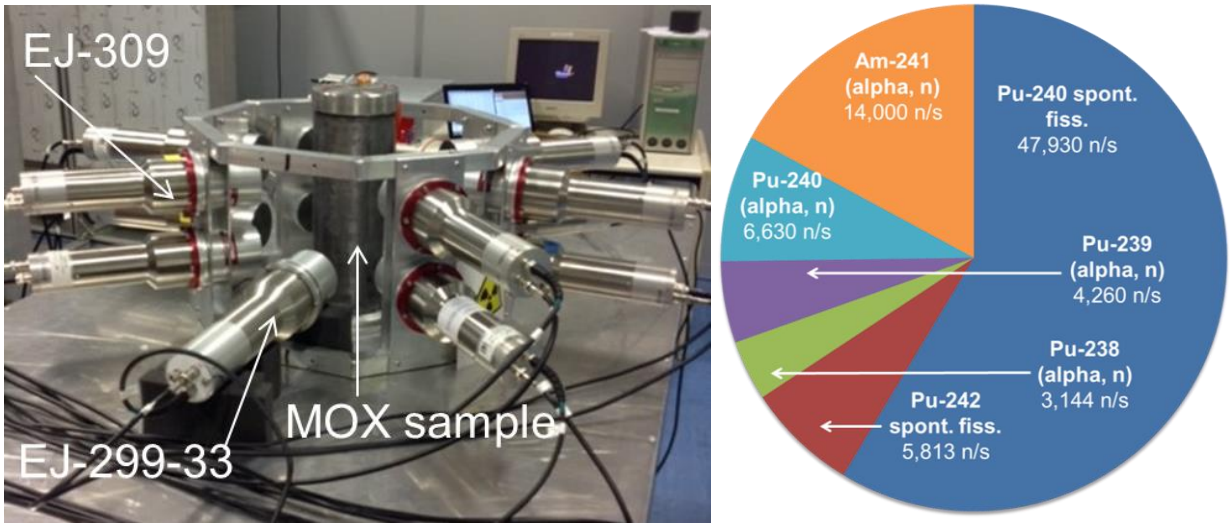

(a) (b)

Fig. 6-3. The setup of the mixed oxide cross-correlation experiment (a) and the mixed oxide neutron emissions (b) [27].

Plutonium metal plates were measured with EJ-309 and stilbene at Idaho National Laboratory in August 2015. The experimental setup is shown in Figure 6-4a. Eight EJ-309 liquids and eight stilbene scintillators were positioned 17 centimeters around a single plutonium metal plate, using a similar pattern as that used for the MOX experiment in ISPRA. Stilbene and EJ-309 liquid detectors were arranged in a checkerboard pattern. Detectors were gain-matched to a ^{137}Cs Compton edge of 400 mV. The PANN plutonium plate has a mass of 105 g and consists of 94.2 wt% ^{239}Pu, 4.5 wt% ^{240}Pu, 0.04 wt% ^{241}Pu, 0.005 wt% ^{242}Pu, 0.2 wt% ^{241}Am, and 1.1 wt% Al. The neutron source emissions from the plutonium plate sample are given in Figure 6-4b;

the source emitted approximately 4,800 neutrons per second from spontaneous fission. Separate 1.3-centimeter lead pieces were placed in front of each detector to limit detections of 59-keV ^{241}Am gamma rays [42]. Waveforms were recorded for 70 minutes using the CAEN V1730 digitizer, with 500-MHz sampling rate, 14-bit vertical resolution, and 2-Volt dynamic range.

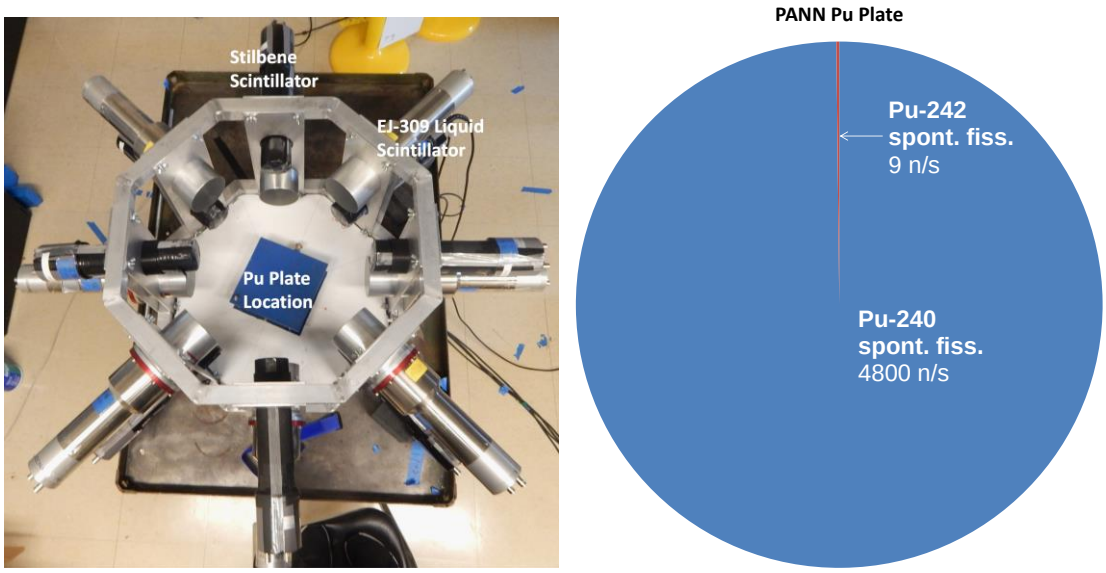

(a) (b)

Fig. 6-4. The setup of the plutonium plate cross-correlation experiment (a) and its corresponding neutron emissions (b).

6.2. PSD Results

Charge integration was performed offline to classify digitized pulses as gamma rays and neutrons. Because the detectors used in the MOX experiment were operated at a different gain than in the ^{252}Cf and plutonium plate experiments, PSD was optimized separately for each detector in each experiment. The double-pulse rejection method was determined by measuring the gamma ray-to-neutron ratio from each measurement after using fractional rejection. Table 6-1 shows that each measurement had a gamma ray-to-neutron ratio well below 100 in part because of the presence of lead in the MOX and plutonium plate measurements. When processing these measurements, no double-pulse rejection was applied when determining the final results.

Table 6-1. Measured gamma ray-to-neutron ratio for each cross-correlation experiment.

Detector	Gamma Ray-to-Neutron Ratio		
	^{252}Cf	MOX	Pu Plate
Stilbene	9.0	--	56.8
EJ-309	4.6	29.2	38.9
EJ-299-33	7.4	13.2	--

Figure 6-5 shows the tail-vs-total integral surfaces for each scintillator type in each experiment. Stilbene and EJ-309 liquid were capable of clear separation between the neutron and gamma-ray regions when processed at 36-keVee and 70-keVee light output thresholds, respectively. The EJ-299-33 plastic needed to raise its detection threshold to 150 keVee for minimal separation. Stilbene and EJ-309 liquid gave similar separation between the gamma ray and neutron regions at lower total integrals despite stilbene operating at a lower detection threshold. The EJ-299-33 plastic gave the worst separation despite using a higher threshold in the plastic.

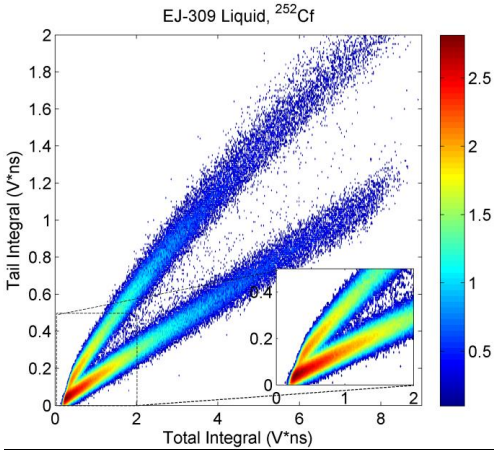

(a)

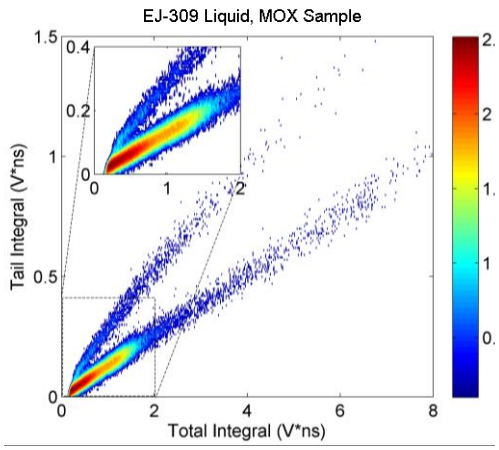

(b)

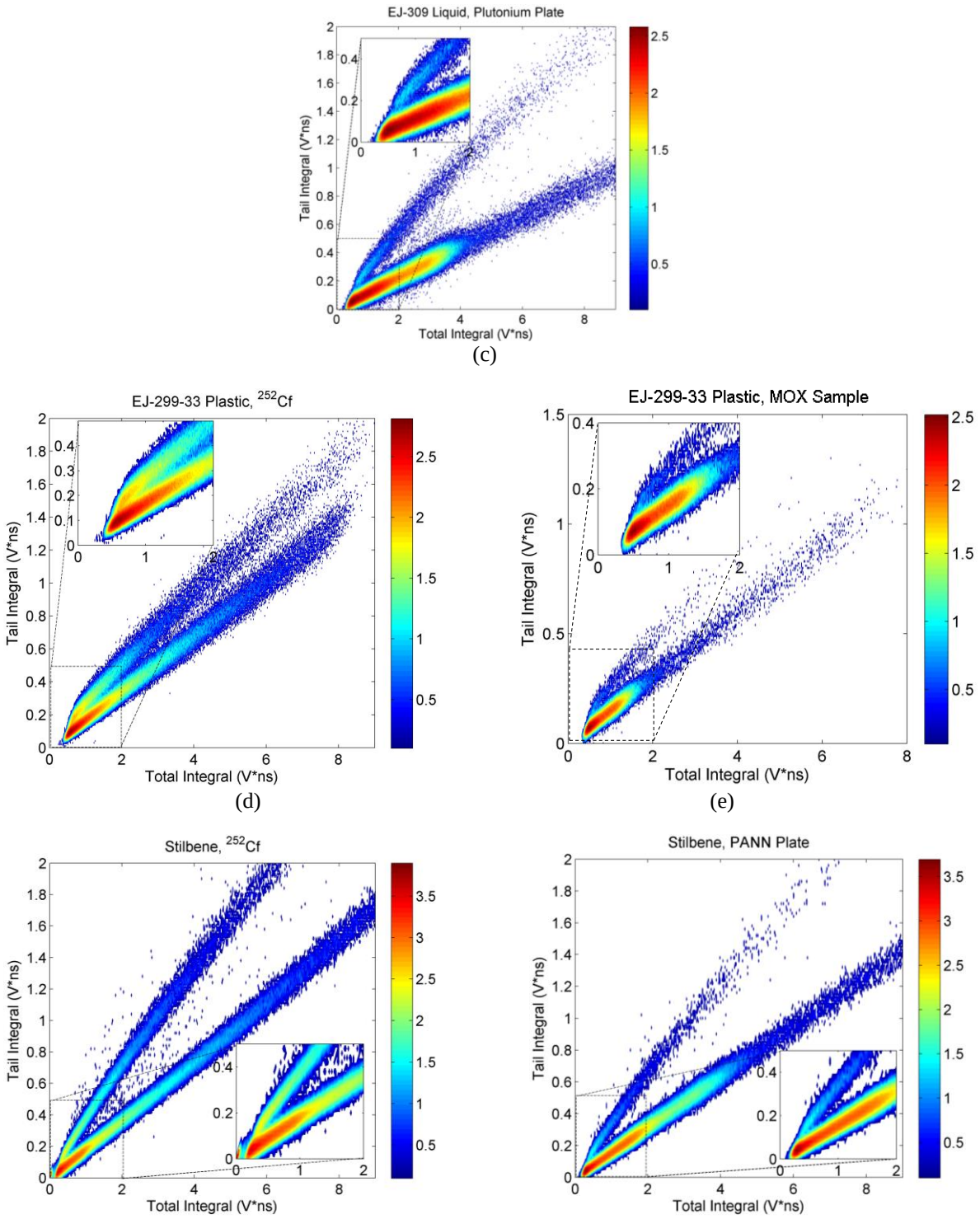

Fig. 6-5. PSD tail-vs-total integral plots for EJ-309 measuring ^{252}Cf, mixed oxide, and plutonium metal plate (a, b, c) and EJ-299-33 measuring ^{252}Cf and mixed oxide (d, e), and stilbene measuring ^{252}Cf and plutonium metal plate (f, g). Pulses were processed at a 36-keVee light output threshold for stilbene, 70-keVee light output threshold for EJ-309 liquid, and a 150-keVee light output threshold for EJ-299-33 plastic.

Each PSD plot was processed using a specialized MATLAB routine designed to apply PSD to measured pulses dependent on the tail and total integral of each pulse [20]. The routine starts by slicing each integral plot in Figure 6-5 perpendicular to the average of the slopes of the neutron and gamma-ray regions. Within each slice, pulses are histogrammed by their tail-to-total integral ratio, creating photon and neutron peaks such as that shown in Figure 6-6. The resulting histogram is fit as a sum of two Gaussians, where each Gaussian represents particles classified as either gamma rays or neutrons. The individual Gaussian fits are used to find the tail-to-total integral ratio that minimizes the overlap of the two distributions. The discrimination points from every slice exhibit an accurate fit to a 2nd-order polynomial, yielding the discrimination curve that classified every pulse as a neutron or gamma ray. The routine functions best when applied to low-count rate ^{252}Cf data.

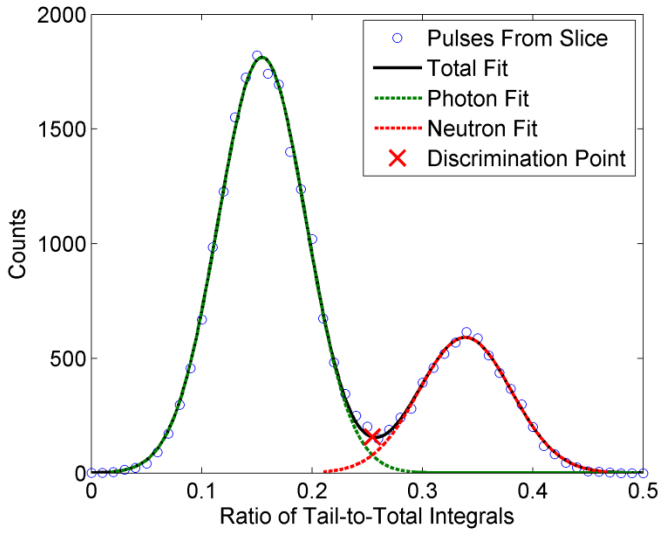

Fig. 6-6. Tail-to-total integral ratio histogram for one slice from EJ-309, illustrating the algorithm used by the MATLAB routine for finding PSD in each experiment.

6.3. Monte Carlo modeling

MCNPX-PoliMi was used for modeling these cross-correlation experiments. MPPost was used to convert collision output into the cross-correlation distributions for each detector pair using the measured light output functions from Chapter 3 for EJ-299-33 and stilbene and light output measured in [34] for EJ-309 liquid. Figure 6-7 shows the simulated geometry used for the ^{252}Cf and MOX experiments. For the ^{252}Cf experiment, the detectors were modeled 10 cm above a steel table with a thickness of 3 mm. The ^{252}Cf source was simulated as a point source located in the center of the geometry 20 cm from each detector, using the built-in MCNPX-PoliMi

source. The EJ-299-33 plastic and stilbene assembly PMT geometry is not well understood, so only the PMTs for the EJ-309 liquids were modeled.

In the MOX and Pu plate simulations, each sample was aged from its known isotopics to the same month of each experiment. The aged isotopics were then used to estimate the source intensity from spontaneous fission or (α, n) of each isotope; these were simulated using the mixed source specification in MCNPX-PoliMi. The aluminum detector holder, the experiment table, shielding, and dry air were simulated.

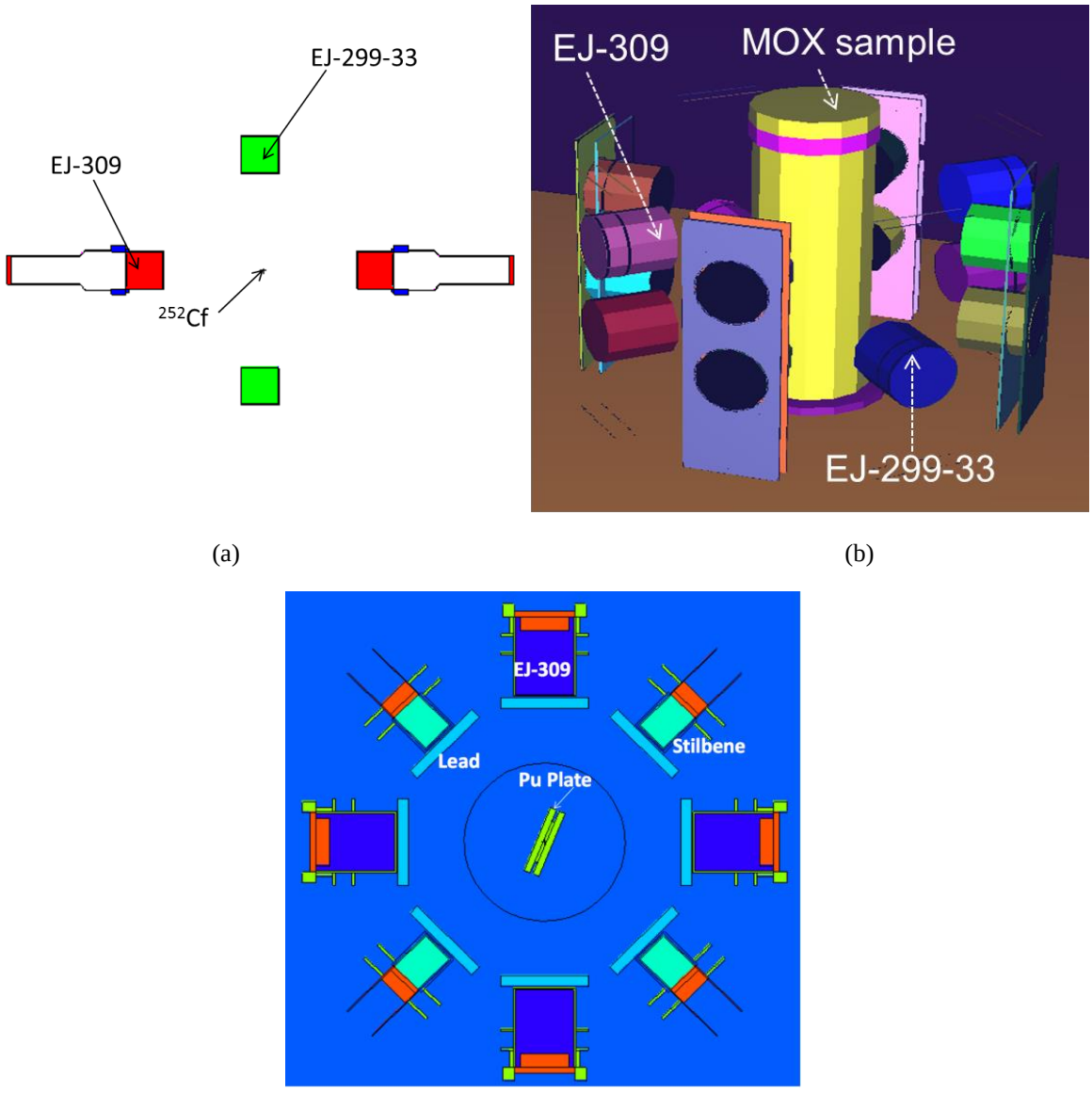

(a) (b)

(c)

Fig. 6-7. Modeled geometry for the ^{252}Cf (a), MOX (b), and Pu plate (c) experiments.

6.4. Cross-Correlation Distributions

Constant fraction timing, taken at half of the pulse amplitude along the leading edge, was applied to all correlated pulses measured in 180-degree detector pairs to determine the time at which a pulse occurred. Correlated pulse times were subtracted, and these time differences were histogrammed by correlation type to obtain the cross-correlation distribution for each experiment. Figure 6-8 shows the measured and simulated cross-correlation distributions for ^{252}Cf, MOX, and plutonium metal plate using EJ-309 liquid, EJ-299-33 plastic, and stilbene scintillators. Particles classified as neutrons (N) and gamma-ray photons (P) are labeled in each correlation type. It follows that the shape of each curve is dependent on the time-of-flight of each particle; NN and PP correlations appear symmetric about 0 nanoseconds, while NP and PN correlations appear shifted by ±10 nanoseconds.

The EJ-299-33 contains significant peaks in the PP correlation at ±10 ns; since correlated photon emissions should be detected simultaneously; these were identified as NP and PN correlations that were misclassified as PP correlations. The EJ-299-33 also contains a higher peak in the NP and PN correlations at 0 ns relative to the EJ-309 and stilbene, identified primarily as PP correlations misclassified as NP and PN correlations. The MCNPX-PoliMi model shows that secondary photon production will also contribute to this peak.

The MCNPX-PoliMi model is most accurate when predicting the EJ-309 and stilbene detector responses to ^{252}Cf, where NN, NP, and PN agree to within 10%. EJ-299-33 is also predicted quite well, although inaccurate PSD makes it impossible to directly match detector response at lower light output (corresponding to longer neutron times of flight). The simulated PP contribution appears low because the aged ^{252}Cf source includes numerous gamma-emitting isotopes that are not included in the model. This effect is magnified in the MOX and plutonium metal samples, because plutonium has many more decay channels than ^{252}Cf.

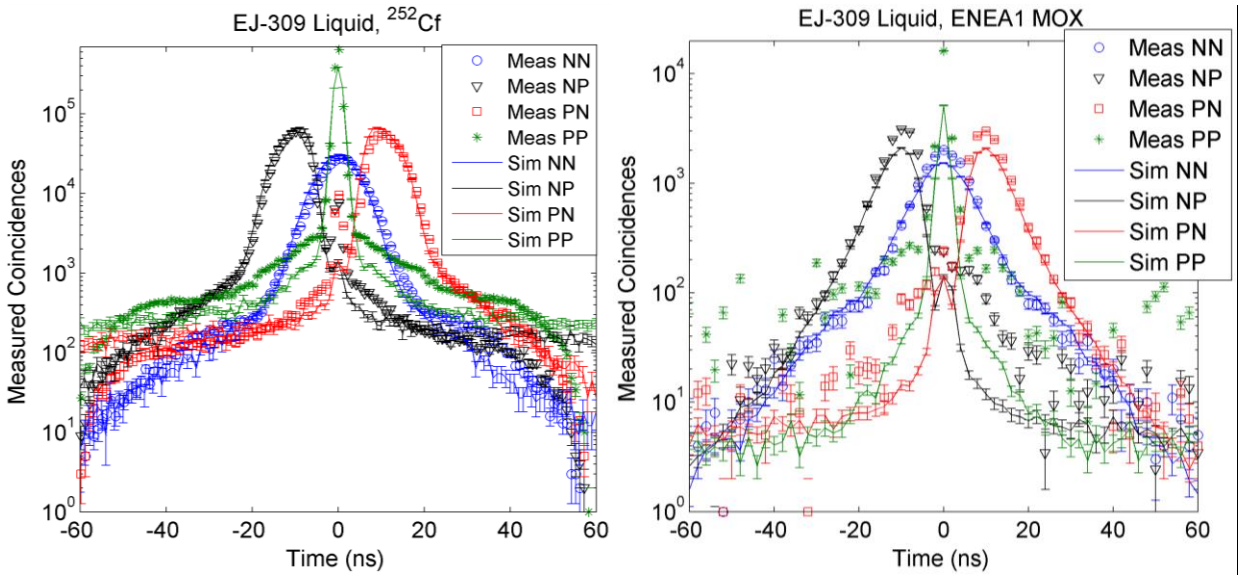
EJ-309 Liquid, ^{252}Cf
Measured Coincidences
Time (ns)
Meas NN
Meas NP
Meas PN
Meas PP
Sim NN
Sim NP
Sim PN
Sim PP

(a)

EJ-309 Liquid, ENEA1 MOX
Measured Coincidences
Time (ns)
Meas NN
Meas NP
Meas PN
Meas PP
Sim NN
Sim NP
Sim PN
Sim PP

(b)

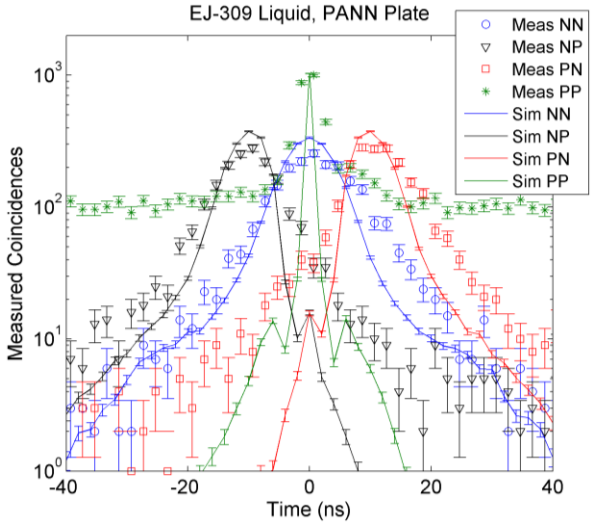
EJ-309 Liquid, PANN Plate
Measured Coincidences
Time (ns)
Meas NN
Meas NP
Meas PN
Meas PP
Sim NN
Sim NP
Sim PN
Sim PP

(c)

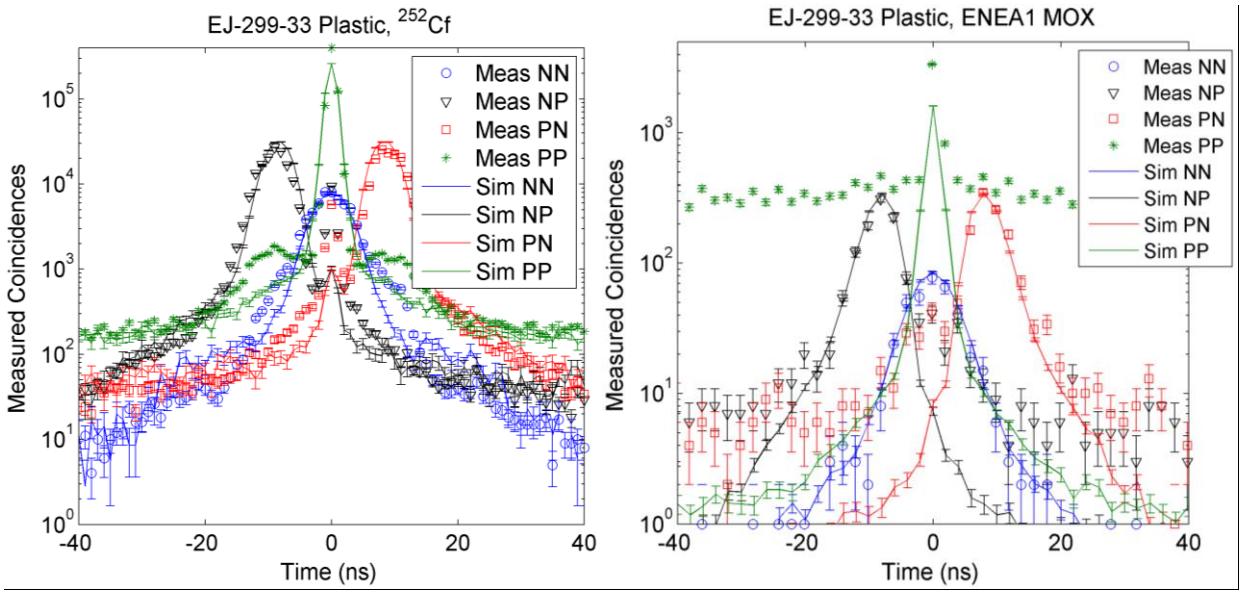

(d) (e)

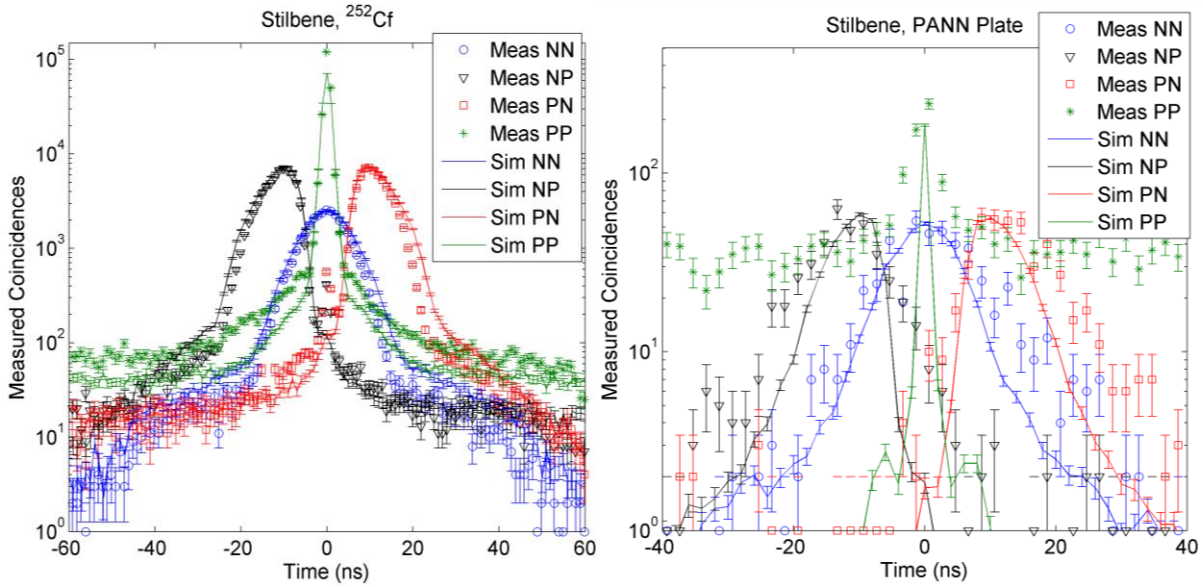

(f) (g)

Fig. 6-8. Cross-correlation distributions from 180-degree pairs from EJ-309 measuring ^{252}Cf, mixed oxide, and PANN plutonium metal (a-c), EJ-299-33 measuring ^{252}Cf and mixed oxide (d, e), and stilbene measuring ^{252}Cf and PANN plutonium metal (f, g). Pulses were processed at a 36-keVee threshold for stilbene, 70-keVee threshold for EJ-309 liquid, and 150-keVee threshold for EJ-299-33 plastic.

NN efficiency is directly compared in each detector pair by scaling each experiment to its measurement time, detector thickness, and the square of solid angle to account for geometric efficiency in correlated experiments. Table 6-2 shows the NN efficiency for each detector pair. The EJ-309 detector was more efficient at recording NN correlations than the EJ-299-33

detector, giving approximately a factor-of-5 increase in the ^{252}Cf experiment and a factor-of-10 increase in the MOX experiment. The lower detection threshold allowed stilbene to exhibit 25% greater efficiency than the EJ-309 liquid in the ^{252}Cf experiment and 50% greater efficiency in the PANN plate experiment.

Table 6-2. Normalized NN integrals for each detector pair.

Detector	NN Integral (NN / s-cm-steradian^2)		
	^{252}Cf	MOX	PANN Plate
Stilbene	11000	--	200
EJ-309	8800	2100	120
EJ-299-33	1800	170	--

6.5. Discriminating Pu Samples from ^{252}Cf

The cross-correlation distributions of ^{252}Cf, MOX, and plutonium metal allows for separate identification of each. ^{252}Cf has higher neutron multiplicity than even-numbered isotopes of plutonium. Significant (α, n) events in the MOX source add additional uncorrelated neutron counts to this experiment. This fact, when combined with the lower multiplicity in even-numbered plutonium isotopes, suggests the uncorrelated-to-correlated neutron ratio, or neutron singles-to-doubles ratio, should be higher in plutonium samples than in ^{252}Cf. Singles-to-doubles ratio is a robust metric that accounts for sources with different source intensity and is only weakly dependent on source shielding since both the singles and doubles rates are dependent on source shielding. Table 6-3 shows that the neutron singles-to-doubles ratio is approximately a factor-of-8 greater in the MOX sample and a factor-of-4 greater in the plutonium metal sample than ^{252}Cf, confirming this ratio can be used for discriminating plutonium samples from ^{252}Cf. There is also a factor-of-2 increase in singles-to-doubles ratio in MOX over the plutonium metal plate in the EJ-309, allowing for discriminating plutonium metal samples from plutonium oxide.

Table 6-3. Singles-to-doubles ratio used to discriminate ^{252}Cf from mixed oxide and plutonium metal samples, computed for each scintillator.

Detector	Singles-to- Doubles Ratio		
	^{252}Cf	MOX	PANN Plate
EJ-309	160	1200	600
EJ-299-33	370	3100	--
Stilbene	240	--	1100

6.6. Remarks

Cross-correlation analysis was performed for ^{252}Cf, MOX, and plutonium metal samples using EJ-309 liquid, EJ-299-33 plastic, and stilbene scintillators. Charge integration PSD was used to identify neutron and gamma-ray pulses. EJ-299-33 sacrifices detection efficiency and PSD capability relative to EJ-309 and stilbene; despite this limitation, EJ-299-33 was still capable of distinguishing ^{252}Cf from MOX using the measured neutron singles-to-doubles ratio. As long as accurate particle classification is not needed at lower light output, EJ-299-33 can be used to characterize correlated samples in cross-correlation experiments.

Both EJ-309 and stilbene showed the ability to separate ^{252}Cf from plutonium metal using the measured singles-to-doubles ratio. This analysis does not demonstrate advantages of using organic scintillators over a ^{3}He system; ^{3}He possesses high neutron efficiency with negligible gamma-ray misclassification, more than sufficient to use the singles-to-doubles ratio to discriminate between ^{252}Cf and plutonium sources.

With the excellent PSD capabilities that rival EJ-309, stilbene has demonstrated its potential use in safeguards applications. Future work will seek to utilize stilbene to obtain more information about correlated sources, such as anisotropy of particle emissions and decay product buildup, to show improvements over an equivalent ^{3}He-based coincidence counting system. Future work will also seek to improve the data acquisition system to allow a higher data throughput rate, reducing the need for lead when measuring plutonium samples in cross-correlation. The cross-correlation analysis may see additional benefit from implementing the double-pulse rejection algorithms developed in this thesis.

Chapter 7. Summary and Conclusions

Alternate detection technologies are crucial to meeting demand for neutron detectors, for the current production of ^{3}He is insufficient by itself. Organic scintillation detectors are a strong candidate as a ^{3}He alternate due to their high efficiency, fast timing properties, and PSD capabilities for separately identifying gamma-ray and neutron pulses. Their use in environments with numerous gamma rays ran the risk of misclassifying gamma rays as neutrons, limiting their use for neutron counting without using lead or decreasing detection efficiency. Through the development of a hybridized double-pulse rejection technique, this work showed that organic scintillation detectors could count neutrons in environments containing numerous gamma rays, including SNM measurements of plutonium, with very few gamma rays misclassified as neutrons and without using lead shielding.

Stilbene managed between 15-19% intrinsic neutron efficiency when measuring ^{252}Cf with the three rejection methods and 13-17% intrinsic neutron efficiency when adding 1000 external gamma rays per ^{252}Cf neutron. Misclassification rates ranged from 10^{-6}–10^{-5} for the three rejection methods. EJ-309 liquid sacrifices 10% neutron efficiency and BB3-5 sacrifices a factor-of-2 in neutron efficiency to obtain PSD with misclassification rate a factor-of-5 worse when compared to stilbene. It was determined that plastic scintillators sacrifice too much in performance relative to stilbene to be worth utilizing in strong gamma-ray fields without lead shielding. Stilbene needs to use lead or increase its detection threshold to match the gamma rejection level of ^{3}He systems.

Plutonium experiments were performed with stilbene to give greater clarity towards which rejection method was best for each sample. Through this work, Monte Carlo models were developed for each experiment using the measured light output function from a ^{252}Cf time-of-flight experiment. The model acted as a benchmark for each measured result to predict. The optimal double-pulse rejection method varies with the detected gamma ray-to-neutron ratio measured by either fractional or hybrid rejection. It was best to use template or no rejection when

the gamma ray-to-neutron ratio was less than 10 to preserve neutron counts and fractional or hybrid rejection when the gamma ray-to-neutron ratio exceeded 100. Stilbene was capable of measuring the expected neutron light output distribution for the ^{252}Cf source and plutonium sources except the PAHN plutonium plate without lead shielding.

Both PSD-capable plastic and stilbene scintillators demonstrated their use in cross-correlation applications, where the goal is to detect correlated neutrons and gamma rays from a source. Fission sources containing plutonium are more interesting than ^{252}Cf or single neutron-emitting sources such as (α, n) from AmLi. By comparing the single and correlated neutrons from each source, stilbene and PSD-capable plastic scintillators managed to discriminate plutonium metal and oxide samples separate from a ^{252}Cf spontaneous fission source. This capability is particularly promising for the EJ-299-33 plastic scintillator, whose PSD capabilities are noticeably worse than both stilbene and EJ-309 liquid scintillators.

7.1. Future Work

7.1.1. Real-Time Implementation of Double-Pulse Rejection Algorithms

The next challenge is to implement the double-pulse rejection algorithms into a real-time data acquisition system. Ideally, the system would be both capable of identifying double pulses and performing charge-integration PSD, as it is no longer needed to store entire waveforms. In addition, the data acquisition system would be capable of higher data throughput rates.

7.1.2. Application into Inorganic Scintillation Detectors

The double-pulse rejection algorithms developed in this thesis are best used for detector systems with dual sensitivity to gamma rays and neutrons. Inorganic scintillators such as Cs_2LiYCl_6 (CLYC) are in development by Radiation Monitoring Devices that are capable of detecting gamma rays and neutrons. CLYC was initially designed to use ^{6}Li as a capture target for thermal neutron detection, but it was found that fast neutrons were also being detected due to the presence of ^{35}Cl [43]. PSD is utilized as the primary means of identifying neutron pulses from gamma-ray pulses, yielding clear separation for thermal neutron pulses but only marginal separation for fast neutron pulses. While CLYC has not been demonstrated its functionality in fields with numerous gamma rays, it is expected that the double-pulse rejection algorithms would both improve classification of fast neutrons in the scintillator and improve detector resolution of gamma-ray events in fields containing numerous gamma rays.

7.1.3. Using Birks and Voltz to Model Light Output

The neutron energy-to-light output relationship is fit to an expression initially utilized in [34]. This method has been shown to be sufficient that gives good agreement with measured neutron pulse height spectra, but the relationship does not have physical basis. An expression is currently being implemented by other students in the DNNG research group that accounts for stopping power and light quenching. Applying this expression to simulations of ^{252}Cf light output distributions yields improved light output agreement for measured results for scintillation detectors larger than the stilbene and BB3-5 plastic scintillators in Chapter 3, and for light outputs lower than 300 keVee in preliminary work.

7.1.4. Double-Pulse Rejection by Pulse Fitting

One of the drawbacks to the hybridized double-pulse rejection method is that all pulses with multiple particle interactions in the same detection window are simply discarded, removing what may have been a neutron pulse in the process. If there were a way to identify pulses are neutrons or gamma rays without relying on charge integration, the rejection method could theoretically reduce gamma ray misclassification rate without lowering neutron efficiency. One method would be to fit each waveform to the combination of one or more pulses. Then the measured waveform would represent the sum of its components that could be separately compared to the neutron and gamma ray templates for each detector.

Previous experiments have shown that the shape of gamma-ray pulses stays very consistent with varying pulse height, but neutron pulse shape deviates with vaying pulse height. Any fitting technique would need to account for this change while automatically finding the range of each individual pulse contained within the waveform.

7.1.5. Well Counter Measurements Without Lead

The hybridized double-pulse rejection technique, when combined with the excellent PSD capabilities of stilbene, should allow for using less lead when characterizing plutonium samples with numerous gamma rays. Stilbene could then obtain greater insight into both source anisotropy and decay product build-up when measuring without using lead. The biggest hurdle would come from increasing the data throughput threshold of the data acquisition system.

Appendix A. MCNPX-PoliMi Input Files

^{252}Cf Experiment with Stilbene

```
Cf252 Measurement with Stilbene
c CELL CARDS
30 5 -1.16 -300 IMP:N,P=1 $ Stilbene
98 6 -1.20479e-03 -999 300     IMP:N,P=1 $Inside Universe
99 0 999 IMP:N,P=0 $Outside Universe
c END CELL CARDS - BLANK LINE FOLLOWS


c SURFACE CARDS
c Defined point resting on top of the center of table as origin
300 RCC 0 0 34.6075 0 0 5.08  2.54 $  Top Stilbene (approximate as cylinder)
999 RPP -10 10 -10 10 -1 45 $Universe
c END SURFACE CARDS - BLANK LINE FOLLOWS


c DATA CARDS
MODE  N P
NPS  1e8
PRINT 10 40 50 100 110 126 140 160
PHYS:N  J     20  $ increase to highest source energy for PoliMi
PHYS:P  J     1
CUT:N   2J    0
CUT:P   2J    0
PRDMP 2J 1
DBCN
C
c POLIMI CARDS
IPOL  1 0 2 1 J 1 1 30
RPOL  0.001 0.001
```

```
FILES  21  DUMN2
c
c VARIANCE REDUCTION
c SOURCE SPECIFICATION
SDEF  POS=0 0 0
c
c MATERIAL SPECIFICATION
c    ZZAAA.XXc    atom_fraction OR -mass_fraction
c     zaid number followed by available neutron library, use atom ratio or
mass fraction of each isotope
c    PLIB = 04p, NLIB = XXc assigns ALL isotopes with library
M5   1001.70c  .4615        $ Stilbene
     6012.42c  .5385
     PLIB = 04p
M6   6000.24c -0.000124     $ Air
     7014.62c -0.7523238
     7015.70c -0.0029442
     8016.62c -0.231686881
     8017.66c -0.00009411898831
     18000.59c -0.012827
c TALLY SPECIFICATION
F1:N 300.1 300.2 300.3
E1 1 8i 10
C1 0 1
c END OF FILE
```

^{252}Cf Experiment with EJ-299-33

```
Cf252 Measurement with EJ-299-33
c CELL CARDS
22 2 -2.7 -202 206 IMP:N,P=1 $Aluminum Casing Bottom
26 4 -1.08 -206 IMP:N,P=1 $Scintillator Bottom
98 0         -999 #22 #26 IMP:N,P=1 $Inside Universe
99 0          999 IMP:N,P=0 $Outside Universe
c
```

```
c
c END CELL CARDS - BLANK LINE FOLLOWS


c SURFACE CARDS
202 RCC   0 -107  0             0 -7.73  0     3.9625 $ My Bottom Detector
206 RCC    0 -107.152 0            0 -7.426   0     3.8105 $ My Bottom EJ299
Scintillator
999 RPP  -20 20         -120 20        -20 20           $ My Universe, Touches
bottom of table to top of aluminum case / Left of table to right of table
c END SURFACE CARDS - BLANK LINE FOLLOWS


c DATA CARDS
MODE  N P
NPS  4e8
PRINT 10 40 50 100 110 126 140 160
PHYS:N  J     20  $ increase to highest source energy for PoliMi
PHYS:P  J     1
CUT:N   2J    0
CUT:P   2J    0
PRDMP 2J 1
DBCN
c
c POLIMI CARDS
IPOL  1 0 2 1 J 1 1 26
RPOL  0.001 0.001
FILES  21  DUMN1
c
c VARIANCE REDUCTION
c SOURCE SPECIFICATION
SDEF  POS=0 0 0
c
c MATERIAL SPECIFICATION
M2   13027 1.0000           $ Al casing
```

```
     NLIB = 60c  PLIB = 04p
M4   1001.66c   0.514       $ Plastic Scintillator
     6000.70c   0.486
     PLIB = 04p
c
c TALLY SPECIFICATION
c END OF FILE
```

CBNM61 Experiment with Stilbene

```
CBNM61 Pu Oxide Measurement with Stilbene
c Based on outer dimensions from the Scionix drawing
c and thicknesses from the 5x5" EJ309 Eljen drawing
c
c Cell Card
c
c Detectors
c
100 5 -1.16  -13  imp:n,p=1   $ stilbene
101 5 -1.16  -14  imp:n,p=1   $ stilbene
c Source
c
200 7 -10.49  -20  imp:n,p=1   $ PuO2
c
c Measurement Geometry
c
c 300 2 -11.34  -51 50 imp:n,p=1  $ Pb ring
998 1 -0.001 -99 13 14 20 imp:n,p=1 $ air
999 0         99             imp:n,p=0 $ The Void
c
c Blank line follows

c Surface Card
c
```

```
c Detectors
c
13 rcc -13  0 0 -5.08  0 0 2.54  $ stilbene
14 rcc -12  -5.08 0 -4.68  -1.985 0 2.54  $ stilbene 2
c
c Sample
c
20 rcc 0 0 -0.21 0  0  0.38  0.7455
c
c Lead rings
c
c 50 rcc 0 0 -4.5  0  0  9  3.6
c 51 rcc 0 0 -4.5  0  0  9  5.25
c
99 rpp -25 10 -20 10 -10 10 $ air box
c
c Blank Line Follows

c Data Card
c
C      Materials
m1      8016.70c   0.16
        7014.70c   0.84
        plib=04p            $ air
c
m2      82000.42c  1
        plib=04p            $ Pb
c
m5     1001      .4615
       6000      .5385
        plib=04p            $ EJ-315 liquid scintillator
c
```

```
m7      94238.42c   -0.00943
        94239.60c   -0.61623
        94240.60c   -0.24984
        94241.60c   -0.01377
        94242.60c   -0.04135
        95241.61c   -0.05587
        08016.60c   -0.01350
        plib=04p            $ Pu Oxide
c
c
SDEF cel=200 pos=0 0 -0.21 axs=0 0 1 rad=d1 ext=d2 erg=d3
SI1  0 0.743
SI2  0 0.364
SI3  L 3 4 38 39 40 41
SP3  0.2426 0.0680 0.2598 0.0483 0.0724 0.3090
C       The following two PHYS cards are essential for analog MC
PHYS:N  J     20  $ increase to highest source energy for PoliMi
PHYS:P  J     1
CUT:N   2J    0
CUT:P   2J    0
PRDMP 2J 1
DBCN
IPOL   99 1 2 1 J 1 2 100 101
RPOL   .001 .001
NPS    1e8
MODE n p
FILES  21  DUMN1
PRINT
c Tallies
F1:N  13.2
E1 .01 .1 1 2 3 5 10 100
C1  0 1
```

```
F11:P 13.2

E11 0 99i 10

C11 0 1
```

CBNM84 Experiment with Stilbene

```
3x3" EJ309 Scionix liquid scintillator based on dimensions from scionix
drawing

c Based on outer dimensions from the Scionix drawing

c and thicknesses from the 5x5" EJ309 Eljen drawing

c

c Cell Card

c

c Detectors

c

100 5 -1.16  -13  imp:n,p=1   $ stilbene

101 5 -1.16  -14  imp:n,p=1   $ stilbene

c Source

c

200 7 -10.07  -20  imp:n,p=1   $ PuO2

c

c Measurement Geometry

c

c 300 2 -11.34  -51 50 imp:n,p=1  $ Pb ring

998 1 -0.001 -99 13 14 20 imp:n,p=1 $ air

999 0         99             imp:n,p=0 $ The Void

c

c Blank line follows


c Surface Card

c

c Detectors

c

13 rcc -13  0 0 -5.08  0 0 2.54  $ stilbene

14 rcc -12  -5.08 0 -4.68  -1.985 0 2.54  $ stilbene 2
```

```
c
c Sample
c
20 rcc 0 0 -0.21 0  0  0.38  0.7455
c
c Lead rings
c
c 50 rcc 0 0 -4.5  0  0  9  3.6
c 51 rcc 0 0 -4.5  0  0  9  5.25
c
99 rpp -25 10 -20 10 -10 10 $ air box
c
c Blank Line Follows

c Data Card
c
C      Materials
m1      8016.70c   0.16
        7014.70c   0.84
        plib=04p            $ air
c
m2      82000.42c  1
        plib=04p            $ Pb
c
m5     1001      .4615
       6000      .5385
        plib=04p            $ stilbene scintillator
c
m7      94238.42c   -0.00055
        94239.60c   -0.83068
        94240.60c   -0.13961
        94241.60c   -0.00249
```

```
        94242.60c   -0.00352
        95241.61c   -0.00964
        08016.60c   -0.01350
        plib=04p            $ Pu Oxide
C
SDEF cel=200 pos=0 0 -0.21 axs=0 0 1 rad=d1 ext=d2 erg=d3
SI1  0 0.741
SI2  0 0.385
SI3  L 3 4 38 39 40 41
SP3  0.4297 0.0184 0.0484 0.2063 0.1283 0.1690
C       The following two PHYS cards are essential for analog MC
PHYS:N  J     20  $ increase to highest source energy for PoliMi
PHYS:P  J     1
CUT:N   2J    0
CUT:P   2J    0
PRDMP 2J 1
DBCN
IPOL   99 1 2 1 J 1 2 100 101
RPOL   .001 .001
NPS    1e8
MODE n p
FILES  21  DUMN1
PRINT
c Tallies
F1:N  13.2
E1 .01 .1 1 2 3 5 10 100
C1  0 1
F11:P 13.2
E11 0 99i 10
C11 0 1
```

Bare PuGa207-211 Experiment with Stilbene

Stilbene scintillator, measuring PuGa disks from Ispra

```
c Cell Card
c
c Detectors
c
100 5 -1.16  -13  imp:n,p=1   $ stilbene
101 5 -1.16  -14  imp:n,p=1   $ stilbene
c Source
c
207 7 -14.763  -20  imp:n,p=1   $ PuGa Disk 207
208 7 -14.710  -21  imp:n,p=1   $ PuGa Disk 208
209 7 -15.132  -22  imp:n,p=1   $ PuGa Disk 209
210 7 -15.608  -23  imp:n,p=1   $ PuGa Disk 210
211 7 -15.622  -24  imp:n,p=1   $ PuGa Disk 211
c
c Measurement Geometry
c
998 1 -0.001 -98  13 14 20 21 22 23 24 imp:n,p=1 $ air
999 0         98               imp:n,p=0 $ The Void
c
c Blank line follows

c Surface Card
c
c Detectors
c
13 rcc -10  0 0 -5.08  0 0 2.54  $ stilbene
14 rcc -8.66  -5 0 -4.40 -2.54 0 2.54  $ stilbene
c
c Sample
c
20 rcc 0 0 -0.0101 0  0  0.02  1
21 rcc 0 0  0.0699 0  0  0.06  0.575
```

```
22 rcc 0 0  0.0099 0  0  0.06  0.825
23 rcc 0 0 -0.0701 0  0  0.06  1.3
24 rcc 0 0 -0.1301 0  0  0.06  1.825
c
c Lead rings
c
c 50 rcc 0 0 -4.5  0  0  9  3.6
c 51 rcc 0 0 -4.5  0  0  9  5.25
c
c 981 cz  1.825               $ air box for debugging
c 982 cz  1.3                 $ air box for debugging
c 983 cz  1                   $ air box for debugging
c 984 cz  0.825               $ air box for debugging
c 985 cz  0.575               $ air box for debugging
c 991 pz -0.13                $ air box for debugging
c 992 pz -0.07                $ air box for debugging
c 993 pz -0.01                $ air box for debugging
c 994 pz  0.01                $ air box for debugging
c 995 pz  0.07                $ air box for debugging
c 996 pz  0.13                $ air box for debugging
98 rpp -20  10 -20  10 -10 10 $ air box
c 99 rpp  -20 10 -2.6  10 -10 10 $ air box (sources)
c
c Blank Line Follows

c Data Card
c
C      Materials
m1      8016.70c   0.16
        7014.70c   0.84
        plib=04p            $ air
c
```

```
m5     1001      .4615
       6000      .5385
        plib=04p            $ stilbene scintillator
c
m7      94238.42c   -0.00113
        94239.60c   -0.73888
        94240.60c   -0.20956
        94241.60c   -0.00768
        94242.60c   -0.00748
        95241.61c   -0.00018
        31000.66c   -0.03509
        plib=04p            $ Pu Oxide
c
SDEF x=0 y=0 z=d1 axs=0 0 1 erg=d8 rad=fz d2 ext=fz d3
c SDEF pos=d1 axs=0 0 1 erg=d8 rad=fpos d2 ext=fpos d3
c SI1  L 0 0 -0.1299 0 0 -0.0699 0 0 -0.0099 0 0 0.0101 0 0 0.0701
c SP1  0.5283 0.2678 0.0499 0.1046 0.0494
SI1  L -0.13 -0.07 -0.01  0.01  0.07
SP1  0.5283 0.2678 0.0499 0.1046 0.0494
DS2  S  21 22 23 24 25
DS3  S  31 32 33 34 35
c DS2  Q D21 D22 D23 D24 D25
c DS3  Q D31 D32 D33 D34 D35
SI8  L 3 4
SP8  0.943 0.057
SI21  0 1.825
SI22  0 1.3
SI23  0 1
SI24  0 0.825
SI25  0 0.575
SI31 0 0.06
SI32 0 0.06
```

```
SI33 0 0.02
SI34 0 0.06
SI35 0 0.06
c SDEF
c VOID 100 101 207 208 209 210 211 998
C       The following two PHYS cards are essential for analog MC
PHYS:N  J     20  $ increase to highest source energy for PoliMi
PHYS:P  J     1
CUT:N   2J    0
CUT:P   2J    0
PRDMP 2J 1
DBCN
IPOL   99 1 2 1 J 1 2 100 101
RPOL   .001 .001
NPS    1e8
MODE n p
FILES  21  DUMN1
PRINT
c Tallies
c F1:N  13.2
c E1 .01 .1 1 2 3 5 10 100
c C1  0 1
c F11:P 13.2
c E11 0 99i 10
c C11 0 1
```

Shielded PuGa207-211 Experiment with Stilbene

```
Stilbene scintillator, measuring PuGa disks from Ispra
c
c Cell Card
c
c Detectors
c
```

```
100 5 -1.16  -13  imp:n,p=1   $ stilbene
101 5 -1.16  -14  imp:n,p=1   $ stilbene
c Source
c
207 7 -14.763  -20  imp:n,p=1   $ PuGa Disk 207
208 7 -14.710  -21  imp:n,p=1   $ PuGa Disk 208
209 7 -15.132  -22  imp:n,p=1   $ PuGa Disk 209
210 7 -15.608  -23  imp:n,p=1   $ PuGa Disk 210
211 7 -15.622  -24  imp:n,p=1   $ PuGa Disk 211
c
c Measurement Geometry
c
300 2 -11.34  -50    imp:n,p=1  $ Pb shield
301 2 -11.34  -51    imp:n,p=1  $ Pb shield
998 1 -0.001 -98  13 14 20 21 22 23 24 50 51 imp:n,p=1 $ air
999 0         98              imp:n,p=0 $ The Void
c
c Blank line follows

c Surface Card
c
c Detectors
c
13 rcc -10.635  0 0 -5.08  0 0 2.54  $ stilbene
14 rcc -9.21  -5.3175 0 -4.40 -2.54 0 2.54  $ stilbene
c
c Sample
c
20 rcc 0 0 -0.0101 0  0  0.02  1
21 rcc 0 0  0.0699 0  0  0.06  0.575
22 rcc 0 0  0.0099 0  0  0.06  0.825
23 rcc 0 0 -0.0701 0  0  0.06  1.3
```

```
24 rcc 0 0 -0.1301 0  0  0.06  1.825
c
c Lead piece
c
50 rcc -10 0 0  -0.635  0  0  2.54
51 rcc -8.66 -5 0  -0.550 -0.3175  0  2.54
c
c 981 cz  1.825               $ air box for debugging
c 982 cz  1.3                 $ air box for debugging
c 983 cz  1                   $ air box for debugging
c 984 cz  0.825               $ air box for debugging
c 985 cz  0.575               $ air box for debugging
c 991 pz -0.13                $ air box for debugging
c 992 pz -0.07                $ air box for debugging
c 993 pz -0.01                $ air box for debugging
c 994 pz  0.01                $ air box for debugging
c 995 pz  0.07                $ air box for debugging
c 996 pz  0.13                $ air box for debugging
98 rpp -20  10 -20  10 -10 10 $ air box
c 99 rpp  -20 10 -2.6  10 -10 10 $ air box (sources)
c
c Blank Line Follows

c Data Card
c
C      Materials
m1      8016.70c   0.16
        7014.70c   0.84
        plib=04p            $ air
c
m2      82000.42c  1
        plib=04p            $ Pb
```

```
c
m5     1001      .4615
       6000      .5385
        plib=04p            $ stilbene scintillator
c
m7      94238.42c   -0.00113
        94239.60c   -0.73888
        94240.60c   -0.20956
        94241.60c   -0.00768
        94242.60c   -0.00748
        95241.61c   -0.00018
        31000.66c   -0.03509
        plib=04p            $ Pu Oxide
c
m8      14028      -0.323138999
        8016       -0.483882614
        5011       -0.033384805
        56138      -0.027496631
        11023      -0.077153875
        19039      -0.052216449
        33075      -0.002726626
        nlib=70c plib=04p   $ BK7
c
SDEF x=0 y=0 z=d1 axs=0 0 1 erg=d8 rad=fz d2 ext=fz d3
c SDEF pos=d1 axs=0 0 1 erg=d8 rad=fpos d2 ext=fpos d3
c SI1  L 0 0 -0.1299 0 0 -0.0699 0 0 -0.0099 0 0 0.0101 0 0 0.0701
c SP1  0.5283 0.2678 0.0499 0.1046 0.0494
SI1  L -0.13 -0.07 -0.01  0.01  0.07
SP1  0.5283 0.2678 0.0499 0.1046 0.0494
DS2  S  21 22 23 24 25
DS3  S  31 32 33 34 35
c DS2  Q D21 D22 D23 D24 D25
```

```
c DS3  Q D31 D32 D33 D34 D35
SI8  L 3 4
SP8  0.943 0.057
SI21  0 1.825
SI22  0 1.3
SI23  0 1
SI24  0 0.825
SI25  0 0.575
SI31 0 0.06
SI32 0 0.06
SI33 0 0.02
SI34 0 0.06
SI35 0 0.06
c SDEF
c VOID 100 101 207 208 209 210 211 998
C       The following two PHYS cards are essential for analog MC
PHYS:N  J     20  $ increase to highest source energy for PoliMi
PHYS:P  J     1
CUT:N   2J    0
CUT:P   2J    0
PRDMP 2J 1
DBCN
IPOL   99 1 2 1 J 1 2 100 101
RPOL   .001 .001
NPS    1e8
MODE n p
FILES  21  DUMN1
PRINT
c Tallies
c F1:N  13.2
c E1 .01 .1 1 2 3 5 10 100
c C1  0 1
```

```
c F11:P 13.2
c E11 0 99i 10
c C11 0 1
```

Shielded PuGa73240 Experiment with Stilbene

```
Stilbene scintillator measuring PuGa disks from Ispra
c
c
c
c Cell Card
c
c Detectors
c
100 5 -1.16  -13  imp:n,p=1   $ stilbene
101 5 -1.16  -14  imp:n,p=1   $ stilbene
c Source
c
207 7 -14.651  -20  imp:n,p=1   $ PuGa Disk 19
208 7 -15.396  -21  imp:n,p=1   $ PuGa Disk 26
209 7 -15.490  -22  imp:n,p=1   $ PuGa Disk 30
210 7 -15.786  -23  imp:n,p=1   $ PuGa Disk 31
211 7 -15.295  -24  imp:n,p=1   $ PuGa Disk 32
c
c Measurement Geometry
c
300 2 -11.34  -50    imp:n,p=1  $ Pb shield
301 2 -11.34  -51    imp:n,p=1  $ Pb shield
998 1 -0.001 -98  13 14 20 21 22 23 24 50 51 imp:n,p=1 $ air
999 0         98              imp:n,p=0 $ The Void
c
c Blank line follows

c Surface Card
```

```
c
c Detectors
c
13 rcc -10.635  0 0 -5.08  0 0 2.54  $ stilbene
14 rcc -9.21  -5.3175 0 -4.40 -2.54 0 2.54  $ stilbene
c
c Sample
c
20 rcc 0 0 -0.0101 0  0  0.02  1
21 rcc 0 0  0.0699 0  0  0.06  0.575
22 rcc 0 0  0.0099 0  0  0.06  0.825
23 rcc 0 0 -0.0701 0  0  0.06  1.3
24 rcc 0 0 -0.1301 0  0  0.06  1.825
c
c Lead piece
c
50 rcc -10 0 0  -0.635  0  0  2.54
51 rcc -8.66 -5 0  -0.550 -0.3175  0  2.54
c
c 981 cz  1.825               $ air box for debugging
c 982 cz  1.3                 $ air box for debugging
c 983 cz  1                   $ air box for debugging
c 984 cz  0.825               $ air box for debugging
c 985 cz  0.575               $ air box for debugging
c 991 pz -0.13                $ air box for debugging
c 992 pz -0.07                $ air box for debugging
c 993 pz -0.01                $ air box for debugging
c 994 pz  0.01                $ air box for debugging
c 995 pz  0.07                $ air box for debugging
c 996 pz  0.13                $ air box for debugging
98 rpp -20  10 -20  10 -10 10 $ air box
c 99 rpp  -20 10 -2.6  10 -10 10 $ air box (sources)
```

```
c
c Blank Line Follows

c Data Card
c
C      Materials
m1      8016.70c   0.16
        7014.70c   0.84
        plib=04p            $ air
c
m2      82000.42c  1
        plib=04p            $ Pb
c
m5     1001      .4615
       6000      .5385
        plib=04p            $ stilbene scintillator
c
m7      94238.42c   -0.00010
        94239.60c   -0.92043
        94240.60c   -0.05777
        94241.60c   -0.00070
        94242.60c   -0.00031
        95241.61c   -0.00001
        31000.66c   -0.02068
        plib=04p            $ PuGa
c
SDEF x=0 y=0 z=d1 axs=0 0 1 erg=d8 rad=fz d2 ext=fz d3
c SDEF pos=d1 axs=0 0 1 erg=d8 rad=fpos d2 ext=fpos d3
c SI1  L 0 0 -0.1299 0 0 -0.0699 0 0 -0.0099 0 0 0.0101 0 0 0.0701
c SP1  0.5283 0.2678 0.0499 0.1046 0.0494
SI1  L -0.13 -0.07 -0.01  0.01  0.07
SP1  0.5191 0.27184 0.05187 0.10743 0.04976
```

```
DS2  S  21 22 23 24 25
DS3  S  31 32 33 34 35
c DS2  Q D21 D22 D23 D24 D25
c DS3  Q D31 D32 D33 D34 D35
SI8  L 3 4
SP8  0.991 0.009
SI21  0 1.825
SI22  0 1.3
SI23  0 1
SI24  0 0.825
SI25  0 0.575
SI31 0 0.06
SI32 0 0.06
SI33 0 0.02
SI34 0 0.06
SI35 0 0.06
c SDEF
c VOID 100 101 207 208 209 210 211 998
C       The following two PHYS cards are essential for analog MC
PHYS:N  J     20  $ increase to highest source energy for PoliMi
PHYS:P  J     1
CUT:N   2J    0
CUT:P   2J    0
PRDMP 2J 1
DBCN
IPOL   99 1 2 1 J 1 2 100 101
RPOL   .001 .001
NPS    1e8
MODE n p
FILES  21  DUMN1
PRINT
c Tallies
```

```
c F1:N  13.2
c E1 .01 .1 1 2 3 5 10 100
c C1  0 1
c F11:P 13.2
c E11 0 99i 10
c C11 0 1
```

Shielded ENEA-2 Experiment with Stilbene

```
c ENEA2 MOX Measurement with Stilbene
c ~~~~~~~~~~~~~~~~~~~~~~~~~~~~~~~~~~
c  Cells
c ~~~~~~~~~~~~~~~~~~~~~~~~~~~~~~~~~~
c   Stilbene Detectors
c ~~~~~~~~~~~~~~~~~~~~~~~~~~~~~~~~~~
  101   1  -1.16    -11           imp:N,P=1   $ detector
  102   1  -1.16    -12           imp:N,P=1   $ detector
c ~~~~~~~~~~~~~~~~~~~~~~~~~~~~~~~~~~
c   Lead Shielding
c ~~~~~~~~~~~~~~~~~~~~~~~~~~~~~~~~~~
  501   3 -11.34     -51           imp:N,P=1   $ lead shield
  502   3 -11.34     -52           imp:N,P=1   $ lead shield
c ~~~~~~~~~~~~~~~~~~~~~~~~~~~~~~~~~~
c Ground
c ~~~~~~~~~~~~~~~~~~~~~~~~~~~~~~~~~~
c 601   6  -2.3      -500 -61       imp:N,P=1   $ concrete floor
c ~~~~~~~~~~~~~~~~~~~~~~~~~~~~~~~~~~
c   MOX Source
c ~~~~~~~~~~~~~~~~~~~~~~~~~~~~~~~~~~
  701     0          -73 87 -82     imp:n,p=1  $vaccum on top of powder
  702     7   -0.7   -73 81 -87     imp:n,p=1  $MOX powder
  703     8   -7.92   73 -74 81 -82 imp:n,p=1  $inner steel cylinder
  704     8   -7.92  -74 80 -81     imp:n,p=1  $steel inner bottom
  705     8   -7.92  -74 82 -83     imp:n,p=1  $steel inner top
```

```
  706     0           74 -75 80 -83 imp:n,p=1  $surroundeing vacuum cylinder
  707     0          -75 79 -80     imp:n,p=1  $bottom vacuum
  708     0          -75 83 -84     imp:n,p=1  $top vacuum
  709     0          -72 84 -85     imp:n,p=1  $another top vacuum
  710     8   -7.92   75 -76 79 -84 imp:n,p=1  $outer steel cylinder
  711     8   -7.92  -76 89 -79     imp:n,p=1  $steel outer bottom
  712     8   -7.92   72 -77 84 -85 imp:n,p=1  $steel cylinder top
  713     8   -7.92  -77 85 -86     imp:n,p=1  $steel outer top
c ~~~~~~~~~~~~~~~~~~~~~~~~~~~~~~~~~
c  Environment
c ~~~~~~~~~~~~~~~~~~~~~~~~~~~~~~~~~
  901   2  -1.205E-3 -500 11 12 51 52 #701 #702 #703 #704 #705 #706 #707
                    #708 #709 #710 #711 #712 #713  imp:n,p=1
  999   0    500                     imp:n,p=0


c ~~~~~~~~~~~~~~~~~~~~~~~~~~~~~~~~~
c  Surfaces
c ~~~~~~~~~~~~~~~~~~~~~~~~~~~~~~~~~
c   Stilbene Detectors
c ~~~~~~~~~~~~~~~~~~~~~~~~~~~~~~~~~
  11   RCC    -52.635     0   0  -5.0800   0  0  2.5400
  12   RCC    -52.34666 -5.50186   0  -5.05217  -0.53100  0  2.5400
c ~~~~~~~~~~~~~~~~~~~~~~~~~~~~~~~~~
c   Lead Shielding
c ~~~~~~~~~~~~~~~~~~~~~~~~~~~~~~~~~
  51   RCC    -52          0        0     -0.635   0  0    2.54
  52   RCC    -51.68514       -5.42548    0     -0.63152 -0.06638 0  2.54
c   51   CZ   6.4        $outer cylinder
c   52   PZ  -16.25      $bottom of Pb
c ~~~~~~~~~~~~~~~~~~~~~~~~~~~~~~~~~
c Ground
c ~~~~~~~~~~~~~~~~~~~~~~~~~~~~~~~~~
```

```
c   61 PZ     -108    $ Floor level
c ~~~~~~~~~~~~~~~~~~~~~~~~~~~~~~~~~
c MOX Source Container
c ~~~~~~~~~~~~~~~~~~~~~~~~~~~~~~~~~
  72 CZ   5.1         $Support cylinder outer and upper empty space cylinder
  73 CZ   4.14        $inner contaner cylinder inner wall
  74 CZ   4.445       $inner container cylinder outer wall
  75 CZ   5.2         $outer container cylinder inner wall
  76 CZ   5.4         $outer container cylinder outer wall
  77 CZ   6.75        $top steel cylinder
  79 PZ  -14.0982     $outer container - BOTTOM
  80 PZ  -13.8982     $inner container outer surf
  81 PZ  -13.3982     $inner container inner surf
  82 PZ   13.4018     $inner container inner surf
  83 PZ   13.9018     $inner container outer surf
  84 PZ   14.1018     $outer container
  85 PZ   16.1018     $outer container
  86 PZ   18.1018     $outer container
  87 PZ   13.4017     $top of PuO powder
  89 PZ  -15.0982     $bottom
c ~~~~~~~~~~~~~~~~~~~~~~~~~~~~~~~~~
c  Environment
c ~~~~~~~~~~~~~~~~~~~~~~~~~~~~~~~~~
 500 RPP -60 10   -60 10   -20 20


c ~~~~~~~~~~~~~~~~~~~~~~~~~~~~~~~~~
c Data
c ~~~~~~~~~~~~~~~~~~~~~~~~~~~~~~~~~
c Physics
c ~~~~~~~~~~~~~~~~~~~~~~~~~~~~~~~~~
  MODE n p
  PHYS:N J 20
```

```
  PHYS:P 0 1 1
  CUT:P 2J 0
c ~~~~~~~~~~~~~~~~~~~~~~~~~~~~~~~~
c Source
c ~~~~~~~~~~~~~~~~~~~~~~~~~~~~~~~~
  IPOL  99 1 2 1 J 1 2 101 102
  SDEF cel=702 pos=0 0 -13.39 axs=0 0 1 rad=d1 ext=d2 erg=D5 $ tme=d4 erg=D5
  SC1  Source radius (inner outer)
  SI1  0 4.14
  SC2  Source height
  SI2  0 26.79
c   SC4  Uniform time distribution in interval 0 to 3600 sec (1s=10^8 shakes)
c   SI4  0 360000000000
c   SP4  0 1
  SI5  L 2 3 4 38 39 40 41
  SP5  0.00009 0.4179 0.05092 0.05875 0.08023 0.12478 0.26733
c   NPS 15905094 $ 190861128 = Number of reactions in 3600 sec (aged MOX src)
  NPS 2e8 $ 190861128 = Number of reactions in 3600 sec (aged MOX src)
  FILES 21 DUMN1
  DBCN
  PRDMP 2J 1
c ~~~~~~~~~~~~~~~~~~~~~~~~~~~~~~~~
c Materials
c ~~~~~~~~~~~~~~~~~~~~~~~~~~~~~~~~
c  stilbene scintillator d=-1.16
c ~~~~~~~~~~~~~~~~~~~~~~~~~~~~~~~~
  m1   nlib=60c  plib=04p
       1001      .4615
       6000      .5385
c ~~~~~~~~~~~~~~~~~~~~~~~~~~~~~~~~
c Air, Dry (near sea level) d=-1.205E-3
c (Mat. Compendium PNNL)
```

```
c ~~~~~~~~~~~~~~~~~~~~~~~~~~~~~~~~
  m2  nlib=60c  plib=04p
      6000     -0.000124
      7014     -0.755268
      8016     -0.231781
     18000.42c -0.012827
c ~~~~~~~~~~~~~~~~~~~~~~~~~~~~~~~~
c  Lead Shielding d=-11.34
c
c ~~~~~~~~~~~~~~~~~~~~~~~~~~~~~~~~
  m3  82000.42c 1
c ~~~~~~~~~~~~~~~~~~~~~~~~~~~~~~~~
c ~~~~~~~~~~~~~~~~~~~~~~~~~~~~~~~~
c Concrete (Mat. Compendium PNNL) d=-2.3
c (Mat. Compendium PNNL)
c ~~~~~~~~~~~~~~~~~~~~~~~~~~~~~~~~
  m6  nlib=60c  plib=04p
      1001     -0.022100
      6000     -0.002484
      8016     -0.574930
     11023     -0.015208
     12000     -0.001266
     13027     -0.019953
     14000     -0.304627
     19000     -0.010045
     20000     -0.042951
     26000.42c -0.006435
c ~~~~~~~~~~~~~~~~~~~~~~~~~~~~~~~~
c  MOX sample d=-0.7
c (ENEA-02)
c ~~~~~~~~~~~~~~~~~~~~~~~~~~~~~~~~
  m7  8016.60c    -0.15982
```

```
      94238.42c   -0.00023
      94239.60c   -0.11032
      94240.60c   -0.04636
      94241.60c   -0.00149
      94242.60c   -0.00333
      95241.61c   -0.00521
      92234.60c   -0.00005
      92235.60c   -0.00477
      92236.60c   -0.00005
      92238.60c   -0.66836
c ~~~~~~~~~~~~~~~~~~~~~~~~~~~~~~~~
c    Steel
c ~~~~~~~~~~~~~~~~~~~~~~~~~~~~~~~~
  m8  26000.55c -0.6950
      24000.50c -0.1900
      28000.50c -0.0950
      25055.51c  -0.0200
c ~~~~~~~~~~~~~~~~~~~~~~~~~~~~~~~~
c  Tallies
c ~~~~~~~~~~~~~~~~~~~~~~~~~~~~~~~~
```

PAHN Plate Experiment with Stilbene

```
Stilbene scintillator measurement of PAHN plate
c
c Cell Card
c
c Detectors
c
100 5 -1.16  -13  imp:n,p=1   $ stilbene
c Source
c
200 7 -15.08  -700  imp:n,p=1   $ PAHN plate
201 8  -8.00  700 -701  imp:n,p=1   $ cladding
```

```
c
c Holder
c
850  6  -2.7  -800 IMP:N,P=1 $left holder
851  6  -2.7  -801 IMP:N,P=1 $right holder
852  6  -2.7  -802 IMP:N,P=1 $bottom
c
c Measurement Geometry
c
c 300 2 -11.34  -51 50 imp:n,p=1  $ Pb ring
998 1 -0.001 -99 13 701 800 801 802 imp:n,p=1 $ air
999 0         99             imp:n,p=0 $ The Void
c
c Blank line follows

c Surface Card
c
c Detectors
c
13 rcc -49.45875  0 0 -5.08  0 0 2.54  $ stilbene
c
c Sample
c
700  RPP -0.14097 0.14097  -2.52222 2.52222 -3.17 3.17        $core
701  RPP -0.15875 0.15875  -2.54    2.54    -3.81 3.81        $cladding
c
c Lead rings
c
c 50 rcc 0 0 -4.5  0  0  9  3.6
c 51 rcc 0 0 -4.5  0  0  9  5.25
c
c Source holder
```

```
c
800    RPP    -0.95875    -0.15875  -4    4       -3.81  6  $ left
801    RPP     0.15875     0.95875   -4    4       -3.81  6   $ right
802    RPP      -6      6           -6    6       -4.81 -3.81   $ bottom
c
99 rpp -60 10 -10 10 -10 10 $ air box
c
c Blank Line Follows

c Data Card
c
C      Materials
m1      8016.70c   0.16
        7014.70c   0.84
        plib=04p            $ air
c
m2      82000.42c  1
        plib=04p            $ Pb
c
m5     1001      .4615
       6000      .5385
        plib=04p            $ stilbene scintillator
m6     13027     1
       nlib=60c  plib=04p
c ~~~~~~~~~~~~~~~~~~~~~~~~~~~~~~~~
c  PAHN Plates
c ~~~~~~~~~~~~~~~~~~~~~~~~~~~~~~~~
m7    nlib=66c $pu rho 15.08 g/cm3
       94239   -0.73758
       94240   -0.22139
       94241   -0.00599
       94242   -0.00622
```

```
        95241   -0.01729
        13027   -0.01153
m8    nlib=66c  $cladding rho 8 g/cm3
        26054  -0.04074
        26056  -0.63953
        26057  -0.01477
        26058  -0.00197
        24050  -0.00799
        24052  -0.15417
        24053  -0.01748
        24054  -0.00435
        28058  -0.06059
        28060  -0.02334
        28061  -0.00101
        28062  -0.00323
        28064  -0.00082
        25055  -0.017
        6000   -0.012
C
SDEF cel=200  pos=0 0 0 axs=0 0 1 rad=d1 ext=d2
SI1  0 3.8
SI2  -3.17  3.17
SI3  L 3 4 38 39 40 41
SP3  0.2426 0.0680 0.2598 0.0483 0.0724 0.3090
C       The following two PHYS cards are essential for analog MC
PHYS:N  J     20  $ increase to highest source energy for PoliMi
PHYS:P  J     1
CUT:N   2J    0
CUT:P   2J    0
PRDMP 2J 1
DBCN
IPOL   3 1 2 1 J 1 1 100
```

```
RPOL   .001 .001

NPS    1e8

MODE n p

FILES  21  DUMN1

PRINT

c Tallies

F1:N  13.2

E1 .01 .1 1 2 3 5 10 100

C1  0 1

F11:P 13.2

E11 0 99i 10

C11 0 1
```

^{252}Cf Cross-Correlation Experiment with Stilbene

```
Stilbene Cf Cross-Correlation Measurement

c CELL CARDS

10 3 -7.872 -100 IMP:N,P=1 $Steel Table

20 5 -1.16 -200 201 202 203 204 IMP:N,P=1 $Bottom Stilbene

30 5 -1.16 -300 301 302 303 304 IMP:N,P=1 $Top Stilbene

98 0 (-999 200 300 100):-201:-202:-203:-204 IMP:N,P=1 $Inside Universe

99 0 999 IMP:N,P=0 $Outside Universe

c END CELL CARDS - BLANK LINE FOLLOWS


c SURFACE CARDS

100 RPP 32.54 97.62  0 130.16  -.5 0 $Table

200 RPP 62.8787 67.281214  40 45.08  7.57648835 12.42351165 $Bottom Stilbene
Box

201 WED 62.8787 40 7.57648835  1.442075 0 0  0 0 1.2371  0 5.08 0 $Bottom
Left Stilbene vacuum

202 WED 62.8787 40 12.42351165 1.194188 0 0  0 0 -1.2099233  0 5.08 0 $Top
Left Stilbene vacuum

203 WED 67.281214 40 7.57648835   -1.360353 0 0  0 0 1.599824  0 5.08 0
$Bottom Right Stilbene vacuum

204 WED 67.281214 40 12.42351165  -1.32974 0 0  0 0 -1.21316  0 5.08 0 $Top
Right Stilbene vacuum
```

```
300 RCC 65.08 85.08 10  0 5.08 0  2.54 $Top Stilbene (approximate as
cylinder)

999 RPP 0 130.16  0 130.16  -.51 13 $Universe

c END SURFACE CARDS - BLANK LINE FOLLOWS


c DATA CARDS

MODE  N P

NPS  1e8

PRINT 10 40 50 100 110 126 140 160

PHYS:N  J     20  $ increase to highest source energy for PoliMi

PHYS:P  J     1

CUT:N   2J    0

CUT:P   2J    0

PRDMP 2J 1

DBCN

c

c POLIMI CARDS

IPOL  1 0 2 1 J 2 2 20 30

RPOL  0.001 0.001

FILES  21  DUMN1

c

c VARIANCE REDUCTION

c SOURCE SPECIFICATION

SDEF  POS=65.08 65.08 10

c

c MATERIAL SPECIFICATION

c    ZZAAA.XXc    atom_fraction OR -mass_fraction

c    zaid number followed by available neutron library, use atom ratio or
mass fraction of each isotope

c    PLIB = 04p, NLIB = XXc assigns ALL isotopes with library

m1      1001.66c   0.555

        6000.70c   0.445

        plib=04p            $ EJ-309 liquid scintillator
```

```
M2   13027 1.0000          $ Al casing
     NLIB = 60c  PLIB = 04p
M3   6000   -.0006          $ Steel
     25055  -.0035
     26054  -.05676
     26056  -.9149
     26057  -.02132
     26058  -.00289
     NLIB = 60c  PLIB = 04p
M4   1001.66c   0.514       $ Plastic Scintillator
     6000.70c   0.486
     PLIB = 04p
M5   1001.70c  .4618        $ Stilbene
     6012.42c  .5382
     PLIB = 04p
c TALLY SPECIFICATION
c END OF FILE
```

^{252}Cf Cross-Correlation Experiment with EJ-309 and EJ-299-33

```
EJ-309+EJ-299-33 Cf252 CROSS-CORRELATION Measurement
c CELL CARDS
10 3 -7.873 -100 IMP:N,P=1 $Steel Table
c 20 2 -2.7 -200 204 IMP:N,P=1 $Aluminum Casing Left
c 21 2 -2.7 -201 205 IMP:N,P=1 $Aluminum Casing Right
22 2 -2.7 -202 206 IMP:N,P=1 $Aluminum Casing Bottom
23 2 -2.7 -203 207 IMP:N,P=1 $Aluminum Casing Top
c 24 1 -.935 -204 IMP:N,P=1 $Scintillator Left
c 25 1 -.935 -205 IMP:N,P=1 $Scintillator Right
26 4 -1.08 -206 IMP:N,P=1 $Scintillator Bottom
27 4 -1.08 -207 IMP:N,P=1 $Scintillator Top
c
c EJ-309 complex model
c Left EJ-309
```

```
102 2  -2.7  -10  11 -22      IMP:N,P=1  $ Al cap front
101 2  -2.7  -11 -22  23  12  IMP:N,P=1  $ Al cap sides
24  1  -.935 -11 -23  13 #110 IMP:N,P=1  $ EJ-309 scintillator, left
103 2  -2.7  -12  13 -26  23  IMP:N,P=1  $ Al step
104 2  -2.7  -13  14 -27  23  IMP:N,P=1  $ Al ring
105 6 -8.747 -14  15 -25  24  IMP:N,P=1  $ large PMT
106 6 -8.747 -16  20 -28  30 imp:n,p=1 $ skinny PMT front, mu metal
107 1 -2.70  -20  19 -28  29 imp:n,p=1 $ skinny PMT middle
108 1 -2.70  -19  21 -28     imp:n,p=1 $ skinny PMT cap
109 6 -8.747  18 -17  16 -15 imp:n,p=1 $ cone
110 5 -2.23  -31 -32  13     imp:n,p=1 $ pyrex optical window
c Right EJ-309
112 2  -2.7   40 -41 -22      IMP:N,P=1  $ Al cap front
111 2  -2.7   41 -22  23 -42  IMP:N,P=1  $ Al cap sides
25  1  -.935  41 -23 -43 #120 IMP:N,P=1  $ EJ-309 scintillator, left
113 2  -2.7   42 -43 -26  23  IMP:N,P=1  $ Al step
114 2  -2.7   43 -44 -27  23  IMP:N,P=1  $ Al ring
115 6 -8.747  44 -45 -25  24  IMP:N,P=1  $ large PMT
116 6 -8.747  46 -50 -28  30 imp:n,p=1 $ skinny PMT front, mu metal
117 1 -2.70   50 -49 -28  29 imp:n,p=1 $ skinny PMT middle
118 1 -2.70   49 -51 -28  49 imp:n,p=1 $ skinny PMT cap
119 6 -8.747  48 -47 -46  45 imp:n,p=1 $ cone
120 5 -2.23  -31  52 -43     imp:n,p=1 $ pyrex optical window
c
98 0         -999 #10 #22 #23 #24 #25 #26 #27 #101 #102 #103 #104 #105 #106
       #107 #108 #109 #110 #111 #112 #113 #114 #115 #116 #117 #118 #119 #120
       IMP:N,P=1 $Inside Universe
99 0          999 IMP:N,P=0 $Outside Universe
c
c
c END CELL CARDS - BLANK LINE FOLLOWS
```

```
c SURFACE CARDS
100 RPP  -76.2 76.2   -54.5 97.9   -11.8 -11.5       $ My Steel Table
c 200 RCC  -20  0  0            -7.73  0  0     3.9625 $ My Left Detector
c 201 RCC   20  0  0             7.73  0  0     3.9625 $ My Right Detector
202 RCC   0 -20  0             0 -7.73  0     3.9625 $ My Bottom Detector
203 RCC   0  20  0             0  7.73  0     3.9625 $ My Top Detector
c 204 RCC  -20.152 0  0          -7.426 0  0    3.8105 $ My Left EJ309
Scintillator
c 205 RCC   20.152 0  0           7.426 0  0    3.8105 $ My Right EJ309
Scintillator
206 RCC   0 -20.152 0          0 -7.426  0    3.8105 $ My Bottom EJ299
Scintillator
207 RCC   0  20.152 0          0  7.426  0    3.8105 $ My Top EJ299
Scintillator
c
c EJ-309 complex model
c
10 px -20.      $ front outer scint
11 px -20.152   $ front inner wall
12 px -27.09    $ scint step
13 px -27.73    $ ring front
14 px -30.71   $ large PMT start
15 px -36.07   $ large PMT end
16 px -37.2425 $ skinny PMT start outer
17 kx -40.068032787 1.082664654 1
18 kx -39.970388525 1.082664654 1
19 px -51.4875 $ skinny PMT end cap
20 px -47.0425 $ skinny PMT middle
21 px -52.44   $ PMT outer back
22 cx 3.9625  $ outer wall scint
23 cx 3.8105  $ inner wall scint
24 cx 4.0584  $ inner large PMT
25 cx 4.16    $ outer large PMT
26 cx 4.52125 $ outer scint step
```

```
27 cx 5.08    $ outer ring
28 cx 2.94    $ outer skinny PMT
29 cx 2.74    $ inner skinny PMT middle
30 cx 2.8384  $ inner skinny PMT front, mu metal
31 cx 3.3     $ optical window (guessed)
32 px -27.5     $ optical window front (guessed)
40 px 20.      $ front outer scint
41 px 20.152   $ front inner wall
42 px 27.09    $ scint step
43 px 27.73    $ ring front
44 px 30.71   $ large PMT start
45 px 36.07   $ large PMT end
46 px 37.2425 $ skinny PMT start outer
47 kx 40.068032787 1.082664654 -1
48 kx 39.970388525 1.082664654 -1
49 px 51.4875 $ skinny PMT end cap
50 px 47.0425 $ skinny PMT middle
51 px 52.44   $ PMT outer back
52 px 27.5     $ optical window front (guessed)
999 RPP  -78 78        -56 100       -13 10          $ My Universe, Touches
bottom of table to top of aluminum case / Left of table to right of table
c END SURFACE CARDS - BLANK LINE FOLLOWS


c DATA CARDS
MODE  N P
NPS  2e7
PRINT 10 40 50 100 110 126 140 160
PHYS:N  J     20  $ increase to highest source energy for PoliMi
PHYS:P  J     1
CUT:N   2J    0
CUT:P   2J    0
PRDMP 2J 1
DBCN
```

```
C
c POLIMI CARDS
IPOL  1 0 2 1 J 2 4 24 25 26 27
RPOL  0.001 0.001
FILES  21  DUMN1
C
c VARIANCE REDUCTION
c SOURCE SPECIFICATION
SDEF  POS=0 0 0
C
c MATERIAL SPECIFICATION
m1      1001.66c   0.555
        6000.70c   0.445
        plib=04p            $ EJ-309 liquid scintillator
M2   13027 1.0000           $ Al casing
     NLIB = 60c  PLIB = 04p
M3   6000.70c   -.0006          $ Steel
       25055  -.0035
       26054  -.05676
       26056  -.9149
       26057  -.02132
       26058  -.00289
     NLIB = 60c  PLIB = 04p
M4   1001.66c   0.514       $ Plastic Scintillator
       6000.70c   0.486
       PLIB = 04p
M5     5011.70c  -0.040064
       8016.70c  -0.539562
       11023.70c  -0.028191
       13027.70c  -0.011644
       14000.21c  -0.377220
       19000.66c  -0.003321
```

```
       PLIB = 04p           $ pyrex
M6     28000.50c   0.8
       42000.66c   0.05
       14000.21c   0.005
       29063.70c   0.0002
       26056.70c   0.1448
       PLIB = 04p           $ mu-metal
c
c TALLY SPECIFICATION
c END OF FILE
```

ENEA-01 MOX Cross-Correlation Experiment with EJ-309 and EJ-299-33

```
c DNNG FMMC: MOX 1 with 1 cm Pb
c ~~~~~~~~~~~~~~~~~~~~~~~~~~~~~~~~~
c  Cells
c ~~~~~~~~~~~~~~~~~~~~~~~~~~~~~~~~~
c   EJ-299 Detector Cells
c ~~~~~~~~~~~~~~~~~~~~~~~~~~~~~~~~~
  110   9  -1.080    -20           imp:N,P=1   $ detector
  114   9  -1.080    -24           imp:N,P=1   $ detector
c   116   1  -.935     -26           imp:N,P=1   $ detector
c ~~~~~~~~~~~~~~~~~~~~~~~~~~~~~~~~~
c   EJ-309 Detector Cells
c ~~~~~~~~~~~~~~~~~~~~~~~~~~~~~~~~~
  c Al cap front
  1000  5  -2.7    200 -210 -350   imp:N,P=1
  1001  5  -2.7    201 -211 -351   imp:N,P=1
  1002  5  -2.7    202 -212 -352   imp:N,P=1
  1003  5  -2.7    203 -213 -353   imp:N,P=1
  1004  5  -2.7    204 -214 -354   imp:N,P=1
  1005  5  -2.7    205 -215 -355   imp:N,P=1
  1006  5  -2.7    200 -210 -356   imp:N,P=1
  1007  5  -2.7    201 -211 -357   imp:N,P=1
```

```
1008  5  -2.7    202 -212 -358   imp:N,P=1
1009  5  -2.7    203 -213 -359   imp:N,P=1
1010  5  -2.7    204 -214 -360   imp:N,P=1
1011  5  -2.7    205 -215 -361   imp:N,P=1
c Al cap sides
1015  5  -2.7    210 -220 -350  365   imp:N,P=1
1016  5  -2.7    211 -221 -351  366   imp:N,P=1
1017  5  -2.7    212 -222 -352  367   imp:N,P=1
1018  5  -2.7    213 -223 -353  368   imp:N,P=1
1019  5  -2.7    214 -224 -354  369   imp:N,P=1
1020  5  -2.7    215 -225 -355  370   imp:N,P=1
1021  5  -2.7    210 -220 -356  371   imp:N,P=1
1022  5  -2.7    211 -221 -357  372   imp:N,P=1
1023  5  -2.7    212 -222 -358  373   imp:N,P=1
1024  5  -2.7    213 -223 -359  374   imp:N,P=1
1025  5  -2.7    214 -224 -360  375   imp:N,P=1
1026  5  -2.7    215 -225 -361  376   imp:N,P=1
c detector 101 103 104 105 107 108 109 110 111 112 113 114 115 116
101   1  -.935   210 -230 -365 #1135  imp:N,P=1
103   1  -.935   211 -231 -366 #1136  imp:N,P=1
104   1  -.935   212 -232 -367 #1137  imp:N,P=1
105   1  -.935   213 -233 -368 #1138  imp:N,P=1
107   1  -.935   214 -234 -369 #1139  imp:N,P=1
108   1  -.935   215 -235 -370 #1140  imp:N,P=1
109   1  -.935   210 -230 -371 #1141  imp:N,P=1
111   1  -.935   211 -231 -372 #1142  imp:N,P=1
112   1  -.935   212 -232 -373 #1143  imp:N,P=1
113   1  -.935   213 -233 -374 #1144  imp:N,P=1
115   1  -.935   214 -234 -375 #1145  imp:N,P=1
116   1  -.935   215 -235 -376 #1146  imp:N,P=1
c Al step
1030  5  -2.7    220 -230 -410  365   imp:N,P=1
```

```
  1031  5  -2.7    221 -231 -411  366   imp:N,P=1
  1032  5  -2.7    222 -232 -412  367   imp:N,P=1
  1033  5  -2.7    223 -233 -413  368   imp:N,P=1
  1034  5  -2.7    224 -234 -414  369   imp:N,P=1
  1035  5  -2.7    225 -235 -415  370   imp:N,P=1
  1036  5  -2.7    220 -230 -416  371   imp:N,P=1
  1037  5  -2.7    221 -231 -417  372   imp:N,P=1
  1038  5  -2.7    222 -232 -418  373   imp:N,P=1
  1039  5  -2.7    223 -233 -419  374   imp:N,P=1
  1040  5  -2.7    224 -234 -420  375   imp:N,P=1
  1041  5  -2.7    225 -235 -421  376   imp:N,P=1
  c Al ring
  1045  5  -2.7    230 -240 -425  365   imp:N,P=1
  1046  5  -2.7    231 -241 -426  366   imp:N,P=1
  1047  5  -2.7    232 -242 -427  367   imp:N,P=1
  1048  5  -2.7    233 -243 -428  368   imp:N,P=1
  1049  5  -2.7    234 -244 -429  369   imp:N,P=1
  1050  5  -2.7    235 -245 -430  370   imp:N,P=1
  1051  5  -2.7    230 -240 -431  371   imp:N,P=1
  1052  5  -2.7    231 -241 -432  372   imp:N,P=1
  1053  5  -2.7    232 -242 -433  373   imp:N,P=1
  1054  5  -2.7    233 -243 -434  374   imp:N,P=1
  1055  5  -2.7    234 -244 -435  375   imp:N,P=1
  1056  5  -2.7    235 -245 -436  376   imp:N,P=1
  c large PMT
c  1060 10  -8.747  240 -250 -395  380   imp:N,P=1
c  1061 10  -8.747  241 -251 -396  381   imp:N,P=1
c  1062 10  -8.747  242 -252 -397  382   imp:N,P=1
c  1063 10  -8.747  243 -253 -398  383   imp:N,P=1
c  1064 10  -8.747  244 -254 -399  384   imp:N,P=1
c  1065 10  -8.747  245 -255 -400  385   imp:N,P=1
c  1066 10  -8.747  240 -250 -401  386   imp:N,P=1
```

```
c  1067 10  -8.747  241 -251 -402  387   imp:N,P=1
c  1068 10  -8.747  242 -252 -403  388   imp:N,P=1
c  1069 10  -8.747  243 -253 -404  389   imp:N,P=1
c  1070 10  -8.747  244 -254 -405  390   imp:N,P=1
c  1071 10  -8.747  245 -255 -406  391   imp:N,P=1
  c skinny PMT front, mu metal
c  1075 10  -8.747  260 -320 -440  470   imp:N,P=1
c  1076 10  -8.747  261 -321 -441  471   imp:N,P=1
c  1077 10  -8.747  262 -322 -442  472   imp:N,P=1
c  1078 10  -8.747  263 -323 -443  473   imp:N,P=1
c  1079 10  -8.747  264 -324 -444  474   imp:N,P=1
c  1080 10  -8.747  265 -325 -445  475   imp:N,P=1
c  1081 10  -8.747  260 -320 -446  476   imp:N,P=1
c  1082 10  -8.747  261 -321 -447  477   imp:N,P=1
c  1083 10  -8.747  262 -322 -448  478   imp:N,P=1
c  1084 10  -8.747  263 -323 -449  479   imp:N,P=1
c  1085 10  -8.747  264 -324 -450  480   imp:N,P=1
c  1086 10  -8.747  265 -325 -451  481   imp:N,P=1
  c skinny PMT middle
c  1090  5  -2.7    320 -310 -440  455   imp:N,P=1
c  1091  5  -2.7    321 -311 -441  456   imp:N,P=1
c  1092  5  -2.7    322 -312 -442  457   imp:N,P=1
c  1093  5  -2.7    323 -313 -443  458   imp:N,P=1
c  1094  5  -2.7    324 -314 -444  459   imp:N,P=1
c  1095  5  -2.7    325 -315 -445  460   imp:N,P=1
c  1096  5  -2.7    320 -310 -446  461   imp:N,P=1
c  1097  5  -2.7    321 -311 -447  462   imp:N,P=1
c  1098  5  -2.7    322 -312 -448  463   imp:N,P=1
c  1099  5  -2.7    323 -313 -449  464   imp:N,P=1
c  1100  5  -2.7    324 -314 -450  465   imp:N,P=1
c  1101  5  -2.7    325 -315 -451  466   imp:N,P=1
  c skinny PMT cap
```

```
c  1105  5  -2.7    310 -330 -440        imp:N,P=1
c  1106  5  -2.7    311 -331 -441        imp:N,P=1
c  1107  5  -2.7    312 -332 -442        imp:N,P=1
c  1108  5  -2.7    313 -333 -443        imp:N,P=1
c  1109  5  -2.7    314 -334 -444        imp:N,P=1
c  1110  5  -2.7    315 -335 -445        imp:N,P=1
c  1111  5  -2.7    310 -330 -446        imp:N,P=1
c  1112  5  -2.7    311 -331 -447        imp:N,P=1
c  1113  5  -2.7    312 -332 -448        imp:N,P=1
c  1114  5  -2.7    313 -333 -449        imp:N,P=1
c  1115  5  -2.7    314 -334 -450        imp:N,P=1
c  1116  5  -2.7    315 -335 -451        imp:N,P=1
  c cone
c  1120 10  -8.747  290 -270 -260  250   imp:N,P=1
c  1121 10  -8.747  291 -271 -261  251   imp:N,P=1
c  1122 10  -8.747  292 -272 -262  252   imp:N,P=1
c  1123 10  -8.747  293 -273 -263  253   imp:N,P=1
c  1124 10  -8.747  294 -274 -264  254   imp:N,P=1
c  1125 10  -8.747  295 -275 -265  255   imp:N,P=1
c  1126 10  -8.747  296 -276 -260  250   imp:N,P=1
c  1127 10  -8.747  297 -277 -261  251   imp:N,P=1
c  1128 10  -8.747  298 -278 -262  252   imp:N,P=1
c  1129 10  -8.747  299 -279 -263  253   imp:N,P=1
c  1130 10  -8.747  300 -280 -264  254   imp:N,P=1
c  1131 10  -8.747  301 -281 -265  255   imp:N,P=1
  c pyrex optical window
  1135 11  -2.23   340 -230 -485        imp:N,P=1
  1136 11  -2.23   341 -231 -486        imp:N,P=1
  1137 11  -2.23   342 -232 -487        imp:N,P=1
  1138 11  -2.23   343 -233 -488        imp:N,P=1
  1139 11  -2.23   344 -234 -489        imp:N,P=1
  1140 11  -2.23   345 -235 -490        imp:N,P=1
```

```
  1141 11  -2.23   340 -230 -491        imp:N,P=1
  1142 11  -2.23   341 -231 -492        imp:N,P=1
  1143 11  -2.23   342 -232 -493        imp:N,P=1
  1144 11  -2.23   343 -233 -494        imp:N,P=1
  1145 11  -2.23   344 -234 -495        imp:N,P=1
  1146 11  -2.23   345 -235 -496        imp:N,P=1
c ~~~~~~~~~~~~~~~~~~~~~~~~~~~~~~~~~~
c   Table
c ~~~~~~~~~~~~~~~~~~~~~~~~~~~~~~~~~~
  201   5  -2.7      -31           imp:n,p=1   $ Surface
  206   5  -2.7      -32           imp:n,p=1   $ Support
  207   5  -2.7      -33           imp:n,p=1   $ Support
  208   5  -2.7      -34           imp:n,p=1   $ Support
  209   5  -2.7      -35           imp:n,p=1   $ Support
  215   5  -2.7      -36           imp:n,p=1   $ Leg
  216   5  -2.7      -37           imp:n,p=1   $ Leg
  218   5  -2.7      -38           imp:n,p=1   $ Leg
  219   5  -2.7      -39           imp:n,p=1   $ Leg
  220   5  -2.7      -40           imp:n,p=1   $ Leg
  221   5  -2.7      -41           imp:n,p=1   $ Leg
  222   8  -7.92     -42           imp:n,p=1   $ source stand
c ~~~~~~~~~~~~~~~~~~~~~~~~~~~~~~~~~~
c   Detector Structure
c ~~~~~~~~~~~~~~~~~~~~~~~~~~~~~~~~~~
  300   5  -2.7      -90 350 356     imp:N,P=1   $ front plate
  301   5  -2.7      -91 410 416     imp:N,P=1   $ back plate
c   302   5  -2.7      -92 20     imp:N,P=1   $ front plate
c   303   5  -2.7      -93 20     imp:N,P=1   $ back plate
  304   5  -2.7      -94 351 357     imp:N,P=1   $ front plate
  305   5  -2.7      -95 411 417     imp:N,P=1   $ back plate
  306   5  -2.7      -96 352 358     imp:N,P=1   $ front plate
  307   5  -2.7      -97 412 418     imp:N,P=1   $ back plate
```

```
  308   5  -2.7      -98 353 359     imp:N,P=1   $ front plate
  309   5  -2.7      -99 413 419     imp:N,P=1   $ back plate
c   310   5  -2.7     -100 24     imp:N,P=1   $ front plate
c   311   5  -2.7     -101 24     imp:N,P=1   $ back plate
  312   5  -2.7     -102 354 360     imp:N,P=1   $ front plate
  313   5  -2.7     -103 414 420     imp:N,P=1   $ back plate
  314   5  -2.7     -104 355 361     imp:N,P=1   $ front plate
  315   5  -2.7     -105 415 421     imp:N,P=1   $ back plate
  316   5  -2.7 -106:-110:-112:
               -114:-118:-120 imp:N,P=1  $ bottom bar
  317   5  -2.7 -107:-111:-113:
               -115:-119:-121 imp:N,P=1  $ top bar
c ~~~~~~~~~~~~~~~~~~~~~~~~~~~~~~~~~~
c   Lead Shielding
c ~~~~~~~~~~~~~~~~~~~~~~~~~~~~~~~~~~
  501   3 -11.34     -51 76 -84 52 imp:N,P=1   $lead shield
c ~~~~~~~~~~~~~~~~~~~~~~~~~~~~~~~~~~
c Ground
c ~~~~~~~~~~~~~~~~~~~~~~~~~~~~~~~~~~
  601   6  -2.3      -500 -61       imp:N,P=1   $ concrete floor
c ~~~~~~~~~~~~~~~~~~~~~~~~~~~~~~~~~~
c   MOX Source
c ~~~~~~~~~~~~~~~~~~~~~~~~~~~~~~~~~~
  701     0          -73 87 -82     imp:n,p=1  $vaccum on top of powder
  702     7   -0.7   -73 81 -87     imp:n,p=1  $MOX powder
  703     8   -7.92   73 -74 81 -82 imp:n,p=1  $inner steel cylinder
  704     8   -7.92  -74 80 -81     imp:n,p=1  $steel inner bottom
  705     8   -7.92  -74 82 -83     imp:n,p=1  $steel inner top
  706     0           74 -75 80 -83 imp:n,p=1  $surroundeing vacuum cylinder
  707     0          -75 79 -80     imp:n,p=1  $bottom vacuum
  708     0          -75 83 -84     imp:n,p=1  $top vacuum
  709     0          -72 84 -85     imp:n,p=1  $another top vacuum
```

```
  710     8   -7.92   75 -76 79 -84 imp:n,p=1  $outer steel cylinder
  711     8   -7.92  -76 89 -79     imp:n,p=1  $steel outer bottom
  712     8   -7.92   72 -77 84 -85 imp:n,p=1  $steel cylinder top
  713     8   -7.92  -77 85 -86     imp:n,p=1  $steel outer top
c ~~~~~~~~~~~~~~~~~~~~~~~~~~~~~~~~~
c  Environment
c ~~~~~~~~~~~~~~~~~~~~~~~~~~~~~~~~~
  901   2  -1.205E-3 -500 61 20 24 31 32 33 34 35 36 37 38
        39 40 41 42 90 91 94 95 96 97 98 99 102 103 104 105
        #316 #317 #713 (-52 :51 :84 ) (77 :-84 :86 )
        #101 #103 #104 #105 #107 #108 #109 #111 #112 #113 #115 #116
        #1000 #1001 #1002 #1003 #1004 #1005 #1006 #1007 #1008 #1009
        #1010 #1011 #1015 #1016 #1017 #1018 #1019 #1020 #1021 #1022
        #1023 #1024 #1025 #1026 #1030 #1031 #1032 #1033 #1034 #1035
        #1036 #1037 #1038 #1039 #1040 #1041 #1045 #1046 #1047 #1048
        #1049 #1050 #1051 #1052 #1053 #1054 #1055 #1056 imp:n,p=1
c #1060 #1061
c        #1062 #1063 #1064 #1065 #1066 #1067 #1068 #1069 #1070 #1071
c        #1075 #1076 #1077 #1078 #1079 #1080 #1081 #1082 #1083 #1084
c        #1085 #1086 #1090 #1091 #1092 #1093 #1094 #1095 #1096 #1097
c        #1098 #1099 #1100 #1101 #1105 #1106 #1107 #1108 #1109 #1110
c        #1111 #1112 #1113 #1114 #1115 #1116 #1120 #1121 #1122 #1123
c        #1124 #1125 #1126 #1127 #1128 #1129 #1130 #1131 #1135 #1136
c        #1137 #1138 #1139 #1140 #1141 #1142 #1143 #1144 #1145 #1146
  902   2  -1.205E-3 52 -76 -89     imp:n,p=1
  999   0    500                   imp:n,p=0

c ~~~~~~~~~~~~~~~~~~~~~~~~~~~~~~~~~
c  Surfaces
c ~~~~~~~~~~~~~~~~~~~~~~~~~~~~~~~~~
c   EJ-299 Detector cells
c ~~~~~~~~~~~~~~~~~~~~~~~~~~~~~~~~~
```

```
c 11   RCC    16.92  0   5.31        7.6200  0  0     4.52125
c 13 2 RCC    16.92  0   5.31        7.6200  0  0     4.52125
c 14 3 RCC    16.92  0   5.31        7.6200  0  0     4.52125
c 15 4 RCC    16.92  0   5.31        7.6200  0  0     4.52125
c 17 6 RCC    16.92  0   5.31        7.6200  0  0     4.52125
c 18 7 RCC    16.92  0   5.31        7.6200  0  0     4.52125
c 19   RCC    16.92  0  -5.31        7.6200  0  0     4.52125
20 1 RCC    16.92  0  -5.31        7.6200  0  0     3.8100
c 21 2 RCC    16.92  0  -5.31        7.6200  0  0     4.52125
c 22 3 RCC    16.92  0  -5.31        7.6200  0  0     4.52125
c 23 4 RCC    16.92  0  -5.31        7.6200  0  0     4.52125
24 5 RCC    16.92  0  -5.31        7.6200  0  0     3.8100
c 25 6 RCC    16.92  0  -5.31        7.6200  0  0     4.52125
c 26 7 RCC    16.92  0  -5.31        7.6200  0  0     4.52125
c ~~~~~~~~~~~~~~~~~~~~~~~~~~~~~~~~~
c   EJ-309 Detector model
c ~~~~~~~~~~~~~~~~~~~~~~~~~~~~~~~~~
c Front outer wall
  200   PX     16.768
  201 2 PX     16.768
  202 3 PX     16.768
  203 4 PX     16.768
  204 6 PX     16.768
  205 7 PX     16.768
c Front inner wall
  210   PX     16.92
  211 2 PX     16.92
  212 3 PX     16.92
  213 4 PX     16.92
  214 6 PX     16.92
  215 7 PX     16.92
c Scint step
```

```
  220   PX     23.858
  221 2 PX     23.858
  222 3 PX     23.858
  223 4 PX     23.858
  224 6 PX     23.858
  225 7 PX     23.858
c Ring front
  230   PX     24.498
  231 2 PX     24.498
  232 3 PX     24.498
  233 4 PX     24.498
  234 6 PX     24.498
  235 7 PX     24.498
c Large PMT start
  240   PX     27.478
  241 2 PX     27.478
  242 3 PX     27.478
  243 4 PX     27.478
  244 6 PX     27.478
  245 7 PX     27.478
c Large PMT end
c   250   PX     32.838
c   251 2 PX     32.838
c   252 3 PX     32.838
c   253 4 PX     32.838
c   254 6 PX     32.838
c   255 7 PX     32.838
c skinny PMT start outer
c  260   PX     34.0105
c  261 2 PX     34.0105
c  262 3 PX     34.0105
c  263 4 PX     34.0105
```

```
c  264 6 PX     34.0105
c  265 7 PX     34.0105
c cone, outer
c  270   K/X    36.836032787 0 -5.31 1.082664654 -1
c  271 2 K/X    36.836032787 0 -5.31 1.082664654 -1
c  272 3 K/X    36.836032787 0 -5.31 1.082664654 -1
c  273 4 K/X    36.836032787 0 -5.31 1.082664654 -1
c  274 6 K/X    36.836032787 0 -5.31 1.082664654 -1
c  275 7 K/X    36.836032787 0 -5.31 1.082664654 -1
c  276   K/X    36.836032787 0  5.31 1.082664654 -1
c  277 2 K/X    36.836032787 0  5.31 1.082664654 -1
c  278 3 K/X    36.836032787 0  5.31 1.082664654 -1
c  279 4 K/X    36.836032787 0  5.31 1.082664654 -1
c  280 6 K/X    36.836032787 0  5.31 1.082664654 -1
c  281 7 K/X    36.836032787 0  5.31 1.082664654 -1
c cone, inner
c  290   K/X    36.738388525 0 -5.31 1.082664654 -1
c  291 2 K/X    36.738388525 0 -5.31 1.082664654 -1
c  292 3 K/X    36.738388525 0 -5.31 1.082664654 -1
c  293 4 K/X    36.738388525 0 -5.31 1.082664654 -1
c  294 6 K/X    36.738388525 0 -5.31 1.082664654 -1
c  295 7 K/X    36.738388525 0 -5.31 1.082664654 -1
c  296   K/X    36.738388525 0  5.31 1.082664654 -1
c  297 2 K/X    36.738388525 0  5.31 1.082664654 -1
c  298 3 K/X    36.738388525 0  5.31 1.082664654 -1
c  299 4 K/X    36.738388525 0  5.31 1.082664654 -1
c  300 6 K/X    36.738388525 0  5.31 1.082664654 -1
c  301 7 K/X    36.738388525 0  5.31 1.082664654 -1
c skinny PMT end cap
c  310   PX     48.2555
c  311 2 PX     48.2555
c  312 3 PX     48.2555
```

```
c  313 4 PX     48.2555
c  314 6 PX     48.2555
c  315 7 PX     48.2555
c skinny PMT middle
c  320   PX     43.8105
c  321 2 PX     43.8105
c  322 3 PX     43.8105
c  323 4 PX     43.8105
c  324 6 PX     43.8105
c  325 7 PX     43.8105
c PMT outer back
c  330   PX     49.208
c  331 2 PX     49.208
c  332 3 PX     49.208
c  333 4 PX     49.208
c  334 6 PX     49.208
c  335 7 PX     49.208
c Optical window front
  340   PX     24.268
  341 2 PX     24.268
  342 3 PX     24.268
  343 4 PX     24.268
  344 6 PX     24.268
  345 7 PX     24.268
c Outer wall scintillator
  350   C/X   0  5.31 3.9625
  351 2 C/X   0  5.31 3.9625
  352 3 C/X   0  5.31 3.9625
  353 4 C/X   0  5.31 3.9625
  354 6 C/X   0  5.31 3.9625
  355 7 C/X   0  5.31 3.9625
  356   C/X   0 -5.31 3.9625
```

```
  357 2 C/X   0 -5.31 3.9625
  358 3 C/X   0 -5.31 3.9625
  359 4 C/X   0 -5.31 3.9625
  360 6 C/X   0 -5.31 3.9625
  361 7 C/X   0 -5.31 3.9625
c Inner wall scintillator
  365   C/X   0  5.31 3.8105
  366 2 C/X   0  5.31 3.8105
  367 3 C/X   0  5.31 3.8105
  368 4 C/X   0  5.31 3.8105
  369 6 C/X   0  5.31 3.8105
  370 7 C/X   0  5.31 3.8105
  371   C/X   0 -5.31 3.8105
  372 2 C/X   0 -5.31 3.8105
  373 3 C/X   0 -5.31 3.8105
  374 4 C/X   0 -5.31 3.8105
  375 6 C/X   0 -5.31 3.8105
  376 7 C/X   0 -5.31 3.8105
c Inner large PMT
c  380   C/X   0  5.31 4.0584
c  381 2 C/X   0  5.31 4.0584
c  382 3 C/X   0  5.31 4.0584
c  383 4 C/X   0  5.31 4.0584
c  384 6 C/X   0  5.31 4.0584
c  385 7 C/X   0  5.31 4.0584
c  386   C/X   0 -5.31 4.0584
c  387 2 C/X   0 -5.31 4.0584
c  388 3 C/X   0 -5.31 4.0584
c  389 4 C/X   0 -5.31 4.0584
c  390 6 C/X   0 -5.31 4.0584
c  391 7 C/X   0 -5.31 4.0584
c Outer Large PMT
```

```
c  395   C/X   0  5.31 4.16
c  396 2 C/X   0  5.31 4.16
c  397 3 C/X   0  5.31 4.16
c  398 4 C/X   0  5.31 4.16
c  399 6 C/X   0  5.31 4.16
c  400 7 C/X   0  5.31 4.16
c  401   C/X   0 -5.31 4.16
c  402 2 C/X   0 -5.31 4.16
c  403 3 C/X   0 -5.31 4.16
c  404 4 C/X   0 -5.31 4.16
c  405 6 C/X   0 -5.31 4.16
c  406 7 C/X   0 -5.31 4.16
c Outer Scintillator step
  410   C/X   0  5.31 4.52125
  411 2 C/X   0  5.31 4.52125
  412 3 C/X   0  5.31 4.52125
  413 4 C/X   0  5.31 4.52125
  414 6 C/X   0  5.31 4.52125
  415 7 C/X   0  5.31 4.52125
  416   C/X   0 -5.31 4.52125
  417 2 C/X   0 -5.31 4.52125
  418 3 C/X   0 -5.31 4.52125
  419 4 C/X   0 -5.31 4.52125
  420 6 C/X   0 -5.31 4.52125
  421 7 C/X   0 -5.31 4.52125
c Outer ring
  425   C/X   0  5.31 5.08
  426 2 C/X   0  5.31 5.08
  427 3 C/X   0  5.31 5.08
  428 4 C/X   0  5.31 5.08
  429 6 C/X   0  5.31 5.08
  430 7 C/X   0  5.31 5.08
```

```
  431   C/X   0 -5.31 5.08
  432 2 C/X   0 -5.31 5.08
  433 3 C/X   0 -5.31 5.08
  434 4 C/X   0 -5.31 5.08
  435 6 C/X   0 -5.31 5.08
  436 7 C/X   0 -5.31 5.08
c Outer skinny PMT
c  440   C/X   0  5.31 2.94
c  441 2 C/X   0  5.31 2.94
c  442 3 C/X   0  5.31 2.94
c  443 4 C/X   0  5.31 2.94
c  444 6 C/X   0  5.31 2.94
c  445 7 C/X   0  5.31 2.94
c  446   C/X   0 -5.31 2.94
c  447 2 C/X   0 -5.31 2.94
c  448 3 C/X   0 -5.31 2.94
c  449 4 C/X   0 -5.31 2.94
c  450 6 C/X   0 -5.31 2.94
c  451 7 C/X   0 -5.31 2.94
c Inner skinny PMT middle
c  455   C/X   0  5.31 2.74
c  456 2 C/X   0  5.31 2.74
c  457 3 C/X   0  5.31 2.74
c  458 4 C/X   0  5.31 2.74
c  459 6 C/X   0  5.31 2.74
c  460 7 C/X   0  5.31 2.74
c  461   C/X   0 -5.31 2.74
c  462 2 C/X   0 -5.31 2.74
c  463 3 C/X   0 -5.31 2.74
c  464 4 C/X   0 -5.31 2.74
c  465 6 C/X   0 -5.31 2.74
c  466 7 C/X   0 -5.31 2.74
```

```
c Inner skinny PMT front, mu metal
c  470   C/X   0  5.31 2.8384
c  471 2 C/X   0  5.31 2.8384
c  472 3 C/X   0  5.31 2.8384
c  473 4 C/X   0  5.31 2.8384
c  474 6 C/X   0  5.31 2.8384
c  475 7 C/X   0  5.31 2.8384
c  476   C/X   0 -5.31 2.8384
c  477 2 C/X   0 -5.31 2.8384
c  478 3 C/X   0 -5.31 2.8384
c  479 4 C/X   0 -5.31 2.8384
c  480 6 C/X   0 -5.31 2.8384
c  481 7 C/X   0 -5.31 2.8384
c Optical window
  485   C/X   0  5.31 3.3
  486 2 C/X   0  5.31 3.3
  487 3 C/X   0  5.31 3.3
  488 4 C/X   0  5.31 3.3
  489 6 C/X   0  5.31 3.3
  490 7 C/X   0  5.31 3.3
  491   C/X   0 -5.31 3.3
  492 2 C/X   0 -5.31 3.3
  493 3 C/X   0 -5.31 3.3
  494 4 C/X   0 -5.31 3.3
  495 6 C/X   0 -5.31 3.3
  496 7 C/X   0 -5.31 3.3
c ~~~~~~~~~~~~~~~~~~~~~~~~~~~~~~~~
c   Table
c ~~~~~~~~~~~~~~~~~~~~~~~~~~~~~~~~
  31 8 BOX  -50   -100   -0.5   100   0 0    0 200   0   0 0   0.5   $
Surface
  32 8 BOX  -50   -100   -4.9     4.4 0 0    0 200   0   0 0   4.4   $
Support
```

```
  33 8 BOX   45.6 -100   -4.9     4.4 0 0    0 200   0   0 0   4.4   $
Support
  34 8 BOX  -45.6 -100   -4.9    91.2 0 0    0   4.4 0   0 0   4.4   $
Support
  35 8 BOX  -45.6   95.6 -4.9    91.2 0 0    0   4.4 0   0 0   4.4   $
Support
  36 8 BOX  -50     -2.2 -4.9     4.4 0 0    0   4.4 0   0 0 -85.5   $ Leg
  37 8 BOX   45.6   -2.2 -4.9     4.4 0 0    0   4.4 0   0 0 -85.5   $ Leg
  38 8 BOX  -50   -100   -4.9     4.4 0 0    0   4.4 0   0 0 -85.5   $ Leg
  39 8 BOX   45.6 -100   -4.9     4.4 0 0    0   4.4 0   0 0 -85.5   $ Leg
  40 8 BOX  -50     95.6 -4.9     4.4 0 0    0   4.4 0   0 0 -85.5   $ Leg
  41 8 BOX   45.6   95.6 -4.9     4.4 0 0    0   4.4 0   0 0 -85.5   $ Leg
  42   RCC   0 0 -17.25  0 0 1      8.5
c ~~~~~~~~~~~~~~~~~~~~~~~~~~~~~~~~~
c   Lead Shielding
c ~~~~~~~~~~~~~~~~~~~~~~~~~~~~~~~~~
  51   CZ   6.4        $outer cylinder
  52   PZ  -16.25      $bottom of Pb
c ~~~~~~~~~~~~~~~~~~~~~~~~~~~~~~~~~
c Ground
c ~~~~~~~~~~~~~~~~~~~~~~~~~~~~~~~~~
  61 PZ     -108   $ Floor level
c ~~~~~~~~~~~~~~~~~~~~~~~~~~~~~~~~~
c MOX Source Container
c ~~~~~~~~~~~~~~~~~~~~~~~~~~~~~~~~~
  72 9 CZ   5.1        $Support cylinder outer and upper empty space cylinder
  73 9 CZ   4.14       $inner contaner cylinder inner wall
  74 9 CZ   4.445      $inner container cylinder outer wall
  75 9 CZ   5.2        $outer container cylinder inner wall
  76 9 CZ   5.4        $outer container cylinder outer wall
  77 9 CZ   6.75       $top steel cylinder
  79 9 PZ  -14.0982    $outer container - BOTTOM
  80 9 PZ  -13.8982    $inner container outer surf
  81 9 PZ  -13.3982    $inner container inner surf
```

```
  82 9 PZ   13.4018    $inner container inner surf

  83 9 PZ   13.9018    $inner container outer surf

  84 9 PZ   14.1018    $outer container

  85 9 PZ   16.1018    $outer container

  86 9 PZ   18.1018    $outer container

  87 9 PZ   13.4017    $top of PuO powder

  89 9 PZ  -15.0982    $bottom

c ~~~~~~~~~~~~~~~~~~~~~~~~~~~~~~~~

c  Detector Structure

c ~~~~~~~~~~~~~~~~~~~~~~~~~~~~~~~~

  90   RPP  22      22.3175   -5.10     5.10   -17.25  13.35   $front
vertical plate

  91   RPP  24.1805 24.498    -5.10     5.10   -17.25  13.35   $back vertical
plate

c   92 1 RPP  22      22.3175   -5.05     5.05   -17.25  13.35   $front
vertical plate

c   93 1 RPP  24.1805 24.498    -5.05     5.05   -17.25  13.35   $back
vertical plate

  94 2 RPP  22      22.3175   -5.10     5.10   -17.25  13.35   $front
vertical plate

  95 2 RPP  24.1805 24.498    -5.10     5.10   -17.25  13.35   $back vertical
plate

  96 3 RPP  22      22.3175   -5.10     5.10   -17.25  13.35   $front
vertical plate

  97 3 RPP  24.1805 24.498    -5.10     5.10   -17.25  13.35   $back vertical
plate

  98 4 RPP  22      22.3175   -5.10     5.10   -17.25  13.35   $front
vertical plate

  99 4 RPP  24.1805 24.498    -5.10     5.10   -17.25  13.35   $back vertical
plate

c  100 5 RPP  22      22.3175   -5.05     5.05   -17.25  13.35   $front
vertical plate

c  101 5 RPP  24.1805 24.498    -5.05     5.05   -17.25  13.35   $back
vertical plate

 102 6 RPP  22      22.3175   -5.10     5.10   -17.25  13.35   $front
vertical plate

 103 6 RPP  24.1805 24.498    -5.10     5.10   -17.25  13.35   $back vertical
plate

 104 7 RPP  22      22.3175   -5.10     5.10   -17.25  13.35   $front
vertical plate
```

```
 105 7 RPP  24.1805 24.498    -5.10     5.10   -17.25  13.35   $back vertical
plate
 106   RPP  22.3176 24.1805   -10.0333 10.0333 -17.25 -15.345  $bottom bar
 107   RPP  22.3176 24.1805   -10.0333 10.0333  11.445 13.35   $top bar
c  108 1 RPP  22.3176 24.1805   -10.0333 10.0333 -17.25 -15.345  $bottom bar
c  109 1 RPP  22.3176 24.1805   -10.0333 10.0333  11.445 13.35   $top bar
 110 2 RPP  22.3176 24.1805   -10.0333 10.0333 -17.25 -15.345  $bottom bar
 111 2 RPP  22.3176 24.1805   -10.0333 10.0333  11.445 13.35   $top bar
 112 3 RPP  22.3176 24.1805   -10.0333 10.0333 -17.25 -15.345  $bottom bar
 113 3 RPP  22.3176 24.1805   -10.0333 10.0333  11.445 13.35   $top bar
 114 4 RPP  22.3176 24.1805   -10.0333 10.0333 -17.25 -15.345  $bottom bar
 115 4 RPP  22.3176 24.1805   -10.0333 10.0333  11.445 13.35   $top bar
c  116 5 RPP  22.3176 24.1805   -10.0333 10.0333 -17.25 -15.345  $bottom bar
c  117 5 RPP  22.3176 24.1805   -10.0333 10.0333  11.445 13.35   $top bar
 118 6 RPP  22.3176 24.1805   -10.0333 10.0333 -17.25 -15.345  $bottom bar
 119 6 RPP  22.3176 24.1805   -10.0333 10.0333  11.445 13.35   $top bar
 120 7 RPP  22.3176 24.1805   -10.0333 10.0333 -17.25 -15.345  $bottom bar
 121 7 RPP  22.3176 24.1805   -10.0333 10.0333  11.445 13.35   $top bar
c ~~~~~~~~~~~~~~~~~~~~~~~~~~~~~~~~
c  Environment
c ~~~~~~~~~~~~~~~~~~~~~~~~~~~~~~~~
 500 RPP -500 500   -500 500   -500 500


c ~~~~~~~~~~~~~~~~~~~~~~~~~~~~~~~~
c Data
c ~~~~~~~~~~~~~~~~~~~~~~~~~~~~~~~~
c Translations
c ~~~~~~~~~~~~~~~~~~~~~~~~~~~~~~~~
  TR1  0 0 0   0.7071  0.7071  0   -0.7071  0.7071  0   0  0  1
  TR2  0 0 0   0       1       0   -1       0       0   0  0  1
  TR3  0 0 0  -0.7071  0.7071  0   -0.7071 -0.7071  0   0  0  1
  TR4  0 0 0  -1       0       0    0      -1       0   0  0  1
  TR5  0 0 0  -0.7071 -0.7071  0    0.7071 -0.7071  0   0  0  1
```

```
  TR6  0 0 0   0       -1       0    1       0       0   0  0  1
  TR7  0 0 0   0.7071 -0.7071  0    0.7071  0.7071  0   0  0  1
  TR8  0 0 -17.25
  TR9  0 0  1.1482
c ~~~~~~~~~~~~~~~~~~~~~~~~~~~~~~~~~
c Physics
c ~~~~~~~~~~~~~~~~~~~~~~~~~~~~~~~~~
  MODE n p
  PHYS:N J 20
  PHYS:P 0 1 1
  CUT:P 2J 0
c ~~~~~~~~~~~~~~~~~~~~~~~~~~~~~~~~~
c Source
c ~~~~~~~~~~~~~~~~~~~~~~~~~~~~~~~~~
  SDEF cel=702 pos=0 0 -13.39 axs=0 0 1 rad=d1 ext=d2 erg=D5 $ tme=d4
  SC1  Source radius (inner outer)
  SI1  0 4.14
  SC2  Source height
  SI2  0 26.79
  SC4  Uniform time distribution in interval 0 to 3600 sec (1s=10^8 shakes)
  SI4  0 360000000000
  SP4  0 1
  SI5  L 2 3 4 38 39 40 41
  SP5  0.000087 0.4233 0.0516 0.0598 0.0804 0.1250 0.2599
  DBCN
  PRDMP 2J 1
c ~~~~~~~~~~~~~~~~~~~~~~~~~~~~~~~~~
c Materials
c ~~~~~~~~~~~~~~~~~~~~~~~~~~~~~~~~~
c  EJ-309 liquid scintillator d=-0.916
c (Eljen Technologies, EJ-309 Fact Sheet)
c ~~~~~~~~~~~~~~~~~~~~~~~~~~~~~~~~~
```

```
  m1   nlib=60c  plib=04p
       1001      0.548
       6000      0.452
c ~~~~~~~~~~~~~~~~~~~~~~~~~~~~~~~~~
c Air, Dry (near sea level) d=-1.205E-3
c (Mat. Compendium PNNL)
c ~~~~~~~~~~~~~~~~~~~~~~~~~~~~~~~~~
  m2  nlib=60c  plib=04p
      6000     -0.000124
      7014     -0.755268
      8016     -0.231781
     18000.42c -0.012827
c ~~~~~~~~~~~~~~~~~~~~~~~~~~~~~~~~~
c  Lead Shielding d=-11.34
c
c ~~~~~~~~~~~~~~~~~~~~~~~~~~~~~~~~~
  m3  82000.42c 1
c ~~~~~~~~~~~~~~~~~~~~~~~~~~~~~~~~~
c Polyethylene d=-0.9300
c (Mat. Compendium PNNL)
c ~~~~~~~~~~~~~~~~~~~~~~~~~~~~~~~~~
  m4  nlib=60c  plib=04p
      1001 -0.143716
      6000 -0.856284
c ~~~~~~~~~~~~~~~~~~~~~~~~~~~~~~~~~
c Aluminum table d=-2.70
c ~~~~~~~~~~~~~~~~~~~~~~~~~~~~~~~~~
  m5  nlib=60c  plib=04p
     13027     -1
c ~~~~~~~~~~~~~~~~~~~~~~~~~~~~~~~~~
c Concrete (Mat. Compendium PNNL) d=-2.3
c (Mat. Compendium PNNL)
```

```
c ~~~~~~~~~~~~~~~~~~~~~~~~~~~~~~~~~
  m6  nlib=60c  plib=04p
      1001     -0.022100
      6000     -0.002484
      8016     -0.574930
     11023     -0.015208
     12000     -0.001266
     13027     -0.019953
     14000     -0.304627
     19000     -0.010045
     20000     -0.042951
     26000.42c -0.006435
c ~~~~~~~~~~~~~~~~~~~~~~~~~~~~~~~~~
c  MOX sample d=-0.7
c (ENEA-01)
c ~~~~~~~~~~~~~~~~~~~~~~~~~~~~~~~~~
  m7  8016.60c    -0.16443
      94238.42c   -0.00023
      94239.60c   -0.11061
      94240.60c   -0.04649
      94241.60c   -0.00165
      94242.60c   -0.00334
      95241.61c   -0.00507
      92234.60c   -0.00005
      92235.60c   -0.00474
      92236.60c   -0.00005
      92238.60c   -0.66332
c ~~~~~~~~~~~~~~~~~~~~~~~~~~~~~~~~~
c    Steel
c ~~~~~~~~~~~~~~~~~~~~~~~~~~~~~~~~~
  m8  26000.55c -0.6950
      24000.50c -0.1900
```

```
      28000.50c -0.0950
      25055.51c  -0.0200
c ~~~~~~~~~~~~~~~~~~~~~~~~~~~~~~~~~
c    EJ-299 Plastic Scintillator
c ~~~~~~~~~~~~~~~~~~~~~~~~~~~~~~~~~
  m9  1001.66c   0.514
      6000.70c   0.486
      PLIB = 04p
c ~~~~~~~~~~~~~~~~~~~~~~~~~~~~~~~~~
c    Mu metal
c ~~~~~~~~~~~~~~~~~~~~~~~~~~~~~~~~~
  m10  28000.50c   0.8
       42000.66c   0.05
       14000.21c   0.005
       29063.70c   0.0002
       26056.70c   0.1448
       PLIB = 04p
c ~~~~~~~~~~~~~~~~~~~~~~~~~~~~~~~~~
c    Pyrex glass
c ~~~~~~~~~~~~~~~~~~~~~~~~~~~~~~~~~
  m11   5011.70c  -0.040064
        8016.70c  -0.539562
       11023.70c  -0.028191
       13027.70c  -0.011644
       14000.21c  -0.377220
       19000.66c  -0.003321
       PLIB = 04p
c ~~~~~~~~~~~~~~~~~~~~~~~~~~~~~~~~~
c  Tallies
c ~~~~~~~~~~~~~~~~~~~~~~~~~~~~~~~~~
c detectors
c ~~~~~~~~~~~~~~~~~~~~~~~~~~~~~~~~~
```

```
c  F31:n 11.3 12.3 13.3 14.3 15.3 16.3 17.3 18.3 19.3
c  E31 0 0.5 0.7 29i 1 899i 10 100
c  C31 0 1
c  F41:p 11.3
c  E41 0 999i 10
c  C41 0 1
c ~~~~~~~~~~~~~~~~~~~~~~~~~~~~~~~~~
  IPOL  99 1 2 1 J 2 12 101 103 104 105 107 108 109 111 112 113 115 116
  RPOL 0.001 0.001
  NPS  1e8 $ 15905094 $ 190861128 = Number of reactions in 3600 sec (aged MOX
src)
  FILES 21 DUMN1
```

PANN Plate Cross-Correlation Experiment with EJ-309 and Stilbene

```
c CVT DNNG FNMC
c 1/2"x4"x8" lead shielding, 1 plate PANN
c *** CELLS *** ------------------------------------------------------------
-
c ---------------------------------------------------------------------------
-
c ~~~~~~~~~~~~~~~~~~~~~~~~~~~~~~~~~~~~~~~~~~~~~~~~~~~~~~~~~~~~~~~~~~~~~~~~~~
c    EJ-309 Detectors
c ~~~~~~~~~~~~~~~~~~~~~~~~~~~~~~~~~~~~~~~~~~~~~~~~~~~~~~~~~~~~~~~~~~~~~~~~~~
c Detector 1
10  1  -0.965  -12 11         IMP:N,P=1              $EJ-309 Liquid
11  9  -2.510  -10            IMP:N,P=1              $Optical Coupling
12  9  -2.510  -11            IMP:N,P=1              $Optical Window
13  5  -2.6989 -13 12         IMP:N,P=1              $Detector Casing
14  5  -2.6989 -14 15         IMP:N,P=1              $Large Ring
15  5  -2.6989 -16 17         IMP:N,P=1              $Small Ring
c Detector 2
20  1  -0.965  -22 21         IMP:N,P=1              $EJ-309 Liquid
21  9  -2.510  -20            IMP:N,P=1              $Optical Coupling
22  9  -2.510  -21            IMP:N,P=1              $Optical Window
23  5  -2.6989 -23 22         IMP:N,P=1              $Detector Casing
```

```
24  5  -2.6989 -24 25        IMP:N,P=1              $Large Ring
25  5  -2.6989 -26 27        IMP:N,P=1              $Small Ring
c Detector 3
30  1  -0.965  -32 31        IMP:N,P=1              $EJ-309 Liquid
31  9  -2.510  -30           IMP:N,P=1              $Optical Coupling
32  9  -2.510  -31           IMP:N,P=1              $Optical Window
33  5  -2.6989 -33 32        IMP:N,P=1              $Detector Casing
34  5  -2.6989 -34 35        IMP:N,P=1              $Large Ring
35  5  -2.6989 -36 37        IMP:N,P=1              $Small Ring
c Detector 4
40  1  -0.965  -42 41        IMP:N,P=1              $EJ-309 Liquid
41  9  -2.510  -40           IMP:N,P=1              $Optical Coupling
42  9  -2.510  -41           IMP:N,P=1              $Optical Window
43  5  -2.6989 -43 42        IMP:N,P=1              $Detector Casing
44  5  -2.6989 -44 45        IMP:N,P=1              $Large Ring
45  5  -2.6989 -46 47        IMP:N,P=1              $Small Ring
c Detector 5
50  1  -0.965  -52 51        IMP:N,P=1              $EJ-309 Liquid
51  9  -2.510  -50           IMP:N,P=1              $Optical Coupling
52  9  -2.510  -51           IMP:N,P=1              $Optical Window
53  5  -2.6989 -53 52        IMP:N,P=1              $Detector Casing
54  5  -2.6989 -54 55        IMP:N,P=1              $Large Ring
55  5  -2.6989 -56 57        IMP:N,P=1              $Small Ring
c Detector 6
60  1  -0.965  -62 61        IMP:N,P=1              $EJ-309 Liquid
61  9  -2.510  -60           IMP:N,P=1              $Optical Coupling
62  9  -2.510  -61           IMP:N,P=1              $Optical Window
63  5  -2.6989 -63 62        IMP:N,P=1              $Detector Casing
64  5  -2.6989 -64 65        IMP:N,P=1              $Large Ring
65  5  -2.6989 -66 67        IMP:N,P=1              $Small Ring
c Detector 7
70  1  -0.965  -72 71        IMP:N,P=1              $EJ-309 Liquid
```

```
71  9  -2.510  -70           IMP:N,P=1              $Optical Coupling
72  9  -2.510  -71           IMP:N,P=1              $Optical Window
73  5  -2.6989 -73 72        IMP:N,P=1              $Detector Casing
74  5  -2.6989 -74 75        IMP:N,P=1              $Large Ring
75  5  -2.6989 -76 77        IMP:N,P=1              $Small Ring
c Detector 8
80  1  -0.965  -82 81        IMP:N,P=1              $EJ-309 Liquid
81  9  -2.510  -80           IMP:N,P=1              $Optical Coupling
82  9  -2.510  -81           IMP:N,P=1              $Optical Window
83  5  -2.6989 -83 82        IMP:N,P=1              $Detector Casing
84  5  -2.6989 -84 85        IMP:N,P=1              $Large Ring
85  5  -2.6989 -86 87        IMP:N,P=1              $Small Ring
c ~~~~~~~~~~~~~~~~~~~~~~~~~~~~~~~~~~~~~~~~~~~~~~~~~~~~~~~~~~~~~~~~~
c    STILBENE Detectors
c ~~~~~~~~~~~~~~~~~~~~~~~~~~~~~~~~~~~~~~~~~~~~~~~~~~~~~~~~~~~~~~~~~
c Detector 9
90  13 -1.160  -90              IMP:N,P=1              $Stilbene
91  12 -1.190  -91 90           IMP:N,P=1              $Tape
92  11 -1.050  -92 91 90        IMP:N,P=1              $ABS Cover
93  9  -2.510  -93              IMP:N,P=1              $Optical Coupling
94  9  -2.510  -94              IMP:N,P=1              $Optical Window
95  10 -8.747  -95 96 94 93     IMP:N,P=1              $PMT Mumetal
c Detector 10
100  13 -1.160  -100            IMP:N,P=1              $Stilbene
101  12 -1.190  -101 100        IMP:N,P=1              $Tape
102  11 -1.050  -102 101 100    IMP:N,P=1              $ABS Cover
103  9  -2.510  -103            IMP:N,P=1              $Optical Coupling
104  9  -2.510  -104            IMP:N,P=1              $Optical Window
105  10 -8.747  -105 106 104 103 IMP:N,P=1              $PMT Mumetal
c Detector 11
110  13 -1.160  -110            IMP:N,P=1              $Stilbene
111  12 -1.190  -111 110        IMP:N,P=1              $Tape
```

```
112  11 -1.050  -112 111 110     IMP:N,P=1              $ABS Cover
113  9  -2.510  -113             IMP:N,P=1              $Optical Coupling
114  9  -2.510  -114             IMP:N,P=1              $Optical Window
115  10 -8.747  -115 116 114 113 IMP:N,P=1              $PMT Mumetal
c Detector 12
120  13 -1.160  -120             IMP:N,P=1              $Stilbene
121  12 -1.190  -121 120         IMP:N,P=1              $Tape
122  11 -1.050  -122 121 120     IMP:N,P=1              $ABS Cover
123  9  -2.510  -123             IMP:N,P=1              $Optical Coupling
124  9  -2.510  -124             IMP:N,P=1              $Optical Window
125  10 -8.747  -125 126 124 123 IMP:N,P=1              $PMT Mumetal
c Detector 13
130  13 -1.160  -130             IMP:N,P=1              $Stilbene
131  12 -1.190  -131 130         IMP:N,P=1              $Tape
132  11 -1.050  -132 131 130     IMP:N,P=1              $ABS Cover
133  9  -2.510  -133             IMP:N,P=1              $Optical Coupling
134  9  -2.510  -134             IMP:N,P=1              $Optical Window
135  10 -8.747  -135 136 134 133 IMP:N,P=1              $PMT Mumetal
c Detector 14
140  13 -1.160  -140             IMP:N,P=1              $Stilbene
141  12 -1.190  -141 140         IMP:N,P=1              $Tape
142  11 -1.050  -142 141 140     IMP:N,P=1              $ABS Cover
143  9  -2.510  -143             IMP:N,P=1              $Optical Coupling
144  9  -2.510  -144             IMP:N,P=1              $Optical Window
145  10 -8.747  -145 146 144 143 IMP:N,P=1              $PMT Mumetal
c Detector 15
150  13 -1.160  -150             IMP:N,P=1              $Stilbene
151  12 -1.190  -151 150         IMP:N,P=1              $Tape
152  11 -1.050  -152 151 150     IMP:N,P=1              $ABS Cover
153  9  -2.510  -153             IMP:N,P=1              $Optical Coupling
154  9  -2.510  -154             IMP:N,P=1              $Optical Window
155  10 -8.747  -155 156 154 153 IMP:N,P=1              $PMT Mumetal
```

```
c Detector 16
160  13 -1.160  -160             IMP:N,P=1               $Stilbene
161  12 -1.190  -161 160         IMP:N,P=1               $Tape
162  11 -1.050  -162 161 160     IMP:N,P=1               $ABS Cover
163  9  -2.510  -163             IMP:N,P=1               $Optical Coupling
164  9  -2.510  -164             IMP:N,P=1               $Optical Window
165  10 -8.747  -165 166 164 163 IMP:N,P=1               $PMT Mumetal
c ~~~~~~~~~~~~~~~~~~~~~~~~~~~~~~~~~~~~~~~~~~~~~~~~~~~~~~~~~~~~~~~~~~~~~~~~
c    Detector Structure
c ~~~~~~~~~~~~~~~~~~~~~~~~~~~~~~~~~~~~~~~~~~~~~~~~~~~~~~~~~~~~~~~~~~~~~~~~
200   5  -2.7      -200 13 92        IMP:N,P=1      $Front Plate
201   5  -2.7      -210 13 95        IMP:N,P=1      $Back Plate
202   5  -2.7      -201 23 102       IMP:N,P=1      $Front Plate
203   5  -2.7      -211 23 105       IMP:N,P=1      $Back Plate
204   5  -2.7      -202 33 112       IMP:N,P=1      $Front Plate
205   5  -2.7      -212 33 115       IMP:N,P=1      $Back Plate
206   5  -2.7      -203 43 122       IMP:N,P=1      $Front Plate
207   5  -2.7      -213 43 125       IMP:N,P=1      $Back Plate
208   5  -2.7      -204 53 132       IMP:N,P=1      $Front Plate
209   5  -2.7      -214 53 135       IMP:N,P=1      $Back Plate
210   5  -2.7      -205 63 142       IMP:N,P=1      $Front Plate
211   5  -2.7      -215 63 145       IMP:N,P=1      $Back Plate
212   5  -2.7      -206 73 152       IMP:N,P=1      $Front Plate
213   5  -2.7      -216 73 155       IMP:N,P=1      $Back Plate
214   5  -2.7      -207 83 162       IMP:N,P=1      $Front Plate
215   5  -2.7      -217 83 165       IMP:N,P=1      $Back Plate
216   5  -2.7 -220:-221:-222:-223:-224:-225:-226:-227 IMP:N,P=1  $Bottom Bar
217   5  -2.7 -230:-231:-232:-233:-234:-235:-236:-237 IMP:N,P=1  $Top Bar
c ~~~~~~~~~~~~~~~~~~~~~~~~~~~~~~~~~~~~~~~~~~~~~~~~~~~~~~~~~~~~~~~~~~~~~~~~
c    Table
c ~~~~~~~~~~~~~~~~~~~~~~~~~~~~~~~~~~~~~~~~~~~~~~~~~~~~~~~~~~~~~~~~~~~~~~~~
300   5  -2.7      -300           IMP:N,P=1   $Surface
```

```
301   5  -2.7      -301          IMP:N,P=1   $Support
302   5  -2.7      -302          IMP:N,P=1   $Support
303   5  -2.7      -303          IMP:N,P=1   $Support
304   5  -2.7      -304          IMP:N,P=1   $Support
305   5  -2.7      -305          IMP:N,P=1   $Leg
306   5  -2.7      -306          IMP:N,P=1   $Leg
307   5  -2.7      -307          IMP:N,P=1   $Leg
308   5  -2.7      -308          IMP:N,P=1   $Leg
309   5  -2.7      -309          IMP:N,P=1   $Leg
310   5  -2.7      -310          IMP:N,P=1   $Leg
c ~~~~~~~~~~~~~~~~~~~~~~~~~~~~~~~~~~~~~~~~~~~~~~~~~~~~~~~~~~~~~~~~~
c    Lead Shielding
c ~~~~~~~~~~~~~~~~~~~~~~~~~~~~~~~~~~~~~~~~~~~~~~~~~~~~~~~~~~~~~~~~~
400   3  -11.34     -400  IMP:N,P=1   $Lead Shield
401   3  -11.34     -401  IMP:N,P=1   $Lead Shield
403   3  -11.34     -403  IMP:N,P=1   $Lead Shield
402   3  -11.34     -402  IMP:N,P=1   $Lead Shield
404   3  -11.34     -404  IMP:N,P=1   $Lead Shield
405   3  -11.34     -405  IMP:N,P=1   $Lead Shield
406   3  -11.34     -406  IMP:N,P=1   $Lead Shield
407   3  -11.34     -407  IMP:N,P=1   $Lead Shield
c ~~~~~~~~~~~~~~~~~~~~~~~~~~~~~~~~~~~~~~~~~~~~~~~~~~~~~~~~~~~~~~~~~
c    Floor
c ~~~~~~~~~~~~~~~~~~~~~~~~~~~~~~~~~~~~~~~~~~~~~~~~~~~~~~~~~~~~~~~~~
500   6  -2.3       -600 -500  IMP:N,P=1        $Floor
c ~~~~~~~~~~~~~~~~~~~~~~~~~~~~~~~~~~~~~~~~~~~~~~~~~~~~~~~~~~~~~~~~~
c    Plutonium Plates
c ~~~~~~~~~~~~~~~~~~~~~~~~~~~~~~~~~~~~~~~~~~~~~~~~~~~~~~~~~~~~~~~~~
c ~~ Center Plate ~~~~~~~~~~~~~~~~~~~~~~~~~~~~~~~~~~~~~~~~~~~~~~~~
800   15  -15.08    -700 -798 799 IMP:N,P=1 $Pu ~~~~~~~~~~~~
700   0             -700  798      IMP:N,P=1 $Void Top
900   0             -700 -799      IMP:N,P=1 $Void Bot
```

```
701   16   -8.00    -701  700 IMP:N,P=1 $Cladding
c ~~ Right Plates ~~~~~~~~~~~~~~~~~~~~~~~~~~~~~~~~~~~~
c 801   15  -15.08    -702 -798 799 IMP:N,P=1 $Pu ~~~~~~~~~~~
c 702   0             -702  798 IMP:N,P=1 $Void Top
c 902   0             -702 -799 IMP:N,P=1 $Void Bot
c 703   16   -8.00    -703  702 IMP:N,P=1 $Cladding
c 802   15  -15.08    -704 -798 799 IMP:N,P=1 $Pu ~~~~~~~~~~~
c 704   0             -704  798 IMP:N,P=1 $Void Top
c 904   0             -704 -799 IMP:N,P=1 $Void Bot
c 705   16   -8.00    -705  704 IMP:N,P=1 $Cladding
c 803   15  -15.08    -706 -798 799 IMP:N,P=1 $Pu ~~~~~~~~~~~
c 706   0             -706  798 IMP:N,P=1 $Void Top
c 906   0             -706 -799 IMP:N,P=1 $Void Bot
c 707   16   -8.00    -707  706 IMP:N,P=1 $Cladding
c 804   15  -15.08    -708 -798 799 IMP:N,P=1 $Pu ~~~~~~~~~~~
c 708   0             -708  798 IMP:N,P=1 $Void Top
c 908   0             -708 -799 IMP:N,P=1 $Void Bot
c 709   16   -8.00    -709  708 IMP:N,P=1 $Cladding
c 805   15  -15.08    -710 -798 799 IMP:N,P=1 $Pu ~~~~~~~~~~~
c 710   0             -710  798 IMP:N,P=1 $Void Top
c 910   0             -710 -799 IMP:N,P=1 $Void Bot
c 711   16   -8.00    -711  710 IMP:N,P=1 $Cladding
c 806   15  -15.08    -712 -798 799 IMP:N,P=1 $Pu ~~~~~~~~~~~
c 712   0             -712  798 IMP:N,P=1 $Void Top
c 912   0             -712 -799 IMP:N,P=1 $Void Bot
c 713   16   -8.00    -713  712 IMP:N,P=1 $Cladding
c 807   15  -15.08    -714 -798 799 IMP:N,P=1 $Pu ~~~~~~~~~~~
c 714   0             -714  798 IMP:N,P=1 $Void Top
c 914   0             -714 -799 IMP:N,P=1 $Void Bot
c 715   16   -8.00    -715  714 IMP:N,P=1 $Cladding
c 808   15  -15.08    -716 -798 799 IMP:N,P=1 $Pu ~~~~~~~~~~~
c 716   0             -716  798 IMP:N,P=1 $Void Top
```

```
c 916   0            -716 -799 IMP:N,P=1 $Void Bot
c 717   16   -8.00    -717  716 IMP:N,P=1 $Cladding
c 809   15  -15.08    -718 -798 799 IMP:N,P=1 $Pu ~~~~~~~~~~~
c 718   0            -718  798 IMP:N,P=1 $Void Top
c 918   0            -718 -799 IMP:N,P=1 $Void Bot
c 719   16   -8.00    -719  718 IMP:N,P=1 $Cladding
c 810   15  -15.08    -720 -798 799 IMP:N,P=1 $Pu ~~~~~~~~~~~
c 720   0            -720  798 IMP:N,P=1 $Void Top
c 920   0            -720 -799 IMP:N,P=1 $Void Bot
c 721   16   -8.00    -721  720 IMP:N,P=1 $Cladding
c 811   15  -15.08    -722 -798 799 IMP:N,P=1 $Pu ~~~~~~~~~~~
c 722   0            -722  798 IMP:N,P=1 $Void Top
c 922   0            -722 -799 IMP:N,P=1 $Void Bot
c 723   16   -8.00    -723  722 IMP:N,P=1 $Cladding
c ~~ Left Plates ~~~~~~~~~~~~~~~~~~~~~~~~~~~~~~~~~~~~
c 812   15  -15.08    -750 -798 799 IMP:N,P=1 $Pu ~~~~~~~~~~~
c 750   0            -750  798 IMP:N,P=1 $Void Top
c 950   0            -750 -799 IMP:N,P=1 $Void Bot
c 751   16   -8.00    -751  750 IMP:N,P=1 $Cladding
c 813   15  -15.08    -752 -798 799  IMP:N,P=1 $Pu ~~~~~~~~~~~
c 752   0            -752  798 IMP:N,P=1 $Void Top
c 952   0            -752 -799 IMP:N,P=1 $Void Bot
c 753   16   -8.00    -753  752 IMP:N,P=1 $Cladding
c 814   15  -15.08    -754 -798 799  IMP:N,P=1 $Pu ~~~~~~~~~~~
c 754   0            -754  798 IMP:N,P=1 $Void Top
c 954   0            -754 -799 IMP:N,P=1 $Void Bot
c 755   16   -8.00    -755  754 IMP:N,P=1 $Cladding
c 815   15  -15.08    -756 -798 799  IMP:N,P=1 $Pu ~~~~~~~~~~~
c 756   0            -756  798 IMP:N,P=1 $Void Top
c 956   0            -756 -799 IMP:N,P=1 $Void Bot
c 757   16   -8.00    -757  756 IMP:N,P=1 $Cladding
c 816   15  -15.08    -758 -798 799  IMP:N,P=1 $Pu ~~~~~~~~~~~
```

```
c 758   0             -758  798 IMP:N,P=1 $Void Top
c 958   0             -758 -799 IMP:N,P=1 $Void Bot
c 759   16   -8.00    -759  758 IMP:N,P=1 $Cladding
c 817   15  -15.08    -760 -798 799  IMP:N,P=1 $Pu ~~~~~~~~~~~
c 760   0             -760  798 IMP:N,P=1 $Void Top
c 960   0             -760 -799 IMP:N,P=1 $Void Bot
c 761   16   -8.00    -761  760 IMP:N,P=1 $Cladding
c 818   15  -15.08    -762 -798 799  IMP:N,P=1 $Pu ~~~~~~~~~~~
c 762   0             -762  798 IMP:N,P=1 $Void Top
c 962   0             -762 -799 IMP:N,P=1 $Void Bot
c 763   16   -8.00    -763  762 IMP:N,P=1 $Cladding
c 819   15  -15.08    -764 -798 799  IMP:N,P=1 $Pu ~~~~~~~~~~~
c 764   0             -764  798 IMP:N,P=1 $Void Top
c 964   0             -764 -799 IMP:N,P=1 $Void Bot
c 765   16   -8.00    -765  764 IMP:N,P=1 $Cladding
c 820   15  -15.08    -766 -798 799  IMP:N,P=1 $Pu ~~~~~~~~~~~
c 766   0             -766  798 IMP:N,P=1 $Void Top
c 966   0             -766 -799 IMP:N,P=1 $Void Bot
c 767   16   -8.00    -767  766 IMP:N,P=1 $Cladding
c 821   15  -15.08    -768 -798 799  IMP:N,P=1 $Pu ~~~~~~~~~~~
c 768   0             -768  798 IMP:N,P=1 $Void Top
c 968   0             -768 -799 IMP:N,P=1 $Void Bot
c 769   16   -8.00    -769  768 IMP:N,P=1 $Cladding
c 822   15  -15.08    -770 -798 799  IMP:N,P=1 $Pu ~~~~~~~~~~~
c 770   0             -770  798 IMP:N,P=1 $Void Top
c 970   0             -770 -799 IMP:N,P=1 $Void Bot
c 771   16   -8.00    -771  770 IMP:N,P=1 $Cladding
c   Holder
c
850  5  -2.7  -800 IMP:N,P=1 $left holder
851  5  -2.7  -801 IMP:N,P=1 $right holder
852  5  -2.7  -802 IMP:N,P=1 $bottom
```

```
c    Environment
c ~~~~~~~~~~~~~~~~~~~~~~~~~~~~~~~~~~~~~~~~~~~~~~~~~~~~~~~~~~~~
600   2  -1.205E-3  -600 601 500
            #10 #11 #12 #13 #14 #15
            #20 #21 #22 #23 #24 #25
            #30 #31 #32 #33 #34 #35
            #40 #41 #42 #43 #44 #45
            #50 #51 #52 #53 #54 #55
            #60 #61 #62 #63 #64 #65
            #70 #71 #72 #73 #74 #75
            #80 #81 #82 #83 #84 #85
            #90 #91 #92 #93 #94 #95
            #100 #101 #102 #103 #104 #105
            #110 #111 #112 #113 #114 #115
            #120 #121 #122 #123 #124 #125
            #130 #131 #132 #133 #134 #135
            #140 #141 #142 #143 #144 #145
            #150 #151 #152 #153 #154 #155
            #160 #161 #162 #163 #164 #165
            200 201 202 203 204 205 206 207 #216    $Detector Structure
            210 211 212 213 214 215 216 217 #217    $Detector Structure
            300 301 302 303 304 305 306 307 308 309 310 $Table
            400 401 402 403 404 405 406 407            $Lead Bricks
            IMP:N,P=1
601   2  -1.205E-3 -601
            701 $Center Plate
            800 801 802
            IMP:N,P=1
c ~~~~~~~~~~~~~~~~~~~~~~~~~~~~~~~~~~~~~~~~~~~~~~~~~~~~~~~~~~~~
c    Graveyard
c ~~~~~~~~~~~~~~~~~~~~~~~~~~~~~~~~~~~~~~~~~~~~~~~~~~~~~~~~~~~~
999   0              600           IMP:N,P=0
```

```
c ------------------------------------------------------------------------
-
c *** END CELLS *** ----------------------------------------------------
-


c *** SURFACES *** -----------------------------------------------------
-
c ------------------------------------------------------------------------
-
c ~~~~~~~~~~~~~~~~~~~~~~~~~~~~~~~~~~~~~~~~~~~~~~~~~~~~~~~~~~~~
c    EJ-309 Detectors
c ~~~~~~~~~~~~~~~~~~~~~~~~~~~~~~~~~~~~~~~~~~~~~~~~~~~~~~~~~~~~
c    EJ-309 1: Detector 1  (High)
c ~~~~~~~~~~~~~~~~~~~~~~~~~~~~~~~~~~~~~~~~~~~~~~~~~~~~~~~~~~~~
10    RCC 27.175 0 5.31  -0.635 0 0   3.9075          $Optical Coupling
11    RCC 26.540  0 5.31  -1.6   0 0   3.25            $Optical Window
12    RCC 26.540  0 5.31  -9.2   0 0   3.81            $3" Detector Cell
13    RCC 26.540  0 5.31  -9.352 0 0   3.962           $Detector Casing
14    RCC 26.540  0 5.31   1.54  0 0   5.08            $Large Ring Outside
15    RCC 26.540  0 5.31   1.54  0 0   3.9075          $Large Ring Inside
16    RCC 24.540  0 5.31   2     0 0   4.362           $Small Ring Outside
17    RCC 24.540  0 5.31   2     0 0   3.962           $Small Ring Inside
c ~~~~~~~~~~~~~~~~~~~~~~~~~~~~~~~~~~~~~~~~~~~~~~~~~~~~~~~~~~~~
c    EJ-309 2: Detector 2  (Low)
c ~~~~~~~~~~~~~~~~~~~~~~~~~~~~~~~~~~~~~~~~~~~~~~~~~~~~~~~~~~~~
20 2  RCC 27.175 0 -5.31  -0.635 0 0   3.9075         $Optical Coupling
21 2  RCC 26.540  0 -5.31  -1.6   0 0   3.25           $Optical Window
22 2  RCC 26.540  0 -5.31  -9.2   0 0   3.81           $3" Detector Cell
23 2  RCC 26.540  0 -5.31  -9.352 0 0   3.962          $Detector Casing
24 2  RCC 26.540  0 -5.31   1.54  0 0   5.08           $Large Ring Outside
25 2  RCC 26.540  0 -5.31   1.54  0 0   3.9075         $Large Ring Inside
26 2  RCC 24.540  0 -5.31   2     0 0   4.362          $Small Ring Outside
27 2  RCC 24.540  0 -5.31   2     0 0   3.962          $Small Ring Inside
c ~~~~~~~~~~~~~~~~~~~~~~~~~~~~~~~~~~~~~~~~~~~~~~~~~~~~~~~~~~~~
```

```
c    EJ-309 3: Detector 3  (High)
c ~~~~~~~~~~~~~~~~~~~~~~~~~~~~~~~~~~~~~~~~~~~~~~~~~~~~~~~~~~~~
30 3  RCC 27.175 0 5.31  -0.635 0 0   3.9075          $Optical Coupling
31 3  RCC 26.540  0 5.31  -1.6   0 0   3.25            $Optical Window
32 3  RCC 26.540  0 5.31  -9.2   0 0   3.81            $3" Detector Cell
33 3  RCC 26.540  0 5.31  -9.352 0 0   3.962           $Detector Casing
34 3  RCC 26.540  0 5.31   1.54  0 0   5.08            $Large Ring Outside
35 3  RCC 26.540  0 5.31   1.54  0 0   3.9075          $Large Ring Inside
36 3  RCC 24.540  0 5.31   2     0 0   4.362           $Small Ring Outside
37 3  RCC 24.540  0 5.31   2     0 0   3.962           $Small Ring Inside
c ~~~~~~~~~~~~~~~~~~~~~~~~~~~~~~~~~~~~~~~~~~~~~~~~~~~~~~~~~~~~
c    EJ-309 4: Detector 4  (Low)
c ~~~~~~~~~~~~~~~~~~~~~~~~~~~~~~~~~~~~~~~~~~~~~~~~~~~~~~~~~~~~
40 4  RCC 27.175 0 -5.31  -0.635 0 0   3.9075         $Optical Coupling
41 4  RCC 26.540  0 -5.31  -1.6   0 0   3.25           $Optical Window
42 4  RCC 26.540  0 -5.31  -9.2   0 0   3.81           $3" Detector Cell
43 4  RCC 26.540  0 -5.31  -9.352 0 0   3.962          $Detector Casing
44 4  RCC 26.540  0 -5.31   1.54  0 0   5.08           $Large Ring Outside
45 4  RCC 26.540  0 -5.31   1.54  0 0   3.9075         $Large Ring Inside
46 4  RCC 24.540  0 -5.31   2     0 0   4.362          $Small Ring Outside
47 4  RCC 24.540  0 -5.31   2     0 0   3.962          $Small Ring Inside
c ~~~~~~~~~~~~~~~~~~~~~~~~~~~~~~~~~~~~~~~~~~~~~~~~~~~~~~~~~~~~
c    EJ-309 5: Detector 5  (High)
c ~~~~~~~~~~~~~~~~~~~~~~~~~~~~~~~~~~~~~~~~~~~~~~~~~~~~~~~~~~~~
50 5  RCC 27.175 0 5.31  -0.635 0 0   3.9075          $Optical Coupling
51 5  RCC 26.540  0 5.31  -1.6   0 0   3.25            $Optical Window
52 5  RCC 26.540  0 5.31  -9.2   0 0   3.81            $3" Detector Cell
53 5  RCC 26.540  0 5.31  -9.352 0 0   3.962           $Detector Casing
54 5  RCC 26.540  0 5.31   1.54  0 0   5.08            $Large Ring Outside
55 5  RCC 26.540  0 5.31   1.54  0 0   3.9075          $Large Ring Inside
56 5  RCC 24.540  0 5.31   2     0 0   4.362           $Small Ring Outside
57 5  RCC 24.540  0 5.31   2     0 0   3.962           $Small Ring Inside
```

```
c ~~~~~~~~~~~~~~~~~~~~~~~~~~~~~~~~~~~~~~~~~~~~~~~~~~~~
c    EJ-309 6: Detector 6  (Low)
c ~~~~~~~~~~~~~~~~~~~~~~~~~~~~~~~~~~~~~~~~~~~~~~~~~~~~
60 6  RCC 27.175 0 -5.31  -0.635 0 0   3.9075         $Optical Coupling
61 6  RCC 26.540  0 -5.31  -1.6   0 0   3.25           $Optical Window
62 6  RCC 26.540  0 -5.31  -9.2   0 0   3.81           $3" Detector Cell
63 6  RCC 26.540  0 -5.31  -9.352 0 0   3.962          $Detector Casing
64 6  RCC 26.540  0 -5.31   1.54  0 0   5.08           $Large Ring Outside
65 6  RCC 26.540  0 -5.31   1.54  0 0   3.9075         $Large Ring Inside
66 6  RCC 24.540  0 -5.31   2     0 0   4.362          $Small Ring Outside
67 6  RCC 24.540  0 -5.31   2     0 0   3.962          $Small Ring Inside
c ~~~~~~~~~~~~~~~~~~~~~~~~~~~~~~~~~~~~~~~~~~~~~~~~~~~~
c    EJ-309 7: Detector 7  (High)
c ~~~~~~~~~~~~~~~~~~~~~~~~~~~~~~~~~~~~~~~~~~~~~~~~~~~~
70 7   RCC 27.175 0 5.31  -0.635 0 0   3.9075          $Optical Coupling
71 7  RCC 26.540  0 5.31  -1.6   0 0   3.25            $Optical Window
72 7  RCC 26.540  0 5.31  -9.2   0 0   3.81            $3" Detector Cell
73 7  RCC 26.540  0 5.31  -9.352 0 0   3.962           $Detector Casing
74 7  RCC 26.540  0 5.31   1.54  0 0   5.08            $Large Ring Outside
75 7  RCC 26.540  0 5.31   1.54  0 0   3.9075          $Large Ring Inside
76 7  RCC 24.540  0 5.31   2     0 0   4.362           $Small Ring Outside
77 7  RCC 24.540  0 5.31   2     0 0   3.962           $Small Ring Inside
c ~~~~~~~~~~~~~~~~~~~~~~~~~~~~~~~~~~~~~~~~~~~~~~~~~~~~
c    EJ-309 8: Detector 8  (Low)
c ~~~~~~~~~~~~~~~~~~~~~~~~~~~~~~~~~~~~~~~~~~~~~~~~~~~~
80 8   RCC 27.175 0 -5.31  -0.635 0 0   3.9075         $Optical Coupling
81 8  RCC 26.540  0 -5.31  -1.6   0 0   3.25           $Optical Window
82 8  RCC 26.540  0 -5.31  -9.2   0 0   3.81           $3" Detector Cell
83 8  RCC 26.540  0 -5.31  -9.352 0 0   3.962          $Detector Casing
84 8  RCC 26.540  0 -5.31   1.54  0 0   5.08           $Large Ring Outside
85 8  RCC 26.540  0 -5.31   1.54  0 0   3.9075         $Large Ring Inside
86 8  RCC 24.540  0 -5.31   2     0 0   4.362          $Small Ring Outside
```

```
87 8  RCC 24.540  0 -5.31   2     0 0   3.962          $Small Ring Inside
c ~~~~~~~~~~~~~~~~~~~~~~~~~~~~~~~~~~~~~~~~~~~~~~~~~~~~~~~~~~~~~~~~~~~~~~~
c    STILBENE Detectors
c ~~~~~~~~~~~~~~~~~~~~~~~~~~~~~~~~~~~~~~~~~~~~~~~~~~~~~~~~~~~~~~~~~~~~~~~
c    STILBENE 1: Detector 9  (Low)
c ~~~~~~~~~~~~~~~~~~~~~~~~~~~~~~~~~~~~~~~~~~~~~~~~~~~~~~~~~~~~~~~~~~~~~~~
90    RCC 22.608 0 -5.31  -5.08  0 0  2.54           $2" Detector Cell
91    RCC 22.608 0 -5.31  -5.17  0 0  2.65           $Vinyl Tape, th= 0.8 mm
92    RCC 22.608 0 -5.31  -5.42  0 0  2.88           $ABS Cover
93    RCC 23.243 0 -5.31  -0.635 0 0  2.6            $Optical Coupling
94    RCC 24.843 0 -5.31  -1.6   0 0  2.6            $Optical Window
95    RCC 30.228 0 -5.31  -7.62  0 0  2.65           $PMT Mumetal
96    RCC 30.228 0 -5.31  -5.385 0 0  2.6            $Void PMT
c ~~~~~~~~~~~~~~~~~~~~~~~~~~~~~~~~~~~~~~~~~~~~~~~~~~~~~~~~~~~~~~~~~~~~~~~
c    STILBENE 2: Detector 10 (High)
c ~~~~~~~~~~~~~~~~~~~~~~~~~~~~~~~~~~~~~~~~~~~~~~~~~~~~~~~~~~~~~~~~~~~~~~~
100 2  RCC 22.608 0 5.31  -5.08  0 0  2.54           $2" Detector Cell
101 2  RCC 22.608 0 5.31  -5.17  0 0  2.65           $Vinyl Tape, th= 0.8 mm
102 2  RCC 22.608 0 5.31  -5.42  0 0  2.88           $ABS Cover
103 2  RCC 23.243 0 5.31  -0.635 0 0  2.6            $Optical Coupling
104 2  RCC 24.843 0 5.31  -1.6   0 0  2.6            $Optical Window
105 2  RCC 30.228 0 5.31  -7.62  0 0  2.65           $PMT Mumetal
106 2  RCC 30.228 0 5.31  -5.385 0 0  2.6            $Void PMT
c ~~~~~~~~~~~~~~~~~~~~~~~~~~~~~~~~~~~~~~~~~~~~~~~~~~~~~~~~~~~~~~~~~~~~~~~
c    STILBENE 3: Detector 11 (Low)
c ~~~~~~~~~~~~~~~~~~~~~~~~~~~~~~~~~~~~~~~~~~~~~~~~~~~~~~~~~~~~~~~~~~~~~~~
110 3  RCC 22.608 0 -5.31  -5.08  0 0  2.54           $2" Detector Cell
111 3  RCC 22.608 0 -5.31  -5.17  0 0  2.65           $Vinyl Tape, th= 0.8
mm
112 3  RCC 22.608 0 -5.31  -5.42  0 0  2.88           $ABS Cover
113 3  RCC 23.243 0 -5.31  -0.635 0 0  2.6            $Optical Coupling
114 3  RCC 24.843 0 -5.31  -1.6   0 0  2.6            $Optical Window
115 3  RCC 30.228 0 -5.31  -7.62  0 0  2.65           $PMT Mumetal
```

```
116 3  RCC 30.228 0 -5.31  -5.385 0 0  2.6             $Void PMT
c ~~~~~~~~~~~~~~~~~~~~~~~~~~~~~~~~~~~~~~~~~~~~~~~~~~~~
c    STILBENE 4: Detector 12 (High)
c ~~~~~~~~~~~~~~~~~~~~~~~~~~~~~~~~~~~~~~~~~~~~~~~~~~~~
120 4  RCC 22.608 0 5.31  -5.08  0 0  2.54            $2" Detector Cell
121 4  RCC 22.608 0 5.31  -5.17  0 0  2.65            $Vinyl Tape, th= 0.8 mm
122 4  RCC 22.608 0 5.31  -5.42  0 0  2.88            $ABS Cover
123 4  RCC 23.243 0 5.31  -0.635 0 0  2.6             $Optical Coupling
124 4  RCC 24.843 0 5.31  -1.6   0 0  2.6             $Optical Window
125 4  RCC 30.228 0 5.31  -7.62  0 0  2.65            $PMT Mumetal
126 4  RCC 30.228 0 5.31  -5.385 0 0  2.6             $Void PMT
c ~~~~~~~~~~~~~~~~~~~~~~~~~~~~~~~~~~~~~~~~~~~~~~~~~~~~
c    STILBENE 5: Detector 13 (Low)
c ~~~~~~~~~~~~~~~~~~~~~~~~~~~~~~~~~~~~~~~~~~~~~~~~~~~~
130 5   RCC 22.608 0 -5.31  -5.08  0 0  2.54            $2" Detector Cell
131 5  RCC 22.608 0 -5.31  -5.17  0 0  2.65            $Vinyl Tape, th= 0.8
mm
132 5  RCC 22.608 0 -5.31  -5.42  0 0  2.88            $ABS Cover
133 5  RCC 23.243 0 -5.31  -0.635 0 0  2.6             $Optical Coupling
134 5  RCC 24.843 0 -5.31  -1.6   0 0  2.6             $Optical Window
135 5  RCC 30.228 0 -5.31  -7.62  0 0  2.65            $PMT Mumetal
136 5  RCC 30.228 0 -5.31  -5.385 0 0  2.6             $Void PMT
c ~~~~~~~~~~~~~~~~~~~~~~~~~~~~~~~~~~~~~~~~~~~~~~~~~~~~
c    STILBENE 6: Detector 14 (High)
c ~~~~~~~~~~~~~~~~~~~~~~~~~~~~~~~~~~~~~~~~~~~~~~~~~~~~
140 6   RCC 22.608 0 5.31  -5.08  0 0  2.54            $2" Detector Cell
141 6  RCC 22.608 0 5.31  -5.17  0 0  2.65            $Vinyl Tape, th= 0.8 mm
142 6  RCC 22.608 0 5.31  -5.42  0 0  2.88            $ABS Cover
143 6  RCC 23.243 0 5.31  -0.635 0 0  2.6             $Optical Coupling
144 6  RCC 24.843 0 5.31  -1.6   0 0  2.6             $Optical Window
145 6  RCC 30.228 0 5.31  -7.62  0 0  2.65            $PMT Mumetal
146 6  RCC 30.228 0 5.31  -5.385 0 0  2.6             $Void PMT
c ~~~~~~~~~~~~~~~~~~~~~~~~~~~~~~~~~~~~~~~~~~~~~~~~~~~~
```

```
c    STILBENE 7: Detector 15 (Low)
c ~~~~~~~~~~~~~~~~~~~~~~~~~~~~~~~~~~~~~~~~~~~~~~~~~~~~~~~~~~~~~~~~~~~~~~~~
150 7  RCC 22.608 0 -5.31  -5.08  0 0  2.54            $2" Detector Cell
151 7  RCC 22.608 0 -5.31  -5.17  0 0  2.65            $Vinyl Tape, th= 0.8
mm
152 7  RCC 22.608 0 -5.31  -5.42  0 0  2.88            $ABS Cover
153 7  RCC 23.243 0 -5.31  -0.635 0 0  2.6             $Optical Coupling
154 7  RCC 24.843 0 -5.31  -1.6   0 0  2.6             $Optical Window
155 7  RCC 30.228 0 -5.31  -7.62  0 0  2.65            $PMT Mumetal
156 7  RCC 30.228 0 -5.31  -5.385 0 0  2.6            $Void PMT
c ~~~~~~~~~~~~~~~~~~~~~~~~~~~~~~~~~~~~~~~~~~~~~~~~~~~~~~~~~~~~~~~~~~~~~~~~
c    STILBENE 8: Detector 16 (High)
c ~~~~~~~~~~~~~~~~~~~~~~~~~~~~~~~~~~~~~~~~~~~~~~~~~~~~~~~~~~~~~~~~~~~~~~~~
160 8  RCC 22.608 0 5.31   -5.08  0 0  2.54            $2" Detector Cell
161 8  RCC 22.608 0 5.31   -5.17  0 0  2.65            $Vinyl Tape, th= 0.8
mm
162 8  RCC 22.608 0 5.31   -5.42  0 0  2.88            $ABS Cover
163 8  RCC 23.243 0 5.31   -0.635 0 0  2.6             $Optical Coupling
164 8  RCC 24.843 0 5.31   -1.6   0 0  2.6             $Optical Window
165 8  RCC 30.228 0 5.31   -7.62  0 0  2.65            $PMT Mumetal
166 8  RCC 30.228 0 5.31   -5.385 0 0  2.6            $Void PMT
c ~~~~~~~~~~~~~~~~~~~~~~~~~~~~~~~~~~~~~~~~~~~~~~~~~~~~~~~~~~~~~~~~~~~~~~~~
c    Detector Structure
c ~~~~~~~~~~~~~~~~~~~~~~~~~~~~~~~~~~~~~~~~~~~~~~~~~~~~~~~~~~~~~~~~~~~~~~~~
200    RPP  22      22.3175  -5.05  5.05   -17.25  13.35       $Front Plate
210    RPP  24.2225 24.540    -5.05  5.05   -17.25  13.35       $Back Plate
201 2  RPP  22      22.3175  -5.05  5.05   -17.25  13.35       $Front Plate
211 2  RPP  24.2225 24.540    -5.05  5.05   -17.25  13.35       $Back Plate
202 3  RPP  22      22.3175  -5.05  5.05   -17.25  13.35       $Front Plate
212 3  RPP  24.2225 24.540    -5.05  5.05   -17.25  13.35       $Back Plate
203 4  RPP  22      22.3175  -5.05  5.05   -17.25  13.35       $Front Plate
213 4  RPP  24.2225 24.540    -5.05  5.05   -17.25  13.35       $Back Plate
204 5  RPP  22      22.3175  -5.05  5.05   -17.25  13.35       $Front Plate
```

```
214 5  RPP  24.2225 24.540    -5.05  5.05   -17.25  13.35       $Back Plate
205 6  RPP  22      22.3175  -5.05  5.05   -17.25  13.35       $Front Plate
215 6  RPP  24.2225 24.540    -5.05  5.05   -17.25  13.35       $Back Plate
206 7  RPP  22      22.3175  -5.05  5.05   -17.25  13.35       $Front Plate
216 7  RPP  24.2225 24.540    -5.05  5.05   -17.25  13.35       $Back Plate
207 8  RPP  22      22.3175  -5.05  5.05   -17.25  13.35       $Front Plate
217 8  RPP  24.2225 24.540    -5.05  5.05   -17.25  13.35       $Back Plate
c ------------------------------
220    RPP  22.3176 24.2224   -10.0333 10.0333 -17.25 -15.345  $Bottom Bar
230    RPP  22.3176 24.2224   -10.0333 10.0333  11.445 13.35   $Top Bar
221 2  RPP  22.3176 24.2224   -10.0333 10.0333 -17.25 -15.345  $Bottom Bar
231 2  RPP  22.3176 24.2224   -10.0333 10.0333  11.445 13.35   $Top Bar
222 3  RPP  22.3176 24.2224   -10.0333 10.0333 -17.25 -15.345  $Bottom Bar
232 3  RPP  22.3176 24.2224   -10.0333 10.0333  11.445 13.35   $Top Bar
223 4  RPP  22.3176 24.2224   -10.0333 10.0333 -17.25 -15.345  $Bottom Bar
233 4  RPP  22.3176 24.2224   -10.0333 10.0333  11.445 13.35   $Top Bar
224 5  RPP  22.3176 24.2224   -10.0333 10.0333 -17.25 -15.345  $Bottom Bar
234 5  RPP  22.3176 24.2224   -10.0333 10.0333  11.445 13.35   $Top Bar
225 6  RPP  22.3176 24.2224   -10.0333 10.0333 -17.25 -15.345  $Bottom Bar
235 6  RPP  22.3176 24.2224   -10.0333 10.0333  11.445 13.35   $Top Bar
226 7  RPP  22.3176 24.2224   -10.0333 10.0333 -17.25 -15.345  $Bottom Bar
236 7  RPP  22.3176 24.2224   -10.0333 10.0333  11.445 13.35   $Top Bar
227 8  RPP  22.3176 24.2224   -10.0333 10.0333 -17.25 -15.345  $Bottom Bar
237 8  RPP  22.3176 24.2224   -10.0333 10.0333  11.445 13.35   $Top Bar
c ~~~~~~~~~~~~~~~~~~~~~~~~~~~~~~~~~~~~~~~~~~~~~~~~~~~~~~~~~~~~
c    Table
c ~~~~~~~~~~~~~~~~~~~~~~~~~~~~~~~~~~~~~~~~~~~~~~~~~~~~~~~~~~~~
300 1 BOX  -50   -100   -0.5   100   0 0    0 200   0   0 0   0.5   $ Surface
301 1 BOX  -50   -100   -4.9     4.4 0 0    0 200   0   0 0   4.4   $ Support
302 1 BOX   45.6 -100   -4.9     4.4 0 0    0 200   0   0 0   4.4   $ Support
303 1 BOX  -45.6 -100   -4.9    91.2 0 0    0   4.4 0   0 0   4.4   $ Support
304 1 BOX  -45.6   95.6 -4.9    91.2 0 0    0   4.4 0   0 0   4.4   $ Support
```

```
305 1 BOX  -50     -2.2 -4.9     4.4 0 0    0   4.4 0   0 0 -85.5   $ Leg
306 1 BOX   45.6   -2.2 -4.9     4.4 0 0    0   4.4 0   0 0 -85.5   $ Leg
307 1 BOX  -50   -100   -4.9     4.4 0 0    0   4.4 0   0 0 -85.5   $ Leg
308 1 BOX   45.6 -100   -4.9     4.4 0 0    0   4.4 0   0 0 -85.5   $ Leg
309 1 BOX  -50     95.6 -4.9     4.4 0 0    0   4.4 0   0 0 -85.5   $ Leg
310 1 BOX   45.6   95.6 -4.9     4.4 0 0    0   4.4 0   0 0 -85.5   $ Leg
c ~~~~~~~~~~~~~~~~~~~~~~~~~~~~~~~~~~~~~~~~~~~~~~~~~~~~~~~~~~~~~~~~~~~~~~~
c    Lead Shielding
c ~~~~~~~~~~~~~~~~~~~~~~~~~~~~~~~~~~~~~~~~~~~~~~~~~~~~~~~~~~~~~~~~~~~~~~~
400    RPP  15.73 17.00  -5.08 5.08  -10.16  10.16    $2"x4"x8" Lead Brick
401 2  RPP  15.73 17.00  -5.08 5.08  -10.16  10.16    $2"x4"x8" Lead Brick
402 3  RPP  15.73 17.00  -5.08 5.08  -10.16  10.16    $2"x4"x8" Lead Brick
403 4  RPP  15.73 17.00  -5.08 5.08  -10.16  10.16    $2"x4"x8" Lead Brick
404 5  RPP  15.73 17.00  -5.08 5.08  -10.16  10.16    $2"x4"x8" Lead Brick
405 6  RPP  15.73 17.00  -5.08 5.08  -10.16  10.16    $2"x4"x8" Lead Brick
406 7  RPP  15.73 17.00  -5.08 5.08  -10.16  10.16    $2"x4"x8" Lead Brick
407 8  RPP  15.73 17.00  -5.08 5.08  -10.16  10.16    $2"x4"x8" Lead Brick
c ~~~~~~~~~~~~~~~~~~~~~~~~~~~~~~~~~~~~~~~~~~~~~~~~~~~~~~~~~~~~~~~~~~~~~~~
c    Floor
c ~~~~~~~~~~~~~~~~~~~~~~~~~~~~~~~~~~~~~~~~~~~~~~~~~~~~~~~~~~~~~~~~~~~~~~~
500    PZ   -108                                                $Floor Level
c ~~~~~~~~~~~~~~~~~~~~~~~~~~~~~~~~~~~~~~~~~~~~~~~~~~~~~~~~~~~~~~~~~~~~~~~
c    Environment
c ~~~~~~~~~~~~~~~~~~~~~~~~~~~~~~~~~~~~~~~~~~~~~~~~~~~~~~~~~~~~~~~~~~~~~~~
600    RPP  -100 100     -100 100     -150 100                $Environment
601    SO     10                                              $Environment
c ~~~~~~~~~~~~~~~~~~~~~~~~~~~~~~~~~~~~~~~~~~~~~~~~~~~~~~~~~~~~~~~~~~~~~~~
c    Plutonium Plates, Even = Core, Odd = Cladding
c ~~~~~~~~~~~~~~~~~~~~~~~~~~~~~~~~~~~~~~~~~~~~~~~~~~~~~~~~~~~~~~~~~~~~~~~
c    Central PLate
c ~~~~~~~~~~~~~~~~~~~~~~~~~~~~~~~~~~~~~~~~~~~~~~~~~~~~~~~~~~~~~~~~~~~~~~~
700 10 RPP -0.14097 0.14097  -2.52222 2.52222 -3.17 3.17        $core
```

```
701 10 RPP -0.15875 0.15875  -2.54    2.54    -3.81 3.81        $cladding
c ~~~~~~~~~~~~~~~~~~~~~~~~~~~~~~~~~~~~~~~~~~~~~~~~~~~~~~~~~~~~~~~~~~~~~~~
c    Right Plates
c ~~~~~~~~~~~~~~~~~~~~~~~~~~~~~~~~~~~~~~~~~~~~~~~~~~~~~~~~~~~~~~~~~~~~~~~
c 702 10 RPP  0.17653 0.45847  -2.52222 2.52222 -3.17 3.17        $core
c 703 10 RPP  0.15875 0.47625  -2.54    2.54    -3.81 3.81        $cladding
c 704 10 RPP  0.49403 0.77597  -2.52222 2.52222 -3.17 3.17        $core
c 705 10 RPP  0.47625 0.79375  -2.54    2.54    -3.81 3.81        $cladding
c 706 10 RPP  0.81153 1.09347  -2.52222 2.52222 -3.17 3.17        $core
c 707 10 RPP  0.79375 1.11125  -2.54    2.54    -3.81 3.81        $cladding
c 708 10 RPP  1.12903 1.41097  -2.52222 2.52222 -3.17 3.17        $core
c 709 10 RPP  1.11125 1.42875  -2.54    2.54    -3.81 3.81        $cladding
c 710 10 RPP  1.44653 1.72847  -2.52222 2.52222 -3.17 3.17        $core
c 711 10 RPP  1.42875 1.74625  -2.54    2.54    -3.81 3.81        $cladding
c 712 10 RPP  1.76403 2.04597  -2.52222 2.52222 -3.17 3.17        $core
c 713 10 RPP  1.74625 2.06375  -2.54    2.54    -3.81 3.81        $cladding
c 714 10 RPP  2.08153 2.36347  -2.52222 2.52222 -3.17 3.17        $core
c 715 10 RPP  2.06375 2.38125  -2.54    2.54    -3.81 3.81        $cladding
c 716 10 RPP  2.39903 2.68097  -2.52222 2.52222 -3.17 3.17        $core
c 717 10 RPP  2.38125 2.69875  -2.54    2.54    -3.81 3.81        $cladding
c 718 10 RPP  2.71653 2.99847  -2.52222 2.52222 -3.17 3.17        $core
c 719 10 RPP  2.69875 3.01625  -2.54    2.54    -3.81 3.81        $cladding
c 720 10 RPP  3.03403 3.31597  -2.52222 2.52222 -3.17 3.17        $core
c 721 10 RPP  3.01625 3.33375  -2.54    2.54    -3.81 3.81        $cladding
c 722 10 RPP  3.35153 3.63347  -2.52222 2.52222 -3.17 3.17        $core
c 723 10 RPP  3.33375 3.65125  -2.54    2.54    -3.81 3.81        $cladding
c ~~~~~~~~~~~~ 10 Plates right side, extra plates below ~~~~~~~
c 724  RPP  3.66903 3.95097  -2.52222 2.52222 -3.17 3.17        $core
c 725  RPP  3.65125 3.96875  -2.54    2.54    -3.81 3.81        $cladding
c 726  RPP  3.98653 4.26847  -2.52222 2.52222 -3.17 3.17        $core
c 727  RPP  3.96875 4.28625  -2.54    2.54    -3.81 3.81        $cladding
c 728  RPP  4.30403 4.58597  -2.52222 2.52222 -3.17 3.17        $core
```

```
c 729  RPP  4.28625 4.60375  -2.54    2.54    -3.81 3.81        $cladding
c 730  RPP  4.62153 4.90347  -2.52222 2.52222 -3.17 3.17        $core
c 731  RPP  4.60375 4.92125  -2.54    2.54    -3.81 3.81        $cladding
c 732  RPP  4.93903 5.22097  -2.52222 2.52222 -3.17 3.17        $core
c 733  RPP  4.92125 5.23875  -2.54    2.54    -3.81 3.81        $cladding
c 734  RPP  5.25653 5.53847  -2.52222 2.52222 -3.17 3.17        $core
c 735  RPP  5.23875 5.55625  -2.54    2.54    -3.81 3.81        $cladding
c 736  RPP  5.57403 5.85597  -2.52222 2.52222 -3.17 3.17        $core
c 737  RPP  5.55625 5.87375  -2.54    2.54    -3.81 3.81        $cladding
c ~~~~~~~~~~~~~~~~~~~~~~~~~~~~~~~~~~~~~~~~~~~~~~~~~~~~~~~~~~~~~~~~~~~~~~~
c    Left Plates
c ~~~~~~~~~~~~~~~~~~~~~~~~~~~~~~~~~~~~~~~~~~~~~~~~~~~~~~~~~~~~~~~~~~~~~~~
c 750 10 RPP -0.45847 -0.17653  -2.52222 2.52222 -3.17 3.17       $core
c 751 10 RPP -0.47625 -0.15875  -2.54    2.54    -3.81 3.81       $cladding
c 752 10 RPP -0.77597 -0.49403  -2.52222 2.52222 -3.17 3.17       $core
c 753 10 RPP -0.79375 -0.47625  -2.54    2.54    -3.81 3.81       $cladding
c 754 10 RPP -1.09347 -0.81153  -2.52222 2.52222 -3.17 3.17       $core
c 755 10 RPP -1.11125 -0.79375  -2.54    2.54    -3.81 3.81       $cladding
c 756 10 RPP -1.41097 -1.12903  -2.52222 2.52222 -3.17 3.17       $core
c 757 10 RPP -1.42875 -1.11125  -2.54    2.54    -3.81 3.81       $cladding
c 758 10 RPP -1.72847 -1.44653  -2.52222 2.52222 -3.17 3.17       $core
c 759 10 RPP -1.74625 -1.42875  -2.54    2.54    -3.81 3.81       $cladding
c 760 10 RPP -2.04597 -1.76403  -2.52222 2.52222 -3.17 3.17       $core
c 761 10 RPP -2.06375 -1.74625  -2.54    2.54    -3.81 3.81       $cladding
c 762 10 RPP -2.36347 -2.08153  -2.52222 2.52222 -3.17 3.17       $core
c 763 10 RPP -2.38125 -2.06375  -2.54    2.54    -3.81 3.81       $cladding
c 764 10 RPP -2.68097 -2.39903  -2.52222 2.52222 -3.17 3.17       $core
c 765 10 RPP -2.69875 -2.38125  -2.54    2.54    -3.81 3.81       $cladding
c 766 10 RPP -2.99847 -2.71653  -2.52222 2.52222 -3.17 3.17       $core
c 767 10 RPP -3.01625 -2.69875  -2.54    2.54    -3.81 3.81       $cladding
c 768 10 RPP -3.31597 -3.03403  -2.52222 2.52222 -3.17 3.17       $core
c 769 10 RPP -3.33375 -3.01625  -2.54    2.54    -3.81 3.81       $cladding
```

```
c 770 10 RPP -3.63347 -3.35153  -2.52222 2.52222 -3.17 3.17       $core
c 771 10 RPP -3.65125 -3.33375  -2.54    2.54    -3.81 3.81       $cladding
c ~~~~~~~~~~~~~ 10 Plates left side, extra plates below ~~~~~~~
c 772  RPP -3.95097 -3.66903  -2.52222 2.52222 -3.17 3.17       $core
c 773  RPP -3.96875 -3.65125  -2.54    2.54    -3.81 3.81       $cladding
c 774  RPP -4.26847 -3.98653  -2.52222 2.52222 -3.17 3.17       $core
c 775  RPP -4.28625 -3.96875  -2.54    2.54    -3.81 3.81       $cladding
c 776  RPP -4.58597 -4.30403  -2.52222 2.52222 -3.17 3.17       $core
c 777  RPP -4.60375 -4.28625  -2.54    2.54    -3.81 3.81       $cladding
c 778  RPP -4.90347 -4.62153  -2.52222 2.52222 -3.17 3.17       $core
c 779  RPP -4.92125 -4.60375  -2.54    2.54    -3.81 3.81       $cladding
c 780  RPP -5.22097 -4.93903  -2.52222 2.52222 -3.17 3.17       $core
c 781  RPP -5.23875 -4.92125  -2.54    2.54    -3.81 3.81       $cladding
c 782  RPP -5.53847 -5.25653  -2.52222 2.52222 -3.17 3.17       $core
c 783  RPP -5.55625 -5.23875  -2.54    2.54    -3.81 3.81       $cladding
c 784  RPP -5.85597 -5.57403  -2.52222 2.52222 -3.17 3.17       $core
c 785  RPP -5.87375 -5.55625  -2.54    2.54    -3.81 3.81       $cladding
c ~~~~~~~~~~~~~ Void Planes, core centered in z-direction ~~~~~~~
798 10 PZ     2.4460
799 10 PZ    -2.4460
c ~~~~~~~~~~~~~~~~~ Plate holder
800 10 RPP    -0.95875    -0.15875  -4    4       -3.81  6  $ left
801 10 RPP     0.15875     0.95875   -4    4       -3.81  6   $ right
802 10 RPP      -6      6           -6    6       -4.81 -3.81   $ bottom
c *** END SURFACES *** ------------------------------------------------------
-


c *** DATA *** ---------------------------------------
c ------------------------------------------------------------------------
-
c ~~~~~~~~~~~~~~~~~~~~~~~~~~~~~~~~~~~~~~~~~~~~~~~~~~~~~
c    Translations
c ~~~~~~~~~~~~~~~~~~~~~~~~~~~~~~~~~~~~~~~~~~~~~~~~~~~~~
```

```
  TR2  0 0 0       0.7071  0.7071  0   -0.7071  0.7071  0   0  0  1
  TR3  0 0 0       0       1       0   -1       0       0   0  0  1
  TR4  0 0 0      -0.7071  0.7071  0   -0.7071 -0.7071  0   0  0  1
  TR5  0 0 0      -1       0       0    0      -1       0   0  0  1
  TR6  0 0 0      -0.7071 -0.7071  0    0.7071 -0.7071  0   0  0  1
  TR7  0 0 0       0      -1       0    1       0       0   0  0  1
  TR8  0 0 0       0.7071 -0.7071  0    0.7071  0.7071  0   0  0  1
  TR1  0 0 -17.25
  TR9  16.92 0 5.31
  *TR10 0 0 0    22.5 112.5 90 -67.5 22.5 90 90 90 0  $ConfigAr
c *TR10 0 0 0      0 -90 90  -90 90 0  -90 -180 -90 1 $ConfigB
c *TR10 0 0 0    -90  90  0  -90 0 -90 -180 -90 -90 1 $ConfigC
c ~~~~~~~~~~~~~~~~~~~~~~~~~~~~~~~~~~~~~~~~~~~~~~~~~~~~~~~~~~~~
c    Physics
c ~~~~~~~~~~~~~~~~~~~~~~~~~~~~~~~~~~~~~~~~~~~~~~~~~~~~~~~~~~~~
  MODE n p
  PHYS:N J 20
  PHYS:P 100 1 1 j j
  CUT:P 2J 0
c ~~~~~~~~~~~~~~~~~~~~~~~~~~~~~~~~~~~~~~~~~~~~~~~~~~~~~~~~~~~~
c    Source
c ~~~~~~~~~~~~~~~~~~~~~~~~~~~~~~~~~~~~~~~~~~~~~~~~~~~~~~~~~~~~
  SDEF CEL=D1  AXS=0 0 1  POS 0 0 0  RAD d2 EXT d3
  SI1 L 800 $ 801 $ 802 $ 803 $ 804 $ 805 $ 806 $ 807 $ 808 $ 809 $ 810 811
  SP1   1   $ 1 $ 1 $ 1 $ 1 $ 1 $ 1 $ 1 $ 1 $ 1 $ 1 1
  SI2  0   3.8
  SI3 -3.17   3.17
  IPOL 3 1 2 0 J 2 16 10 20 30 40 50 60 70 80 90
                   100 110 120 130 140 150 160
  RPOL 0.01 0.01
  c CUT:n  j  0.0001
  NPS 5e6 $ 2742777 = Number of reactions in 3600 sec (aged PM src)
```

```
  FILES 21 DUMN1
  DBCN
  PRDMP 2J 1
C ~~~~~~~~~~~~~~~~~~~~~~~~~~~~~~~~~~~~~~~~~~~~~~~~~~~~~~~~~~~~~~~
c    Materials
C ~~~~~~~~~~~~~~~~~~~~~~~~~~~~~~~~~~~~~~~~~~~~~~~~~~~~~~~~~~~~~~~
c  EJ-309 liquid scintillator d=-0.916
c (Eljen Technologies, EJ-309 Fact Sheet)
C ~~~~~~~~~~~~~~~~~~~~~~~~~~~~~~~~~~
    m1   nlib=60c  plib=04p
       1001      0.548
       6000      0.452
C ~~~~~~~~~~~~~~~~~~~~~~~~~~~~~~~~~~
c Air, Dry (near sea level) d=-1.205E-3
c (Mat. Compendium PNNL)
C ~~~~~~~~~~~~~~~~~~~~~~~~~~~~~~~~~~
  m2  NLIB=70c PLIB=04p
      7014  -0.755636   $ N
      8016  -0.231475   $ O
      18040.70c -0.012838 $ Ar-40 at 99.6035 percent of natural Ar
      18036.70c -0.000043 $ Ar-36 at 0.3336 percent of natural Ar
      18038.70c -0.000008 $ Ar-38 at 0.00629 percent of natural Ar
C ~~~~~~~~~~~~~~~~~~~~~~~~~~~~~~~~~~
c  Lead Shielding d=-11.34
c
C ~~~~~~~~~~~~~~~~~~~~~~~~~~~~~~~~~~
  m3  82000.50c 1
c tungsten rho = 19.25
  m31 74000.60c 1
C ~~~~~~~~~~~~~~~~~~~~~~~~~~~~~~~~~~
c Polyethylene d=-0.9300
c (Mat. Compendium PNNL)
```

```
c ~~~~~~~~~~~~~~~~~~~~~~~~~~~~~~~~~
  m4  nlib=60c  plib=04p
      1001 -0.143716
      6000 -0.856284
c ~~~~~~~~~~~~~~~~~~~~~~~~~~~~~~~~~
c Aluminum table d=-2.70
c ~~~~~~~~~~~~~~~~~~~~~~~~~~~~~~~~~
  m5  nlib=60c  plib=04p
     13027     -1
c ~~~~~~~~~~~~~~~~~~~~~~~~~~~~~~~~~
c Concrete (Mat. Compendium PNNL) d=-2.3
c (Mat. Compendium PNNL)
c ~~~~~~~~~~~~~~~~~~~~~~~~~~~~~~~~~
  m6  nlib=60c  plib=04p
      1001     -0.022100
      6000     -0.002484
      8016     -0.574930
     11023     -0.015208
     12000     -0.001266
     13027     -0.019953
     14000     -0.304627
     19000     -0.010045
     20000     -0.042951
     26000.42c -0.006435
c ~~~~~~~~~~~~~~~~~~~~~~~~~~~~~~~~~
c  Pu Metal Sample d=-22.4
c (PM3)
c ~~~~~~~~~~~~~~~~~~~~~~~~~~~~~~~~~
  m7  94238.42c   -0.00023
      94239.60c   -0.85141
      94240.60c   -0.07891
      94241.60c   -0.00089
```

```
      94242.60c   -0.00044
      95241.61c   -0.00888
      28058.60c   -0.01148
      28060.60c   -0.00442
      28061.60c   -0.00019
      28062.60c   -0.00061
      29063.60c   -0.02951
      29065.60c   -0.01316
c ~~~~~~~~~~~~~~~~~~~~~~~~~~~~~~~~
c Steel d=-7.92
c (Mat. Compendium PNNL)
c ~~~~~~~~~~~~~~~~~~~~~~~~~~~~~~~~
  m8  26000.55c -0.6950
      24000.50c -0.1900
      28000.50c -0.0950
      25055.51c -0.0200
c ~~~~~~~~~~~~~~~~~~~~~~~~~~~~~~~~
c BK7
c ~~~~~~~~~~~~~~~~~~~~~~~~~~~~~~~~
  m9 NLIB=70c PLIB=04p
      14028 -0.323138999
      8016  -0.483882614
      5011  -0.033384805
      56138.60c -0.027496631
      11023 -0.077153875
      19039 -0.052216449
      33075 -0.002726626
c ~~~~~~~~~~~~~~~~~~~~~~~~~~~~~~~~
c mumetal
c ~~~~~~~~~~~~~~~~~~~~~~~~~~~~~~~~
   m10 28000.50c 0.8             $ mu-metal
       42000.60c    0.05
```

```
       14000.60c    0.005
       29063     0.0002          nlib = 60c
       26056     0.1448          nlib = 70c
c ~~~~~~~~~~~~~~~~~~~~~~~~~~~~~~~~~~
c ABS   rho = 1.06
c ~~~~~~~~~~~~~~~~~~~~~~~~~~~~~~~~~~
   m11  1001.70c  .07        $ ABS
        6012.42c  .93
c ~~~~~~~~~~~~~~~~~~~~~~~~~~~~~~~~~~
c vinyl  rho = 1.19
c ~~~~~~~~~~~~~~~~~~~~~~~~~~~~~~~~~~
   m12  1001.70c  .07        $ vinyl
        6012.42c  .559
        8016.60c  .371
c ~~~~~~~~~~~~~~~~~~~~~~~~~~~~~~~~~~
c stilbene  rho = 1.16
c ~~~~~~~~~~~~~~~~~~~~~~~~~~~~~~~~~~
   m13  1001.70c  .4615        $ Stilbene
        6012.42c  .5385
c ~~~~~~~~~~~~~~~~~~~~~~~~~~~~~~~~~~
c  PAHN Plates
c ~~~~~~~~~~~~~~~~~~~~~~~~~~~~~~~~~~
 m15  nlib=66c $pu rho 15.08 g/cm3
       94239   -0.94153
       94240   -0.04475
       94241   -0.00043
       94242   -0.00622
       95241   -0.00222
       13027   -0.01102
 m16  nlib=66c  $cladding rho 8 g/cm3
       26054  -0.04074
       26056  -0.63953
```

```
        26057  -0.01477
        26058  -0.00197
        24050  -0.00799
        24052  -0.15417
        24053  -0.01748
        24054  -0.00435
        28058  -0.06059
        28060  -0.02334
        28061  -0.00101
        28062  -0.00323
        28064  -0.00082
        25055  -0.017
        6000   -0.012
c ~~~~~~~~~~~~~~~~~~~~~~~~~~~~~~~~~~~~~~~~~~~~~~~~~~~~~~~~~~~~~~~
c    Tallies
c ~~~~~~~~~~~~~~~~~~~~~~~~~~~~~~~~~~~~~~~~~~~~~~~~~~~~~~~~~~~~~~~
c *** END DATA *** ------------------------------------------------------------
```

Appendix B. Source Specification Sheets

^{252}Cf Source FTC-CF-5276

Usage Procedures for FTC-CF-5276

This document describes procedures for Detection for Nuclear Nonproliferation Group researchers (faculty, staff, and students) performing measurements with ^{252}Cf source FTC-CF-5276

Source information as of 8-May-2015:

Mass: 10.5 μg Cf-252
Activity: (10.5 μg)(536.3 μCi/μg) = 5.63 mCi
Neutron output: 6.44×10^{6} fissions/s (2.41×10^{7} n/s)

CBNM Plutonium Oxide Sources

Certified Nuclear Reference Material

Certificate of Analysis

CBNM-NRM271

CBNM NUCLEAR REFERENCE MATERIAL 271
Pu isotope Abundances and ^{241}Am Concentration
Certified Reference Material (PuO_2) for Gamma-Ray Spectrometry

$\frac{Pu(iso)}{Pu(total)}$, $\frac{^{241}Am}{Pu(total)}$ abundances and uncertainties (95 % confidence level) valid at 20 June 1986

- atom per cent (at %)

Material / Isotope	^{238}Pu	^{239}Pu	^{240}Pu	^{241}Pu	^{242}Pu	$^{241}Am^*$
CBNM Pu93	0.0117 2	93.4392 40	6.2386 39	0.2215 4	0.0390 3	0.1039 21
CBNM Pu84	0.0706 6	84.3985 84	14.1578 85	1.0197 18	0.3534 10	0.2157 22
CBNM Pu70	0.8506 18	73.4248 98	18.2445 87	5.4257 34	2.0544 23	1.1624 116
CBNM Pu61	1.2045 25	62.6562 283	25.3526 241	6.6376 87	4.1491 64	1.4362 144

- mass per cent (m%)

Material / Isotope	^{238}Pu	^{239}Pu	^{240}Pu	^{241}Pu	^{242}Pu	$^{241}Am^*$	Mass g
CBNM Pu93	0.0117 2	93.4123 40	6.3131 39	0.2235 4	0.0395 3	0.1047 21	6.625
CBNM Pu84	0.0703 6	84.3377 84	14.2069 85	1.0275 18	0.3576 10	0.2173 22	6.650
CBNM Pu70	0.8458 18	73.3191 98	18.2945 87	5.4634 34	2.0772 23	1.1705 117	6.665
CBNM Pu61	1.1969 25	62.5255 283	25.4058 241	6.6793 87	4.1925 64	1.4452 144	6.626

This certificate applies to the reference samples : CBNM Pu 93 0/1
CBNM Pu 84 0/1
CBNM Pu 70 0/1
CBNM Pu 61 0/1

Commission of the European Communities
Joint Research Centre
Central Bureau for Nuclear Measurements

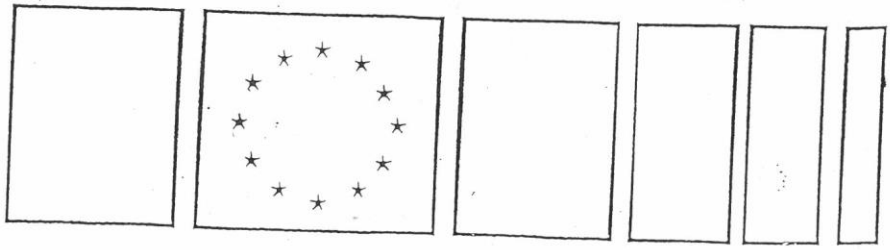

PuGa 207-211 Disks

5. CERTIFIED PLUTONIUM MASSES IN THE NDA SOURCES

The discs of PuGa were electropolished prior to weighing in an active handling facility, in a pure nitrogen atmosphere. The discs were directly weighed on a Satorius electronic analytical balance (type R160P) with a sensitivity of 0.01mg. The balance was calibrated using weights traceable to the International Organisation of Legal Metrology Class E2 standard. The certified plutonium masses of the PuGa alloy disc sources are given in the following table.

Source number	PuGa Weight/g	Disc diameter/ mm	Disc thickness/ mm	Pu Weight/g
201	0.00954 ±0.00005	2.0	0.2	0.00920 ±0.00005
202	0.01820 ±0.00005	2.8	0.2	0.01755 ±0.00005
203	0.04639 ±0.00012	4.5	0.2	0.04472 ±0.00013
204	0.09725 ±0.00008	6.5	0.2	0.09376 ±0.00009
205	0.18715 ±0.00010	9.0	0.2	0.18043 ±0.00013
206	0.45580 ±0.00005	14.0	0.2	0.43943 ±0.00013
207	0.92759 ±0.00006	20.0	0.2	0.89428 ±0.00021
208	0.91673 ±0.00007	11.5	0.6	0.88381 ±0.00022
209	1.94130 ±0.00010	16.5	0.6	1.87159 ±0.00041
210	4.97190 ±0.00005	26.0	0.6	4.79336 ±0.00084
211	9.80750 ±0.00016	36.5	0.6	9.45531 ±0.00173

The uncertainties for the quoted weights of PuGa have been estimated by adding the fixed uncertainty for the calibration weight at the appropriate level to the random measurement uncertainty obtained from the replicate weighings. The total uncertainty for the Pu weight has been calculated from the uncertainty in the PuGa weight plus the uncertainty in the Pu content of the alloy.

6. SOURCE ENCAPSULATION

The standard sources are contained in single encapsulation stainless steel assemblies, sealed by an arc welding procedure. The completed sources were subjected to the BS 5288, D3.1 bubble leak test, BS 5288, D3.4 helium leak test and BS 5288, D2.1 freedom from surface contamination test. All encapsulations passed these tests. The standard sources containing up to 0.1g Pu are classified as BS5288/C22213: the sources containing greater than 0.1g Pu are classified as BS5288/E22213.

It should be noted that the capsule design does not have design approval as a transport container for special form radioactive material.

7. SURFACE RADIATION OUTPUT

Surface radiation measurements were made on the encapsulated sources using TLD extremity dosemeters to obtain typical dose rates to fingers for direct handling of the sources. The measured dose rates are shown in the following table.

Source Number	Surface radiation/mSv.hr^{-1}
201	3.5
202	3.1
203	6.1
204	11
205	24
206	21
207	37
208	32
209	34
210	29
211	39

8. AUTHORISATION FOR ISSUE

J W A Tushingham
Manager, Actinide Analysis and Standards

J W McMillan
Manager, Nuclear Materials Analysis Section

3. CERTIFIED COMPOSITION VALUES

a. Plutonium Mass Content

The certified plutonium mass content of the PuGa material based on measurements by CPC is 96.409% (reference date: April 1996). The standard deviation of the coulometric measurements is ±0.016%. The CPC measurements were made with respect to the reference material UK Pu1.

b. Isotopic Composition

The plutonium isotopic composition is given in the following table

Plutonium Isotope	238	239	240	241	242
Weight per cent	0.1336	75.6606	21.4898	1.9510	0.7651
% rsd	0.04%	0.03%	0.07%	0.93%	0.38%

The mass spectrometric measurements were made in July 1996 and were corrected for mass fractionation effects by the use of the 1:1:1 ^{239}Pu:^{240}Pu:^{242}Pu reference material, UK Pu3.

The value for the weight ratio of americium to plutonium based on LSC measurements is 0.0186:1, with a total uncertainty of ± 0.0002:1 (reference date: July 1996).

4. IMPURITIES AND ALLOYING CONSTITUENT

Gallium and impurity elements determined by the methods given in Section 2 were found to be present at the levels given in the following table.

Impurity	Content, ppm	Impurity	Content, ppm
Ga	15000	Hg	<0.5
Si	350	In	<8
Fe	270	Ir	<5
Ni	180	K	<20
C	160	Li	<1
Cl	140	Lu	<0.2
Cu	120	Mo	<1
Al	65	Na	<7
Ta	49	Nb	<2
Cr	46	Nd	<5
F	25	Pb	<3
Mn	8	Rb	<60
Be	4	Re	<3
Tm	4	Rh	<3
Mg	1	Ru	<3
Ca	1	Sb	<5
Ag	<2	Sc	<0.2
As	<4	Sm	<13
Au	<2	Sn	<2
B	<7	Sr	<0.5
Ba	<0.5	Th	<4
Cd	<0.5	Ti	<2
Ce	<20	U	<100
Co	<1	V	<1
Dy	<2	W	<5
Eu	<1	Y	<0.5
Gd	<8	Zn	<1
Hf	<2	Zr	<1

PuGa73240 Disks

CERTIFICATE OF ANALYSIS

PuGa Source Material No. 73240

1. DESCRIPTION

The Pu - 1.5% Ga alloy was prepared at Harwell as a single casting. The alloy was homogenised by repeated sub-dividing, melting and recasting. The homogenised PuGa alloy was arc melted into buttons which were pressed into plates ca. 3.5mm thick. These plates were subsequently rolled to foils 0.2mm and 0.6mm thick.

NDA sources in disc form of the required size were produced from the Pu-Ga alloy foils and sealed in stainless steel encapsulation assemblies.

2. METHOD OF CHARACTERISATION

The PuGa source material was characterised for plutonium mass content by Controlled Potential Coulometry (CPC). The plutonium isotopic composition was determined by thermal ionisation mass spectrometry. Alpha spectrometry was used to obtain the ^{238}Pu value whilst liquid scintillation counting (LSC) was used to determine the ^{241}Am content of the plutonium.

The PuGa alloy was analysed for a range of impurity elements. The carbon content was determined by a combustion technique followed by manometric measurement of evolved carbon dioxide. The fluoride and chloride contents were determined using ion selective electrodes, following separation by pyrohydrolysis. The iron content was determined by a direct spectrophotometric method whilst gallium was determined by isotope dilution mass spectrometry. Additional impurities were determined by inductively coupled plasma optical emission spectroscopy (ICPOES) following separation by reverse phase chromatography using DHDECMP extractant.

3. CERTIFIED COMPOSITION VALUES

a. Plutonium Mass Content

The certified plutonium mass content of the PuGa material based on measurements by CPC is 97.935% (reference date: April 1996). The standard deviation of the coulometric measurements is ±0.065%. The CPC measurements were made with respect to the reference material UK Pu1.

b. Isotopic Composition

The plutonium isotopic composition is given in the following table

Plutonium Isotope	238	239	240	241	242
Weight per cent	0.0117	93.8773	5.9009	0.1785	0.0316
% rsd	<0.01%	<0.01%	0.11%	0.95%	5.5%

The mass spectrometric measurements were made in July 1996 and were corrected for mass fractionation effects by the use of the 1:1:1 ^{239}Pu:^{240}Pu:^{242}Pu reference material, UK Pu3.

The value for the weight ratio of americium to plutonium based on LSC measurements is 0.00126:1, with a total uncertainty of ± 0.00001:1 (reference date: July 1996).

4. IMPURITIES AND ALLOYING CONSTITUENT

Gallium and impurity elements determined by the methods given in Section 2 were found to be present at the levels given in the following table.

Impurity	Content, ppm	Impurity	Content, ppm
Ga	14910	Hg	<0.5
Si	520	In	<8
Fe	200	Ir	<5
C	190	K	<20
Cl	120	Li	<1
Al	110	Lu	<0.2
Cu	89	Mo	<1
Tm	83	Na	<7
Be	70	Nb	<2
Mn	60	Nd	<5
Ni	40	Pb	<3
Ta	39	Rb	<60
Cr	28	Re	<3
F	20	Rh	<3
Mg	3	Ru	<3
Ca	2	Sb	<5
Ag	<2	Sc	<0.2
As	<4	Sm	<13
Au	<2	Sn	<2
B	<7	Sr	<0.5
Ba	<0.5	Th	<4
Cd	<0.5	Ti	<2
Ce	<20	U	<100
Co	<1	V	<1
Dy	<2	W	<5
Eu	<1	Y	<0.5
Gd	<8	Zn	<1
Hf	<2	Zr	<1

5. CERTIFIED PLUTONIUM MASSES IN THE NDA SOURCES

The discs of PuGa were electropolished prior to weighing in an active handling facility, in a pure nitrogen atmosphere. The discs were directly weighed on a Satorius electronic analytical balance (type R160P) with a sensitivity of 0.01mg. The balance was calibrated using weights traceable to the International Organisation of Legal Metrology Class E2 standard. The certified plutonium masses of the PuGa alloy disc sources are given in the following table.

Source number	PuGa Weight/g	Disc diameter/ mm	Disc thickness/ mm	Pu Weight/g
37	0.00929 ±0.00005	2.0	0.2	0.00910 ±0.00005
38	0.01888 ±0.00008	2.8	0.2	0.01849 ±0.00009
15	0.04670 ±0.00007	4.5	0.2	0.04574 ±0.00010
16	0.10519 ±0.00007	6.5	0.2	0.10302 ±0.00014
17	0.19349 ±0.00012	9.0	0.2	0.18949 ±0.00024
18	0.48157 ±0.00007	14.0	0.2	0.47163 ±0.00037
19	0.92057 ±0.00019	20.0	0.2	0.90156 ±0.00077
26	0.95950 ±0.00010	11.5	0.6	0.93969 ±0.00070
30	1.98725 ±0.00009	16.5	0.6	1.94621 ±0.00134
31	5.02867 ±0.00020	26.0	0.6	4.92482 ±0.00336
32	9.60256 ±0.00018	36.5	0.6	9.40427 ±0.00623

The uncertainties for the quoted weights of PuGa have been estimated by adding the fixed uncertainty for the calibration weight at the appropriate level to the random measurement uncertainty obtained from the replicate weighings. The total uncertainty for the Pu weight has been calculated from the uncertainty in the PuGa weight plus the uncertainty in the Pu content of the alloy.

6. SOURCE ENCAPSULATION

The standard sources are contained in single encapsulation stainless steel assemblies, sealed by an arc welding procedure. The completed sources were subjected to the BS 5288, D3.1 bubble leak test, BS 5288, D3.4 helium leak test and BS 5288, D2.1 freedom from surface contamination test. All encapsulations passed these tests. The standard sources containing up to 1g Pu are classified as BS5288/C22213: the 2g, 5g and 10g Pu sources are classified as BS5288/E22213.

It should be noted that the capsule design does not have design approval as a transport container for special form radioactive material.

7. SURFACE RADIATION OUTPUT

Surface radiation measurements were made on the encapsulated sources using TLD extremity dosemeters to obtain typical dose rates to fingers for direct handling of the sources. The measured dose rates are shown in the following table.

Source Number	Surface radiation/mSv.hr^{-1}
37	0.7
38	0.3
15	0.5
16	0.8
17	1.4
18	2.8
19	3.3
26	2.9
30	3.4
31	4.2
32	3.5

8. AUTHORISATION FOR ISSUE

J W A Tushingham
Manager, Actinide Analysis and Standards

J W McMillan
Manager, Nuclear Materials Analysis Section

ENEA MOX Canisters

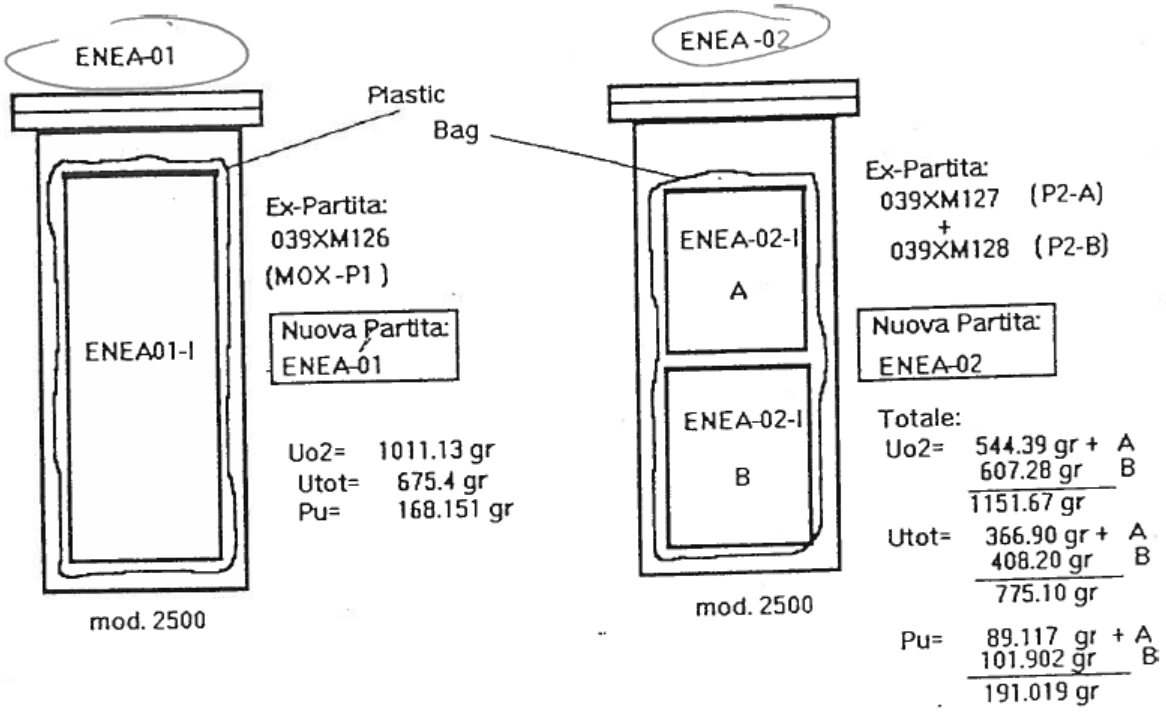

Figura 1

Mox - UNCP U/Pu

PF 89 ... qualificati il 30/08/88 ... 3.583

Uranio

U 234 = 0,008 %
U 235 = 0,709
U 236 = 0,008
U 238 = 99,275

Plutonio

Pu 238 = 0,17 %
Pu 239 = 66,54
Pu 240 = 28,02
Pu 241 = 3,26 →
Pu 242 = 2,01

Americio

2.7 Ci/l (Pu 97.6 g/l) al 14/12/88 0.07 ppm

PAHN/PANN Plutonium Metal Plates

Plate Family Series		PAHN		
Plate Vendor		54		
Plate Family Identification No.		215		
Size, inches		1/8 × 2 × 3		
Size, cm		0.32 × 5.08 × 7.62		
Clad, g	Fe, g	18.25		
	Cr, g	4.83		
	Ni, g	2.34		
	Mn, g	0.45		
	Other, g	0.31		
		Original assay values (July 1, 1983)	Decay-corrected composition values (Sept 22, 2014)	
Core, g	^{238}Pu	0.0003	0.0002	<0.01 wt%
	^{239}Pu	79.763	79.691	75.93 wt%
	^{240}Pu	24.000	23.921	22.79 wt%
	^{241}Pu	3.050	0.673	0.64 wt%
	^{242}Pu	0.671	0.671	0.64 wt%
	^{241}Am	1.966	4.247	
	Al	1.246		
	Total Pu Mass, g	107.484	104.957	

Plate Family Series		PANN			
Plate Vendor		18			
Plate Family Identification No.		146			
Size, inches		1/8 × 2 × 3			
Size, cm		0.32 × 5.08 × 7.62			
Clad, g	Fe, g	16.26			
	Cr, g	4.57			
	Ni, g	2.22			
	Mn, g	0.42			
	Other, g	0.293			
		Original assay values (July 1, 1983)		Decay-corrected composition values (Sept 22, 2014)	
Core, g	^{238}Pu	Trace		Trace	< 0.01 wt%
	^{239}Pu	98.982		98.894	95.42 wt%
	^{240}Pu	4.716		4.701	4.54 wt%
	^{241}Pu	0.211		0.046	0.04 wt%
	^{242}Pu	0.005		0.005	<0.01 wt%
	^{241}Am	0.245		0.397	
	Al	1.158			
	Total Pu Mass, g	103.914		103.646	

Appendix C. PSD Surface Plots for Plutonium Sources

CBNM Plutonium Oxide Sources, Hybrid Rejection

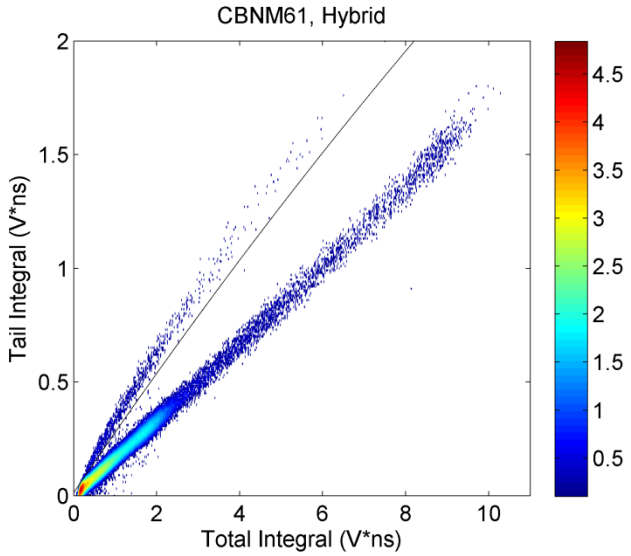

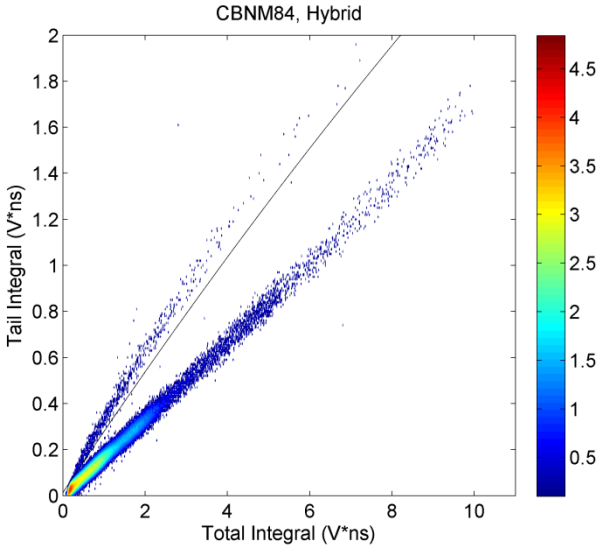

PuGa73240 Disks

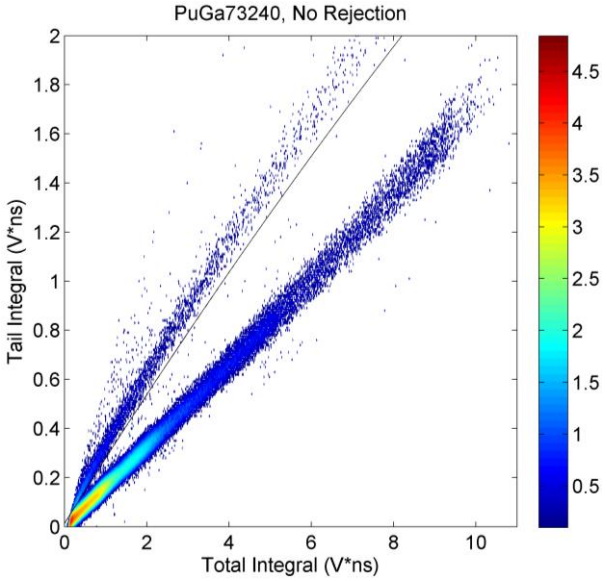

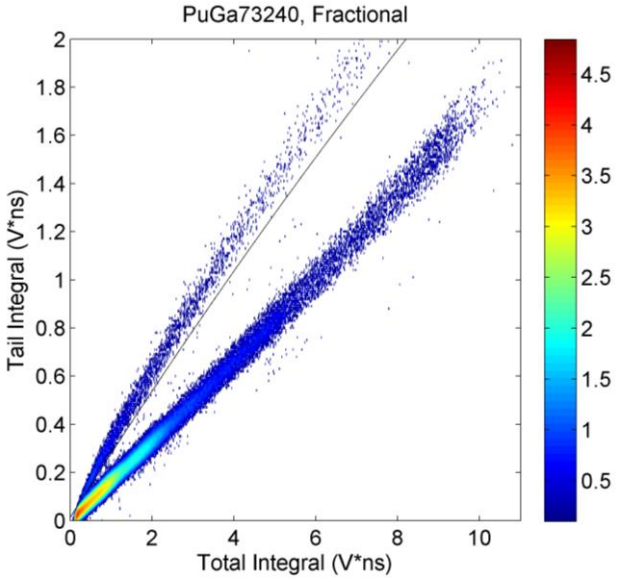

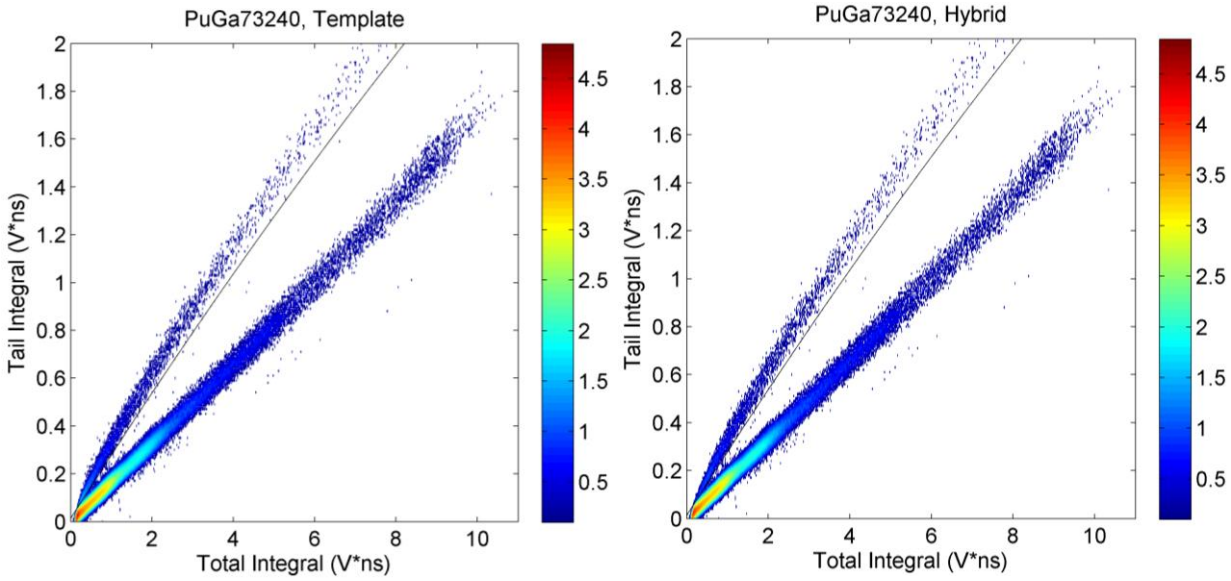

PuGa207-211 Disks, Hybrid Rejection

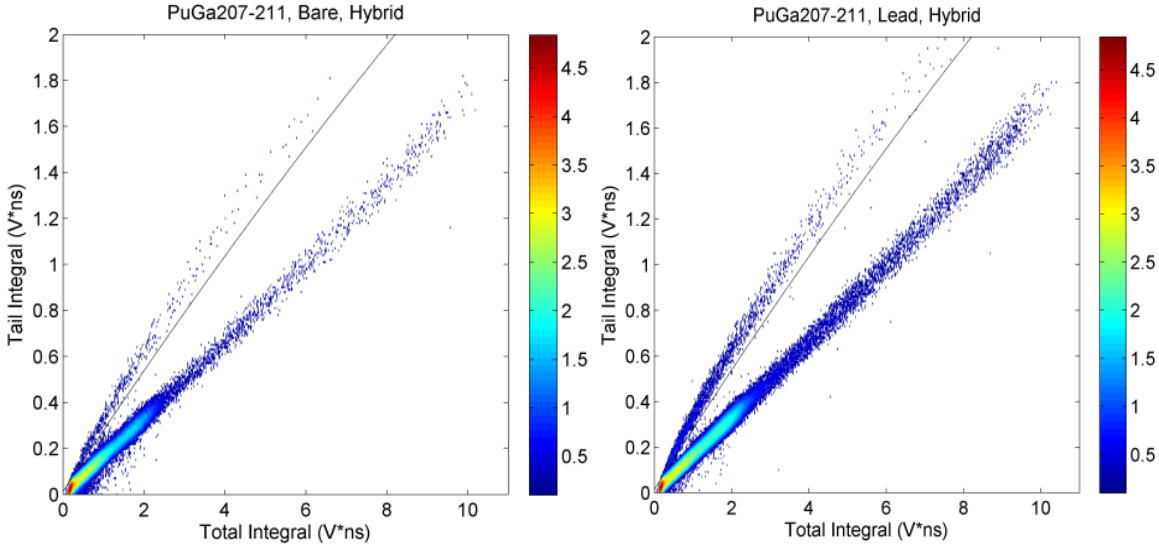

References

1. The White House (2012), "Remarks by President Obama at Opening Plenary Session of the Nuclear Security Summit," Retrieved on July 25, 2015 from https://www.whitehouse.gov/the-press-office/2012/03/26/remarks-president-obama-opening-plenary-session-nuclear-security-summit.

2. D.A. Shea and D. Morgan, "The Helium-3 Shortage: Supply, Demand, and Options for Congress," Congressional Research Service, 21 September 2010.

3. Office of Science: U.S. Department of Energy (2015), "Isotope Development & Production for Research and Applications (IDPRA): Supply and Demand for Helium-3," Retrieved on July 29, 2015 from http://science.energy.gov/np/research/idpra/3he-fact-sheet/.

4. F.D. Brooks, "Development of Organic Scintillators," *Nuclear Instruments and Methods*, 162, pp. 477-505, 1979.

5. American National Standards Institute, "American National Standard for Evaluation and Performance of Radiation Detection Portal Monitors for Use in Homeland Security," ANSI N42.35-2006, Institute of Electrical and Electronics Engineers, Inc., 2007.

6. S.L. Blatt, J. Mahieux, and D. Kohler, "Elimination of Pulse Pileup Distortion in Nuclear Radiation Spectra," *Nuclear Instruments and Methods in Physics Research Section A*, 60, pp. 221-230, 1968.

7. Southern Innovation, *Technology Briefing Document*, Retrieved January 11, 2016 from http://southerninnovation.com/uploads/SITOROTechnologySummary.pdf.

8. G. H.V. Bertrand, M. Hamel, S. Normand, and F. Sguerra, "Pulse Shape Discrimination Between (Fast or Thermal) Neutrons and Gamma Rays with Plastic Scintillators: State of the Art," *Nuclear Instruments and Methods in Physics Research Section A*, 776, pp. 114-128, 2015.

9. S.V. Budakovsky, N.Z. Galunov, N.L. Karavaeva, J.K. Kim, Y.K. Kim, O.A. Tarasenko, and E.V. Martynenko, "New Effective Organic Scintillators for Fast Neutron and Short-Range Radiation Detection," *IEEE Transactions on Nuclear Science*, 54 (6), pp. 2734-2740, 2007.

10. L. Carman, N. Zaitseva, H. Paul Martinez, B. Rupert, I. Pawelczak, A. Glenn, H. Mulcahy, R. Leif, K. Lewis, and S. Payne, "The Effect of Material Purity on the Optical and Scintillation Properties of Solution-Grown Trans-Stilbene Crystals," *Journal of Crystal Growth*, 368, pp. 56-61, 2013.

11. D. Reilly, N. Ensslin, H. Smith Jr., and S. Kreiner (1991), *Passive Nondestructive Assay of Nuclear Materials*, Washington, DC: U.S. Government Printing Office.

12. J. Fuller, "Verification on the Road to Zero: Issues for Nuclear Warhead Dismantlement," *Arms Control Today*, pp. 1-11, 2010.

13. H. Furci, M. Arribére, and S. R. Guevara, "Self-Shielding Corrections in Cylindrical Samples in Gamma Spectroscopy with Germanium Well-Type Detectors," *Nuclear Instruments and Methods in Physics Research Section A*, 705, pp. 132-139, 2013.

14. S.D. Clarke, S.A. Pozzi, M. Flaska, R.B. Oberer, and L.G. Chiang, "Monte Carlo Analysis of Gamma-ray Spectroscopy of Uranium-Oxide Samples," Transactions of the 2012 Conference for the Institute of Nuclear Materials Management (INMM 2012), Orlando, FL, USA, July 15 – 19, 2012.

15. Saint-Gobain Crystals, *Gas-Filled Radiation Detectors: Helium-3 Proportional Counters*, Retrieved November 6, 2015 from http://www.oilandgas.saint-gobain.com/uploadedFiles/SGoilandgas/Documents/Detectors/Detectors-Helium-3-Tubes.pdf.

16. G.F. Knoll (2010), *Radiation Detection and Measurement*, Hoboken, NJ: John Wiley & Sons, Inc.

17. N. Ensslin, W.C. Harker, M.S. Krick, D.G. Langner, M.M. Pickrell, and J.E. Stewart, "Application Guide to Neutron Multiplicity Counting," Los Alamos Report LA-13422-M, 1998.

18. A.P. Simpson, S. Jones, M.J. Clapham, and S.A. McElhaney, "A Review of Neutron Detection Technology Alternatives to Helium-3 for Safeguards Applications," Transactions of the 2011 Conference for the Institute of Nuclear Materials Management (INMM 2011), July 17-21, 2011, Palm Desert, CA.

19. R.T. Kouzes, J.R. Ely, A.T. Lintereur, and D.L. Stephens, 2009, "Neutron Detector Gamma Insensitivity Criteria," PNNL-18903.

20. J.K. Polack, M. Flaska, A. Enqvist, C.S. Sosa, C.C. Lawrence, and S.A. Pozzi, "An Algorithm for Charge-Integration, Pulse-Shape Discrimination and Estimation of Neutron/Photon Misclassification in Organic Scintillators," *Nuclear Instruments and Methods in Physics Section A* (2015), http://dx.doi.org/10.1016/j.nima.2015.05.048.

21. N.Z. Galunov, O.A. Tarasenko, and V.A. Tarasov, "Determination of the Light Yield of Organic Scintillators," *Functional Materials*, 20(3), pp. 304-309, 2013.

22. N. Zaitseva, A. Glenn, L. Carman, H. P. Martinez, R. Hatarik, H. Klapper, and S. Payne, "Scintillation Properties of Solution-Grown Trans-Stilbene Single Crystals," *Nuclear Instruments and Methods in Physics Research Section A*, 789, pp. 8-15, 2015.

23. D. Cester, G. Nebbia, L. Stevanato, F. Pino, and G. Viesti, "Experimental Tests of the New Plastic Scintillator With Pulse Shape Discrimination Capabilities EJ-299-33," *Nuclear Instruments and Methods in Physics Section A*, 735, pp. 202-206, 2014.

24. Eljen Technology (2010), *EJ-309 Liquid Scintillator Pulse-Shape Discrimination Properties*, Retrieved August 6, 2015 from http://www.eljentechnology.com/index.php/products/liquid-scintillators/73-ej-309.

25. Eljen Technology (2014), *EJ-299-33A PSD Plastic Scintillator*, Retrieved August 6, 2015 from http://www.eljentechnology.com/index.php/products/plastic-scintillators/114-ej-299-33.

26. U. Shirwadkar, E.V.D. Van Loef, G. Markosyan, J. Glodo, L. Soundara-Pandian, V. Biteman, A. Gueorguiev, K.S. Shah, S. Pozzi, S. Clarke, and M. Bourne, "New Generation Plastic Scintillators for Fast Neutron Spectroscopy and Pulse Shape Discrimination," Transactions of the Nuclear Science Symposium and Medical Imaging Conference (IEEE 2013), October 27 – November 2, 2013, Seoul, South Korea.

27. J.L. Dolan, M. Flaska, A. Poitrasson-Rivière, A. Enqvist, P. Peerani, D.L. Chichester, and S.A. Pozzi, "Plutonium Measurements with a Fast Neutron Multiplicity Counter for Nuclear Safeguards Applications," *Nuclear Instruments and Methods in Physics Research Section A,* 763, pp. 565-574, 2014.

28. S.D. Clarke, M. Flaska, S.A. Pozzi, and P. Peerani, "Neutron and Gamma-Ray Cross-Correlation Measurements of Plutonium Oxide Powder," *Nuclear Instruments and Methods in Physics Research Section A,* 604(3), pp. 618-623, 2009.

29. E.C. Miller, S.D. Clarke, A. Enqvist, S.A. Pozzi, P. Marleau, and J.K. Mattingly, "Characterization of Special Nuclear Material Using a Time-Correlated Pulse-Height Analysis," *Journal of Nuclear Materials Management,* 51(1), pp. 32-37, 2012.

30. P. Harihar and H. Chen, "Scintillation Decays in a Trans-Stilbene Crystal," *Nuclear Instruments and Methods in Physics Research Section A,* 336, pp. 176-178, 1993.

31. N. Zaitseva, A. Glenn, L. Carman, R. Hatarik, S. Hamel, M. Faust, B. Schabes, N. Cherepy, and S. Payne, "Pulse Shape Discrimination in Impure and Mixed Single-Crystal Organic Scintillators," *IEEE Transactions on Nuclear Science,* 58, pp. 3411-3420, 2011.

32. CAEN, (2015), *Digitizer Families*, Retrieved November 17, 2015 from http://www.caen.it/csite.

33. ET Enterprises, (2011), *Photomultipliers from ET Enterprises Ltd*, Retrieved December 20, 2012 from http://www.et-enterprises.com/.

34. A. Enqvist, C.C. Lawrence, B.M. Weiger, S.A. Pozzi, and T.N. Massey, "Neutron Light Output Response and Resolution Functions in EJ-309 Liquid Scintillation Detectors," *Nuclear Instruments and Methods in Physics Research Section A,* 715, pp. 79-86, 2013.

35. E. Padovani, S.A. Pozzi, S.D. Clarke, and E.C. Miller, "MCNPX-PoliMi," *RSICC package number C00791 MNYCP 00,* www.rsicc.ornl.gov.

36. E.C. Miller, A. Poitrasson-Rivière, A. Enqvist, J.L. Dolan, S. Prasad, M.M. Bourne, K. Weinfurther, S.D. Clarke, M. Flaska, S.A. Pozzi, E. Padovani, and J. Mattingly,

"MCNPX-PoliMi Post-Processor (MPPost) Manual," *RSICC package number C00791 MNYCP 00*, www.rsicc.ornl.gov.

37. S.A. Pozzi, M. Flaska, A. Enqvist, and I. Pázsit, "Monte Carlo and Analytical Models of Neutron Detection with Organic Scintillation Detectors," *Nuclear Instruments and Methods in Physics Research Section A*, 582(2), pp. 629-637, 2007.

38. M.M. Bourne, S.D. Clarke, N. Adamowicz, S.A. Pozzi, N. Zaitseva, and L. Carman, "Neutron Detection in a High-Gamma Field Using Solution-Grown Stilbene," *Nuclear Instruments and Methods in Physics Research Section A*, currently under review.

39. A.C. Kaplan, M. Flaska, A. Enqvist, J.L. Dolan, and S.A. Pozzi, "EJ-309 Pulse Shape Discrimination Performance with a High Gamma-ray-to-Neutron Ratio and Low Threshold," *Nuclear Instruments and Methods in Physics Section A*, 729, pp. 463-468, 2013.

40. M.M. Bourne, J.J. Whaley, J.L. Dolan, K. Polack, M. Flaska, S.D. Clarke, A. Tomanin, P. Peerani, and S.A. Pozzi, "Cross-Correlation Measurements with the EJ-299-33 Plastic Scintillator," *Nuclear Instruments and Methods in Physics Research Section A*, Volume 784, pp. 460-464, 2015.

41. S.A. Pozzi, B. Wieger, A. Enqvist, S.D. Clarke, M. Flaska, M. Marcath, E. Larsen, R.C. Haight, and E. Padovani, "Correlated Neutrons Emissions from ^{252}Cf," *Nuclear Science and Engineering*, 178(2), pp. 250-260, 2014.

42. E.M. Baum, M.C. Ernesti, H.D. Knox, T.R. Miller, and A.M. Watson (2010), *Chart of the Nuclides*, Schenectady, NY: Knolls Atomic Power Laboratory.

43. A. Giaz, L. Pellegri, F. Camera, N. Blasi, S. Brambilla, S. Ceruti, B. Million, S. Riboldi, C. Cazzaniga, G. Gorini, M. Nocente, A. Pietropaolo, M. Pillon, M. Rebai, and M. Tardocchi, "The CLYC-6 and CLYC-7 Response to γ-rays, Fast and Thermal Neutrons," *Nuclear Instruments and Methods in Physics Research Section A*, 810, pp. 132-139, 2016.